TUFTS UNIVERSITY

DOE/ER/40702-1
Tufts University
April 30, 1992

Coherent Production of Pions and Rho Mesons in Neutrino Charged Current Interactions on Neon Nuclei at the Fermilab Tevatron

Stéphane Willocq

(Ph.D. Thesis - Tufts University)

U.S. DEPARTMENT OF ENERGY

GRANT

DE-FG02-92ER40702

APRIL 30, 1992

NOTICE

Coherent Production of Pions and Rho Mesons in Neutrino Charged Current Interactions on Neon Nuclei at the Fermilab Tevatron

A dissertation

submitted by

Stéphane Willocq

In partial fulfillment of the requirements

for the degree of

Doctor of Philosophy

in

Physics

TUFTS UNIVERSITY

May, 1992

ABSTRACT OF THE DISSERTATION

Coherent Production of Pions and Rho Mesons in Neutrino Charged Current Interactions on Neon Nuclei at the Fermilab Tevatron

by Stéphane Willocq, Ph.D.

Dissertation Director: Prof. J. Schneps

The coherent production of single pions and ρ mesons in charged current interactions of neutrinos and antineutrinos on neon nuclei has been studied. The data were obtained using the Fermilab 15-foot Bubble Chamber, filled with a heavy Ne–H_2 mixture and exposed to the Quadrupole Triplet neutrino beam produced by 800 GeV protons from the Tevatron. The average beam energy was 86 GeV. In a sample of 330 000 frames, 1032 two-prong $\nu_\mu + \overline{\nu}_\mu$ charged current interactions were selected.

The goal of this study was to investigate the low Q^2 high ν region where the hadron dominance model can be tested. In this model, the vector and axial-vector parts of the weak hadronic current are dominated by the ρ and a_1 mesons respectively. Moreover, the Partially Conserved Axial Current (PCAC) hypothesis can be tested by studying the coherent production of single pions.

The coherent signal was extracted using the distributions in the variable $|t|$, the square of the four-momentum transferred to the neon nucleus. The signal for single pion coherent production was found to be 52.1 ± 9.4 events at $|t| < 0.1$ GeV^2. After correction for the experimental losses, the number of events was estimated to be 86.6 ± 19.6 events. This corresponds to a production rate with respect to the total number of charged current interactions of $(0.31 \pm 0.07)\%$. The cross section for coherent single pion production was thus calculated to be $(313 \pm 72) \times 10^{-40}$ cm^2 / neon nucleus. The cross section and kinematical characteristics of these events were found to be in good agreement with the predictions of a model based on the PCAC hypothesis and the hadron dominance model.

The signal for coherent single ρ meson production was found to be 19.2 ± 6.8 events at $|t| < 0.1$ GeV^2, i.e. 62.8 ± 27.0 events after correction for the experimental losses. The production rate with respect to the total number of charged current interactions was determined to be $(0.23 \pm 0.10)\%$. The corresponding single ρ meson coherent production was then calculated to be $(227 \pm 98) \times 10^{-40}$ cm^2 / neon nucleus. The cross section and the kinematical characteristics of these events were found to be in reasonable agreement with the predictions based on the hadron dominance model.

Acknowledgements

There are many people without whom this dissertation would have never been possible. In particular, I am indebted to my advisor, Prof. Jacob Schneps, for giving me the opportunity to pursue my endeavors in the Graduate Program in Physics at Tufts University. I am also indebted to Dr. Tomas Kafka for the care with which he has read this manuscript and for his interest in my work over the last four years. I especially wish to thank Dr. Pierre Marage, my "overseas advisor", for many years of friendship and encouragement, and above all, for much help and inspiration.

I have enjoyed working within the Tufts High Energy Physics group and would like to acknowledge all my fellow graduate students, and in particular, Mary Roach-Bellino for her excellent work with the figures.

I thank the scanning and measuring staff of the institutions which have contributed to the film analysis effort undertaken by the E632 Collaboration. Their excellent, yet painstaking work is praised. I thank all our collaborators, in particular Dr. Marie Barth, Dr. Mike Jones and Dr. Kevin Varvell, for their help.

I have benefited from several theoretical discussions with Prof. Gary Goldstein and Dr. Boris Kopeliovich. Prof. W. Anthony Mann is to be thanked for help with the description of quasielastic neutrino interactions.

I wish to thank the people of the Inter-University Institute for High Energies in Brussels, for the very pleasant work atmosphere during my first year and a half of research. Prof. Jean Sacton is acknowledged for allowing me to start working on a thesis project and for his continued support.

Dr. Wes Smart is to be thanked for giving me the opportunity to work on the E632 project at Fermilab and for initiating the quest for a graduate school to allow

me to pursue my goal. During my stay at Fermilab I have made many unforgettable friends. Especially, I would like to thank my dear friend Alma for making life at Fermilab bearable and even exciting, as well as for her enduring friendship. I also wish to acknowledge my friend Homaira for much help during those days. Last but not least, it was during that stay that I met my wife Carrie. I am forever thankful for her support and encouragement during the past five years, and for her proof reading of this manuscript.

This dissertation is dedicated to my parents for their love and support.

Table of Contents

Abstract ii

Acknowledgements iv

List of Tables x

List of Figures xii

1. Introduction 1

2. Theory 7

2.1. Weak Interactions, Current Conservation and Electroweak Theory 8

2.1.1. Vector Current 9

2.1.2. Axial-Vector Current 10

2.1.3. Electroweak Theory 12

2.2. Neutrino Interactions at $Q^2 \to 0$ 17

2.3. Neutrino Interactions at $Q^2 \neq 0$ 21

2.3.1. Vector Meson Dominance in Electromagnetic Interactions 21

2.3.2. Hadron Dominance and Interactions of Neutrinos at Small Q^2 23

2.4. Coherent Scattering of Hadrons 30

2.4.1. Coherence 31

2.4.2. Neutrino Coherent Production of Single Pions; the Rein and Sehgal Formulation 32

2.4.3. Glauber Theory 35
2.4.4. Neutrino Coherent Production of Single Pions; the Glauber Theory Approach of Belkov and Kopeliovich 38

3. Apparatus and Data Acquisition 43
3.1. Description of the Apparatus 43
3.1.1. Neutrino Beam 43
3.1.2. 15-foot Bubble Chamber 46
3.1.3. EMI/IPF System 50
3.2. Film Analysis and Data Processing 53
3.2.1. Scanning 53
3.2.2. Measurement 55
3.2.3. Muon Identification 60

4. Methods of Analysis 64
4.1. Extraction of the Coherent Signal 64
4.1.1. Selection of the Sample 64
4.1.2. Semi-inclusive Coherent Signal 65
4.1.3. Neutrino Beam Direction 70
4.2. Monte Carlo Simulation 73
4.2.1. Coherent Single Pion Production 74
4.2.2. Coherent Single ρ Production 78
4.2.3. Smearing 80
4.2.4. Neutrino Fluxes 86

5. Single Pion Coherent Production 88
5.1. Extraction of the Signal 89
5.2. Corrections to the Coherent Signal 91

5.2.1. Scanning Efficiency 91
5.2.2. $\frac{\Delta p}{p}$ Cut 93
5.2.3. p_μ Cut 94
5.2.4. $|t|$ Cut 94
5.2.5. Total Correction 95
5.3. Inclusive Charged Current Event Sample 96
5.3.1. Scanning Efficiency 97
5.3.2. Unmeasured Events 98
5.3.3. Fraction of Interactions on Neon Nuclei 98
5.3.4. p_μ Cut 98
5.3.5. Total Correction 99
5.4. Background 101
5.4.1. Incoherent Background 101
5.4.2. Coherent Background 105
5.5. Cross Section Results 105
5.5.1. The Integrated Cross Section 105
5.5.2. The Energy Dependence 108
5.6. Kinematical Characteristics 111

6. Single ρ Coherent Production 121
6.1. Selection of the Sample and π^0 Reconstruction 122
6.2. Extraction of the Signal 125
6.3. Corrections to the Coherent Signal 126
6.3.1. Scanning Efficiency 126
6.3.2. $\frac{\Delta p}{p}$ Cut 127
6.3.3. p_μ Cut 127
6.3.4. $|t|$ Cut 127

6.3.5. Gamma Detection Efficiency 128
6.3.6. Total Correction 132
6.4. ρ Production Results 135
6.4.1. The Integrated Cross Section 135
6.4.2. $\mu\pi\gamma$ Events 138
6.4.3. The Energy Dependence 138
6.4.4. Longitudinal ρ Production 140
6.5. Kinematical Characteristics 141

7. Summary of Results 152
7.1. Coherent Production of Single Pions 152
7.2. Coherent Production of Single Rho Mesons 154

Appendix A. E632 Collaboration 155

Appendix B. Derivation of the formula for $|t|$ 157

Appendix C. Definition of the Kinematical Variables 159

References 161

List of Tables

3.1. Summary of the 1985 and 1987-88 runs. 48

3.2. Geometric acceptance for Monte Carlo antineutrino and neutrino charged current events. 61

4.1. Averages of (visible) kinematical variables for 2-prong events. 70

4.2. Belkov-Kopeliovich model parameters for coherent pion-neon scattering as a function of total pion-nucleon cross section, for various nuclear density functions. 77

5.1. Uncorrected signal for $\mu^{\pm}\pi^{\mp}$ events and various choices of the incoherent background sample, normalized at $|t| > 0.2$ GeV^2. 91

5.2. Correction factors for coherent single pion events. 95

5.3. Single pion coherent signal for different cuts on $|t|$. 96

5.4. Correction factors for charged current events in the inclusive data sample. 100

5.5. Number of charged current events ($E > 10$ GeV). 100

5.6. Single pion signal and cross section. 106

5.7. Summary of experimental results on single pion coherent cross sections in (anti)neutrino charged and neutral current interactions. 109

5.8. Average values of kinematical variables for single pion coherent events at $|t| < 0.1$ GeV^2. 114

6.1. Correction factors for coherent single ρ events. 134

6.2. Single ρ coherent signal for different cuts on $|t|$. 134

6.3. Single ρ signal and cross section. 135

6.4. Summary of experimental results on single ρ coherent cross sections in (anti)neutrino charged current interactions. 137

6.5. Average values of kinematical variables for single ρ coherent events at $|t| < 0.1$ GeV^2. 144

List of Figures

2.1. Feynman diagram for the reaction $\nu_\mu + e^- \rightarrow \mu^- + \nu_e$. 15

2.2. Feynman diagram for the reaction $\nu_l + \alpha \rightarrow l + \beta$. 17

2.3. Total cross section as a function of energy for interactions of photons and hadrons. 22

2.4. Hadron Dominance diagram for the reaction $\nu_l + \alpha \rightarrow l + \beta$. . . . 24

2.5. Diffractive scattering of a hadron off a nucleus : a) represents the scattering in terms of Pomeron exchange; b) represents the scattering in terms of multiple gluon exchange between the quarks of the incident hadron and the target nucleus. 33

3.1. Layout of the Fermilab neutrino beam line (not to scale). 44

3.2. Quadrupole Triplet ν_μ and $\overline{\nu}_\mu$ fluxes at the 15-foot Bubble Chamber. 45

3.3. Side view of the 15-foot Bubble Chamber. 47

3.4. The reference system, showing also the definition of the dip angle λ and the azimuthal angle ϕ for a momentum vector $\vec{p}$ in the bubble chamber. 48

3.5. Layout of the IPF and EMI planes. The picture at the bottom shows the arrangement of the various planes in EMIB (looking along the direction of the neutrino beam). 51

3.6. Photograph of a neutrino interaction in the 15-foot Bubble Chamber. 54

4.1. $|t|$-distributions for $\mu^\pm\pi^\mp X^0$ events, normalized at $|t| > 0.2$ GeV^2. . . 67

4.2. $|t|$-distributions for $\mu^\pm\pi^\mp\pi^+ X^0$ events, normalized at $|t| > 0.2$ GeV^2. . 67

4.3. $|t|$-distributions for $\mu^\pm\pi^\mp\pi^\pm\pi^\mp X^0$ events, normalized at $|t| > 0.2$ GeV^2. 68

4.4. Signal for $\mu^{\pm}\pi^{\mp}X^0$ events as a function of the value of $|t|$ cut chosen. 69

4.5. Average proton momentum as a function of $|t|$ for low-multiplicity events in given intervals of proton momentum. 71

4.6. Number of $\mu^{\pm}\pi^{\mp}$ events without stubs at $|t| < 0.1$ GeV^2 for various beam directions. 72

4.7. Average $\frac{\Delta p}{p}$ for muon and charged hadron tracks. 83

4.8. γ momentum distributions for the low multiplicity data sample and the pseudo π^0 Monte Carlo. 84

4.9. Smearing of gamma conversions, the open circles represent the data and the crosses represent the pseudo Monte Carlo simulation; a) $\frac{\Delta p}{p}$ vs momentum, b) $\frac{\Delta p}{p}$ vs distance from the primary vertex, c) $\Delta\lambda$ (in radians) vs momentum, d) $\Delta\phi$ (in radians) vs momentum. 85

4.10. Corrected energy distributions for ν_μ and $\overline{\nu}_\mu$ charged current events with $p_\mu > 10$ GeV/c. 87

5.1. Diagram for the coherent production of single pions. 89

5.2. $|t|$-distributions for $\mu^{\pm}\pi^{\mp}$ events. 90

5.3. Single pion coherent cross section as a function of energy. 110

5.4. Distribution of the total $\mu^{\pm}\pi^{\mp}$ event energy E for $|t| < 0.1$ GeV^2. . . 115

5.5. Distribution of the energy transfer ν for $|t| < 0.1$ GeV^2. 116

5.6. Distribution of the four-momentum transfer squared Q^2 for $|t| < 0.1$ GeV^2. 117

5.7. Distribution of the hadronic mass W for $|t| < 0.1$ GeV^2. 118

5.8. Distribution of the Bjorken x variable for $|t| < 0.1$ GeV^2. 118

5.9. Distribution of the Bjorken y variable for $|t| < 0.1$ GeV^2. 119

5.10. Distribution of the square of the momentum transfer to the nucleus $|t|$ for $|t| < 0.1$ GeV^2. 119

5.11. Distribution of the minimum momentum transfer t_{min} for $|t| < 0.1$ GeV^2. 120
5.12. Distribution of the momentum transfer t' for $|t| < 0.1$ GeV^2. 120
6.1. Diagram for the coherent production of single ρ mesons. 122
6.2. Invariant $\gamma\gamma$ mass distribution for all $\mu^{\pm}\pi^{\mp}\gamma\gamma$ events (14 events have $m_{\gamma\gamma} > 0.4$ GeV) and for events with π^0 fit probability greater than 1 %. 124
6.3. π^0 fit probability distribution for $\gamma\gamma$ pairs with $P(\pi^0) > 1\%$. 124
6.4. $|t|$-distributions for $\mu^{\pm}\pi^{\mp}\pi^0$ events, normalized at $|t| > 0.2$ GeV^2. . . 125
6.5. Gamma multiplicity distribution for $\mu^{\pm}\pi^{\mp}(n_\gamma\gamma)$ events. 128
6.6. γ conversions in $\mu^{\pm}\pi^{\mp}(n_\gamma\gamma)$ events: a) conversion length distribution; b) conversion probability distribution; c) Q_d distribution. . 133
6.7. $\pi^{\pm}\pi^0$ invariant mass for $\mu^{\pm}\pi^{\mp}\pi^0$ events at $|t| < 0.1$ GeV^2. 136
6.8. Single ρ coherent production cross section as a function of energy. . . 139
6.9. Distribution of the cosine of the angle between the daughter charged pion and the parent ρ flight direction in the ρ center of mass. . . 140
6.10. Distribution of the total $\mu^{\pm}\pi^{\mp}\pi^0$ event energy E for $|t| < 0.1$ GeV^2. . 145
6.11. Distribution of the energy transfer ν for $|t| < 0.1$ GeV^2. 146
6.12. Distribution of the four-momentum transfer squared Q^2 for $|t| < 0.1$ GeV^2. 147
6.13. Distribution of the hadronic mass W for $|t| < 0.1$ GeV^2. 148
6.14. Distribution of the Bjorken x variable for $|t| < 0.1$ GeV^2. 148
6.15. Distribution of the Bjorken y variable for $|t| < 0.1$ GeV^2. 149
6.16. Distribution of the square of the momentum transfer to the nucleus $|t|$ for $|t| < 0.1$ GeV^2. 150
6.17. Distribution of the minimum momentum transfer t_{min} for $|t| < 0.1$ GeV^2. 151

6.18. Distribution of the momentum transfer t' for $|t| < 0.1$ GeV^2. 151

C.1. Feynman diagram for the scattering of leptons off nucleon or nuclear targets. 160

Chapter 1
Introduction

Neutrinos, postulated in 1933 and discovered in 1956 [1], are elusive particles which play an important part in the development of our understanding of fundamental forces in nature. Neutrinos carry no electric charge, have little or no mass, and, most importantly, they are subject only to the weak component of the electroweak force. Cross sections for their interaction with matter are extremely small, typically $10^{-36} - 10^{-38}$ cm^2, to be compared to 10^{-28} cm^2 for electromagnetic interactions, and 10^{-26} cm^2 for strong interactions. Consequently, studies of neutrino interactions require high fluxes of neutrinos and very large targets/detectors.

Historically, particle decays were the only "laboratory" to study weak interactions experimentally. It was only the advent of experiments with neutrino beams that enabled us to study weak interactions at higher energies. At first, only neutrino interactions with a charged lepton in the final state were investigated. The beam energies were low, and studies of exclusive reactions at low Q^2 were the order of the day. Weak neutral currents were discovered in a neutrino experiment at CERN in 1974, confirming an important ingredient of the emerging model of electroweak interactions. Another important confirmation of the electroweak theory came in 1983 with the experimental discovery of the W and Z bosons, the mediators of the weak interaction.

The majority of high energy neutrino experiments in the 1970's and 1980's concentrated on the region of high Q^2, square of the momentum transfer between the incoming and outgoing lepton, known as the region of Deep Inelastic Scattering (DIS). In this region, a large amount of information on the structure of hadrons

at small distances (10^{-13} cm or less) was inferred from the neutrino data. In DIS, the quark constituents of hadrons are probed and may be considered to be free at sufficiently high Q^2; this is the property of "asymptotic freedom". Other important analyses involved the study of the fragmentation process in which the produced quarks turn into physical hadrons, the study of charm production via semileptonic decays and the measurement of various parameters of the electroweak theory.

There is an aspect of neutrino interactions which has only recently been investigated : the study of neutrino interactions at small Q^2 and large energy transfer ν (see Ref. [2] for a comprehensive review). The distances probed in small Q^2 processes are larger than in deep inelastic scattering and the nucleon constituents can no longer be considered as free. In this regime, the perturbative theory of strong interactions cannot be used and an alternative approach has to be adopted.

One such approach is based on the ideas of hadron dominance which were first introduced in the context of photon interactions (a complete review may be found in Ref. [3]). In the Vector Meson Dominance model (VMD), the photon state is pictured as a superposition of vector meson states, with the same quantum numbers as those of the photon, plus a "bare" photon component. The interaction between photons and hadrons thus occurs via the hadronic component of the photon, and the photon-hadron interaction takes on all the characteristics of purely hadronic interactions. The VMD model has been quite successful at describing the hadronic behavior of photon interactions at high energy. Piketty and Stodolsky [4] made the remarkable step of extending these ideas to the case of the weak interaction, where the intermediate W and Z bosons may be viewed as superpositions of vector and axial-vector mesons with proper quantum numbers.

Evidence for the existence of a hadronic component in weak interactions was brought to light over the last 10 years. In particular, the observation of neutrino coherent interactions was first reported in 1983 [5] by the Aachen-Padova Collaboration. The evidence was obtained in neutral current production of neutral pions

off aluminum nuclei with a muon-neutrino beam of average energy 2 GeV. These coherent interactions on complex nuclei are essentially diffractive, i.e. they are characterized by an exponentially falling momentum transfer distribution and the target nucleus remains in its ground state. Moreover, the coherent cross section depends on A^2, the square of the atomic mass number of the nucleus, by virtue of the constructive interferences of the scattering amplitudes on each individual nucleon. Other reports of the observation of neutrino coherent interactions followed: signals were observed in neutral and charged current interactions, and detected in both large bubble chambers and electronic detectors. However, only bubble chamber experiments are able to study the details of the interactions. The WA59 Collaboration has contributed a great deal to the study of neutrino interactions in the low Q^2 and high ν domain. The Big European Bubble Chamber (BEBC) filled with a heavy Ne–H_2 liquid was used to study the coherent production of pions and ρ mesons, as well as that of a_1 mesons and non-resonant $\rho\pi$ systems. Furthermore, the WA59 Collaboration reported [6] the first observation of shadowing in neutrino interactions, i.e. a reduction of the cross section per nucleon measured in interactions on neon nuclei with respect to the cross section per nucleon on deuterium. This represents another manifestation of the hadronic component in neutrino interactions.

In the regime of low Q^2 and large ν, it is possible to study the space-time properties of the weak current; that is, the properties of the W and Z bosons. This is in contrast with the DIS studies in which the "bare" W and Z bosons interact with pointlike constituents (quarks). In this regime, we can test the hadron dominance model as well as the Conserved Vector Current (CVC) and Partially Conserved Axial Current (PCAC) hypotheses which are related to the symmetry properties of the weak interaction.

To date, there have been several successful tests of PCAC in neutrino interactions at high energies:

1. the coherent production of single pions in neutral and charged current neutrino

interactions on nuclear targets [2],

2. the measurement of the total cross section in neutrino-proton interactions at $\nu > 2$ GeV and especially at $Q^2 \lesssim 0.2$ GeV^2 where the contribution from PCAC dominates [7], and

3. the measurement of $\Delta(1232)$ resonance production in neutrino-proton interactions at $Q^2 < 1$ GeV^2 [8].

The work presented here is based on the data collected by the E632 Collaboration. This collaboration consists of 17 universities and laboratories from Europe, the United States and India (see Appendix A). In addition, three Russian groups joined the collaboration in 1990 : Moscow State University, Institute for Theoretical and Experimental Physics (ITEP Moscow) and Institute for High Energy Physics (Serpukhov). The data were collected using the Fermilab 15-foot Bubble Chamber during the 1985 and 1987-88 fixed-target running periods of the Tevatron. The bubble chamber was filled with a heavy Ne–H_2 liquid. Moreover, the bubble chamber was equipped with new arrays of proportional tubes, the External Muon Identifier (EMI) and the Internal Picket Fence (IPF), used to identify muons and determine the event time. A total of 448 000 pictures were taken during the two runs, corresponding to a total number of protons on target of 7.0×10^{17}. One of the original features of this experiment is the holographic setup designed to complement the conventional pictures by achieving a high resolution ($\sim$ 100 μm) over a relatively large volume ($\gtrsim$ 3 m^3).

The focus of this work is the study of the coherent production of pions and ρ mesons in (anti)neutrino charged current interactions on neon nuclei, at neutrino energies significantly higher (average beam energy = 86 GeV) than in previous experiments (average beam energy $\simeq$ 30 GeV). Therefore, this study provides a unique opportunity to test the CVC and PCAC hypotheses as well as the hadron dominance model in a range of energy extending beyond the range previously explored.

The dissertation is organized as follows :

- In Chapter 2, we introduce the theoretical concepts and derive some of the formulae used in the analysis of coherent neutrino charged current interactions. We first present the CVC and PCAC hypotheses followed by the electroweak theory. Adler's theorem for the case of interactions at vanishing Q^2 is derived next. Its extension to non-zero Q^2 is then considered in the context of the hadron dominance following Piketty and Stodolsky. Finally, we discuss several aspects of the coherent scattering of hadrons : conditions of coherence, the Rein and Sehgal model, Glauber theory, and the Belkov and Kopeliovich model.

- In Chapter 3, we discuss the experimental aspects pertaining to this work. Specifically, we present the Fermilab neutrino beam line, the 15-foot Bubble Chamber and the EMI/IPF system. We also describe the film analysis procedures used to extract the data from the bubble chamber film.

- In Chapter 4, some of the methods of analysis are outlined : extraction of the coherent signal and the coherent Monte Carlo simulation, with a discussion of the method used to reproduce the experimental smearing. Also, the Rein-Sehgal and Belkov-Kopeliovich parametrizations of the pion-nucleus cross section are described.

- In Chapter 5, the selection of the sample of single pion charged current events is described and the coherent signal is extracted using the method presented in Chapter 4. The losses are then evaluated in order to compute the coherent cross section. A test of the background estimate is carried out by evaluating the contribution from several specific sources of background. The selection of the inclusive charged current event sample is then discussed and the corresponding losses are estimated. Using the latter sample properly normalized, the coherent cross section is computed and compared with the results from previous experiments. Also, the energy dependence of the cross section is compared

with the prediction of the models. Finally, the kinematical characteristics of the data are compared with the predictions.

- In Chapter 6, we study the coherent production of ρ mesons. First, the selection of the sample and the reconstruction of the π^0 mesons are described. Then, the coherent signal is extracted from the $|t|$ distributions and the losses are estimated. In particular, the γ detection efficiency estimate is treated in some detail. Using techniques similar to those described in Chapter 5, we then determine the coherent cross section and compare with the results from previous experiments. The cross sections are also compared with the theoretical predictions. Finally, the kinematical characteristics of the data are compared with the predictions.

- Finally, Chapter 7 summarizes the findings of this study.

Chapter 2

Theory

The description of the coherent production of single mesons by neutrino interactions essentially involves two parts : first, the description of the weak interaction dynamics as well as the characteristics of the space-time structure of the weak current, and second, the description of the coherent scattering of hadrons off nuclear targets. Such a process is restricted to small values of Q^2, the four-momentum squared of the exchanged W boson, and large values of the energy transfer ν, a domain where the perturbative theory of strong interactions (QCD) cannot be used. In this kinematical regime, but also at higher Q^2 if $x = Q^2/2M\nu$ is small, the virtual vector bosons may couple to quark-antiquark pairs forming virtual mesons which then interact with the target. Those virtual quark-antiquark pairs correspond to vacuum polarization fluctuations.

In this chapter, the theoretical grounds for the study of neutrino coherent interactions are laid out. Section 2.1 contains a brief overview of the Fermi current-current formulation of the weak interactions, with an emphasis on the conservation properties of the vector and axial-vector currents. It is then followed by a discussion of the $SU(2)_L \otimes U(1)$ electroweak theory.

In Section 2.2, the cross section for neutrino interactions at vanishing Q^2 is calculated and Adler's theorem is derived by invoking the CVC and PCAC hypotheses.

In Section 2.3, the ideas of the Vector Meson Dominance model are presented, followed by a discussion of the model proposed by Piketty and Stodolsky. This model extends the hadron dominance concepts into the domain of weak interactions at small values of Q^2. The cross section for neutrino interactions can then be expressed in

terms of purely hadronic cross sections.

In Section 2.4, the coherent scattering of hadrons is discussed. First, general ideas about the concept of coherence are described. Then the above formalism is applied to the coherent production of single pions in neutrino interactions. Two models are considered, one formulated by Rein and Sehgal [9] and the other by Belkov and Kopeliovich [10]. In the latter model, the treatment of the elastic hadron-nucleus scattering uses the Glauber theory which is reviewed in Section 2.4.3.

Many aspects of the theory presented in this chapter are reviewed extensively by Kopeliovich and Marage [2].

2.1 Weak Interactions, Current Conservation and Electroweak Theory

In the Fermi current-current formulation of weak interactions, the effective Lagrangian[1] is

$$\begin{aligned} \mathcal{L}_{\text{eff}} &= \frac{G_F}{\sqrt{2}}\, \mathcal{J}^\lambda\, \mathcal{J}^\dagger_\lambda \,, \\ \text{with} \quad \mathcal{J}^\lambda &= j^\lambda + J^\lambda \qquad (\lambda = 1,2,3,4) \,, \end{aligned}$$

where the weak current $\mathcal{J}^\lambda$ is broken into leptonic and hadronic parts

$$\begin{aligned} j^\lambda &= \bar{l}\, \gamma^\lambda\, (1-\gamma_5)\, \nu_l \qquad (l = e, \mu, \tau) \,, \\ J^\lambda &= \bar{n}\, \gamma^\lambda\, (g_V - g_A \gamma_5)\, p \,. \end{aligned}$$

The Dirac spinors l and ν_l represent the charged lepton and its associated neutrino whereas p and n represent the proton and neutron. We have written only the strangeness conserving part of the hadronic current since, in this work, we concentrate on processes which do not involve strangeness. This effective Lagrangian describes purely leptonic processes like muon decay or neutrino-electron scattering and semileptonic processes like nuclear β decay, as well as processes involving

[1] Summation over repeated indices is implied throughout this chapter.

hadrons only. Note that, in this work, we use the notation and normalization conventions of Bjorken and Drell [11] except for the normalization of the Dirac spinors that we take as $\overline{u}u = 2m$ and $\overline{v}v = -2m$.

2.1.1 Vector Current

The Fermi coupling constant deduced from measurements of the muon lifetime is $G_F = 1.166 \times 10^{-5}$ GeV^{-2} [12]. With that value of G_F, the constants g_V and g_A determined in β decay experiments are found to be $g_V = 0.974 \pm 0.001$ [12] and $g_A/g_V = 1.261 \pm 0.004$ [12]. Thus, the coupling to the vector current does not seem to be renormalized by the strong interactions and the coupling to the axial current is only slightly renormalized. In order to explain the non-renormalization of the vector current coupling, Feynman and Gell-Mann [13] proposed[2] that the charged weak vector current ($\bar{n}\,\gamma^\lambda\,p$), its conjugate ($\bar{p}\,\gamma^\lambda\,n$) and the isovector part of the electromagnetic current ($\bar{p}\,\gamma^\lambda\,p$) form an isospin triplet, with third component of isospin $I_3 = -1, +1$ and 0 respectively. Specifically, they argued that the weak current J_V^λ can be built out of the first and second components of the isospin current j_i^λ

$$\begin{aligned} J_V^\lambda &= j_1^\lambda - i\, j_2^\lambda \,, \qquad (2.1) \\ \text{with} \qquad j_i^\lambda &= \overline{\psi}\,\gamma^\lambda\,\tau_i\,\psi \qquad (i = 1,2,3)\,, \end{aligned}$$

where the matrices τ^i are the 2×2 Pauli matrices. The current (2.1) lowers the electric charge by 1 and its conjugate raises it by 1. The electromagnetic current can itself be written in a similar form (using the Gell-Mann - Nishijima rule $Q = I_3 + \frac{1}{2}Y$)

$$J_{em}^\lambda = \overline{\psi}\,\gamma^\lambda \left(\frac{1}{2} + \tau_3\right) \psi$$

[2]This proposal was made when the experimental value of g_V was, within errors, consistent with a value of 1 and before the Cabibbo angle was introduced into the theory.

where $\overline{\psi}\,\gamma^\lambda\,\frac{1}{2}\psi$ is the hypercharge (Y) current and $\overline{\psi}\,\gamma^\lambda\,\tau_3\,\psi$ is the isovector part of the electromagnetic current. Therefore, the charged weak vector current is conserved,

$$\partial_\lambda\ J_V^\lambda = 0\ ,$$

because isospin is conserved by the strong interactions and thus the constant g_V is not renormalized by the strong interactions. It should be noted that the deviation from $g_V = 1$ is now understood by taking into account the Cabibbo mixing angle which introduces a factor $\cos\,\theta_c \simeq 0.975$ to the strangeness conserving hadronic current coupling. The above proposal by Feynman and Gell-Mann is known as the Conserved Vector Current hypothesis (CVC) and is of fundamental importance because it represents one of the first attempts to unify the weak and electromagnetic interactions.

2.1.2 Axial-Vector Current

We have seen from the experimental value of g_A that the axial-vector current is almost conserved. This non-conservation of the axial current leads to the decay of the pion as shown below. The decay $\pi^+ \rightarrow \mu^+\nu_\mu$ is described by the following transition amplitude

$$\frac{G_F}{\sqrt{2}}\ \langle 0|J^\lambda|\pi\rangle\ \bar{\nu}_l\ \gamma_\lambda\ (1-\gamma_5)\ l\ .$$

Lorentz invariance of this amplitude requires $\langle 0|J^\lambda|\pi\rangle$ to be either vector or axial-vector but since the pion has no spin and the only four-vector available is the pion four-momentum q, we have

$$\langle 0|J^\lambda|\pi\rangle = i\,f_\pi\,q^\lambda$$

with f_π, the pion decay constant. Since $\langle 0|J^\lambda|\pi\rangle$ is represented by a vector, only the axial current contributes because both the vacuum and the axial current have even

parity and the pion has odd parity. Furthermore, the pion matrix element is

$$\begin{aligned}\langle 0|J^{\lambda}(x)|\pi\rangle = \langle 0|J_A^{\lambda}(x)|\pi\rangle &= \langle 0|J_A^{\lambda}(0)|\pi\rangle\ e^{-i\,q\cdot x} \\ &= i\,f_{\pi}\,q^{\lambda}\,e^{-i\,q\cdot x}\ .\end{aligned}$$

Taking the divergence of this expression gives

$$\begin{aligned}\langle 0|\partial_{\lambda}J^{\lambda}(x)|\pi\rangle &= f_{\pi}\ q^2\ e^{-i\,q\cdot x} \\ &= f_{\pi}\ m_{\pi}^2\ e^{-i\,q\cdot x}\ ,\end{aligned}$$

from which it is concluded that if the axial current were conserved, then either the pion would not decay ($f_{\pi} = 0$) or it would be massless ($m_{\pi} = 0$). However, the above expression also shows that the divergence of the axial current is small because the pion mass is small in comparison with the nucleon mass. This leads to the idea that the axial current is almost or "partially" conserved.

The above expression has been generalized [14] as the Partially Conserved Axial Current hypothesis (PCAC) according to which the divergence of the axial current is proportional to the pion field

$$\partial_{\lambda}J_A^{\lambda}(x) = f_{\pi}\ m_{\pi}^2\ \phi_{\pi}(x)\ , \tag{2.2}$$

where ϕ_{π} is the interpolating pion field

$$\langle 0|\phi_{\pi}(x)|\pi\rangle = e^{-i\,q\cdot x}$$

and the experimental value of the pion decay constant is $f_{\pi} = 0.932\,m_{\pi}$ [15]. A more explicit form of PCAC [16] corresponds to the assumption that, for $0 \lesssim q^2 \lesssim m_{\pi}^2$, the matrix elements of the divergence of the axial current are given by the following expression

$$\langle\beta|\partial_{\lambda}J_A^{\lambda}|\alpha\rangle = \frac{\langle\beta|\pi+\alpha\rangle}{m_{\pi}^2 - q^2}\ f_{\pi}\,m_{\pi}^2\ . \tag{2.3}$$

PCAC has led to the Goldberger-Treiman relation which relates the pion-nucleon coupling constant to g_A. PCAC has also been successful in the description of some

low energy processes : muon capture and $\Delta(1232)$ production. But there are very few tests of PCAC at high energy and, as will become clear in the following, the study of coherent pion production in neutrino interactions provides a unique opportunity to test the CVC and PCAC hypotheses.

2.1.3 Electroweak Theory

The current-current formulation of the weak interactions is now considered to be the low energy limit of the electroweak theory developed by Glashow, Weinberg and Salam [17]. They successfully unified the weak and electromagnetic interactions in the framework of a gauge theory invariant under transformations of the group $SU(2)_L \otimes U(1)$. Transformations of the group U(1) correspond to phase transformations and transformations of the group $SU(2)_L$ correspond to arbitrary rotations of isospin doublets. Such a gauge theory is attractive because the gauge bosons occur naturally by requiring invariance under local gauge transformations and the theory is renormalizable. However, those gauge bosons are then massless whereas the mediators of the weak interactions are known to be heavy because of the short range of those interactions. In the theory, this difficulty is overcome by introducing new scalar fields to spontaneously break the $SU(2)_L \otimes U(1)$ symmetry, in such a way as to provide the weak interaction vector bosons with mass, while leaving the photon massless. The electroweak theory has been extensively tested and has proved to be extremely successful to this date. One of its most prominent successes has been the prediction of weak neutral currents several years before their discovery in a neutrino bubble chamber experiment. Another crucial discovery was that of the W and Z bosons, mediators of the weak interaction, at the CERN proton-antiproton collider. Moreover, the measured W and Z masses were found to agree with the predictions of the theory.

In this theory, the fermions are arranged into isospin doublets L (isospin $= 1/2$)

of left-handed leptons and quarks

$$\begin{pmatrix} \nu_{eL} \\ e_L \end{pmatrix}, \begin{pmatrix} \nu_{\mu L} \\ \mu_L \end{pmatrix}, \begin{pmatrix} \nu_{\tau L} \\ \tau_L \end{pmatrix}, \begin{pmatrix} u_L \\ d'_L \end{pmatrix}, \begin{pmatrix} c_L \\ s'_L \end{pmatrix}, \begin{pmatrix} t_L \\ b'_L \end{pmatrix},$$

and singlets R (isospin = 0) of right-handed leptons and quarks

$$e_R,\ \mu_R,\ \tau_R,\ u_R,\ d'_R,\ c_R,\ s'_R,\ t_R,\ b'_R,$$

where

$$\psi_{L(R)} = \frac{1}{2}\left(1 \overset{(+)}{-} \gamma_5\right)\psi\ .$$

The fields d', s' and b' are linear combinations of the quark mass eigenstates d, s and b. The coefficients of those linear combinations are determined by the Kobayashi-Maskawa mixing matrix, which is an extension of the Cabibbo mixing matrix used in formulations of the theory with only two generations of quarks and leptons.

The Lagrangian density is comprised of four parts

$$\mathcal{L} = \mathcal{L}_{\text{fermions}} + \mathcal{L}_{\text{gauge}} + \mathcal{L}_{\text{scalars}} + \mathcal{L}_{\text{inter}}\ .$$

The $SU(2)_L \otimes U(1)$ invariant part of the Lagrangian which describes the (massless) fermions is

$$\mathcal{L}_{\text{fermions}} = \overline{R}\, i\gamma^\lambda(\partial_\lambda + \frac{i}{2}g'B_\lambda)R + \overline{L}\, i\gamma^\lambda(\partial_\lambda + \frac{i}{2}g'B_\lambda - ig\frac{\tau^j}{2}A^j_\lambda)L\ ,\quad (j = 1,2,3) \tag{2.4}$$

The gauge fields B_λ and A^j_λ, and their coupling constants g' and g, are associated with the U(1) and $SU(2)_L$ groups respectively. The term $\mathcal{L}_{\text{gauge}}$ describes the self-interaction of those gauge fields and $\mathcal{L}_{\text{scalars}}$ describes the isodoublet of (Higgs) scalar fields which is introduced to break the symmetry spontaneously and provide masses to the gauge bosons via the Higgs mechanism. The last term $\mathcal{L}_{\text{inter}}$ describes the interaction between the scalar fields and the fermions, and also provides the fermion mass terms.

The physical intermediate vector bosons are defined by

$$\begin{aligned} W_\lambda^\pm &= \frac{1}{\sqrt{2}}\left(A_\lambda^1 \mp i A_\lambda^2\right) , \\ Z_\lambda &= \frac{-g A_\lambda^3 + g' B_\lambda}{\sqrt{g^2+g'^2}} , \\ A_\lambda &= \frac{g B_\lambda + g' A_\lambda^3}{\sqrt{g^2+g'^2}} , \end{aligned}$$

which represent the fields of the $W^\pm$ and Z^0 bosons and that of the photon, respectively. The terms describing the interaction between the leptons and the charged intermediate bosons are

$$\frac{g}{2}\,\overline{L}\,\gamma^\lambda\left(\tau^1 A_\lambda^1 + \tau^2 A_\lambda^2\right) L = \frac{g}{\sqrt{2}}\left[\overline{\nu}_l\,\gamma^\lambda \frac{1-\gamma_5}{2}\, l\, W_\lambda^+ + \bar{l}\,\gamma^\lambda \frac{1-\gamma_5}{2}\,\nu_l\, W_\lambda^-\right]$$

i.e. the W bosons couple exclusively to left-handed fermions. The corresponding expression for quarks is similar except for additional factors involving the Kobayashi-Maskawa matrix. The coupling to the neutral vector bosons is

$$\begin{aligned} &\frac{Z_\lambda}{2\sqrt{g^2+g'^2}}\left[g'^2\left(2\,\bar{l}_R\,\gamma^\lambda l_R + \bar{l}_L\,\gamma^\lambda l_L + \overline{\nu}_{lL}\,\gamma^\lambda \nu_{lL}\right) - g^2\left(\bar{l}_L\,\gamma^\lambda l_L - \overline{\nu}_{lL}\,\gamma^\lambda \nu_{lL}\right)\right] \\ &\qquad + \frac{g g'}{\sqrt{g^2+g'^2}}\, A_\lambda\left[\bar{l}_R\,\gamma^\lambda l_R + \bar{l}_L\,\gamma^\lambda l_L\right] . \end{aligned}$$

The electroweak theory therefore predicts the existence of an additional weak boson: the Z^0 boson, mediator of the weak neutral current interaction.

To show that the Fermi current-current formulation is the low energy limit of the electroweak theory, let us write the amplitude for the process $\nu_\mu + e^- \to \mu^- + \nu_e$ represented by the Feynman diagram in Fig. 2.1

$$\mathcal{M} = \frac{g}{\sqrt{2}}\,\nu_e\,\gamma_\kappa\,\frac{1-\gamma_5}{2}\,\overline{e}\,\frac{-g^{\kappa\lambda} + q^\kappa q^\lambda/m_W^2}{q^2 - m_W^2}\,\frac{g}{\sqrt{2}}\,\overline{\mu}\,\gamma_\lambda\,\frac{1-\gamma_5}{2}\,\nu_\mu .$$

At low energy, the W boson four-momentum q is small in comparison with its mass m_W ($q^2 \ll m_W^2$) and the W propagator reduces to $g^{\kappa\lambda}/m_W^2$. Thus, the above expression reduces to that obtained in the context of the current-current formulation provided that

$$\frac{G_F}{\sqrt{2}} = \frac{g^2}{8\,m_W^2} .$$

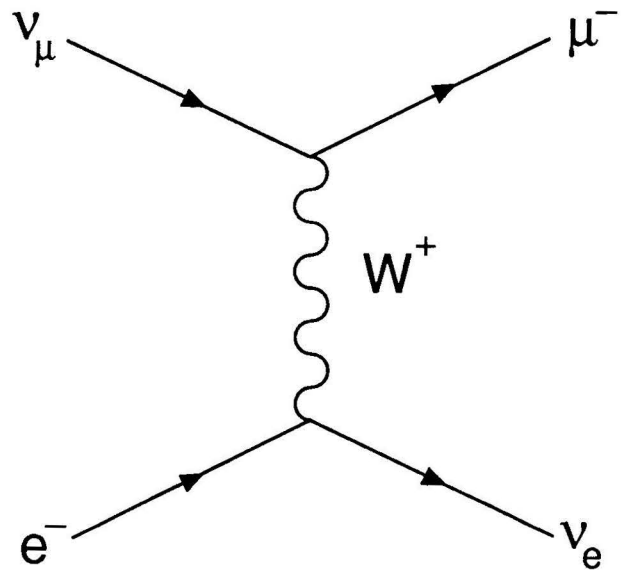

Figure 2.1: Feynman diagram for the reaction $\nu_\mu + e^- \rightarrow \mu^- + \nu_e$.

It can be shown [18] that CVC is a consequence of Eq. (2.4). Indeed, the change in the Lagrangian due to an infinitesimal global SU(2) gauge transformation

$$\psi \rightarrow \psi' = e^{-i\,\vec{\alpha}\cdot\frac{\vec{\tau}}{2}}\,\psi \tag{2.5}$$

is

$$\delta\mathcal{L} = \partial_\lambda\left(\frac{\partial\mathcal{L}}{\partial(\partial^\lambda\psi)}\,\delta\psi\right) = 0\ ,$$

where $\vec{\alpha}$ is an arbitrary transformation isovector which does not depend on the space-time coordinates. $\delta\mathcal{L} = 0$ since the Lagrangian is invariant under global SU(2) transformations. From Eq. (2.4)

$$\frac{\partial\mathcal{L}}{\partial(\partial^\lambda\psi)} \;=\; \overline{\psi}\,i\,\gamma^\lambda$$

and from (2.5)

$$\delta\psi \;\simeq\; -i\,\vec{\alpha}\cdot\frac{\vec{\tau}}{2}\,\psi\ .$$

Thus we have

$$\begin{aligned}\delta\mathcal{L} &= \partial_\lambda\left(\overline{\psi}\,\gamma^\lambda\,\vec{\alpha}\cdot\frac{\vec{\tau}}{2}\,\psi\right)\\ &= \vec{\alpha}\cdot\partial_\lambda\left(\overline{\psi}\,\gamma^\lambda\,\frac{\vec{\tau}}{2}\,\psi\right)\\ &= \vec{\alpha}\cdot\partial_\lambda\vec{J}^\lambda_V\ ,\end{aligned}$$

implying (for $\vec{\alpha}\neq 0$) that the vector current is conserved :

$$\partial_\lambda\,\vec{J}^\lambda_V = 0\ .$$

In the case of the axial current, we find by way of the Dirac equation

$$\begin{aligned}\partial_\lambda\,\vec{J}^\lambda_A &= \partial_\lambda\left(\overline{\psi}\,\gamma^\lambda\,\gamma_5\,\frac{\vec{\tau}}{2}\,\psi\right)\\ &= m_f\,\overline{\psi}\,\gamma_5\,\vec{\tau}\,\psi\ .\end{aligned}$$

Thus, the axial current is not conserved and the Lagrangian is not invariant under global transformations of the type

$$\psi\rightarrow\psi' = e^{-i\,\vec{\alpha}\cdot\frac{\vec{\tau}}{2}\,\gamma_5}\,\psi\ .$$

In the chiral limit ($m_f = 0$), the axial current is conserved and the Lagrangian is invariant under transformations of the group $SU(2)_L\otimes SU(2)_R$. However, the fact that we do not observe a degeneracy of the particle spectrum between states with opposite parity indicates that the chiral symmetry is explicitly broken. The extent of the symmetry breaking is measured by the small but finite masses of the isotriplet of pions which play the role of near-massless Goldstone bosons [19].

The electroweak theory has been further extended to include Quantum Chromodynamics (QCD), the gauge theory of strong interactions. QCD describes the interactions between quarks and gluons, the carriers of the strong interaction. This extension is usually referred to as the Standard Model and corresponds to the larger symmetry group $SU(3)\otimes SU(2)_L\otimes U(1)$.

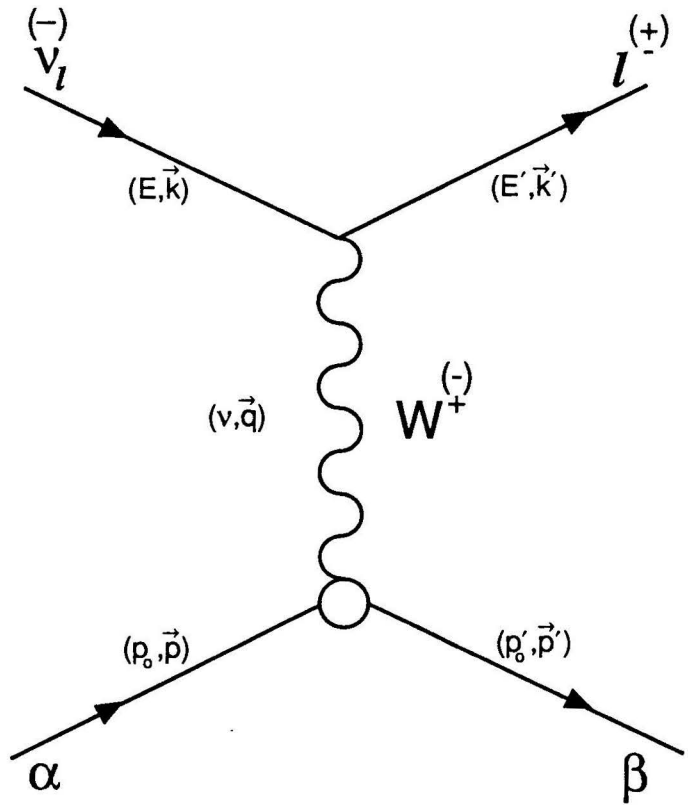

Figure 2.2: Feynman diagram for the reaction $\nu_l + \alpha \rightarrow l + \beta$.

2.2 Neutrino Interactions at $Q^2 \rightarrow 0$

As will be seen below, the ideas presented in the previous section are essential to the description of neutrino charged current interactions at low Q^2. We now consider the interaction[3] of neutrino ν_l with hadron target α yielding a charged lepton l and final state hadronic system β, with four-momenta defined in Fig. 2.2. In the Fermi current-current formulation, the transition amplitude is expressed as the product of a leptonic current j_λ and a hadronic current J^λ :

$$\mathcal{M} = \frac{G_F}{\sqrt{2}}\, j_\lambda\, J^\lambda \,,$$

where G_F is the Fermi coupling constant and the leptonic current is given by

$$j_\lambda = \bar{l}\,\gamma_\lambda\,(1-\gamma_5)\,\nu_l \,.$$

[3]It should be noted that all formulae given in the remainder of this chapter are equally applicable to the case of antineutrino scattering, unless specified otherwise.

The precise form of the hadronic current J^λ is not known because the hadrons cannot be considered to be pointlike and thus the matrix element $\langle\beta|J^\lambda|\alpha\rangle$ cannot be expressed in terms of Dirac spinors.

The transition amplitude squared is thus

$$|\mathcal{M}|^2 = \frac{G_F^2}{2}\, L_{\kappa\lambda}\, \langle\beta|J^\kappa|\alpha\rangle\, \langle\beta|J^\lambda|\alpha\rangle^\dagger\ , \tag{2.6}$$

where the lepton tensor results from summing over all initial and final state lepton spins (no averaging is required for the initial neutrino since it exists in only one helicity state) :

$$L_{\kappa\lambda} = j_\kappa j_\lambda^\dagger = 8\left[k_\kappa k'_\lambda + k_\lambda k'_\kappa - k\cdot k' g_{\kappa\lambda} \overset{(-)}{+} i\epsilon_{\kappa\lambda\eta\delta}k^\eta k'^\delta\right]\ .$$

The lower (upper) sign of the antisymmetric term is for neutrino (antineutrino) scattering. It is understood that a similar averaging and summing is to be carried out for the hadronic current. The square of the four-momentum transfer is

$$\begin{aligned} Q^2 \equiv -q^2 &= -(k-k')^2 \\ &= -k^2 + 2k\cdot k' - k'^2 \\ &\simeq 2k\cdot k' = 2EE'(1-\cos\theta)\ , \end{aligned} \tag{2.7}$$

where θ is the scattering angle between the vectors $\vec{k}$ and $\vec{k}'$ and the lepton mass has been neglected in Eq.(2.7). Thus, the lepton tensor is given by

$$L_{\kappa\lambda} = 8\left[k_\kappa k'_\lambda + k_\lambda k'_\kappa - \frac{Q^2}{2} g_{\kappa\lambda} \overset{(-)}{+} i\epsilon_{\kappa\lambda\eta\delta}k^\eta k'^\delta\right]\ . \tag{2.8}$$

In the limit $Q^2 \to 0$, the vectors $\vec{k}$ and $\vec{k}'$ are parallel and the lepton four-momenta can be expressed in terms of the four-momentum transfer q (the lepton mass is again neglected)

$$\begin{aligned} k_\lambda &= \frac{E}{\nu}\, q_\lambda\ , \\ k'_\lambda &= \frac{E'}{\nu}\, q_\lambda\ . \end{aligned}$$

The last term of (2.8) no longer contributes because $\epsilon_{\kappa\lambda\eta\delta}$ is antisymmetric and the lepton tensor becomes

$$L_{\kappa\lambda}\Big|_{Q^2\to 0} = 16\,\frac{E\,E'}{\nu^2}\,q_\kappa q_\lambda\ .$$

Therefore, Eq. (2.6) can be written as

$$|\mathcal{M}|^2{}_{Q^2\to 0} = 8\,G_F^2\,\frac{E\,E'}{\nu^2}\left|\langle\beta|\partial_\lambda J^\lambda|\alpha\rangle\right|^2\ , \tag{2.9}$$

since $q_\lambda\langle\beta|J^\lambda|\alpha\rangle = -i\partial_\lambda\langle\beta|J^\lambda|\alpha\rangle$.

For $Q^2 = 0$, the scattering process is thus expressed in terms of the divergence of the hadronic current

$$\partial_\lambda J^\lambda = \partial_\lambda(J_V^\lambda + J_A^\lambda) = \partial_\lambda J_A^\lambda\ .$$

Here, the vector and axial-vector parts of the current have been separated and the CVC hypothesis has been applied. As a result, Eq. (2.9) can be rewritten by invoking PCAC (2.3) as

$$|\mathcal{M}|^2{}_{Q^2\to 0} = 8\,G_F^2\,\frac{E\,E'}{\nu^2}\,f_\pi^2\,|\mathcal{A}(\pi+\alpha\to\beta)|^2\ , \tag{2.10}$$

where $\mathcal{A}(\pi+\alpha\to\beta)$ is the transition amplitude for reaction $\pi+\alpha\to\beta$.

The cross section expressed in the lab system is given by

$$\sigma(\nu_l+\alpha\to l+\beta)\Big|_{Q^2\to 0} = \frac{|\mathcal{M}|^2}{4\,E\,m_\alpha}\,dLips$$

with the Lorentz invariant phase space (Lips) factor

$$dLips = (2\pi)^4\,\delta^4(k'+p'-k-p)\,\frac{1}{(2\pi)^3}\,\frac{d^3k'}{2E'}\,\frac{1}{(2\pi)^3}\,\frac{d^3p'}{2p_0'}\ .$$

Similarly, the cross section for reaction $\pi+\alpha\to\beta$ is

$$\sigma(\pi+\alpha\to\beta) = \frac{|\mathcal{A}(\pi+\alpha\to\beta)|^2}{4\,\nu\,m_\alpha}\,(2\pi)^4\,\delta^4(k'+p'-k-p)\,\frac{1}{(2\pi)^3}\,\frac{d^3p'}{2p_0'}$$

with the pion four-momentum given by $p_\pi = q = k - k'$. As a result, the cross section for $Q^2\to 0$ is

$$\frac{d^2\sigma(\nu_l+\alpha\to l+\beta)}{dQ^2\,d\nu}\Big|_{Q^2\to 0} = \frac{G_F^2}{2\pi^2}\,f_\pi^2\,\frac{1}{\nu}\,\frac{E'}{E}\,\sigma(\pi+\alpha\to\beta)\ . \tag{2.11}$$

The above relation is known as Adler's theorem [20]. It has the remarkable consequence of relating the weak interaction process $\nu_l + \alpha \rightarrow l + \beta$ to the strong interaction process $\pi + \alpha \rightarrow \beta$. Note that this relation is only valid for $\alpha \neq \beta$.

Contrary to what Eq. (2.10) seems to indicate, the cross section at $Q^2 = 0$ is not dominated by pion exchange. This was pointed out by Bell [21]. To verify that pion exchange does not dominate, let us represent the hadronic current as the sum of a pion pole term plus another (unspecified) term corresponding to all other contributions

$$M^\lambda = i f_\pi \frac{q^\lambda}{Q^2 + m_\pi^2} \mathcal{A}(\pi + \alpha \rightarrow \beta) + \widetilde{M}^\lambda \,. \tag{2.12}$$

The divergence of (2.12) is then

$$iq_\lambda M^\lambda = f_\pi \frac{Q^2}{Q^2 + m_\pi^2} \mathcal{A}(\pi + \alpha \rightarrow \beta) + iq_\lambda \widetilde{M}^\lambda \,.$$

By PCAC, $iq_\lambda M^\lambda = f_\pi \mathcal{A}(\pi + \alpha \rightarrow \beta)$, which implies that

$$\begin{aligned} iq_\lambda \widetilde{M}^\lambda &= f_\pi \mathcal{A}(\pi + \alpha \rightarrow \beta) \left[1 - \frac{Q^2}{Q^2 + m_\pi^2}\right] \\ &= f_\pi \mathcal{A}(\pi + \alpha \rightarrow \beta) \frac{m_\pi^2}{Q^2 + m_\pi^2} \,, \end{aligned} \tag{2.13}$$

and for $Q^2 \rightarrow 0$,

$$iq_\lambda \widetilde{M}^\lambda = f_\pi \mathcal{A}(\pi + \alpha \rightarrow \beta) \,. \tag{2.14}$$

Therefore, the amplitude $\mathcal{A}(\pi + \alpha \rightarrow \beta)$ originates from the divergence of the non-pionic term of (2.12).

Using Eqs. (2.12) and (2.14), the transition amplitude squared, Eq. (2.6), can easily be computed without neglecting the lepton mass. As demonstrated above, the second term of (2.12) produces the main contribution whereas the pion pole term gives rise to contributions proportional to the lepton mass because it contains the four-vector q^λ (by way of the Dirac equation). The Adler cross section (2.11) then

becomes

$$\left.\frac{d^2\sigma(\nu_l + \alpha \to l + \beta)}{dQ^2\, d\nu}\right|_{Q^2 \lesssim m_\pi^2} = \frac{G_F^2}{2\pi^2} f_\pi^2 \frac{1}{\nu} \frac{E'}{E} \sigma(\pi + \alpha \to \beta) \times \left[1 - \frac{\nu}{E'} \frac{m_l^2}{Q^2 + m_\pi^2} + \frac{\nu^2}{4\,E\,E'} \frac{m_l^2 (Q^2 + m_l^2)}{(Q^2 + m_\pi^2)^2}\right], \quad (2.15)$$

which is valid for $Q^2 \lesssim m_\pi^2$.

2.3 Neutrino Interactions at $Q^2 \neq 0$

An important aspect of Adler's theorem is to show that at $Q^2 \to 0$ neutrino interactions exhibit hadronic properties. However, the domain of validity of the theorem is confined to values of Q^2 not easily accessible to experiment. It is therefore necessary to extrapolate Adler's prediction to non-zero values of Q^2. The extension to higher Q^2 is done by analogy with the Vector Meson Dominance (VMD) model which was originally developed in the context of photoproduction of hadrons. The VMD approach which has been very successful at describing electromagnetic processes at small Q^2 ($\lesssim 1-2$ GeV^2) is briefly introduced in Section 2.3.1. Its extension to the case of weak interactions is then presented in Section 2.3.2.

2.3.1 Vector Meson Dominance in Electromagnetic Interactions

The Vector Meson Dominance model was introduced to explain the observed hadronic properties exhibited by real and virtual photons. The most striking similarities between interactions of photons and hadrons are the following :

1. The behavior of the total cross section as a function of energy (as seen in Fig. 2.3). Interactions of photons display a strong resonance structure at low energy ($W < 2$ GeV) and become structureless at higher energy. The photon-induced processes are weaker by a factor of order of the fine structure constant, $\alpha_{e.m.} = 1/137$.

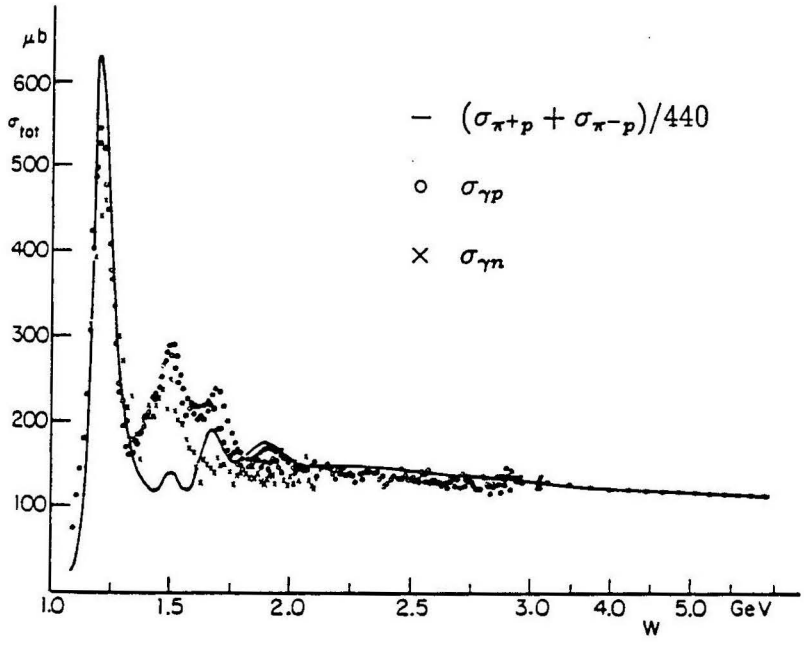

Figure 2.3: Total cross section as a function of energy for interactions of photons and hadrons.

2. The abundant diffractive production of vector mesons.

3. The observation of shadowing in interactions with complex nuclei.

Complete details about the VMD model may be found in Leith [22] as well as in the comprehensive review by Bauer, Spital, Yennie and Pipkin [3].

The basic assumption of the VMD model is that the photon state $|\gamma\rangle$ can be represented by the superposition of a "bare" photon state $|\gamma_B\rangle$, plus a sum of hadronic states with quantum numbers of the photon ($J^{PC} = 1^{--}, Q = B = S = 0$)

$$|\gamma\rangle \simeq \sqrt{Z_3}\,|\gamma_B\rangle + \sqrt{\alpha_{e.m.}}\,|h\rangle \ .$$

Here, all states carry the same momentum $\vec{q}$ and the factor $\sqrt{Z_3}$ is introduced to ensure proper normalization. The simplest version of the VMD model states that only the three lightest vector mesons, ρ^0, ω and ϕ, contribute to $|h\rangle$. Extensions to include heavier vector mesons (ρ', ψ, ...) and continuum are referred to as Generalized Vector Dominance (GVD) [23].

In the VMD model, the transition amplitude for the process $\gamma + \alpha \to \beta$ is written as

$$\mathcal{A}(\gamma + \alpha \to \beta) = \sum_{V=\rho^0,\omega,\phi} \frac{e}{g_V} \frac{m_V^2}{Q^2 + m_V^2} \mathcal{A}(V + \alpha \to \beta) \, .$$

The quantity $e\frac{m_V^2}{g_V}$ is the coupling constant of the vector meson to the photon. We can picture the hadronic states of the photon as vacuum polarization fluctuations into quark-antiquark pairs, realized as (real) hadrons. However, those hadronic fluctuations are only allowed during a time Δt short enough not to violate the uncertainty principle, i.e.

$$\Delta t \lesssim \frac{1}{\Delta E} \, ,$$

where

$$\begin{aligned} \Delta E = \nu - E_V &= \nu - \sqrt{|\vec{q}|^2 + m_V^2} \\ &= \nu - \sqrt{\nu^2 + Q^2 + m_V^2} \\ &\simeq \frac{Q^2 + m_V^2}{2\,\nu} \quad \text{for } \nu \gg \sqrt{Q^2 + m_V^2} \, . \end{aligned}$$

Thus, for small Q^2 and large ν, the lifetime of the hadronic fluctuation is

$$\Delta t \simeq \frac{2\,\nu}{Q^2 + m_V^2} \, . \tag{2.16}$$

From (2.16), it is seen that manifestations of the hadronic component in electromagnetic interactions are most likely to be observed at small values of Q^2 in conjunction with large values of the energy transfer ν, i.e. small values of the Bjorken x variable defined as $x \equiv Q^2/2M\nu$.

2.3.2 Hadron Dominance and Interactions of Neutrinos at Small Q^2

The model describing neutrino interactions at small but non-vanishing Q^2 is due to Piketty and Stodolsky [4]. It is based on an extension of the hadron dominance

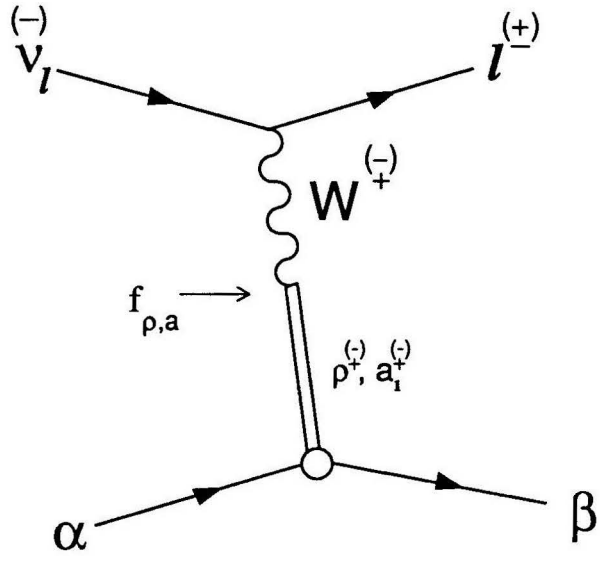

Figure 2.4: Hadron Dominance diagram for the reaction $\nu_l + \alpha \rightarrow l + \beta$.

approach to the weak interactions. The weak hadronic current is again separated into vector and axial-vector parts because of the special role played by PCAC in the case of the axial current. In the model, the vector current is assumed to be dominated by the ρ meson ($J^P = 1^-$) whereas the axial current is dominated by the a_1 meson ($J^P = 1^+$). The axial current also contains a component proportional to the gradient of the pion field, but it can be neglected because it only contributes terms proportional to the lepton mass squared.

In this approach, the neutrino interaction is represented by Fig. 2.4, where the W boson interacts with the target via its hadronic component. The total cross section is thus expressed in terms of the ρ and a_1 cross sections, as well as the π cross section (for the longitudinal part of the axial current via PCAC) :

$$\sigma(\nu_l + \alpha \rightarrow l + \beta) \propto \sum_{i=\rho,a_1,\pi} \sigma(i + \alpha \rightarrow \beta) + \text{interference terms.}$$

(a) Vector Current

The treatment of the weak vector current proceeds along the same lines as that of the electromagnetic current. The square of the transition amplitude for the vector

current can be written in a way similar to that of Eq. (2.6)

$$|\mathcal{M}_V|^2 = \frac{G_F^2}{2}\, L_{\kappa\lambda}\, W_V^{\kappa\lambda} \,, \tag{2.17}$$

where the hadronic tensor $W_V^{\kappa\lambda}$ is obtained after averaging over the initial spins and summing over all final spins and momenta. The most general Lorentz invariant form for $W_V^{\kappa\lambda}$ is constructed using the four-momenta p_λ and q_λ [24]

$$W_V^{\kappa\lambda} = -W_{1V}\, g^{\kappa\lambda} + W_{2V}\, \frac{p^\kappa p^\lambda}{M^2} + W_{4V}\, \frac{q^\kappa q^\lambda}{M^2} + W_{5V}\, \frac{p^\kappa q^\lambda + q^\kappa p^\lambda}{M^2} \,. \tag{2.18}$$

M is the target mass and there are no antisymmetric terms since those arise from the interference between the vector and axial parts of the current. The conservation of the vector current implies that

$$q_\kappa W_V^{\kappa\lambda} = q_\lambda W_V^{\kappa\lambda} = 0 \,,$$

which in turn implies that the functions W_{4V} and W_{5V} can be expressed in terms of W_{1V} and W_{2V}. We have thus

$$W_V^{\kappa\lambda} = W_{1V}\left(-g^{\kappa\lambda} - \frac{q^\kappa q^\lambda}{Q^2}\right) + \frac{W_{2V}}{M^2}\left(p^\kappa + \frac{p\cdot q}{Q^2} q^\kappa\right)\left(p^\lambda + \frac{p\cdot q}{Q^2} q^\lambda\right) \,,$$

with the structure functions W_{1V} and W_{2V} depending only on the kinematical variables Q^2 and ν.

The ρ dominance hypothesis is introduced in the expression for the current [4]

$$J^\kappa = \frac{f_\rho}{Q^2 + m_\rho^2}\left[g^{\kappa\lambda} - \frac{q^\kappa q^\lambda}{m_\rho^2}\right] \mathcal{A}_\lambda(\rho + \alpha \to \beta) \,,$$

where f_ρ is the coupling constant of the ρ meson to the W boson and $\epsilon_i^\lambda \mathcal{A}_\lambda(\rho+\alpha \to \beta)$ represents the amplitude for ρ mesons with polarization ϵ_i (i= 1, 2, 3), see (2.20) below. Moreover, $q^\lambda \mathcal{A}_\lambda = 0$ by conservation of the isospin current. The hadronic tensor can be rewritten as

$$W_V^{\kappa\lambda} = \frac{f_\rho^2}{(Q^2 + m_\rho^2)^2}\, M^{\kappa\lambda} \,, \tag{2.19}$$

where the tensor $M^{\kappa\lambda}$ is defined as the product $\mathcal{A}^{\kappa}\mathcal{A}^{\dagger\lambda}$ averaged and summed over initial and final states. It is useful to express the functions W_{1V} and W_{2V} in terms of the transverse and longitudinal cross sections for reaction $\rho + \alpha \to \beta$

$$\begin{aligned} \sigma_T &= \frac{1}{|\vec{q}|}\,\epsilon_{\kappa}^{*T} M^{\kappa\lambda} \epsilon_{\lambda}^{T}\,, \\ \sigma_L &= \frac{1}{|\vec{q}|}\,\epsilon_{\kappa}^{*L} M^{\kappa\lambda} \epsilon_{\lambda}^{L}\,, \end{aligned}$$

where $|\vec{q}|$, the ρ momentum in the laboratory system, is a flux factor, and the polarization four-vectors are

$$\begin{aligned} \epsilon^{T}(\pm 1) &= \mp\frac{1}{\sqrt{2}}\,(0; 1, \pm i, 0)\,, \\ \epsilon^{L}(0) &= \frac{1}{\sqrt{Q^2}}\,(|\vec{q}|; 0, 0, \nu)\,. \end{aligned} \tag{2.20}$$

Thus, using Eqs. (2.19) and (2.20), with $q\cdot\epsilon = 0$ and p^{λ} evaluated in the laboratory system, we get

$$\sigma_T = \frac{1}{|\vec{q}|}\,\frac{(Q^2+m_\rho^2)^2}{f_\rho^2}\,W_{1V}\,, \tag{2.21}$$

$$\sigma_L = \frac{1}{|\vec{q}|}\,\frac{(Q^2+m_\rho^2)^2}{f_\rho^2}\left[-W_{1V} + W_{2V}\,\frac{|\vec{q}|^2}{Q^2}\right]\,, \tag{2.22}$$

from which W_{1V} and W_{2V} can be expressed in terms of σ_T and σ_L. The transition amplitude squared (2.17) can be computed using the lepton tensor (2.8) as well as expressions (2.21) and (2.22) to give

$$|\mathcal{M}_V|^2 = 4\,G_F^2\,|\vec{q}|\,f_\rho^2\,\frac{Q^2}{(Q^2+m_\rho^2)^2}\left[\sigma_T + \frac{(\sigma_T+\sigma_L)}{2|\vec{q}|^2}\,(4EE' - Q^2)\right]\,.$$

The differential cross section thus becomes

$$\begin{aligned} \frac{d^2\sigma^V(\nu_l + \alpha \to l + \beta)}{dQ^2\,d\nu} &= \frac{G_F^2}{4\pi^2}\,\frac{|\vec{q}|}{E^2}\,f_\rho^2\,\frac{Q^2}{(Q^2+m_\rho^2)^2}\left[\sigma_T + \frac{(\sigma_T+\sigma_L)}{2|\vec{q}|^2}(4EE' - Q^2)\right] \\ &= \frac{G_F^2}{4\pi^2}\,\frac{|\vec{q}|}{E^2}\,\frac{f_\rho^2}{1-\epsilon}\,\frac{Q^2}{(Q^2+m_\rho^2)^2} \\ &\quad \times\,[\sigma_T(\rho+\alpha\to\beta) + \epsilon\,\sigma_L(\rho+\alpha\to\beta)]\,, \end{aligned} \tag{2.23}$$

where

$$\epsilon = \left(1 + \frac{2\,|\vec{q}\,|^2}{4EE' - Q^2}\right)^{-1}$$

is the polarization parameter which is interpreted as the ratio between longitudinal and transverse polarization states of the ρ meson.

(b) Axial Current

The treatment of the axial current is similar to that of the vector current except for the implications of PCAC at $Q^2 \to 0$ and the fact that the axial current is not conserved. As in the case of the vector current, we can write the hadronic tensor in a general form (see Eq. (2.18))

$$W_A^{\kappa\lambda} = -W_{1A}\, g^{\kappa\lambda} + W_{2A}\, \frac{p^\kappa p^\lambda}{M^2} + W_{4A}\, \frac{q^\kappa q^\lambda}{M^2} + W_{5A}\, \frac{p^\kappa q^\lambda + q^\kappa p^\lambda}{M^2}\ . \qquad (2.24)$$

The axial current is not conserved and we cannot reduce the number of independent structure functions. However, the differences only involve terms proportional to q^λ which lead to negligible contributions (proportional to the lepton mass squared).

The hypothesis of hadron dominance leads to an expression for the weak hadronic axial current containing one term corresponding to the a_1 meson and another term corresponding to the pion contribution [4]

$$J^\kappa = \frac{f_a}{Q^2 + m_a^2}\left[g^{\kappa\lambda} - \frac{q^\kappa q^\lambda}{m_a^2}\right] \mathcal{A}_\lambda(a_1 + \alpha \to \beta) + f_\pi\, \frac{q^\kappa}{Q^2 + m_\pi^2}\, \mathcal{A}(\pi + \alpha \to \beta)\ .$$

The factor f_a is the coupling constant of the W boson to the a_1 meson and $\epsilon_i^\lambda \mathcal{A}_\lambda(a_1 + \alpha \to \beta)$ represents the amplitude for a_1 mesons with polarization ϵ_i (i= 1, 2, 3). If the lepton mass is neglected, the pion pole term does not contribute after contraction with the lepton tensor (2.8). Therefore, away from very small Q^2, we find for the cross section an expression similar to that found in the case of the vector current (2.23)

$$\frac{d^2\sigma^A(\nu_l + \alpha \to l + \beta)}{dQ^2\, d\nu} = \frac{G_F^2}{4\pi^2}\, \frac{|\vec{q}\,|}{E^2}\, \frac{f_a^2}{1-\epsilon}\, \frac{Q^2}{(Q^2 + m_a^2)^2} \times \left[\sigma_T(a_1 + \alpha \to \beta) + \epsilon\, \sigma_L(a_1 + \alpha \to \beta)\right]\ , \qquad (2.25)$$

At $Q^2 \to 0$, and using Eq. (2.24), we have

$$q_\kappa W_A^{\kappa\lambda} q_\lambda \Big|_{Q^2\to 0} = W_{2A} \frac{(p\cdot q)^2}{M^2} .$$

Moreover, PCAC imposes a condition on the hadronic tensor, namely

$$q_\kappa W_A^{\kappa\lambda} q_\lambda \Big|_{Q^2\to 0} = f_\pi^2 \frac{1}{|\vec{q}|} \sigma(\pi + \alpha \to \beta) .$$

Thus,

$$W_{2A} \Big|_{Q^2\to 0} = f_\pi^2 \frac{M^2}{(p\cdot q)^2} \frac{1}{|\vec{q}|} \sigma(\pi + \alpha \to \beta) . \tag{2.26}$$

Given the condition (2.26), Adler's relation (2.11) can be reproduced [4]. Comparing Eq. (2.11) with Eq. (2.25) leads to an expression relating the longitudinal a_1 cross section to the pion cross section

$$\frac{f_a^2}{m_a^4} Q^2 \sigma_L^A(a_1 + \alpha \to \beta) \Big|_{Q^2\to 0} = f_\pi^2 \sigma(\pi + \alpha \to \beta) . \tag{2.27}$$

At $Q^2 \to 0$, only the longitudinal part contributes because the pion has no spin. Therefore, in the limit of vanishing Q^2, the cross section for longitudinal a_1 scattering behaves like the cross section for pion scattering.

We have seen in Sec. 2.2 that the non-pionic part of the axial current provides the main contribution to the cross section at $Q^2 \to 0$. It can then be assumed that this non-pionic contribution is dominated by the a_1 meson, which allows the PCAC prediction to be extended to higher values of Q^2 :

$$\frac{d^2\sigma_L^A(\nu_l + \alpha \to l + \beta)}{dQ^2\, d\nu} = \frac{G_F^2}{4\pi^2} \frac{|\vec{q}|}{E^2} f_\pi^2 \frac{\epsilon}{1-\epsilon} \sigma(\pi + \alpha \to \beta) \left(\frac{m_a^2}{Q^2 + m_a^2}\right)^2 . \tag{2.28}$$

Eq. (2.28) reduces to Adler's relation (2.11) in the limit $Q^2 \to 0$, as required by relation (2.27).

Piketty and Stodolsky paradox: It is pointed out in Ref. [4] that extending Eq. (2.27) to higher Q^2 leads to an expression which is contradicted by experiment. Indeed, for $Q^2 = m_a^2$ and $f_a^2 = f_\rho^2 = 2m_\rho^4/\gamma_\rho^2$, and using the experimental value $\gamma_\rho^2/4\pi = 2.4$ from ρ photoproduction experiments, Eq. (2.27) gives

$$\sigma_L(a_1 + \alpha \to \beta) \Big|_{Q^2=m_a^2} \simeq \sigma(\pi + \alpha \to \beta) \Big|_{Q^2=m_a^2} .$$

Thus, considering the cross section for exclusive pion production, we expect

$$\frac{\sigma(a_{1L} \to \pi)\Big|_{Q^2=m_a^2}}{\sigma(\pi \to \pi)\Big|_{Q^2=m_a^2}} = \frac{\sigma(\pi \to a_{1L})\Big|_{Q^2=m_a^2}}{\sigma(\pi \to \pi)\Big|_{Q^2=m_a^2}} \simeq \frac{\sigma(\pi \to a_{1L})\Big|_{Q^2=-m_\pi^2}}{\sigma(\pi \to \pi)\Big|_{Q^2=-m_\pi^2}} \simeq 1 \ .$$

The extrapolation from $Q^2 = m_a^2$ to $Q^2 = -m_\pi^2$ (i.e. for real pions) is assumed to have only a small effect. However, this last equation is not confirmed by the experimental values for the pion cross sections : $\sigma(\pi \to a_{1L})\Big|_{Q^2=-m_\pi^2} = 0.1$ mb and $\sigma(\pi \to \pi)\Big|_{Q^2=-m_\pi^2} = 3$ mb [2].

Kopeliovich and Marage [2] have shown that this paradox can be resolved by a dispersion relation approach in which the current is dominated by multiple poles. In this approach, the longitudinal part of the axial cross section is

$$\frac{d^2\sigma_L^A(\nu_l + \alpha \to l + \beta)}{dQ^2\, d\nu} = \frac{G_F^2}{4\pi^2}\,\frac{|\vec{q}|}{E^2}\,\frac{\epsilon}{1-\epsilon}\left[f_\pi\,\sqrt{\sigma(\pi+\alpha\to\beta)} - Q^2\sum_i \frac{f_i}{m_i}\,\frac{1}{Q^2+m_i^2}\,\sqrt{\sigma_L(a_1+\alpha\to\beta)}\right]^2 . \quad (2.29)$$

The paradox is resolved because the cross section for pion diffractive dissociation integrated over masses is of the same order of magnitude as the cross section for pion elastic scattering [2]. For low Q^2, the Q^2 dependence of Eq. (2.29) can be parametrized by

$$\frac{d\sigma_L^A}{dQ^2} \propto \frac{m^2}{Q^2+m^2} \ .$$

The mass m is an effective mass resulting from the combined effect of the poles

$$\frac{1}{m^2} = < \frac{1}{m_i^2} > = \frac{\sum f_i\, \mathcal{A}_L(i+\alpha\to\beta)/m_i^3}{\sum f_i\, \mathcal{A}_L(i+\alpha\to\beta)/m_i} \ .$$

In the case of single pion production, the value of m is found to be approximately 1.1 GeV (center of gravity of the mass distribution for pion diffractive dissociation). This value is close to the a_1 mass and thus the Q^2 dependence is well approximated by a simple a_1 propagator term as in Eq. (2.28).

(c) Interference between Vector and Axial Currents

The upper limit on the contribution from interference between the vector and axial currents is evaluated to be

$$\frac{d^2\sigma^{VA}(\nu_l + \alpha \to l + \beta)}{dQ^2\, d\nu} \leq \frac{G_F^2}{\pi^2}\,\frac{2E-\nu}{2E^2}\,\frac{f_\rho\, f_a}{(Q^2+m_\rho^2)(Q^2+m_a^2)} \times Q^2\,\sqrt{\sigma_T(\rho+\alpha\to\beta)\cdot\sigma_T(a_1+\alpha\to\beta)}\,.$$

The effect of the interference is usually small. Moreover, its contribution vanishes in the case of coherent production since it contributes only if the same final state β can be produced by both ρ and a_1 mesons.

2.4 Coherent Scattering of Hadrons

In the previous sections, we have shown how the cross section for neutrino scattering at small values of Q^2 can be related to the cross sections for purely hadronic processes : $\sigma(\pi+\alpha\to\beta)$, $\sigma(\rho+\alpha\to\beta)$ and $\sigma(a_1+\alpha\to\beta)$. The next logical step is to determine these cross sections for interactions in which the incoming hadron scatters off a target nucleus coherently.

The concept of coherence and its implications on the type and kinematics of the reaction process are presented first (Section 2.4.1). Next, the Rein and Sehgal model for coherent pion production in neutrino-nucleus interactions is described in Section 2.4.2. However, in this model, the treatment of the absorption of hadrons inside nuclear matter is rather crude. A more elaborate treatment of the coherent hadron-nucleus scattering is possible within the framework of Glauber's theory introduced in Section 2.4.3. Finally, in Section 2.4.4, the Glauber theory is applied to the case of coherent pion production in a model proposed by Belkov and Kopeliovich.

2.4.1 Coherence

Consider the scattering of a hadron with momentum $\vec{q}$ by a nucleus $\mathcal{N}$ of radius $R_{\mathcal{N}}$ containing A nucleons. The scattering amplitude T is a sum of the amplitudes from each individual nucleon

$$T(h\mathcal{N}) = \sum T(hN) \ ,$$

and the cross section is proportional to the square of this amplitude

$$\sigma \ \propto \ |T(h\mathcal{N})|^2 = \left|\sum T(hN)\right|^2 \ .$$

Thus, interferences appear between the scattering amplitudes from different nucleons. In quantum mechanical terms, the scattering is said to be coherent if those interferences are constructive, i.e.

$$\sigma \ \propto \ A^2 \, |T(hN)|^2 \ ,$$

rather than $A\,|T(hN)|^2$ for incoherent processes for which there are no interferences.

It is then concluded that in a coherent process, the nucleons react collectively. In other words, the momentum transferred to a single nucleon is transmitted to the other nucleons via the strong force binding them together in such a way that the nucleus recoils as a whole, without breaking up.

However, there are kinematical restrictions for the coherence effect to take place [25]. In particular, the momentum transfer cannot be too large otherwise the struck nucleon would be knocked out. Moreover, the nucleus is an extended object and each nucleon contributes a different phase factor depending on its position $\vec{r}$: $e^{i\vec{\Delta}\cdot\vec{r}}$ ($\vec{\Delta} = \vec{q} - \vec{q}'$ is the momentum transfer). Thus, the phase factor should not oscillate too rapidly over distances comparable with the nuclear radius

$$\Delta \cdot R_{\mathcal{N}} \lesssim 1 \ .$$

As a consequence, coherence effects can only occur in processes for which the momentum transfer is small.

Coherence effects are also restricted to certain types of reactions. In general, the target nucleus remains in its ground state and there is no transfer of charge, spin or isospin (because this would introduce amplitudes with opposite signs for interactions on neutrons and protons). As observed in coherent production of hadrons by photons and hadrons, coherent processes are essentially diffractive, i.e. they display the following characteristics :

- exponential dependence of the cross section on t (the square of the four-momentum transfer to the nucleus)

$$\frac{d\sigma}{dt} \propto e^{-b|t|}$$

  where the slope parameter b is related to the transverse dimensions of the nucleus ($b \sim R_{\mathcal{N}}^2$);

- the particle exchanged with the nucleus has the same quantum numbers as the vacuum (Pomeron exchange);

- the forward amplitude is mostly imaginary;

- the cross section is essentially independent of energy;

The coherent elastic scattering is represented as in Fig.2.5.

2.4.2 Neutrino Coherent Production of Single Pions; the Rein and Sehgal Formulation

Rein and Sehgal [9] have proposed a model for coherent production of single pions in neutrino interactions based on Adler's relation (2.11). Here, the reaction of interest is

$$\nu_\mu + \mathcal{N} \rightarrow \mu^- + \pi^+ + \mathcal{N} \ ,$$

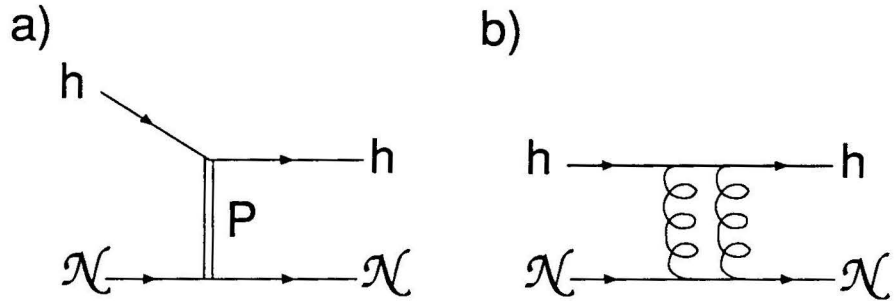

Figure 2.5: Diffractive scattering of a hadron off a nucleus : a) represents the scattering in terms of Pomeron exchange; b) represents the scattering in terms of multiple gluon exchange between the quarks of the incident hadron and the target nucleus.

where initial and final hadronic states are $\alpha = \mathcal{N}$, the target nucleus, and $\beta = \pi^+ + \mathcal{N}$. Adler's relation then becomes

$$\frac{d^3\sigma(\nu_\mu + \mathcal{N} \to \mu^- + \pi^+ + \mathcal{N})}{dQ^2\, d\nu\, dt}\bigg|_{Q^2\to 0} = \frac{G_F^2}{2\pi^2}\, f_\pi^2\, \frac{1}{\nu}\, \frac{E'}{E}\, \frac{d\sigma(\pi^+ + \mathcal{N} \to \pi^+ + \mathcal{N})}{dt}$$

with $\frac{d\sigma(\pi+\mathcal{N}\to\pi+\mathcal{N})}{dt}$ describing the pion-nucleus diffractive scattering. This can also be expressed as a function of the forward (i.e. $t = 0$) pion-nucleon scattering cross section as follows

$$\frac{d\sigma(\pi + \mathcal{N} \to \pi + \mathcal{N})}{dt} = A^2\ |F_{\mathcal{N}}(t)|^2\ \frac{d\sigma(\pi + N \to \pi + N)}{dt}\bigg|_{t=0} \tag{2.30}$$

with the factor A^2 characteristic of coherent processes and a nuclear form factor $F_{\mathcal{N}}(t)$ is introduced. Moreover, the forward scattering cross section can be specified by way of the optical theorem

$$\frac{d\sigma(\pi + N \to \pi + N)}{dt}\bigg|_{t=0} = \frac{1}{16\pi}\ \left(\sigma_{tot}^{\pi N}\right)^2\ (1 + r^2)$$

with the parameter r defined as the ratio between the real and imaginary parts of the forward pion-nucleon scattering amplitude $r \equiv \mathrm{Re}\, f_{\pi N}(0)/\mathrm{Im}\, f_{\pi N}(0)$, and $\sigma_{tot}^{\pi N}$ is the total pion-nucleon cross section. Rein and Sehgal chose the nuclear form factor in (2.30) to be represented by

$$|F_{\mathcal{N}}(t)|^2 = e^{-b|t|}\ F_{\mathbf{abs}}\ ,$$

where the slope parameter is calculated using the following empirical expressions

$$\begin{aligned} b &= \tfrac{1}{3} R_{\mathcal{N}}^2 , \\ \text{with} \quad R_{\mathcal{N}} &= R_0 \, A^{1/3} \qquad (R_0 = 1.12 \text{ fm}). \end{aligned} \tag{2.31}$$

The factor $F_{\rm abs}$ describes the attenuation due to the effects of pion absorption inside the nucleus. It is calculated by treating the nucleus as a homogeneous sphere with uniform density and assuming it takes the simple form

$$F_{\rm abs} = \exp\left(- < x > / \lambda\right) = \exp\left(-\frac{9\, A^{1/3}}{16\, \pi\, R_0^2}\, \sigma_{\rm inel}\right) , \tag{2.32}$$

where $< x >$ is the average distance travelled by the pion inside the nucleus, λ is the mean free path of the pion inside the nucleus and $\sigma_{\rm inel}$ is the inelastic pion-nucleon cross section.

The extrapolation of Adler's relation to non-zero values of Q^2 is performed by simply adding a propagator term $\left(\frac{m_a^2}{Q^2+m_a^2}\right)^2$. As a result, the differential cross section for neutrino coherent production of single pions becomes

$$\begin{aligned} \frac{d^3\sigma(\nu_\mu + \mathcal{N} \to \mu^- + \pi^+ + \mathcal{N})}{dQ^2\, d\nu\, dt} &= \frac{G_F^2}{2\pi^2}\, f_\pi^2\, \frac{1}{\nu}\, \frac{E'}{E}\, \left(\frac{m_a^2}{Q^2+m_a^2}\right)^2 \\ &\quad \times \frac{A^2}{16\pi}\, \left(\sigma_{tot}^{\pi N}\right)^2\, (1+r^2)\, e^{-b|t|}\, F_{\rm abs} . \end{aligned} \tag{2.33}$$

It was pointed out by Belkov and Kopeliovich [10] that, in this model, the crude description of the absorption contradicts the diffractive nature of the pion-nucleon scattering. Indeed, it will be shown below that in the framework of the Glauber theory, the total pion-nucleus cross section actually increases with increasing absorption and, in the limit of scattering by a black disk (i.e. total absorption), the cross section reaches its maximum value of $2\pi R_{\mathcal{N}}^2$. This clearly contradicts the exponential decrease prescribed by Eq.(2.32).

2.4.3 Glauber Theory [26]

In the eikonal approximation, the scattering amplitude for high energy hadron-nucleon elastic scattering can be written as[4]

$$f(\vec{\Delta}) = -\frac{1}{4\pi}\int d^2b \int dz\; e^{i\vec{\Delta}_T\cdot\vec{b}}\; e^{i\Delta_L z}\; U(\vec{b},z)\; e^{-\frac{i}{2|\vec{q}|}\int_{-\infty}^{z} dz'\, U(\vec{b},z')}\;, \tag{2.34}$$

where $U(\vec{b},z)$ is a static scattering potential which is assumed to be of limited range and to vary smoothly with $\vec{r}$; $\vec{b}$ is a two-dimensional vector lying in the plane perpendicular to the z-axis (incident hadron direction) and is thus interpreted as the impact parameter. Furthermore, the momentum transfer to the target is separated into transverse (Δ_T) and longitudinal (Δ_L) components.

Eq. (2.34) can be rewritten as

$$f(\vec{\Delta}) = -\frac{i|\vec{q}|}{2\pi}\int d^2b\; e^{i\vec{\Delta}_T\cdot\vec{b}} \int dz\; e^{i\Delta_L z}\; \frac{\partial}{\partial z}\left[e^{-\frac{i}{2|\vec{q}|}\int_{-\infty}^{z} dz'\, U(\vec{b},z')}\right]\;.$$

In the case of small-angle scattering, the longitudinal momentum transfer can be neglected ($\Delta_L \simeq \frac{1}{2}|\vec{q}|\theta^2$ whereas $\Delta_T \simeq -|\vec{q}|\theta$) and the integral over z can be carried out

$$\begin{aligned} f(\vec{\Delta}) &= -\frac{i|\vec{q}|}{2\pi}\int d^2b\; e^{i\vec{\Delta}_T\cdot\vec{b}}\left\{\; e^{-\frac{i}{2|\vec{q}|}\int_{-\infty}^{+\infty} dz'\, U(\vec{b},z')} - 1\right\} \\ &= \frac{i|\vec{q}|}{2\pi}\int d^2b\; e^{i\vec{\Delta}_T\cdot\vec{b}}\left\{1 - \; e^{i\chi(\vec{b})}\right\}\;, \end{aligned}$$

where we have introduced a phase shift function $\chi(\vec{b}) \equiv -\frac{1}{2|\vec{q}|}\int_{-\infty}^{+\infty} dz\; U(\vec{b},z)$. It is also convenient to introduce a "profile function" defined by

$$\Gamma(\vec{b}) \equiv 1 - e^{i\chi(\vec{b})}\;. \tag{2.35}$$

The scattering amplitude (2.34) reduces then to the simple form

$$f(\vec{\Delta}) = \frac{i|\vec{q}|}{2\pi}\int d^2b\; e^{i\vec{\Delta}_T\cdot\vec{b}}\;\Gamma(\vec{b})\;. \tag{2.36}$$

---

[4]For a more detailed derivation of the expressions given in this section see Refs. [26]–[28].

The profile function provides a description of the scattered wave function in the region immediately behind the target. It can be seen from Eq. (2.36) that the profile function may be interpreted as the Fourier transform of the scattering amplitude.

In order to describe scattering by complex nuclei, Glauber assumed that the overall phase shift is obtained by summing over the phase shifts corresponding to the scattering on each of the individual nucleons :

$$\chi_{\mathcal{N}}(\vec{b}) = \sum_{i=1}^{A} \chi_i(\vec{b} - \vec{s}_i) \; , \tag{2.37}$$

where $\vec{s}_i$ is the coordinate of the ith nucleon in the plane perpendicular to the incident hadron direction. The quantity $\vec{b} - \vec{s}_i$ thus represents the impact parameter with respect to the ith nucleon. In this approach, the nucleons are assumed to be frozen during the short time necessary for the incident wave to pass through the nucleus. It follows from Eqs. (2.35) and (2.37) that the nuclear profile function is given by

$$\Gamma_{\mathcal{N}}(\vec{b}, \vec{s}_1, ..., \vec{s}_A) = 1 - \prod_{i=1}^{A} \left[1 - \Gamma(\vec{b} - \vec{s}_i)\right]$$

and the function $\Gamma_{\mathcal{N}}(\vec{b})$ may be obtained by averaging $\Gamma_{\mathcal{N}}(\vec{b}, \vec{s}_1, ..., \vec{s}_A)$ over the ground state of the nucleus

$$\begin{aligned} \Gamma_{\mathcal{N}}(\vec{b}) &= \left\langle 0 \left| \, 1 - \prod_{i=1}^{A} \left[1 - \Gamma(\vec{b} - \vec{s}_i)\right] \, \right| 0 \right\rangle \\ &= \int d^3r_1 \cdots d^3r_A \; \Psi_0^*(\vec{r}_1, ..., \vec{r}_A) \\ &\quad \times \left\{ 1 - \prod_{i=1}^{A} \left[1 - \Gamma(\vec{b} - \vec{s}_i)\right] \right\} \; \Psi_0(\vec{r}_1, ..., \vec{r}_A) \; , \end{aligned} \tag{2.38}$$

where the nuclear wave function $\Psi_0(\vec{r}_1, ..., \vec{r}_A)$ determines the distribution of nucleons inside the nucleus.

Finally, the hadron-nucleus scattering amplitude can be written in a form analogous to that of Eq. (2.36)

$$F(\vec{\Delta}) = \frac{i|\vec{q}|}{2\pi} \int d^2b \; e^{i\vec{\Delta}_T \cdot \vec{b}} \; \Gamma_{\mathcal{N}}(\vec{b}) \; . \tag{2.39}$$

The nuclear profile function (2.38) can be simplified in the context of the independent particle model. In this model, the following relation holds

$$|\Psi_0|^2 = \rho_{\mathcal{N}}(\vec{r}_1, ..., \vec{r}_A) = \prod_{i=1}^{A} \rho(\vec{r}_i)$$

with $\rho_{\mathcal{N}}(\vec{r}_1, ..., \vec{r}_A)$ describing the nuclear density. Therefore,

$$\begin{aligned} \Gamma_{\mathcal{N}}(\vec{b}) &= 1 - \prod_{i=1}^{A} \int d^3r_i \ \left[1 - \Gamma(\vec{b} - \vec{s}_i)\right] \ \rho(\vec{r}_i) \\ &= 1 - \left[1 - \int d^3r \ \Gamma(\vec{b} - \vec{s}) \ \rho(\vec{r})\right]^A \end{aligned} \tag{2.40}$$

with the normalization condition $\int d^3r \ \rho(\vec{r}) = 1$. From Eq. (2.36) we have that

$$\int d^2s \ \Gamma(\vec{b} - \vec{s}) = \frac{2\pi}{i|\vec{q}|} f(0)$$

and

$$\int d^3r \ \Gamma(\vec{b} - \vec{s}) \ \rho(\vec{r}) \ = \ \frac{2\pi}{i|\vec{q}|} \ f(0) \ \frac{T(\vec{b})}{A}$$

with the "Thickness function" $T(\vec{b})$ defined as

$$T(\vec{b}) = A \int_{-\infty}^{+\infty} dz \ \rho(\vec{b}, z) = \int_{-\infty}^{+\infty} dz \ \rho_{\mathcal{N}}(\vec{b}, z)$$

and the nuclear density normalized according to $\int d^3r \ \rho_{\mathcal{N}}(\vec{r}) = A$. The function $T(\vec{b})$ represents the thickness of the nucleus along the z-axis for a given value of the impact parameter $\vec{b}$. Moreover, the optical theorem relates the forward scattering amplitude to the total hadron-nucleon cross section

$$f(0) = \frac{i|\vec{q}|}{4\pi} \ \sigma_{tot}^{hN} \ (1 - ir)$$

with $r \equiv \mathrm{Re}\, f(0)/\mathrm{Im}\, f(0)$.

As a consequence, the nuclear profile function (2.40) becomes

$$\Gamma_{\mathcal{N}}(\vec{b}) = 1 - \left[1 - \frac{1}{2}(1 - ir) \ \sigma_{tot}^{hN} \ \frac{T(\vec{b})}{A}\right]^A . \tag{2.41}$$

For heavy nuclei, the profile function can be approximated by

$$\Gamma_{\mathcal{N}}(\vec{b}) = 1 - e^{-\frac{1}{2}(1-ir) \ \sigma_{tot}^{hN} \ T(\vec{b})} . \tag{2.42}$$

Therefore, in the limit $A \rightarrow \infty$, we obtain for the hadron-nucleus elastic scattering amplitude the same result as that derived in the optical model,

$$F(\vec{\Delta}) = \frac{i|\vec{q}|}{2\pi} \int d^2b \, e^{i\vec{\Delta}_T \cdot \vec{b}} \left\{ 1 - \, e^{-\frac{1}{2} \, \sigma_{tot}^{hN} \, T(\vec{b})} \right\} \, , \tag{2.43}$$

where $r = 0$ for convenience (note that r is small at high energy). The total cross section for hadron-nucleus scattering can now be determined by invoking the optical theorem

$$\begin{aligned} \sigma_{tot}^{h\mathcal{N}} &= \frac{4\pi}{|\vec{q}|} \, \text{Im} \, F(0) \\ &= 2 \, \text{Re} \left\{ \int d^2b \, \left(1 - e^{-\frac{1}{2} \, \sigma_{tot}^{hN} \, T(\vec{b})} \right) \right\} \, . \end{aligned} \tag{2.44}$$

This last equation is the principal result of the optical model. The exponential term determines the amount of absorption inside the nucleus :

$$\exp \left[-\frac{1}{2} \, \sigma_{tot}^{hN} \int dz \, \rho_{\mathcal{N}}(\vec{b}, z) \right] = \exp \left[-\frac{1}{2} \int \frac{dz}{\lambda} \right] \, ,$$

where λ represents the mean free path inside the nucleus. For typical nuclear densities ($\rho_{\mathcal{N}}(r) = 0.16 \text{ fm}^{-3}$) and $\sigma_{tot}^{hN} = 24$ mb, the mean free path $\lambda = 2.6$ fm. If $\lambda \rightarrow 0$, we find the black disk result $\sigma_{tot}^{h\mathcal{N}} = 2\pi R_{\mathcal{N}}^2$, where $R_{\mathcal{N}}$ is the radius of the nucleus.

2.4.4 Neutrino Coherent Production of Single Pions; the Glauber Theory Approach of Belkov and Kopeliovich

Belkov and Kopeliovich [10] have applied Glauber's theory to describe the pion-nucleus scattering cross section[5] appearing in Adler's relation. Belkov and Kopeliovich start with Adler's relation and choose the following parametrization of the

[5]Note that Lackner [29] also used Glauber's theory in an earlier attempt to describe the coherent production of single pions in neutrino interactions.

differential cross section

$$\frac{d^3\sigma(\nu_\mu + \mathcal{N} \to \mu^- + \pi^+ + \mathcal{N})}{dQ^2\, d\nu\, d\Delta_T^2} = \frac{G_F^2}{2\pi^2}\, f_\pi^2\, \frac{1}{\nu}\, \frac{E'}{E}\, \left|F_{\mathcal{N}}(Q^2)\right|^2\, \frac{d\sigma(\pi^+ + \mathcal{N} \to \pi^+ + \mathcal{N})}{d\Delta_T^2},$$

where Δ_T^2, the square of the transverse part of the momentum transfer to the nucleus, is used instead of t, and $F_{\mathcal{N}}(Q^2)$ is a form factor which is described below. Using Eq.(2.34) with a scattering potential given by $U(\vec{b}, z) = -4\pi\ f(0)\ \rho_{\mathcal{N}}(\vec{b}, z) = -i|\vec{q}|\sigma_{tot}^{\pi N}\ \rho_{\mathcal{N}}(\vec{b}, z)$, based on the results presented in the previous section, we can write the pion-nucleus elastic scattering amplitude as

$$F(\vec{\Delta}) = \frac{i|\vec{q}|}{4\pi} \int d^2b \int dz\ e^{i\vec{\Delta}_T \cdot \vec{b}}\ e^{i\Delta_L z}\ \sigma_{tot}^{\pi N}\ \rho_{\mathcal{N}}(\vec{b}, z)\ e^{-\frac{1}{2}\,\sigma_{tot}^{\pi N} \int_{-\infty}^{z} dz'\, \rho_{\mathcal{N}}(\vec{b}, z')}\ , \quad (2.45)$$

where $\vec{\Delta}_T$ and Δ_L are the transverse and longitudinal components of the momentum transfer with respect to the incident hadron direction (i.e. the W boson direction). The elastic pion-nucleus scattering cross section may be expressed as

$$\begin{aligned} \frac{d\sigma(\pi + \mathcal{N} \to \pi + \mathcal{N})}{d\Delta_T^2} &= \left.\frac{d\sigma(\pi + \mathcal{N} \to \pi + \mathcal{N})}{d\Delta_T^2}\right|_{\Delta=0} \cdot\ e^{-B_T\, \Delta_T^2} \\ &= \frac{\left(\sigma_{tot}^{\pi\mathcal{N}}\right)^2}{16\pi}\, (1 + r^2)\ \cdot\ e^{-B_T\, \Delta_T^2}\ . \end{aligned}$$

This last expression makes use of the optical theorem and an exponential (or Gaussian) parametrization of the dependence on Δ_T^2 is utilized. It can be shown that, for negligible Δ_L^2, and for $\Delta_T^2 \ll 1/R_{\mathcal{N}}^2$, the slope B_T can be represented by

$$B_T = \frac{1}{2} < b^2 > = \frac{1}{\sigma_{tot}^{\pi\mathcal{N}}} \int d^2b\ b^2\ \left(1 - e^{-\frac{1}{2}\,\sigma_{tot}^{\pi N}\, T(\vec{b})}\right) \quad (2.46)$$

with the total pion-nucleus cross section given as in Eq. (2.44) by

$$\sigma_{tot}^{\pi\mathcal{N}} = 2 \int d^2b\ \left(1 - e^{-\frac{1}{2}\,\sigma_{tot}^{\pi N}\, T(\vec{b})}\right) \quad (2.47)$$

(the parameter $r = 0$ for simplicity). Expression (2.46) thus relates the slope B_T to the impact parameter b.

Following Belkov and Kopeliovich, the form factor $F_{\mathcal{N}}(Q^2)$ is written as the product of a nucleon form factor $F_N(Q^2)$ and a nuclear form factor $\tilde{F}_{\mathcal{N}}(Q^2)$

$$F_{\mathcal{N}}(Q^2) = F_N(Q^2)\ \tilde{F}_{\mathcal{N}}(Q^2)\ .$$

The nucleon form factor may be represented by a propagator form with an axial mass m_a corresponding to the a_1 mass

$$F_N^{\rm pole}(Q^2) = \frac{m_a^2}{Q^2 + m_a^2} \ . \tag{2.48}$$

However, there are experimental indications that the axial current may be dominated by non resonant $\rho\,\pi$ systems rather than by the a_1 meson. In this case, the dispersion relation corresponding to the $\rho\,\pi$ cut yields

$$F_N^{\rm cut}(Q^2) = \frac{(m_\rho + m_\pi)^2}{Q^2 + m_\pi^2}\ ln\left[1 + \frac{Q^2 + m_\pi^2}{(m_\rho + m_\pi)^2}\right] \ . \tag{2.49}$$

For small Q^2, the Q^2 dependence of the pole and cut form factors is nevertheless similar.

The nuclear form factor is expressed in the context of the Glauber theory by

$$\tilde{F}_{\mathcal{N}}(Q^2) = \frac{\sigma_{tot}^{\pi N}}{\sigma_{tot}^{\pi \mathcal{N}}} \int d^2b \int dz\ e^{i\Delta_L z}\ \rho_{\mathcal{N}}(\vec{b},z)\ e^{-\frac{1}{2}\sigma_{tot}^{\pi N}\int_z^\infty dz'\ \rho_{\mathcal{N}}(\vec{b},z')} \ .$$

This equation can be obtained from Eq. (2.45) by letting $\Delta_T = 0$ and normalizing it such that $\tilde{F}_{\mathcal{N}}(Q^2 \simeq 0) = 1$. It should be noted that Δ_L and Q^2 are related by

$$\Delta_L^2 \simeq t_{min} \simeq \left(\frac{Q^2 + m^2}{2\nu}\right)^2$$

(see Eq. (2.16)). For negligible Δ_T^2, and for $\Delta_L^2 \ll 1/R_{\mathcal{N}}^2$, $\tilde{F}_{\mathcal{N}}(Q^2)$ may be approximated by

$$\tilde{F}_{\mathcal{N}}(Q^2) = \exp\left(-\frac{1}{2}\, B_L\, \Delta_L^2\right) ,$$

where the slope parameter B_L is the square of the width of the z-distribution averaged over the nucleus

$$B_L = < z^2 > - < z >^2 \ . \tag{2.50}$$

The averaging is carried out as follows

$$< z^n > = \frac{\sigma_{tot}^{\pi N}}{\sigma_{tot}^{\pi \mathcal{N}}} \int d^2b \int dz\ z^n\ \rho_{\mathcal{N}}(\vec{b},z)\ e^{-\frac{1}{2}\sigma_{tot}^{\pi N}\int_z^\infty dz'\ \rho_{\mathcal{N}}(\vec{b},z')} \ . \tag{2.51}$$

Finally, the differential cross section for coherent production of pions is given by

$$\frac{d^3\sigma(\nu_\mu + \mathcal{N} \rightarrow \mu^- + \pi^+ + \mathcal{N})}{dQ^2\, d\nu\, d\Delta_T^2} = \frac{G_F^2}{2\pi^2}\, f_\pi^2\, \frac{1}{\nu}\, \frac{E'}{E}\, \left|F_N(Q^2)\right|^2 \times \frac{\left(\sigma_{\rm tot}^{\pi\mathcal{N}}\right)^2}{16\pi}\, (1+r^2)\, e^{-B_T\, \Delta_T^2}\, e^{-B_L\, \Delta_L^2} \quad (2.52)$$

It should be noted that the above expression was obtained by neglecting the correlation between Δ_T and Δ_L for non-zero values of those quantities. However, a detailed calculation [2] shows that the change in the values of B_T for non-vanishing Δ_L is negligible. The values of $\sigma_{\rm tot}^{\pi\mathcal{N}}$, B_T and B_L have been computed by Belkov and Kopeliovich [10] for several nuclei. For neon, the values obtained using $\sigma_{\rm tot}^{\pi N} = 24$ mb and a Woods-Saxon parametrization of the nuclear density function are

$$\begin{aligned} \sigma_{tot}^{\pi\mathcal{N}} &= 381 \text{ mb}\,, \\ B_L &= 2.85 \text{ fm}^2 = 73.2 \text{ GeV}^{-2}\,, \\ B_T &= 3.49 \text{ fm}^2 = 89.6 \text{ GeV}^{-2}\,, \end{aligned}$$

whereas Rein and Sehgal use a slope parameter of 79.1 GeV^{-2}. Thus, it appears that the values for the different slopes are close. However, for heavier nuclei the slopes B_L and B_T are no longer numerically similar. The reason for this is that the physical origin of the transverse and longitudinal slopes is different : B_T is related to the transverse dimensions of the nucleus (B_T increases as $A^{2/3}$), while B_L is related to the size of nuclear "slice" on which the condition of coherence applies ($\Delta_L \cdot z \lesssim 1$). As A increases, B_L eventually reaches a maximum because of two reasons : i) the mean free path inside nuclear matter is a constant independent of A; ii) because of absorption only the hadrons produced near the backward edge of the nucleus can escape, and thus have to propagate, by virtue of i), through the same amount of nuclear matter. The slope B_L is thus sensitive to the parametrization of the nuclear density near the surface of the nucleus (see Chapter 4 for further discussion).

In order to show that the coherence condition only applies to the longitudinal part of the momentum transfer, let us express the elastic pion-nucleus scattering

cross section [25] using the amplitude (2.45)

$$\begin{aligned}\sigma_{el}^{\pi\mathcal{N}} &= \frac{\pi}{|\vec{q}|^2}\int_0^\infty \frac{d\sigma}{d\Delta_T^2}\,d\Delta_T^2 = \frac{\pi}{|\vec{q}|^2}\int_0^\infty |F(\vec{\Delta})|^2\,d\Delta_T^2 \\ &= \frac{\left(\sigma_{tot}^{\pi N}\right)^2}{16\pi}\int_0^\infty d\Delta_T^2\int d^2b'\int dz'\, e^{-i\vec{\Delta}_T\cdot\vec{b}'}\, e^{-i\Delta_L z'}\,\rho_{\mathcal{N}}(\vec{b}',z')\, e^{-\frac{1}{2}\sigma_{tot}^{\pi N}\int_{-\infty}^{z'} d\tilde{z}'\,\rho_{\mathcal{N}}(\vec{b}',\tilde{z}')} \\ &\quad\times\int d^2b\int dz\, e^{i\vec{\Delta}_T\cdot\vec{b}}\, e^{i\Delta_L z}\,\rho_{\mathcal{N}}(\vec{b},z)\, e^{-\frac{1}{2}\sigma_{tot}^{\pi N}\int_{-\infty}^{z} d\tilde{z}\,\rho_{\mathcal{N}}(\vec{b},\tilde{z})}\,.\end{aligned}$$

The integral over Δ_T^2 can be simplified noting that $d\Delta_T^2 = \frac{1}{\pi}\,d^2\Delta_T$ and

$$\int d^2\Delta_T\, e^{i\vec{\Delta}_T\cdot(\vec{b}-\vec{b}')} = (2\pi)^2\,\delta^2(b-b')\,.$$

Consequently, the cross section becomes

$$\sigma_{el}^{\pi\mathcal{N}} = \frac{1}{4}\left(\sigma_{tot}^{\pi N}\right)^2\int d^2b\,|g(b)|^2\,,$$

where the function $g(b)$ is defined as

$$g(b) \equiv \int dz\, e^{i\Delta_L z}\,\rho_{\mathcal{N}}(b,z)\, e^{-\frac{1}{2}\sigma_{tot}^{\pi N}\int_{-\infty}^{z} dz'\,\rho_{\mathcal{N}}(\vec{b},z')}\,.$$

Therefore, the factor $e^{i\Delta_L z}$ is the only phase factor and thus determines the coherence condition.

For neon nuclei, the radius is measured to be $R_{\mathcal{N}} = 2.80$ fm [30] and the coherence condition sets a limit on the magnitude of the longitudinal momentum transfer

$$\Delta_L \lesssim 1/R_{\mathcal{N}} \;=\; 0.07\ \text{GeV}\,.$$

Chapter 3
Apparatus and Data Acquisition

The E632 experiment collected data during the 1985 and 1987-88 fixed-target runs at the Fermilab Tevatron. The 15-foot Bubble Chamber filled with a heavy Ne–H_2 mixture was exposed to the Quadrupole Triplet neutrino beam. The chamber was also equipped with several new arrays of proportional tubes : the External Muon Identifier (EMI) and the Internal Picket Fence (IPF) which were used to identify muons and determine the event time.

Section 3.1 of this chapter describes the apparatus : the neutrino beam, the 15-foot Bubble Chamber and the EMI/IPF system. Section 3.2 presents the film analysis procedure: scanning, measurement and data processing.

3.1 Description of the Apparatus

3.1.1 Neutrino Beam

The layout of the Fermilab neutrino beam line is shown in Fig. 3.1. Protons accelerated to an energy of 800 GeV were extracted from the Tevatron to collide with a 26.7 cm long (one hadronic interaction length) Beryllium Oxide target. The secondary charged particles produced in the collisions, mostly pions and kaons, were then focused by the Quadrupole Triplet train tuned to 300 GeV/c, i.e. secondaries with momentum of 300 GeV/c were collimated along the beam direction regardless of their production angle whereas secondaries with momentum smaller or greater than 300 GeV/c retained a slight divergence. Following the Quadrupole Triplet

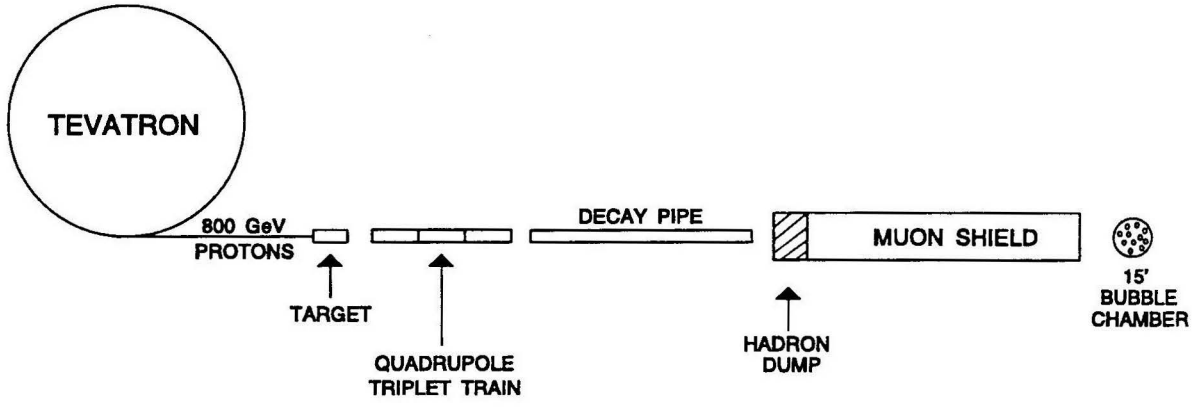

Figure 3.1: Layout of the Fermilab neutrino beam line (not to scale).

train, the secondaries entered a 490 m long decay pipe designed to let charged pions and kaons decay. The neutrino beam was thus produced via the decays:

$$\pi^+(\pi^-) \rightarrow \mu^+(\mu^-) + \nu_\mu(\overline{\nu}_\mu) \qquad \text{(B.R. 100\%)} ,$$

$$K^+(K^-) \rightarrow \mu^+(\mu^-) + \nu_\mu(\overline{\nu}_\mu) \qquad \text{(B.R. 63.5\%)} ,$$

where B.R. is the branching ratio of the particular decay mode listed. The neutrino beam also contained a small $\overset{(-)}{\nu}_e$ component ($\sim$ 3%) arising mostly from 3-body decays of K^0_L and $K^\pm$ mesons. It should be noted that positive and negative secondaries were focused equally by the Quadrupole Triplet train, in contrast with magnetic horn systems which select the charge of the secondaries to be focused.

At the end of the decay pipe, an iron dump was installed to absorb the remaining hadrons. However, this dump did not absorb the decay muons and as a consequence, the bubble chamber had to be separated from the decay pipe by an additional 1000m of steel and earth shielding designed to slow down and eventually absorb the muons.

The intensity of the primary proton beam was monitored by a Secondary Emission Monitor (SEM) and a toroid upstream from the BeO target. In addition, segmented wire ionization chambers were installed both in the decay pipe to monitor the beam size and position, and inside the earth shield to monitor the flux of muons.

The calculated ν_μ and $\overline{\nu}_\mu$ fluxes at the bubble chamber are shown in Fig. 3.2 [31]. The ratio of ν_μ to $\overline{\nu}_\mu$ in the beam was 5:2 with an average ν_μ ($\overline{\nu}_\mu$) beam energy of 80

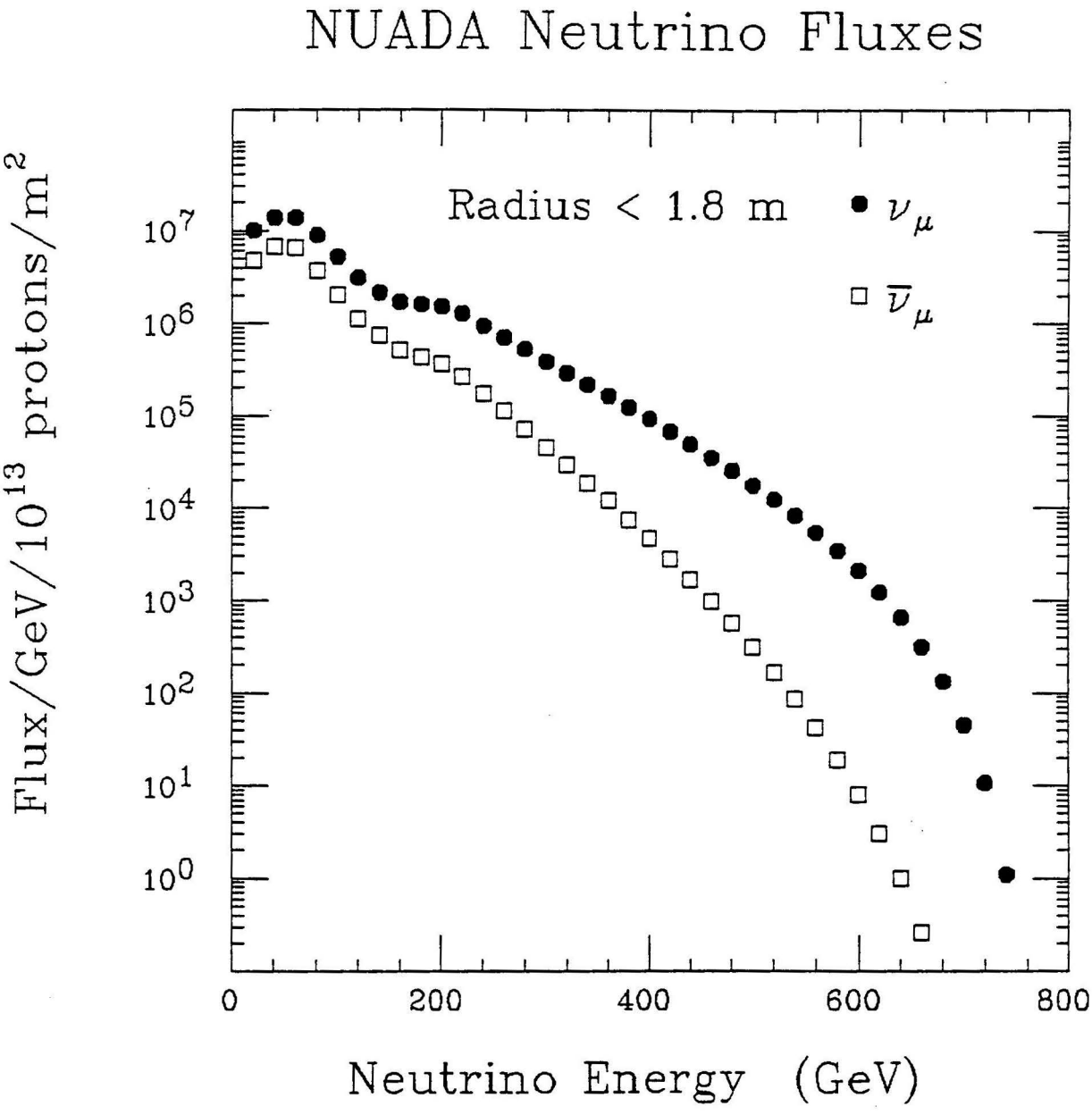

Figure 3.2: Quadrupole Triplet ν_μ and $\overline{\nu}_\mu$ fluxes at the 15-foot Bubble Chamber.

GeV (70 GeV). The corresponding average ν_μ ($\overline{\nu}_\mu$) charged current event energy was 150 GeV (110 GeV). The difference between ν_μ and $\overline{\nu}_\mu$ fluxes is determined by the differences in production rates of positive and negative secondaries in the primary proton-BeO collisions.

A typical accelerator cycle lasted $\sim$ 60 seconds during which there were three extractions to the neutrino beam line, 10 seconds apart. Each extraction contained $\sim 1 - 2 \times 10^{12}$ protons with a duration of 2 to 3 ms. Further information about the neutrino beam line can be found in Ref. [32].

3.1.2 15-foot Bubble Chamber

The 15-foot Bubble Chamber consists of a spherical vessel with a 1.9 m radius and a 33 m^3 capacity (Fig. 3.3). It was filled with a liquid Ne–H_2 mixture, 75 mole percent neon during the 1985 run and 63 mole percent neon during the 1987-88 run corresponding to densities of 0.71 and 0.54 g cm^{-3} respectively. Table 3.1 presents bubble chamber characteristics for both 1985 and 1987-88 runs.

The choice of a heavy liquid, as opposed to H_2 or D_2, provided a higher neutrino interaction rate as well as a good separation between charged hadrons, muons and electrons, and a high photon conversion probability ($\sim$ 90%). The main disadvantages were: (i) increased measurement uncertainties due to higher hadron interaction rates and stronger multiple scattering, and (ii) complications due to nuclear effects like Fermi motion and nuclear reinteraction of secondary hadrons.

A large superconducting magnet generated a nearly uniform magnetic field of 3 Tesla along the vertical direction (Z axis, see Fig. 3.4 for a definition of the reference system). The effect of the magnetic field is to bend the trajectories of charged particles in the plane perpendicular to the direction of the field (XY plane). Their momenta can then be determined through the measurement of the curvature of their trajectories. With this field, the momentum expressed in GeV/c was approximately equal to the radius of curvature expressed in meters (see Eq. (3.2) in Sec. 3.2.2).

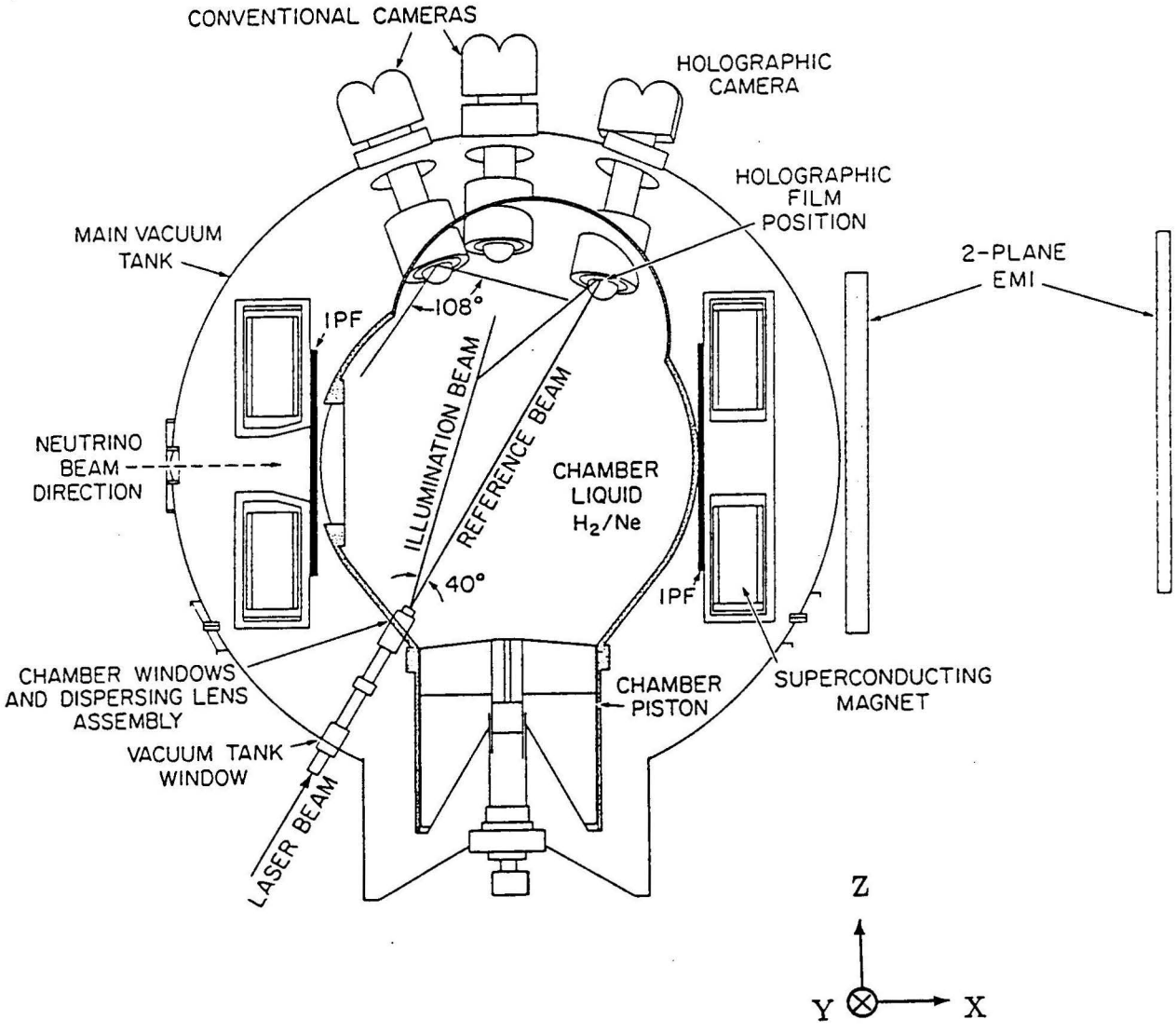

Figure 3.3: Side view of the 15-foot Bubble Chamber.

Table 3.1: Summary of the 1985 and 1987-88 runs.

	1985	1987-88
Total number of frames	155 000	293 000
Total number of frames (this work)	132 000	198 000
Total number of protons on target	2.5×10^{17}	4.5×10^{17}
Total number of protons on target (this work)	2.3×10^{17}	3.2×10^{17}
Ne–H_2 fraction	75% – 25%	63% – 37%
Liquid density (g cm^{-3})	0.71	0.54
Fiducial volume (m^3)	10.0	10.0
Target mass (t)	7.1	5.4
Radiation length (cm)*	41.5	55.0
Interaction length (cm)	153	192

* To find the conversion length multiply by 9/7.

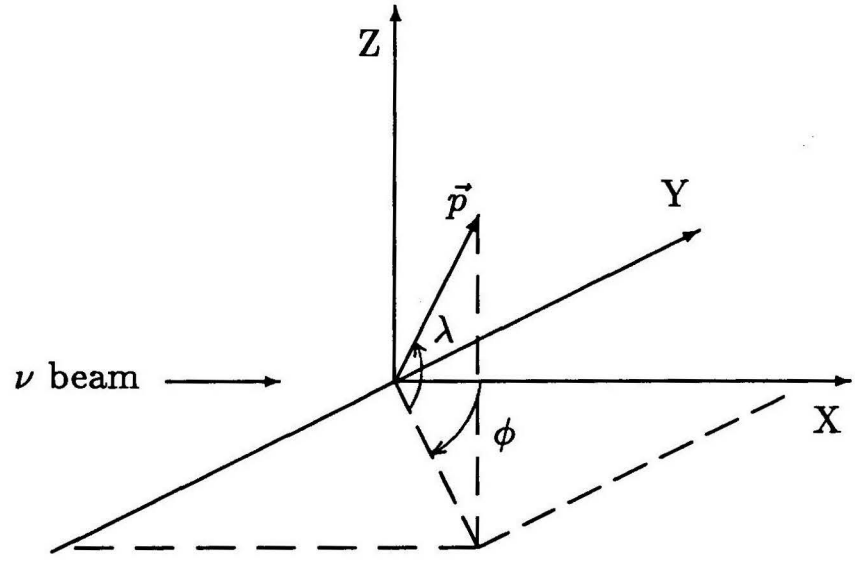

Figure 3.4: The reference system, showing also the definition of the dip angle λ and the azimuthal angle ϕ for a momentum vector $\vec{p}$ in the bubble chamber.

Six camera ports were located at the top of the bubble chamber, four (three in 1985) of which were equipped with conventional optics with a 400–500 μm resolution whereas one was equipped with high resolution conventional optics with a 150–200 μm resolution. The sixth camera port was used to record holograms. Each camera was equipped with a wide angle lens with a field of view of 108° and was separated from the liquid by three concentric fisheye windows. The bright-field illumination was provided by a combination of annular flash tubes located behind the windows and Scotchlite laid onto the bubble chamber walls to retrodirect the light towards the cameras.

This arrangement resulted in a total visible volume of 28 m^3 for the conventional cameras. The visible volume for the high resolution camera was only $\sim$ 1 m^3 due to the fact that in conventional optics the depth of field is proportional to r^{-2}, where r is the resolution. To circumvent this limitation, a holographic system [33] was designed and built to provide high resolution (100 μm) over a large volume ($\gtrsim$ 3 m^3).

The bubble chamber was operated at a temperature of $\sim$ 30 °K, well above the boiling point of the liquid but at a pressure large enough to prevent boiling. Approximately 50 ms before the arrival of the neutrino beam, the pressure was dropped rapidly by lowering the chamber piston. This caused the liquid to become superheated and therefore sensitive to the small amounts of energy lost by ionizing charged particles traversing the liquid. As a consequence, the charged particles produced in neutrino interactions left trails of bubbles along their trajectories. Once those bubbles had grown to their desired sizes they were photographed and the liquid was recompressed. The timing for the expansion was such that the liquid was most sensitive when the neutrino beam entered the chamber. One expansion/recompression cycle lasted $\sim$ 100 ms.

Compared to large electronic detectors with target masses up to $\sim$ 500 tons, the

bubble chamber target mass is relatively small, typically $\sim$ 10 tons for heavy Ne–H_2, resulting in smaller event samples (event counts down by one or two orders of magnitude). However, only bubble chambers provide a detailed and fairly unbiased detection of the showers of secondary particles produced in neutrino interactions, and in particular short recoil tracks crucial for a study of coherent interactions.

3.1.3 EMI/IPF System

The Internal Picket Fence (IPF) consists of a double layer of vertical proportional tubes mounted inside the bubble chamber vacuum tank. The IPF tubes surround the bubble chamber inner vessel, covering 290° in azimuth. There are 96 "pickets" divided into an upstream half (IPFA) and a downstream half (IPFB), see Fig. 3.5a. The pickets are 220 cm long, 11 cm wide and 2.2 cm thick. Each one contains 24 cylindrical proportional tubes, 8 mm in diameter, forming two layers staggered with respect to one another by half a tube width for improved efficiency. The tubes are read out in two groups of six within each layer, resulting in a spatial resolution of 5 cm in the horizontal (XY) plane. A more detailed description of the IPF may be found in Ref. [34].

IPFA was used to veto bubble chamber activity caused by interactions occurring in the material upstream from the bubble chamber liquid whereas IPFB was used to help determine the event time for both neutral and charged current neutrino interactions. The IPF was used extensively in our study of neutral current interactions [35].

The External Muon Identifier consists of three vertical planes (EMIA, EMIB and EMIC) of proportional tubes, located downstream from the bubble chamber (see Fig. 3.5). The technique utilized to identify muons relies on the fact that muons are the only charged particles capable of traversing large amounts of matter. Thus, additional zinc, lead and concrete was installed between the bubble chamber and the various EMI planes to filter out charged particles other than muons. The

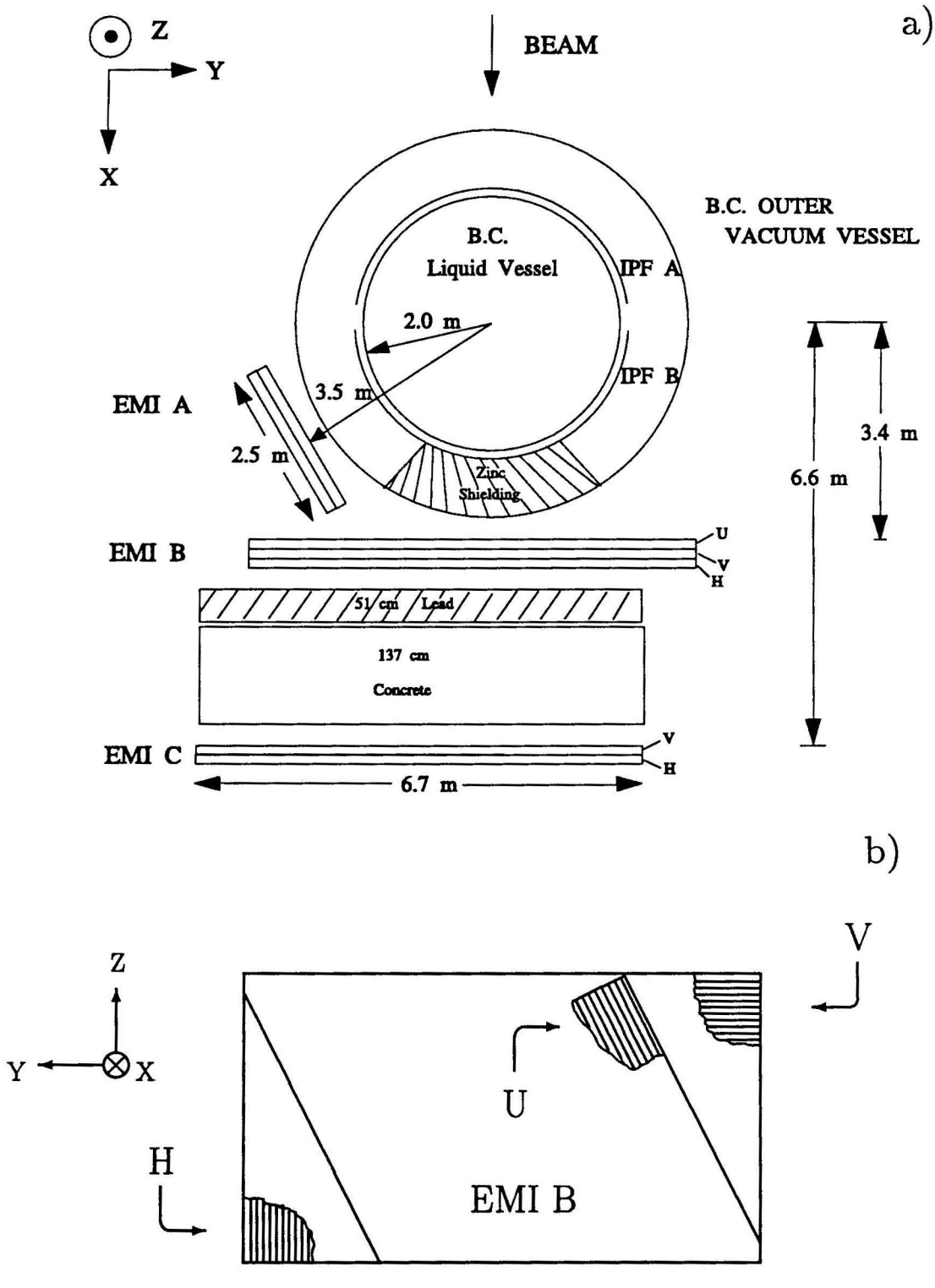

Figure 3.5: Layout of the IPF and EMI planes. The picture at the bottom shows the arrangement of the various planes in EMIB (looking along the direction of the neutrino beam).

various materials located between the chamber vessel and EMIB represent 3 to 5 hadronic interaction lengths whereas the lead and concrete shielding blocks placed between EMIB and EMIC represent 4 to 6 hadronic interaction lengths. The EMIA and EMIC planes comprised four layers of proportional tubes, divided into two sets of double layers to measure coordinates along the horizontal (H) and vertical (V) directions. In addition to those four layers, the EMIB plane also contained two layers to measure the position along a direction 63.5° to the vertical (U). The area covered by EMIB and EMIC is 668 $\times$ 363 cm^2; the EMIA plane, 246 $\times$ 363 cm^2 in area, is not being used in this work.

The cross section of an individual EMI tube was 2.5 $\times$ 2.5 cm^2 and the two layers measuring each coordinate were staggered with respect to one another by half a tube to increase the efficiency of the system. This gave a spatial resolution of $\sim$ 1.3 cm along each direction.

Both EMI and IPF tubes were filled with an 80%–20% Ar–CO_2 gas mixture and contained a 50 μm gold-plated tungsten wire maintained at a high voltage (the rest of the assembly was connected to ground).

The EMI/IPF signals from 16 adjacent tubes were multiplexed onto one cable. These were then demultiplexed and read in via a CAMAC crate. It should be noted that, with the exception of the preamplifiers, all electronics are digital. The data were organized in time segments, or "time slots", each 1 μs long. In the analysis of the EMI/IPF data, signals overlapping two adjacent time slots were treated as if they belonged to a single time slot. For a more detailed account of the EMI/IPF system, refer to [36, 37].

3.2 Film Analysis and Data Processing

3.2.1 Scanning

The bubble chamber film was divided among the collaborating institutions where various scanning and measurement passes were performed. The difficult task of extracting the information from the bubble chamber film was carried out by teams of specially trained scanners using high-magnification film projection devices. The scanners were instructed to examine carefully each frame on three different "views" (i.e. reels of film from three different cameras exposed at the same time) to look for interactions induced by neutral particles which were candidates for neutrino interactions. An example of a neutrino interaction is shown in Fig. 3.6. The "events" thus found were recorded if they satisfied the following criteria :

1. the event is in the field of vision on all three views;

2. the total visible energy of the secondary particles is estimated to be greater than 5 GeV; and

3. the distance between the interaction point and the downstream wall of the chamber is greater than a distance L_{POT} ($L_{POT} \simeq 35$ cm at Z = 0).

For each event the following characteristics were recorded: number of prongs, stubs, electrons and leaving tracks as well as the number of neutral strange particles possibly associated with the event. A "stub" is defined as a straight (or positive) track whose projected length onto the film is smaller than L_{MIN}. The distance L_{MIN} varies with the Z-coordinate of the event but in the middle plane of the chamber (Z = 0) it corresponds to $\sim$ 5 cm ($\sim$ 10 cm) in space for the 1985 (1987-88) film. A track is referred to as a "prong" if it is neither an electron nor a stub.

A second and independent scan was performed on 40% of the film to determine the random efficiency of the first scan.

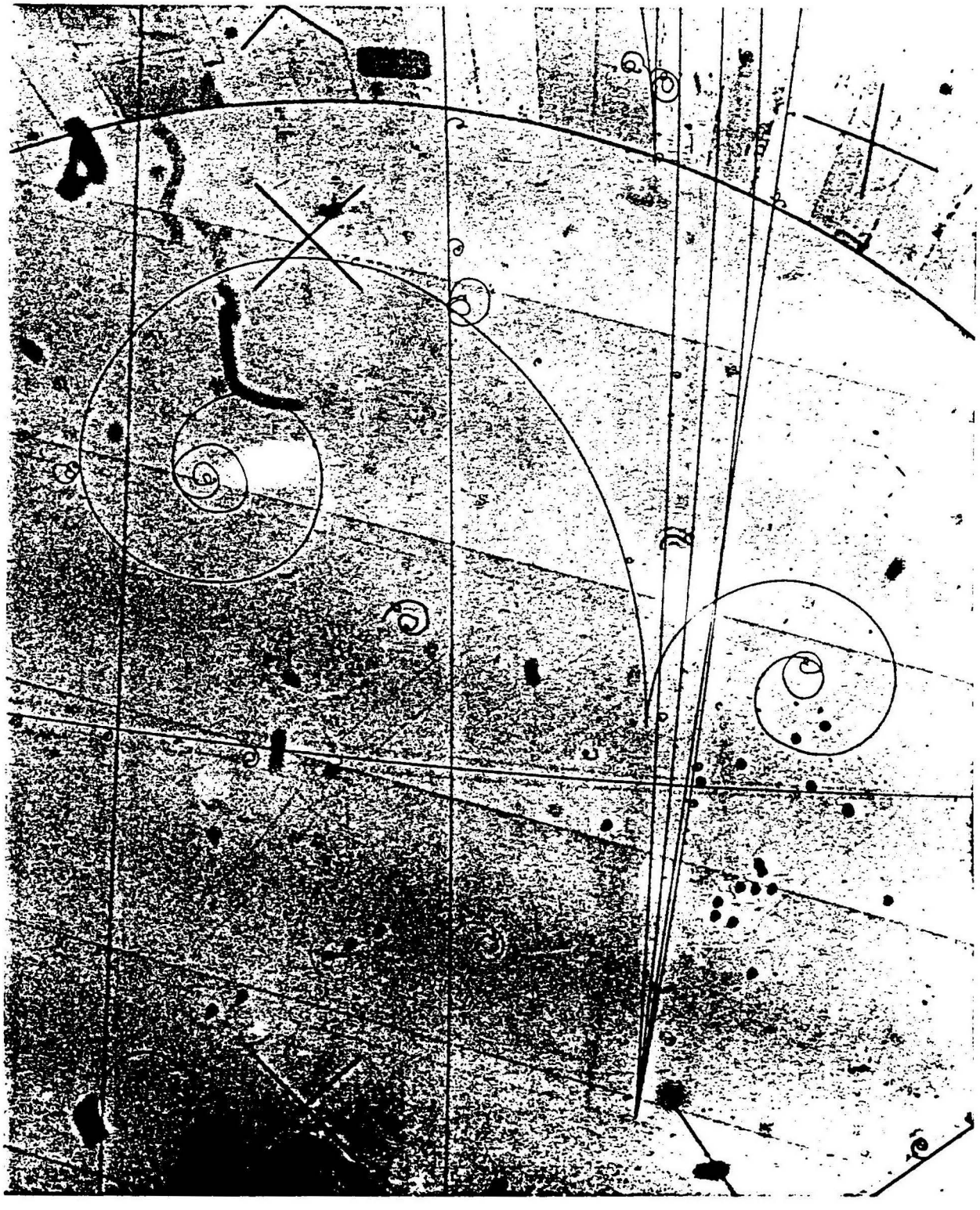

Figure 3.6: Photograph of a neutrino interaction in the 15-foot Bubble Chamber.

This experiment encountered several problems during both data taking periods which affected the quality of the bubble chamber pictures and, by the same token, the efficiency of the scanning. During the 1985 run, the flash delay for the conventional cameras was accidentally set to 1 ms rather than the desired 12 ms. This problem affected approximately 80% of the total 1985 exposure and resulted in smaller bubble sizes causing some events to have tracks with poor visibility. Likewise, during the 1987-88 run, water leaked into the bubble chamber liquid thereby turning into ice which deposited itself mostly on the lower upstream section of the bubble chamber walls. This problem affected about 30% of the total 1987-88 exposure (45% of the 1987-88 exposure used in the present work). As a consequence, tracks are obscured by a non-uniform background of white patches in some sections of the bubble chamber.

It was found that these problems systematically reduced the scanning efficiency, especially for events with low multiplicities which are difficult to find. In order to assess the extent of this or any other systematic loss, a special EMI-directed scan was done on a fraction of the film. This special scan was based on a computer program using the data recorded by the EMI/IPF system to tag frames with muon track candidates. For each muon track candidate, the program provided the scanner with the predicted location of the exit point of the track on the downstream wall of the bubble chamber. The tracks whose exit points were near the predicted locations were then followed backwards to check whether they originated from events. The efficiency for the directed scan to find charged current events varied from 65 to 85% for the different labs.

3.2.2 Measurement

The data used in this work come from the analysis of 330 000 frames corresponding to 5.5×10^{17} protons on target. All events with two prongs found in that sample were measured whereas 29% (78%) of the number of events with three (four)

prongs was measured. Events with three prongs were only measured on the 1987-88 film. (See Table 3.1 for a summary of the experimental conditions for the two data taking periods.)

In this study, the events are required to lie inside a restricted 10 m^3 fiducial volume in order to yield reliable track measurement and good particle detection and identification. Specifically, the distance between the primary vertex and the downstream bubble chamber wall along the beam direction is required to be greater than 1 m, while the other cuts remove events too close to the bubble chamber walls or events which are either too high or too deep in the chamber (i.e. $Z > 100$ cm or $Z < -75$ cm). This restricted volume also reduces the effect of poor track visibility affecting some portions of the film (see Sec. 3.2.1).

Prior to measurement, each event is scrutinized in an attempt to identify the various particles which are associated with it. This is done by looking for some of the following signatures :

- Low momentum electrons lose most of their energy via ionization and therefore follow a spiralling trajectory until they stop inside the bubble chamber. At momenta greater than 80 MeV/c, electrons tend to lose large amounts of energy via bremsstrahlung (when accelerated by the field of a neon nucleus) which often results in a characteristic sudden change of curvature.

- Muons leave the bubble chamber without interacting or losing much energy (they do not undergo severe bremsstrahlung due to their larger mass) and can be separated from other leaving particles by using the EMI/IPF system (see Sec. 3.2.3).

- Charged hadrons can be differentiated from charged leptons if they interact inside the bubble chamber. With an interaction length of 153 cm (192 cm) for the 1985 (1987-88) data and an average potential length of 210 cm, a majority of hadrons interacts inside the bubble chamber. However, there is

no discrimination between pions, kaons and protons over most of the energy range of this experiment.

- Protons with momentum below ~ 1 GeV/c lose considerable amounts of energy through ionization and thus are characterized by heavily ionizing tracks which stop inside the bubble chamber.

- Photons, most of which come from $\pi^0 \rightarrow \gamma\gamma$ decays, have a high probability ($\sim 90\%$) to convert into an electron-positron pair inside the bubble chamber (see Table 3.1 for the radiation lengths).

- Neutral strange particles K^0, Λ and $\overline{\Lambda}$ are identified through their decays :

$$K^0 \rightarrow \pi^+\pi^- \ , \quad \Lambda \rightarrow p\,\pi^- \quad \text{and} \quad \overline{\Lambda} \rightarrow \overline{p}\,\pi^+ \ . \tag{3.1}$$

  These decays give rise to 2-prong configurations called V^0. The probability for these decays to occur inside the bubble chamber is approximately 20% for K^0 and 40% for Λ and $\overline{\Lambda}$ [38].

The measurement itself involves digitizing the position of points on each track in a 2-dimensional projection. This is done in two steps for each view. First, a series of fiducial marks located on the bubble chamber walls is measured. Second, a sequence of points is measured along each track. The fiducial marks, whose positions in space are known, allow the parameters of the transformation between the bubble chamber and the film plane to be determined. The points measured on a film plane are then translated into light rays pointing back into the bubble chamber. In the case of a corresponding point like the origin or end point of a track, the reconstructed vertex location is the space point at which the light rays from the three stereoscopic projections intersect. The reconstruction of tracks is more complicated since there usually are no corresponding points. It proceeds by combining two views at a time (a double) and then by comparing the different sets of doubles. The trajectories are

first fitted to helices to extract the momentum from the track curvature according to the formula:

$$p(\mathrm{GeV/c})\cos\lambda \;=\; 0.003\; B(\mathrm{Tesla})\; R(\mathrm{cm}) \tag{3.2}$$

where B is the magnetic field inside the bubble chamber, R is the radius of curvature of the track and λ is the dip angle of the track with respect to the horizontal plane (see Fig. 3.4). The tracks are then fitted to spirals to take into account the energy loss by ionization for each possible mass hypothesis. In this way, the momentum and angles, and the corresponding error matrix are determined for each track.

All the tracks originating from the primary vertex of each event were measured as well as the tracks of all γ conversions and V^0 decays which appear to originate from the primary vertex. The γ which clearly appear to be due to bremsstrahlung from an upstream electron (or positron) were not measured. Furthermore, some laboratories only measured the five closest γ in events with six or more γ.

The reconstructed γ and V^0 were then processed through a kinematical fitting program based on the least-squares method. The γ were constrained to fit the reaction $\gamma\ (\mathcal{N}) \rightarrow e^+e^-\ (\mathcal{N})$ to all physical origins (the momentum transfer to the nucleus is taken into account in the uncertainty in the γ direction) with the equations of four-momentum conservation as constraints. The fit also constrained the γ, e^+ and e^- directions to be collinear. The total number of constraints is thus four since the γ momentum is not measured. Similarly, the V^0 were constrained to fit the decay hypotheses in Eq. (3.1) to all possible physical origins. For the V^0 fits, the number of constraints is three because there is no collinearity constraint. This number is reduced in case of large $\frac{\Delta p}{p}$ for the V^0 tracks. The fit probability was required to be greater than 10^{-4} for the fit to be retained.

Particular attention was paid to the identification of photons in the 2-, 3- and 4-prong event sample. Because of the high energies available to this experiment the secondary hadrons were often produced in a narrow forward cone. This made it

difficult to separate primary γ from bremsstrahlung γ at the scanning table. Therefore, a special checking program was used after measurement and reconstruction to tag γ which were likely to be due to bremsstrahlung from other (measured) γ. For every $\gamma\gamma$ pair, the vertical and horizontal invariant masses were constructed :

$$m_V = 2\,E_1\,E_2\,(1 - cos\Delta\lambda)\ ,$$

$$m_H = 2\,E_1\,E_2\,(1 - cos\Delta\phi)\ ,$$

where $\Delta\lambda$ is the opening angle between the two photons in the vertical plane and $\Delta\phi$ is the opening angle in the horizontal plane, E_1 and E_2 are the energies of the "parent" and "daughter" photons respectively. The daughter is considered to be a bremsstrahlung candidate if the following set of cuts is satisfied

$$m_V < 0.006 - 0.03\ m_H \quad \text{and} \quad m_H < 0.1\ \text{GeV}\ .$$

Other requirements are that the daughter be further away from the primary vertex than its parent and that $E_2/E_1 < -1.055\,E_2 + 2.105$ for $E_2 \leq 1$ GeV and $E_2 < 1.05\ E_1$ for $E_2 > 1$ GeV (no test on the energies is made in the case $E_2 < 0.1$ GeV). If after removing all the bremsstrahlung candidates there remained an even number of primary γ which could be arranged into $\gamma\gamma$ pairs with invariant masses within $3\,\sigma$ of the π^0 mass ($m_{\pi^0} = 0.135$ GeV), the program stopped. If not, the same procedure was repeated with a looser cut on the vertical mass :

$$m_V < 0.012 - 0.06\ m_H \qquad \text{and} \qquad m_H < 0.1\ \text{GeV}\ .$$

The photons tagged as bremsstrahlung candidates were then examined at the scanning table to check whether they were indeed due to bremsstrahlung from any one of the selected parents.

3.2.3 Muon Identification

The study of ν_μ and $\overline{\nu}_\mu$ charged current interactions relies on the ability to identify muons. The identification is done by combining the bubble chamber measurements with the corresponding EMI/IPF data. First, every track leaving the bubble chamber without interacting is extrapolated through the absorber towards the EMI planes, taking into account the shape of the magnetic field outside the bubble chamber as well as the energy loss by ionization. Second, the EMI/IPF data are analyzed, one time slot at a time, to search for hits in tubes close to the extrapolated position in each layer. The quality of the association between predictions and hits is determined by the value of the chi-square defined as $\chi^2 = d^2/\sigma^2$, where d is the distance between the predicted location and the location of the closest edge of the tube hit; σ is the uncertainty in the predicted location due to the measurement errors in the bubble chamber and the effect of multiple scattering in the absorber. If the tube predicted to be hit registered a hit, the value of χ^2 is set to 0. For each plane and each time slot, there is a match if the best association for any one of the two layers has $\chi^2 = 0$ or a χ^2-probability greater than 5%.

A leaving track is identified as a muon if, within the same time slot, there is a good match in both EMIC planes and at least two of the three EMIB planes. The required number of matches in EMIC is reduced to one in case of EMI readout buffer overflow. This occurred occasionally during the 1985 run and resulted in a loss of data from EMIC. Frames with no EMI/IPF data, representing $\sim$ 1% of the total exposure, are not included in the present analysis.

A kinematical method is also utilized to select muons independently of the above method. It was used primarily as a means to cross-check the EMI muon identification. The quantity F (shown below) is calculated for each muon candidate provided that the event contains no track with $\frac{\Delta p}{p} > 70\%$:

$$F = \frac{p_\mu^L \; p_\mu^T \; p_\mu^{TS}}{[\sum (p_i^{TS})^2]^{1/2}}$$

Table 3.2: Geometric acceptance for Monte Carlo antineutrino and neutrino charged current events. Note that the layout of the EMI planes is not symmetric with respect to the beam axis which contributes to differences between μ^+ and μ^- acceptances.

Momentum (GeV/c)	5 – 10	10 – 20	20 – 50	> 50
μ^+	$(59.9 \pm 3.8)\%$	$(92.3 \pm 1.2)\%$	$(99.6 \pm 0.1)\%$	$\sim 100\%$
μ^-	$(73.7 \pm 2.3)\%$	$(94.5 \pm 0.9)\%$	$(99.4 \pm 0.2)\%$	$\sim 100\%$

where p_μ^L and p_μ^T are the longitudinal and transverse momenta of the muon candidate with respect to the neutrino direction, while p_μ^{TS} and p_i^{TS} are the transverse momenta of the muon candidate and ith hadron with respect to the direction of motion of the hadronic system. The muon is taken to be the leaving track with the largest value of F given that $F > 40$. This method takes advantage of two characteristics of neutrino charged current interactions : the separation between the muon and the W boson in the plane perpendicular to the neutrino direction, and the restricted transverse momentum of the hadrons with respect to the direction of motion of the hadronic system.

The geometric acceptance of the EMI is determined by extrapolating the muons generated in a Monte Carlo simulation (see Sec. 4.2) of (anti)neutrino charged current interactions, which incorporates the specific experimental conditions of this experiment. The acceptance shown in Table 3.2 represents the fraction of muons traversing both EMIB and EMIC planes. It is observed that, below 20 GeV/c, the acceptance decreases sharply with decreasing momentum whereas the acceptance for muons with momentum greater than 20 GeV/c is almost constant and nearly $\sim 100\%$. The overall geometrical acceptance for the last three columns of Table 3.2 (i.e. $p > 10$ GeV/c) is found to be better than 99%.

The combined electronic and processing efficiency for the EMI muon identification is determined either by using high momentum ($p > 20$ GeV/c) beam tracks

traversing the bubble chamber (these tracks are muons produced by neutrino interactions upstream of the bubble chamber) or by using kinematically selected muons with a large value of F ($F > 400$) and $p > 10$ GeV/c. Assuming that those two samples constitute pure samples of muons, the efficiencies are found to be $(93.5 \pm 0.8)\%$ for beam tracks and $(93.5 \pm 0.5)\%$ for kinematical muons from the low multiplicity event sample.

Several background sources can produce fake muons resulting in a contamination of the charged current event sample by neutral current events. The possible sources are the following :

- Decays of pions and kaons in flight occurring inside or outside the bubble chamber.
- Punch-through background caused by hadrons interacting inside the absorber thereby producing hits in EMIB and EMIC that are associated with the corresponding hadron tracks in the bubble chamber.
- Accidental association of hits in the different EMI planes with leaving tracks in the bubble chamber.

The importance of the first two sources can be assessed by computing the rate for events with two muons of the same charge with respect to the total number of charged current events. We assume that this rate represents half of the background because the background is also expected to give rise to events with two muons of opposite charge, but these can also originate from the production and semileptonic decay of charmed hadrons. The contamination is then estimated to be $(0.9 \pm 0.3)\%$ for $p_\mu > 5$ GeV/c and $(0.6 \pm 0.2)\%$ for $p_\mu > 10$ GeV/c, using a sample of inclusive charged current events. For low multiplicity events, the corresponding numbers are $(0.3 \pm 0.1)\%$ and $(0.2 \pm 0.1)\%$ respectively.

The accidental association background is evaluated by combining the bubble chamber measurements in one frame with the EMI/IPF data from another frame.

The background is then determined by the fraction of the total number of events with at least one muon candidate (i.e. a leaving track with $p > 5$ or 10 GeV/c) which is assigned to the charged current event category. It is found to be $(0.7 \pm 0.3)\%$ and $(0.4 \pm 0.3)\%$ for an inclusive sample of events with at least one leaving track with $p > 5$ GeV/c and $p > 10$ GeV/c respectively. For low multiplicity events, the corresponding fractions are $(0.7 \pm 0.3)\%$ and $(0.2 \pm 0.2)\%$ respectively. This background is higher at low momentum because of the increased uncertainty in the extrapolation due to multiple scattering.

As a consequence of the above efficiency and background studies, the muon momentum is required to be greater than 10 GeV/c in the remainder of this analysis.

Chapter 4
Methods of Analysis

In this chapter, we discuss some of the general aspects of the data analysis. In particular, the method followed to extract the coherent signal is outlined in Section 4.1, along with a description of the criteria used in the selection of the sample. In Section 4.2, we present the main features of the Monte Carlo program used to simulate neutrino coherent interactions in the 15-foot Bubble Chamber.

4.1 Extraction of the Coherent Signal

4.1.1 Selection of the Sample

The events used in this analysis are required to lie inside the fiducial volume, to have an identified muon with momentum greater than 10 GeV/c, and not to be associated with other interactions upstream in the bubble chamber. There is no selection on the charge of the muon : both neutrino and antineutrino interactions are studied. With these cuts, the low multiplicity event sample (2-, 3- and 4-prong events) contains 3265 ($\nu_\mu + \overline{\nu}_\mu$) charged current events. If there is more than one muon in a given event, the muon associated with the incoming (anti)neutrino is chosen to be the one with the greater value of the product $p_\mu \cdot p_\mu^T$, where p_μ is the magnitude of the muon momentum and p_μ^T is the magnitude of the transverse momentum of the muon with respect to the neutrino beam direction. Furthermore, in order to determine Q_{ch}, the total electric charge of the event, it is required that none of the primary tracks have $\frac{\Delta p}{p} > 60\%$. This additional cut reduces the above

number of events to 2685, i.e. 2136 ν_μ and 549 $\overline{\nu}_\mu$ charged current interactions.

4.1.2 Semi-inclusive Coherent Signal

The procedure [39] followed to extract the coherent signal uses the characteristic dependence of the cross section on the variable t :

$$\frac{d\sigma}{dt} \propto e^{-b|t|}, \tag{4.1}$$

where t is the square of the four-momentum transfer to the nucleus and b is the slope parameter introduced in Sec. 2.4.2. The above parametrization is a good approximation to the more accurate form introduced in Sec. 2.4.4

$$\frac{d\sigma}{d\Delta_T^2} \propto e^{-B_L\Delta_L^2} \cdot e^{-B_T\Delta_T^2}, \tag{4.2}$$

since, in the case of the neon nucleus, the slope parameters $b \simeq B_L \simeq B_T$ and $|t| = \Delta_L^2 + \Delta_T^2$. Thus we have

$$e^{-B_L\Delta_L^2} \cdot e^{-B_T\Delta_T^2} \simeq e^{-b\,(\Delta_L^2+\Delta_T^2)} = e^{-b|t|}.$$

The value of t cannot be measured directly because the momentum transferred to the nucleus is very small and the nucleus remains undetected. However, t can be computed to a good approximation by using the four-momenta of the observed final state particles. It is shown in Appendix B that $|t|$ can be approximated by :

$$|t| \simeq \left[\sum_i (E_i - p_{iL})\right]^2 + \left[\sum_i \vec{p}_{iT}\right]^2, \tag{4.3}$$

where E_i is the energy and p_{iL} ($\vec{p}_{iT}$) is the longitudinal (transverse) momentum of particle i, relative to the neutrino direction; the sum extends over all observed particles except stubs. Stubs are not used to compute Q_{ch}, $|t|$ or any other kinematical variable.

The $|t|$-distributions are examined for three classes of events :

1. 2-prong events with $Q_{ch} = 0$ consistent with the final state $\mu^{\pm}\pi^{\mp}X^0$ (see Fig. 4.1);

2. 3-prong events with $Q_{ch} = +1$ consistent with the final state $\mu^{\pm}\pi^{\mp}\pi^{+}X^0$ (see Fig. 4.2);

3. 4-prong events with $Q_{ch} = 0$ consistent with the final state $\mu^{\pm}\pi^{\mp}\pi^{\pm}\pi^{\mp}X^0$ (see Fig. 4.3).

X^0 stands for a system of n_0 neutral particles, where n_0 is any positive integer or 0. The above events may also contain any number of stubs. It should be noted that, in the remainder of this work, any charged hadron which is not identified as a stopping proton is considered to be a pion.

In order to extract the coherent signal, each class of events is divided into events with or without stubs. The events with stubs are necessarily non-coherent since they contain nuclear fragments (stubs) indicating that the nucleus was disrupted, while the events without stubs are a mixture of coherent and non-coherent events. Therefore, the events with stubs can be used to estimate the fraction of non-coherent events among the events without stubs.

It is observed that the distribution for 2-prong events without stubs (solid line in Fig. 4.1) has a large peak at small values of $|t|$ ($|t| < 0.1$ GeV^2) whereas the distribution for events with stubs (dashed or dotted line) does not. The distribution for events with stubs is normalized to that for events without stubs at $|t| > 0.2$ GeV^2, a region where coherent events are not expected to contribute significantly. In this analysis, all stopping protons with momentum smaller than 800 MeV/c are considered to be stubs. It can be seen from Fig. 4.1 that the excess of events without stubs at $|t| < 0.1$ GeV^2 is not affected by reducing the maximum stub momentum from 800 to 350 MeV/c. This excess of events without stubs at low $|t|$ is interpreted as due to coherent (anti)neutrino interactions. For $|t| < 0.1$ GeV^2, there are 136

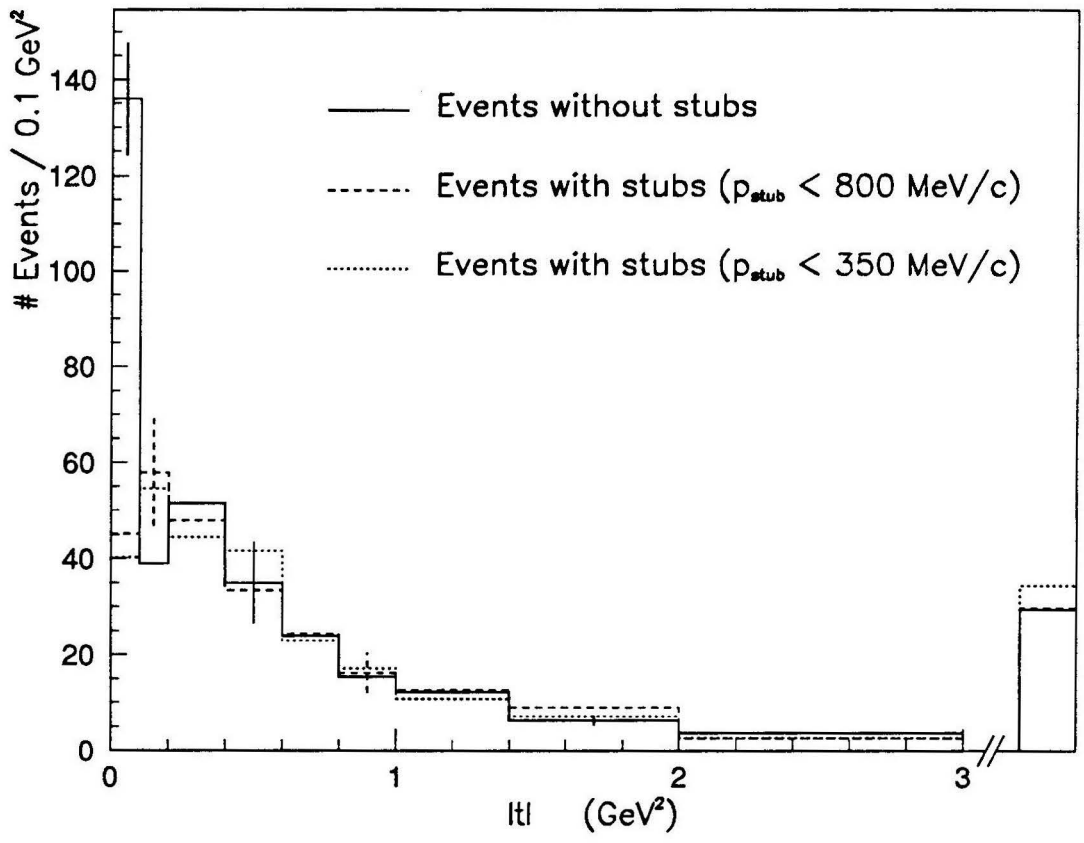

Figure 4.1: $|t|$-distributions for $\mu^{\pm}\pi^{\mp}X^0$ events, normalized at $|t| > 0.2$ GeV^2.

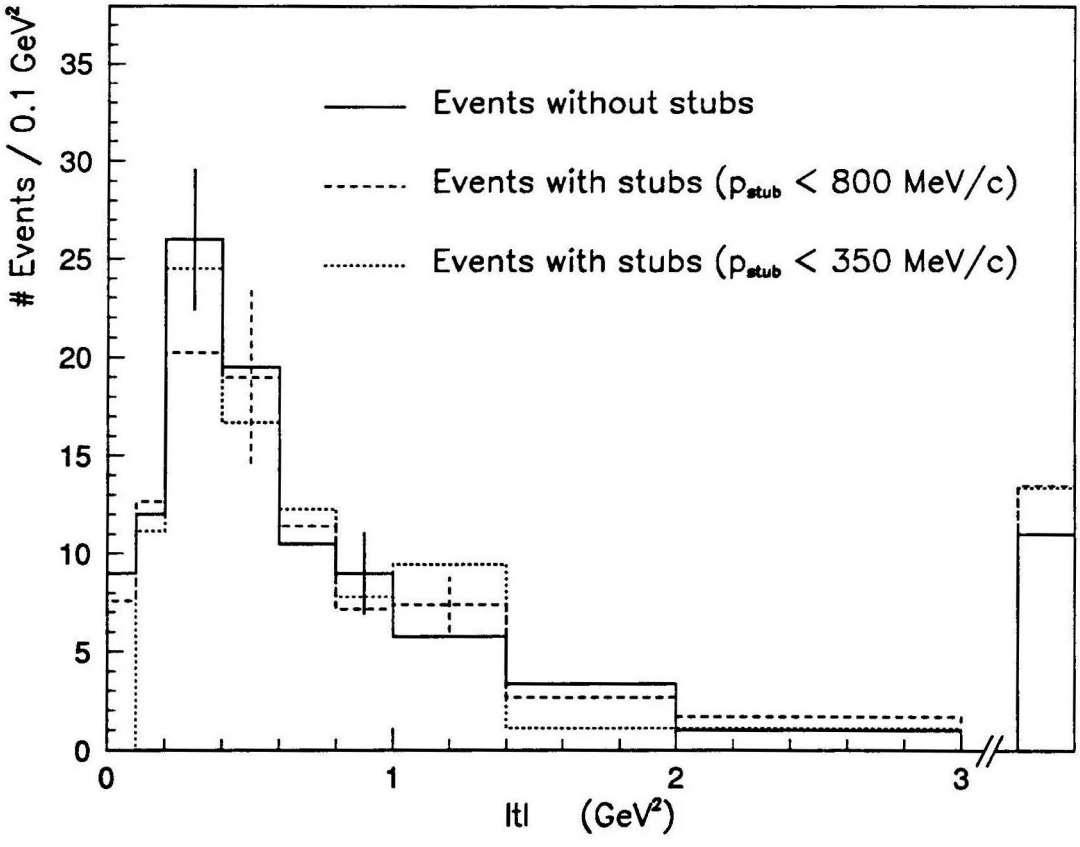

Figure 4.2: $|t|$-distributions for $\mu^{\pm}\pi^{\mp}\pi^{+}X^0$ events, normalized at $|t| > 0.2$ GeV^2.

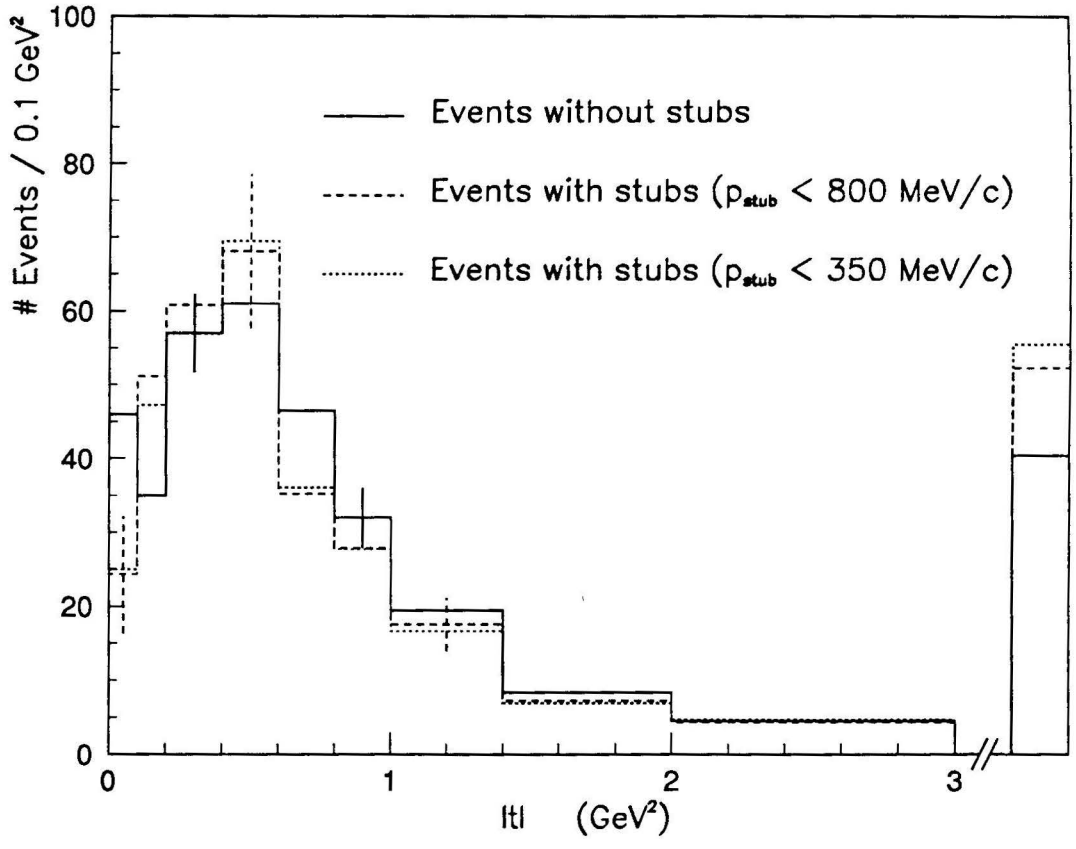

Figure 4.3: $|t|$-distributions for $\mu^{\pm}\pi^{\mp}\pi^{\pm}\pi^{\mp}X^0$ events, normalized at $|t| > 0.2$ GeV^2.

events without stubs and 25 events with stubs ($p_{\text{stub}} < 800$ MeV/c). The excess is thus estimated to be 90.8 ± 15.2 events after subtraction of the non-coherent background (25 events multiplied by a normalization factor of 1.81 ± 0.15). In the case of events with four prongs, the $|t|$-distribution for events without stubs (Fig. 4.3) does not show evidence for a strong peak at small $|t|$.

The extracted signal for $\mu^{\pm}\,\pi^{\mp}\,X^0$ events as a function of the value of the cut on $|t|$ is shown in Fig. 4.4. It is observed that the signal reaches its maximum for a cut of $|t| < 0.1$ GeV^2 and remains approximately constant for higher values of the cut. Note that the signal seems to be slightly lower for $|t| < 0.2$ GeV^2. This is due to the fact that the $|t|$ distribution for events with stubs peaks in the interval between 0.1 and 0.2 GeV^2, while the distribution for events without stubs appears to have a dip in that same interval. The reason for this is not understood. Nevertheless, the signal extracted at $|t| < 0.2$ GeV^2 is not incompatible with that extracted at

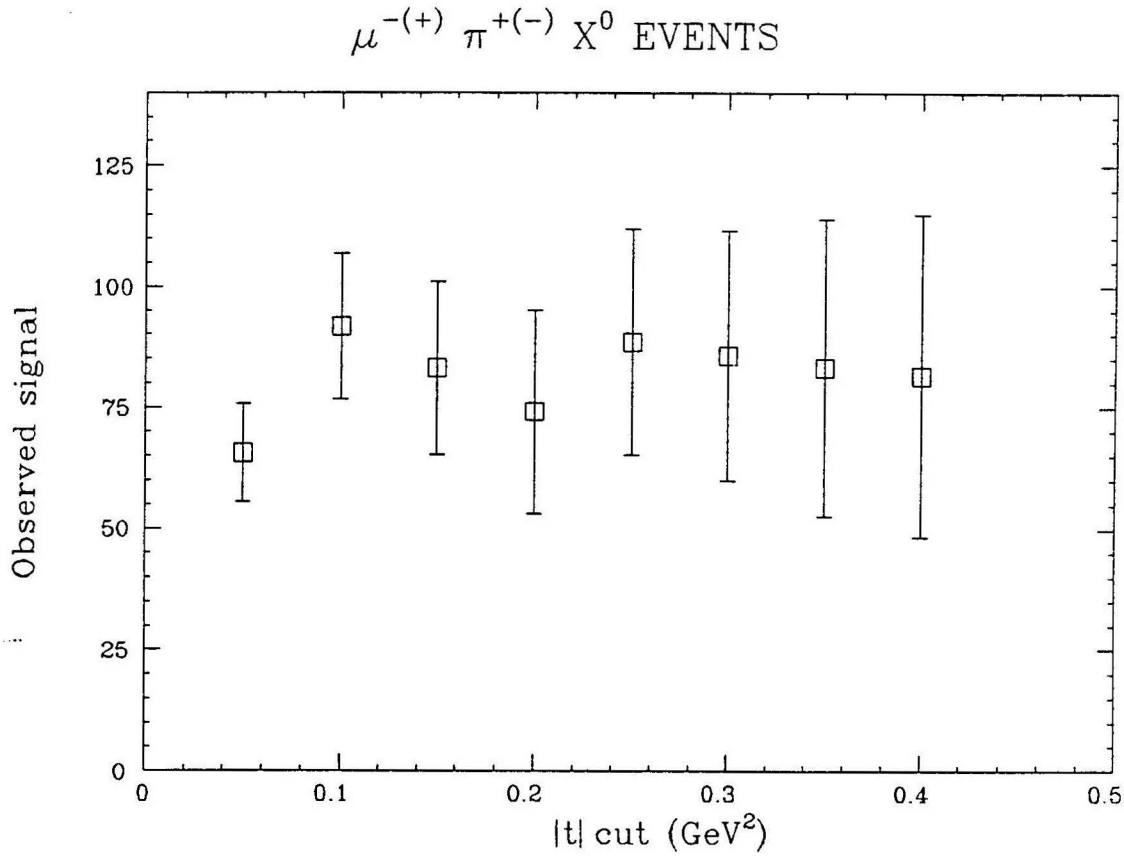

Figure 4.4: Signal for $\mu^{\pm}\,\pi^{\mp}\,X^0$ events as a function of the value of $|t|$ cut chosen. The $|t|$ distributions have been normalized at $|t| > 0.4$ GeV^2.

$|t| < 0.1$ GeV^2.

The validity of the method can be checked by examining the $|t|$-distribution for 3-prong events (Fig. 4.2). In this case, no coherent signal is expected because the total charge Q_{ch} is different from zero. Indeed, the distribution for events without stubs does not display a peak at small values of $|t|$. Moreover, the distributions for events with or without stubs are similar, which supports the use of the events with stubs to estimate the non-coherent background among the events without stubs.

The kinematical characteristics of the 2-prong events are presented in Table 4.1 for events with $|t| < 0.1$ GeV^2 and $|t| > 0.2$ GeV^2. No energy correction is applied to those events. (Definitions of all the kinematical variables can be found in Appendix C.) It is observed that, for $|t| < 0.1$ GeV^2, the events without stubs are characterized

Table 4.1: Averages of (visible) kinematical variables for 2-prong events.

	Evts w/o stubs $\|t\| < 0.1$ GeV^2	Evts with stubs $\|t\| < 0.1$ GeV^2	Evts w/o stubs $\|t\| > 0.2$ GeV^2	Evts with stubs $\|t\| > 0.2$ GeV^2
# Events	136	25	434	240
$< E >$ (GeV)	91.2 ± 5.3	83.8 ± 11.4	101.1 ± 4.1	102.3 ± 4.7
$< \nu >$ (GeV)	16.7 ± 1.6	9.7 ± 2.1	15.6 ± 1.2	13.0 ± 1.2
$< Q^2 >$ (GeV^2)	1.44 ± 0.15	1.68 ± 0.48	9.26 ± 0.68	7.14 ± 0.61
$< W^2 >$ (GeV^2)	30.5 ± 2.8	17.4 ± 3.4	24.4 ± 2.1	19.0 ± 2.0
$< x >$	0.082 ± 0.008	0.126 ± 0.025	0.585 ± 0.032	0.491 ± 0.034
$< y >$	0.210 ± 0.016	0.147 ± 0.029	0.178 ± 0.009	0.144 ± 0.011
$< \|t\| >$ (GeV^2)	0.046 ± 0.002	0.065 ± 0.005	1.99 ± 0.19	1.65 ± 0.16

by smaller values of Q^2 and x and greater values of ν, W^2 and y than those for events with stubs, which is consistent with the expectations for coherent interactions.

In this experiment, protons with momenta below $\sim$ 130 MeV/c cannot be detected as their range in the bubble chamber liquid is less than $\sim$ 0.2 cm. Therefore, it is necessary to check whether the loss of low momentum protons leads to an experimental bias in the $|t|$-distribution for the events with stubs, especially for $|t| < 0.1$ GeV^2. This is done by comparing the average proton momentum obtained at different values of $|t|$ (Fig. 4.5). It is observed that there is no correlation between the momentum of the observed protons and the value of $|t|$ calculated for the event to which they belong. Thus, the t-distribution is not biased by the loss of low momentum protons.

4.1.3 Neutrino Beam Direction

The extraction of the signal from the $|t|$-distribution is sensitive to the knowledge of the neutrino beam direction. Use of an inaccurate value results in a broadening

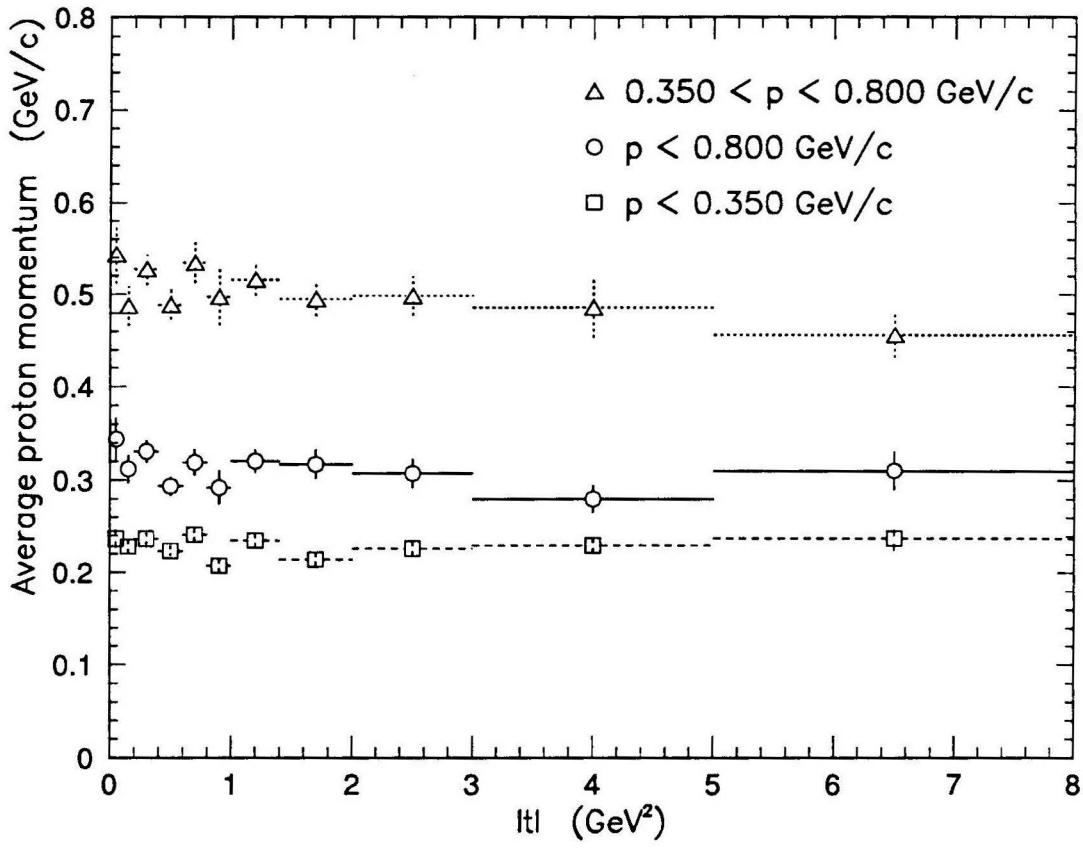

Figure 4.5: Average proton momentum as a function of $|t|$ for low-multiplicity events in given intervals of proton momentum.

of the coherent peak in the $|t|$-distribution and leads to a decrease of the extracted signal.

To determine the beam direction, a sample of events containing kinematically selected muons was utilized. The kinematical method was used instead of the EMI selection because of the asymmetry of the EMI with respect to the beam axis. The beam direction was then determined by computing the median of the dip (λ) and azimuthal (ϕ) angle distributions of the kinematical muons (see Fig. 3.4 for a definition of the angles). The results obtained for the low-multiplicity event sample are

$$\lambda_\nu = 0.3 \text{ mrad}, \quad \phi_\nu = -41.7 \text{ mrad}, \quad 1985 \text{ run},$$

$$\text{and} \quad \lambda_\nu = 1.3 \text{ mrad}, \quad \phi_\nu = -43.4 \text{ mrad}, \quad 1987 - 88 \text{ run}.$$

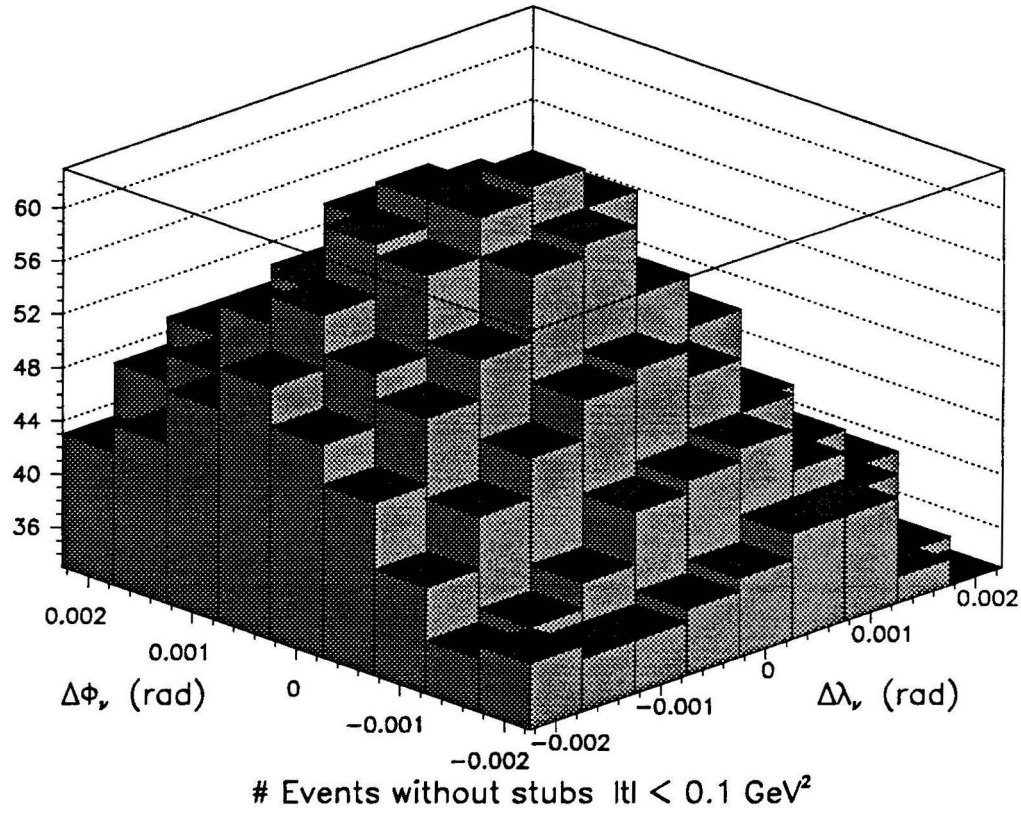

Figure 4.6: Number of $\mu^{\pm}\pi^{\mp}$ events without stubs at $|t| < 0.1$ GeV^2 for various beam directions. $\Delta\lambda_\nu$ and $\Delta\phi_\nu$ represent the deviations from the measured beam direction.

Similar values were obtained from the angular distributions of the total three-momentum of the events. Moreover, the above numbers do not change significantly if the inclusive charged current event sample is used instead of the low multiplicity event sample. By comparing the values obtained using the two different samples and using either the muon or the total three-momentum angular distributions, the uncertainty in the beam direction is assessed to be ~ 0.5 mrad.

As an independent check of the beam direction, the number of $\mu^{\mp}\pi^{\pm}$ events without stubs at $|t| < 0.1$ GeV^2 was plotted for a series of different directions (Fig. 4.6). The variations from the measured direction were performed in steps of 0.5 mrad. It is observed that the number of events is maximum for the beam direction determined by the muon direction as expected since the contribution from coherent interactions is concentrated at low-$|t|$ values and should be maximized if

the beam direction is known accurately.

4.2 Monte Carlo Simulation

The Monte Carlo program utilized to simulate coherent interactions was first developed by P. Marage (Brussels) for studies of the data collected using the Big European Bubble Chamber (BEBC) at CERN. Further work involved the implementation of the conditions specific to the present experiment : characteristics of the Fermilab 15-foot Bubble Chamber and the differences due to the liquid composition, as well as fluxes for the Quadrupole Triplet Train.

The events are generated in two phases. During the first phase, the differential cross section for a given process is integrated using a multi-dimensional partitioning program (DIVONNE4 [40]) which creates partitions inside of which the cross section remains approximately constant. (The precise expressions used for the single pion and single ρ cross sections are given later in this section.) For the processes under consideration, a 3-dimensional space is used, consisting of the variables E, x and y, with ranges of 0 to 600 GeV, 0 to 1, and 0 to 1 respectively. It should be pointed out that the (anti)neutrino flux is taken into account during the integration phase.

In the second phase, the resulting partition is used to generate random values of these three variables in accordance with the differential cross section and the (anti)neutrino flux.

Once the values of E, x and y are generated, the vertex of the event is generated randomly along the beam direction but with radius following the radial dependence of the flux at energy E. Then the value of $|t|$ is chosen according to Eq. (4.1) for the Rein-Sehgal parametrization or according to Eq. (4.2) for the Belkov-Kopeliovich parametrization (the values of the slopes are specified below). At this point, the kinematical variables describing the event are constrained to pass kinematical cuts

which depend on the final state particle to be produced (e.g.: π, ρ, a_1, ...). In particular, the value of $|t|$ is required to be greater than t_{min}, the minimum momentum transfer to produce a given meson.

Using the values of E, x, y and $|t|$, it is possible to generate the four-momenta of the muon and the coherently produced meson. Several isotropic rotations are then carried out : the meson momentum is rotated around the W boson direction, and the plane containing the neutrino and the muon (and the W boson) is rotated around the beam direction.

In the case of ρ or a_1 production, the following decays are also simulated

$$
\begin{aligned}
a_1^{\pm} &\rightarrow \rho^{\pm}\pi^0 , \\
a_1^{\pm} &\rightarrow \rho^0\pi^{\pm} , \\
\rho^{\pm} &\rightarrow \pi^{\pm}\pi^0 , \\
\rho^0 &\rightarrow \pi^+\pi^- , \\
\pi^0 &\rightarrow \gamma\gamma ,
\end{aligned}
$$

and the four-momenta of the decay products are determined. The angular decay characteristics of the ρ meson follow that of Ref. [41].

In the last step, the simulation attempts to reproduce the specific smearing effects due to the experimental conditions, i.e. the limitations of the apparatus and the measurement procedure.

In the following two sections, the differential cross sections for the single pion and single ρ coherent production are given, and the last section outlines the smearing procedure.

4.2.1 Coherent Single Pion Production

Both Rein-Sehgal [9] and Belkov-Kopeliovich [10] models have been used. In the Rein-Sehgal model (see Sec. 2.4.2), the cross section for coherent single pion

production by charged current interactions on neon nuclei is given by (see Eq. (2.33))

$$\frac{d^3\sigma_{RS}(\nu_\mu + Ne \to \mu + \pi + Ne)}{dQ^2\, d\nu\, dt} = \frac{G_F^2}{4\pi^2}\,\frac{|\vec{q}|}{E^2}\, f_\pi^2\,\frac{\epsilon}{1-\epsilon}$$
$$\times \frac{A^2}{16\pi}\,\left(\sigma_{tot}^{\pi N}\right)^2\,(1+r^2)\,e^{-b|t|}\,F_{abs}$$
$$\times \left[\left(\frac{m_a^2}{Q^2+m_a^2}\right)^2 - \frac{\nu}{E'}\,\frac{m_a^2}{Q^2+m_a^2}\,\frac{m_\mu^2}{Q^2+m_\pi^2} + \frac{\nu^2}{4\,E\,E'}\,\frac{m_\mu^2\,(Q^2+m_\mu^2)}{(Q^2+m_\pi^2)^2}\right],$$

where $A = 20$ for neon, $r = -0.2$ [42] and the total pion-nucleon cross section $\sigma_{tot}^{\pi N}$ is extracted from pion cross section data tables [43]. The polarization parameter is given by

$$\epsilon = \left(1 + \frac{2\,|\vec{q}|^2}{4EE' - Q^2}\right)^{-1}.$$

The dependence of the cross section on the pion momentum, evaluated in the lab frame, is taken into account with the pion momentum given by $\sqrt{\nu^2 - m_\pi^2}$. The axial mass m_a is taken to be the a_1 meson mass $m_a = 1.260$ GeV [12] and the slope parameter $b = 79.1$ GeV^{-2} according to Eq. (2.31). This particular value of the slope parameter agrees with the parametrization extracted from ρ^0 photoproduction data [47] : $b = b_0\,A^{2/3}$ with $b_0 = 10.5 \pm 1$ GeV^{-2}, which yields a slope $b = 77.4 \pm 7.4$ GeV^{-2} for neon.

As discussed in Sec. 2.4.2, the parametrization of the absorption factor (2.32) is incorrect. Thus, it is here replaced by an effective absorption factor determined from ρ^0 photoproduction data by computing the following ratio :

$$F_{abs} = \left(\left.\frac{d\sigma_{\mathcal{N}}}{dt}\right|_{|t|=0}\right) \Big/ \left(A^2\,|f_0|^2\right),$$

where $|f_0|^2$ is the cross section on a single nucleon in the forward direction and $\left.\frac{d\sigma_{\mathcal{N}}}{dt}\right|_{|t|=0}$ is the forward cross section for scattering on a nucleus $\mathcal{N}$ with atomic mass number A. Interpolation of the data obtained by Alvensleben et al. [48] for carbon ($A = 12$) and aluminum ($A = 27$) targets gives $F_{abs} = 0.476 \pm 0.064$ for neon ($A = 20$), whereas the data obtained by McClellan et al. [49] for carbon and magnesium ($A = 24$) targets gives $F_{abs} = 0.490 \pm 0.033$ for neon. In both

experiments the incident photon energies were $\sim$ 6 GeV. The average of those two quantities gives for the neon nucleus : $F_{\rm abs} = 0.48 \pm 0.04$, which is the value that we will use to compare the Monte Carlo simulation with the data in chapters 5 and 6.

In the Belkov-Kopeliovich model (see Sec. 2.4.4), the cross section is described by (see Eq. (2.52))

$$\begin{aligned}\frac{d^3\sigma_{BK}(\nu_\mu + Ne \to \mu + \pi + Ne)}{dQ^2\, d\nu\, d\Delta_T^2} &= \frac{G_F^2}{4\pi^2}\,\frac{|\vec{q}|}{E^2}\, f_\pi^2\, \frac{\epsilon}{1-\epsilon} \\ &\times \frac{\left(\sigma_{\rm tot}^{\pi Ne}\right)^2}{16\pi}\,(1+r^2)\, e^{-B_T\,\Delta_T^2}\, e^{-B_L\,\Delta_L^2} \\ &\times \left[\left(\frac{m_a^2}{Q^2+m_a^2}\right)^2 - \frac{\nu}{E'}\,\frac{m_a^2}{Q^2+m_a^2}\,\frac{m_\mu^2}{Q^2+m_\pi^2} + \frac{\nu^2}{4\,E\,E'}\,\frac{m_\mu^2\,(Q^2+m_\mu^2)}{(Q^2+m_\pi^2)^2}\right] ,\end{aligned}$$

where the pole form of the nucleon form factor (2.48) is used. In order to compute the pion-nucleus cross section and the slope parameters B_L and B_T, the following density functions are used :

1. The Woods-Saxon form, also known as 2-parameter Fermi model (2pF),

$$\begin{aligned}\rho_{\mathcal{N}}(r) &= \frac{\rho_0}{1+e^{(r-R_{\mathcal{N}})/a}} , \\ \rho_0 &= \frac{3A}{4\pi R_{\mathcal{N}}^3}\,\frac{1}{1+\pi^2 a^2/R_{\mathcal{N}}^2} .\end{aligned}$$

   The values of the parameters $R_{\mathcal{N}}$ and a have been determined by electron scattering experiments. For neon, these are $R_{\mathcal{N}} = 2.80$ fm and $a = 0.571$ fm [30]. The parameter $R_{\mathcal{N}}$ corresponds to the radius at which the density is exactly half of its maximum value and the parameter a measures the nuclear surface "thickness".

2. The 3-parameter Fermi model (3pF)

$$\rho_{\mathcal{N}}(r) = \frac{\rho_0\,(1+wr^2/R_{\mathcal{N}}^2)}{1+e^{(r-R_{\mathcal{N}})/a}} ,$$

   with $\rho_0 = 0.180$ fm^{-3} to ensure proper normalization, and $R_{\mathcal{N}} = 2.79$ fm, $a = 0.698$ fm and $w = -0.168$ [30].

Table 4.2: Belkov-Kopeliovich model parameters for coherent pion-neon scattering as a function of total pion-nucleon cross section, for various nuclear density functions.

$\sigma_{tot}^{\pi N}$ (mb)	$\sigma_{tot}^{\pi Ne}$ (mb)	B_L (GeV^{-2})	B_T (GeV^{-2})	Model
24	372.1	75.8	88.2	2pF
	370.2	70.6	83.0	3pF
	367.4	68.9	80.8	shell
32	459.6	74.8	91.2	2pF
	456.6	69.3	85.6	3pF
40	534.3	73.8	94.1	2pF
	530.2	68.2	88.4	3pF
50	613.3	72.8	97.7	2pF
	607.9	66.8	91.5	3pF
	598.4	64.8	88.9	shell
100	866.7	70.3	113.1	2pF
	855.1	62.4	104.5	3pF

3. The shell model (harmonic oscillator)

$$\rho_{\mathcal{N}}(r) = \rho_0 \, (1 + \delta \, r^2/R_{\mathcal{N}}^2) \, e^{-r^2/R_{\mathcal{N}}^2} \, ,$$

with $R_{\mathcal{N}} = 1.92$ fm, $\delta = 2.667$ and $\rho_0 = 0.101$ [28].

Note that all density functions satisfy the condition $\int d^3r \; \rho_{\mathcal{N}}(r) = A$. The shell model parametrization is only valid for light nuclei but is used to check the sensitivity to the choice of nuclear density function.

The computations were carried out using Eqs. (2.46), (2.47), (2.50) and (2.51) as well as the above density functions for different values of the total pion-nucleon cross section. The results are given in Table 4.2. The values of $\sigma_{tot}^{\pi Ne}$, B_L and B_T calculated with $\sigma_{tot}^{\pi N} = 24$ mb are close to those obtained by Belkov and Kopeliovich (see Sec. 2.4.4). It is observed that the total pion-nucleus cross section is rather

insensitive to the choice of nuclear density function and the slope parameter B_T only depends slightly on this choice. The slope parameter B_L decreases as $\sigma_{tot}^{\pi N}$ increases. This decrease is due to a corresponding increase of the nuclear absorption which only allows the hadrons produced close to the backward edge of the nucleus to escape.

In the Monte Carlo simulation, we use the parameters obtained with the Woods-Saxon (2pF) density function and the momentum dependence of the differential cross section is taken into account via the dependence of $\sigma_{tot}^{\pi Ne}$, B_L and B_T on the single nucleon cross section $\sigma_{tot}^{\pi N}$, as determined in Table 4.2.

It should be mentioned that, in this experiment, there is a significant contribution at low hadronic energies where resonance production dominates the total pion cross section and where the Glauber theory may not be expected to provide an accurate description. Furthermore, we have not taken into account the inelastic screening corrections to the total cross section $\sigma_{tot}^{\pi Ne}$. These corrections tend to decrease the total cross section but can be neglected for energy transfers $\nu \lesssim 10$ GeV [10]. For higher values of ν (a significant fraction of the data in this experiment is above 10 GeV), those corrections increase with increasing ν but do not exceed 5 to 10% (for experimental results, see Refs. [45, 46]).

4.2.2 Coherent Single ρ Production

The cross section for coherent single ρ production by charged current interactions on neon nuclei is given by (see Eq. (2.23) in Sec. 2.3.2)

$$\frac{d^3\sigma_{BK}(\nu_\mu + Ne \to \mu + \rho + Ne)}{dQ^2\, d\nu\, d\Delta_T^2} = \frac{G_F^2}{4\pi^2}\,\frac{|\vec{q}|}{E^2}\,\frac{f_{\rho^\pm}^2}{1-\epsilon}\,\frac{Q^2}{(Q^2+m_\rho^2)^2} \times (1+\epsilon R)\,\frac{d\sigma_T(\rho + Ne \to \rho + Ne)}{d\Delta_T^2},$$

with the ratio between longitudinal and transverse ρ-nucleus cross sections

$$R = \frac{\sigma_L(\rho + Ne \to \rho + Ne)}{\sigma_T(\rho + Ne \to \rho + Ne)}.$$

Here, the Belkov-Kopeliovich parametrization of the ρ-nucleus elastic cross section is used (see Sec. 2.4.4). Thus, the cross section becomes

$$\frac{d^3\sigma_{BK}(\nu_\mu + Ne \to \mu + \rho + Ne)}{dQ^2\, d\nu\, d\Delta_T^2} = \frac{G_F^2}{4\pi^2}\,\frac{|\vec{q}|}{E^2}\,\frac{f_{\rho^\pm}^2}{1-\epsilon}\,\frac{Q^2}{(Q^2+m_\rho^2)^2} \times (1+\epsilon R)\,\frac{\left(\sigma_{\rm tot}^{\rho Ne}\right)^2}{16\pi}\,(1+r^2)\,e^{-B_T\,\Delta_T^2}\,e^{-B_L\,\Delta_L^2}\,.$$

For comparison, the cross section is also computed using the Rein-Sehgal parametrization of the ρ-nucleus differential cross section (see Sec. 2.4.2). Using this parametrization, the cross section is expressed as

$$\frac{d^3\sigma_{RS}(\nu_\mu + Ne \to \mu + \rho + Ne)}{dQ^2\, d\nu\, dt} = \frac{G_F^2}{4\pi^2}\,\frac{|\vec{q}|}{E^2}\,\frac{f_{\rho^\pm}^2}{1-\epsilon}\,\frac{Q^2}{(Q^2+m_\rho^2)^2} \times (1+\epsilon R)\,\frac{A^2}{16\pi}\,\left(\sigma_{\rm tot}^{\rho N}\right)^2\,(1+r^2)\,e^{-b|t|}\,F_{\rm abs}\,.$$

By CVC, the coupling constant to the W boson, $f_{\rho^\pm}$, is given in terms of f_{ρ^0}, the ρ^0 coupling constant to the photon

$$\begin{aligned} f_{\rho^\pm} &= f_{\rho^0}\,\sqrt{2}\,\cos\theta_c\,, \\ f_{\rho^0} &= m_\rho^2/\gamma_\rho\,, \end{aligned} \tag{4.4}$$

where θ_c is the Cabibbo angle and

$$\frac{\gamma_\rho^2}{4\pi} \simeq 2.4\,.$$

The value of the constant γ_ρ is measured in ρ^0 photoproduction and $\rho^0 \to e^+e^-$ decays [50, 51]. However, the value of γ_ρ is not known precisely. For example, Bauer et al. give an effective value $\gamma_\rho^2/4\pi = 2.2$ [52] which is slightly different from the above value. The factor $\sqrt{2}$ in Eq. (4.4) appears because the coupling of the ρ^0 to the photon is determined by its quark wave function $(u\bar{u} - d\bar{d})/\sqrt{2}$ for which the coupling is $(\frac{2}{3} - \frac{-1}{3})/\sqrt{2} = 1/\sqrt{2}$; the Cabibbo angle is introduced because the W boson couples to the $u\bar{d}$ $(\bar{u}d)$ pairs making up the ρ^+ (ρ^-) mesons.

Two possible Q^2 dependences of the ratio of longitudinal to transverse ρ-nucleus cross sections are considered :

1. $R = 0$,

2. $R = 0.4\ Q^2/m_\rho^2, \quad R \leq 1.$

The second form is suggested by studies of ρ^0 electro- and muoproduction [3]. Furthermore, the total ρ-nucleon cross section is taken to be the same as the total pion-nucleon cross section. This is supported by the indirect measurements carried out in ρ^0 photoproduction experiments (see for example [48]). Therefore, the values for $\sigma_{tot}^{\rho Ne}$, B_L and B_T are the same as in the case of pion scattering described above.

The mass of the $\pi^\pm\pi^0$ system is generated according to the following Breit-Wigner p-wave resonance formula [53]

$$BW = \frac{m_{\pi\pi}}{p} \frac{\Gamma}{(m_{\pi\pi}^2 - m_\rho^2)^2 + m_\rho^2 \Gamma^2},$$

$$\text{with} \quad \Gamma = \Gamma_0 \left(\frac{p}{p_0}\right)^3 \frac{m_\rho}{m_{\pi\pi}},$$

where p represents the magnitude of the pion momentum in the center of mass of the $\pi^\pm\pi^0$ system. The constant $p_0 = 358$ MeV/c is the value of p computed using the nominal value of the ρ mass rather than the effective mass of the system $m_{\pi\pi}$. The full width at half maximum for the charged ρ meson is $\Gamma_0 = 149$ MeV [12] and the nominal value of the ρ mass is $m_\rho = 768$ MeV [12].

4.2.3 Smearing

Special attention was paid to the problem of smearing because of the diffractive nature of coherent interactions. Indeed, the smearing significantly broadens the measured momentum transfer distribution thus affecting the detectability of the coherent peak at small values of $|t|$. Furthermore, it is important to replicate the smearing conditions to compare predictions of the various models with the data.

(a) Charged Tracks

To describe the smearing of charged tracks, the formulae from R. G. Glasser's report [54, 55] have been used. Two main sources of error are considered : multiple scattering errors and measurement errors. The latter arise from the finite width of the bubble chamber tracks and the finite resolution of the measuring system. The measurement errors on the projected curvature k of the track, its slope s (tangent of the dip angle λ) and its azimuthal angle ϕ are determined by the following expressions

$$\sigma_k^2 = \frac{720\,A^2}{N_p\,L^4}\,, \qquad \sigma_\phi^2 = \frac{192\,A^2}{N_p\,L^2}\,,$$

$$\sigma_s^2 = \frac{12(s^2+B^2)\,A^2}{N_p\,L^2}\,, \qquad c(\phi,k) = \frac{L\,\sigma_k^2}{2}\,,$$

$$\text{with} \quad A = \frac{H-z}{\sqrt{2}\,H}\,\Delta_M \quad \text{and} \quad B = \frac{H-z}{D}\,,$$

where the constants D and H represent the distance between the cameras and the center of the bubble chamber along the horizontal and vertical directions respectively; the constant Δ_M is the standard deviation on the measurement in the XY plane. L represents the track length in the XY plane and N_p is the number of points measured along the track on each view. The sign of the correlation $c(\phi,k)$ between the curvature and the azimuthal angle is determined by the charge of the track.

The errors due to multiple scattering are given by

$$\sigma_k^2 = \frac{4\,f}{3\,L\,cos^4\lambda}\,, \qquad \sigma_\phi^2 = \frac{f\,L}{6\,cos^2\lambda}\,,$$

$$\sigma_s^2 = \frac{f\,L}{3}\,, \qquad c(\phi,k) = \frac{f}{6\,L\,cos^3\lambda}\,,$$

$$\text{with} \quad f \equiv \frac{0.015^2}{X_0\,(p\beta)^2}\,,$$

where X_0 is the radiation length, p is the track momentum in GeV/c and β is the velocity.

The constants D and H are set to $D = 100$ cm and $H = 200$ cm. The setting error and the parametrization of the number of points measured as a function of track length have been adjusted such as to reproduce the measurement accuracy obtained in this experiment.

In order to adjust the smearing parameters, a sample of charged current events was generated using the Berkeley/Hawaii TUBES Monte Carlo [55]. These events were smeared using the above formulae and compared with the measured inclusive charged current event sample. This sample is commonly referred to as the "minimum bias" sample since it contains all (anti)neutrino interactions that were found in a given range of frames. For instance, Fig. 4.7 shows the $\frac{\Delta p}{p}$ as a function of p and track length for muon and charged hadron tracks, after adjustment of the smearing parameters. The smearing on the dip and azimuthal angles was also carefully compared and was adjusted to reproduce the data. The setting error was finally set to $\Delta_M = 600$ μm in the XY plane and 1.6 times that along the Z axis.

(b) Gamma Conversions

Contrary to the case of measurement errors on charged tracks, there is no straightforward parametrization of the errors on the gamma conversion momentum and angles. Hence, we have chosen an empirical approach.

The relative error on the momentum $\frac{\Delta p}{p}$ is taken to be proportional to the momentum, with slope and intercept adjusted such as to approximately reproduce the observed momentum dependence of $\frac{\Delta p}{p}$ (see Fig. 4.9a) :

$$\begin{aligned} \frac{\Delta p}{p} &= a + b \cdot p \quad \text{for } p < 4 \text{ GeV/c} , \\ \frac{\Delta p}{p} &= c + d \cdot p \quad \text{for } p \geq 4 \text{ GeV/c} , \end{aligned}$$

where $a = 0.16$ (0.14), $b = 0.025$ (0.025), $c = 0.24$ (0.22) and $d = 0.005$ (0.005) for the 1985 (1987-88) run data. The error on the angles is determined using the distance between the primary and gamma vertices and the average measurement errors on

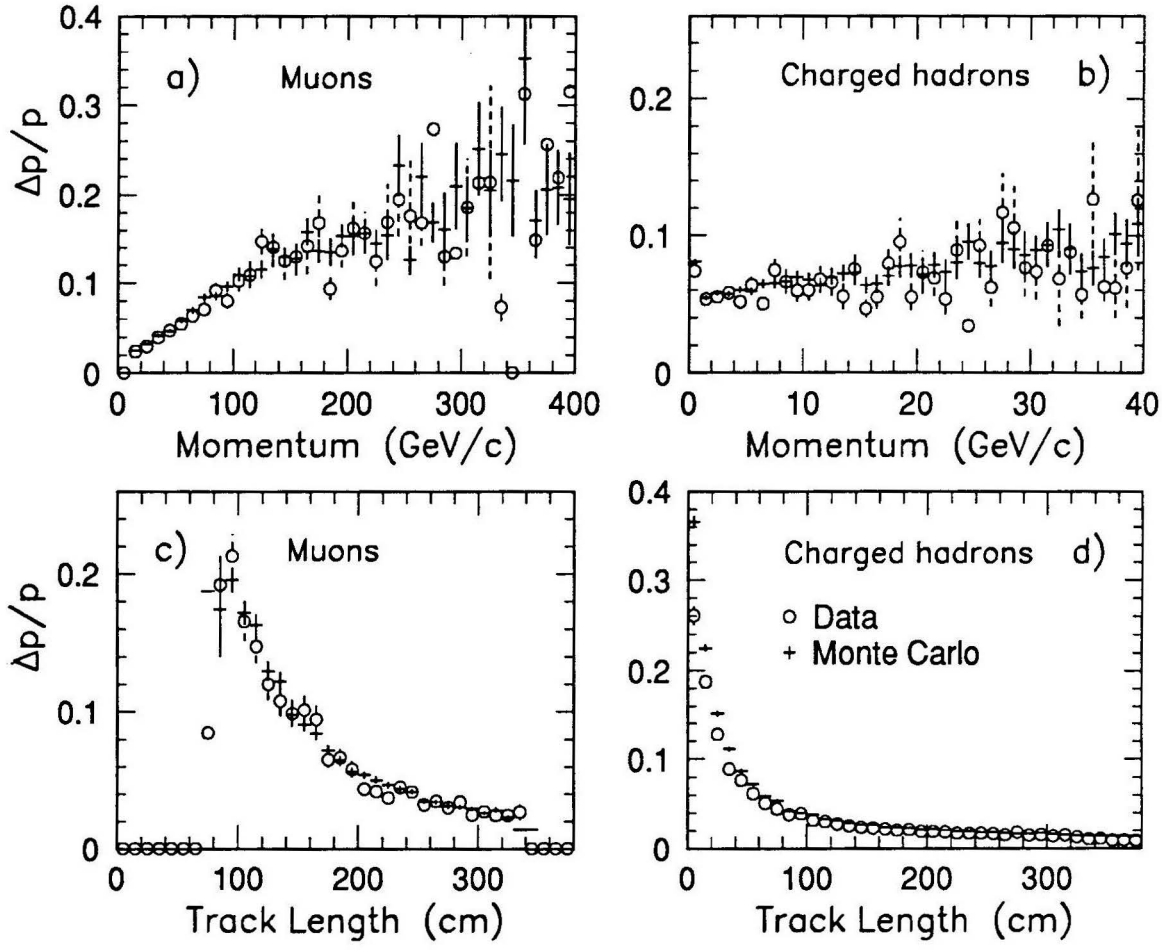

Figure 4.7: Average $\frac{\Delta p}{p}$ for muon and charged hadron tracks, the open circles represent the minimum bias data and the crosses represent the Monte Carlo simulation; a) $\frac{\Delta p}{p}$ vs muon momentum, b) $\frac{\Delta p}{p}$ vs hadron momentum, c) $\frac{\Delta p}{p}$ vs muon track length, d) $\frac{\Delta p}{p}$ vs hadron track length.

the location of the vertices along the X, Y and Z axes: $\Delta_X = 0.15$ cm, $\Delta_Y = 0.09$ cm and $\Delta_Z = 0.19$ cm for the 1985 run data, and $\Delta_X = 0.15$ cm, $\Delta_Y = 0.06$ cm and $\Delta_Z = 0.12$ cm for the 1987-88 run data.

The data were compared with the results of a "pseudo π^0 Monte Carlo" in which the measured momenta and angles of the charged pion tracks were used to generate neutral pions which subsequently decay into pairs of photons. This guaranteed that the simulated momentum spectrum and the angular distributions were similar to the data. The γ momentum distribution is presented in Fig. 4.8 and shows that the distribution obtained with our pseudo Monte Carlo reproduces the data well,

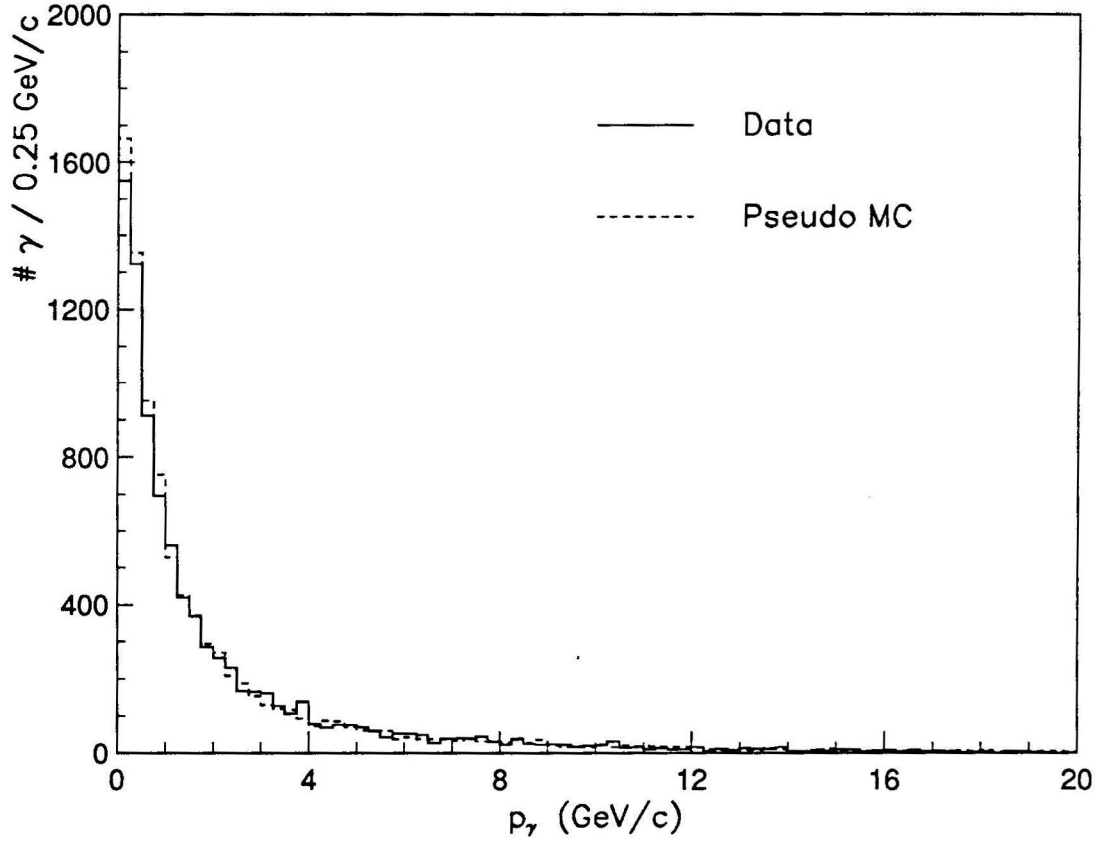

Figure 4.8: γ momentum distributions for the low multiplicity data sample and the pseudo π^0 Monte Carlo. The pseudo Monte Carlo distribution is normalized to the number of events in the data.

except for a slight deviation at low momenta. Fig. 4.9 shows the errors on the gamma conversion parameters as a function of momentum. The angular smearing distributions show good agreement between the smeared pseudo Monte Carlo and the data. It was also checked that the width of the π^0 peak in the $\gamma\,\gamma$ invariant mass distribution obtained in the simulation reproduced the experimental resolution.

(c) Beam Direction

Another source of smearing originates from the uncertainty in the neutrino beam direction. This uncertainty, estimated to be 0.5 mrad (see Sec. 4.1.3), is reproduced in the Monte Carlo simulation.

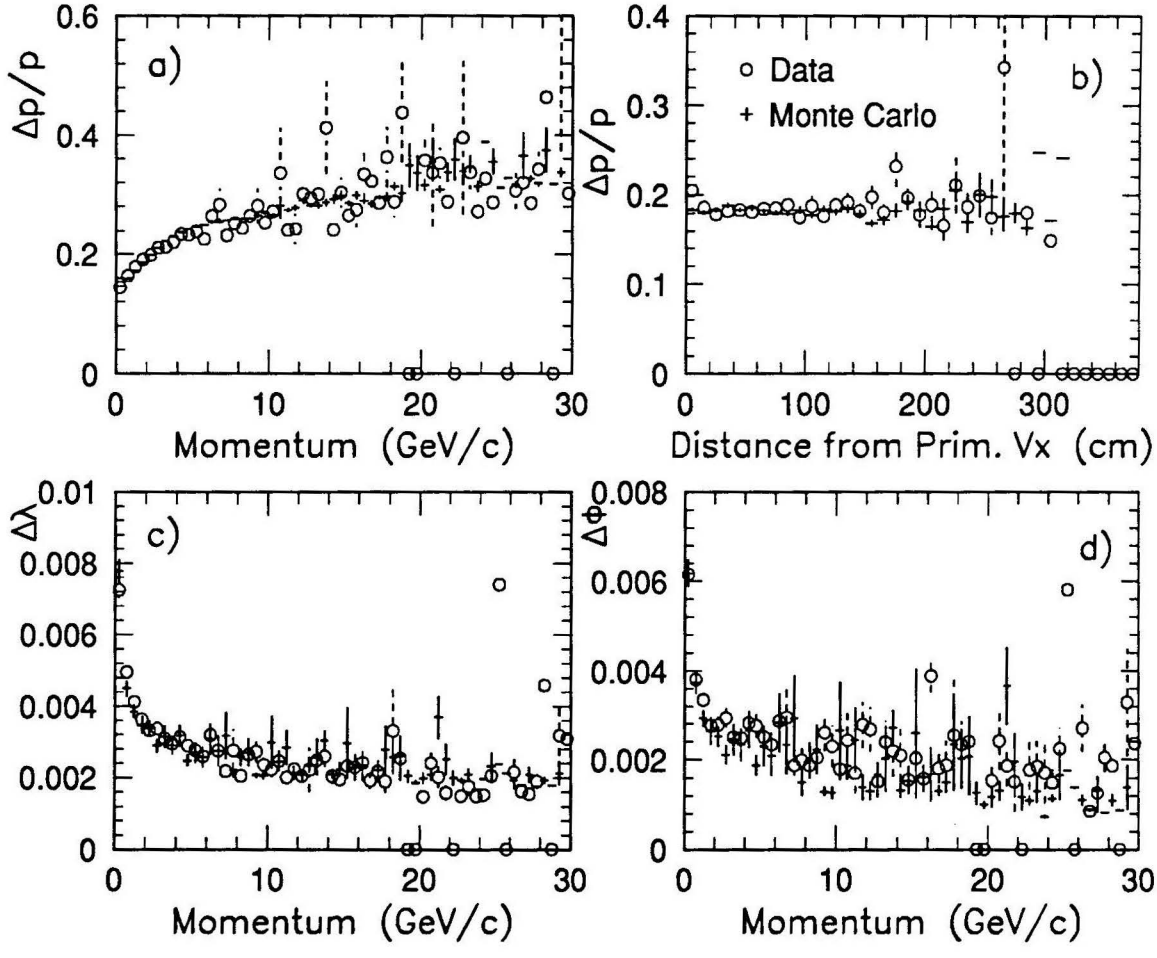

Figure 4.9: Smearing of gamma conversions, the open circles represent the data and the crosses represent the pseudo Monte Carlo simulation; a) $\frac{\Delta p}{p}$ vs momentum, b) $\frac{\Delta p}{p}$ vs distance from the primary vertex, c) $\Delta\lambda$ (in radians) vs momentum, d) $\Delta\phi$ (in radians) vs momentum.

4.2.4 Neutrino Fluxes

The coherent production simulation and the data analysis both rely on knowledge of the (anti)neutrino flux. To check our knowledge of the flux, the measured and simulated distributions of the total energy of the charged current events were compared. Here, the loss of neutral hadrons is corrected by using the Heilmann energy correction method (also known as the "Bonn method" [56]). For the heavy Ne-H_2 liquid, an average of $\sim$ 75 % of the total hadronic energy is detected and the average correction factor for the total energy of the event is $\sim$ 1.1. Fig. 4.10 shows the distributions for neutrino and antineutrino charged current events with muon momentum greater than 10 GeV/c. Even though the Monte Carlo simulation predicts a slightly higher average energy, there is good overall agreement between the data and the TUBES Monte Carlo, indicating that the flux shapes are appropriate.

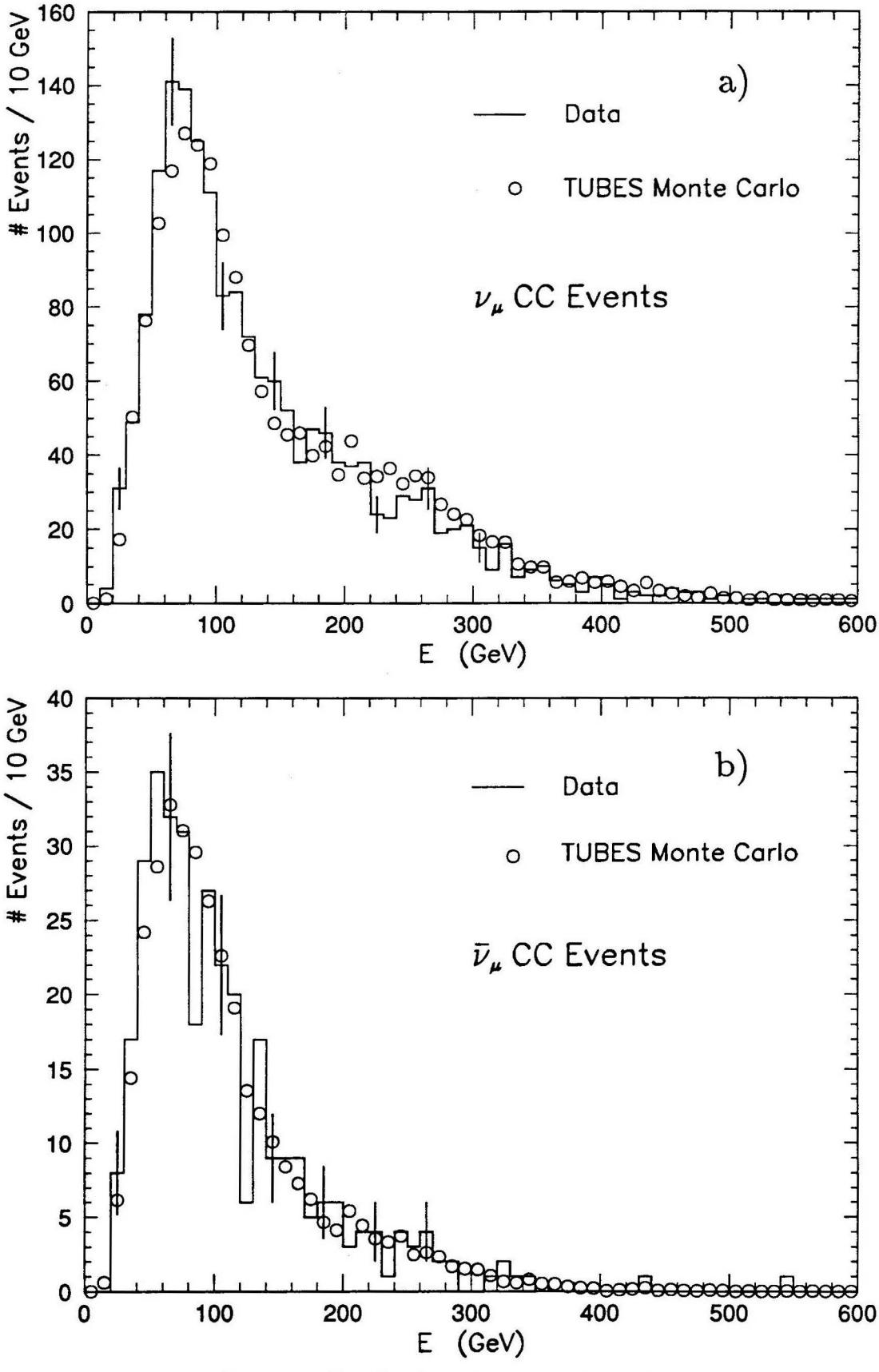

Figure 4.10: Corrected energy distributions for ν_μ and $\overline{\nu}_\mu$ charged current events with $p_\mu > 10$ GeV/c. The TUBES Monte Carlo distributions are normalized to the data.

Chapter 5
Single Pion Coherent Production

In Sec. 4.1, we saw that the $|t|$-distribution for 2-prong events without stubs displays an excess of events at $|t| < 0.1$ GeV^2 in comparison with the distribution for events with stubs. This excess was interpreted as due to coherent interactions. In this chapter, we investigate the main contribution to that semi-inclusive signal : the coherent production of single pions off neon nuclei. In particular, it will be shown that, indeed, the (anti)neutrinos scatter off nuclear rather than nucleon targets. The coherent signal is extracted using the technique described in Chapter 4. In order to compute the cross section for single pion production, it is necessary to correct the observed signal for all losses.

In Section 5.1, the selection of the single pion sample and the extraction of the coherent signal are described. In Section 5.2, the coherent sample correction factors are evaluated to take the losses into account. In Section 5.3, the inclusive charged current sample is selected and various losses are accounted for. Section 5.4 is devoted to a brief study of some of the physical sources of incoherent background. In Section 5.5, the corrected coherent signal and its corresponding inclusive charged current event sample are used to compute the coherent cross section, which is compared with previous results from experiments performed at lower energies. Finally, Section 5.6 presents the kinematical characteristics of the single pion coherent interactions and compares them with the predictions of the Rein-Sehgal and Belkov-Kopeliovich models.

5.1 Extraction of the Signal

The focus of this chapter is the coherent production of single pions in charged current interactions of neutrinos and antineutrinos on neon nuclei (Fig. 5.1) :

$$\begin{aligned} \nu_\mu + Ne &\rightarrow \mu^- + \pi^+ + Ne \,, \\ \overline{\nu}_\mu + Ne &\rightarrow \mu^+ + \pi^- + Ne \,. \end{aligned} \tag{5.1}$$

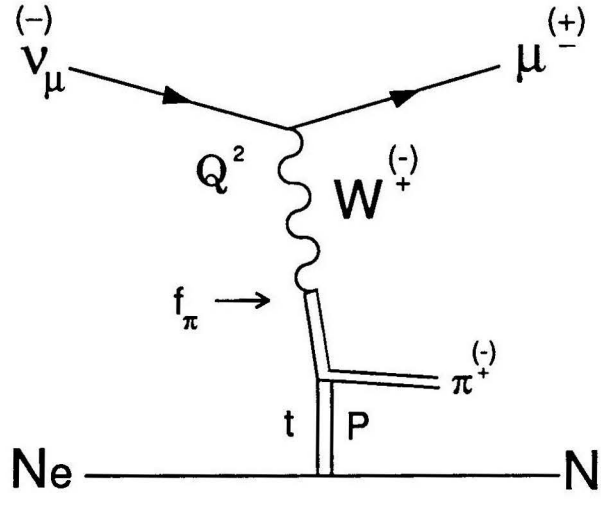

Figure 5.1: Diagram for the coherent production of single pions.

We select events with two prongs and zero total electric charge, having no associated gamma conversions and no V^0 fits. The selected sample amounts to 168 $\mu\pi$ events without stubs and 78 $\mu\pi$ events with stubs ($p_{\rm stub} < 800$ MeV/c).

Fig.5.2 shows the $|t|$-distributions for these 246 events, with the distribution for events with stubs normalized to that for events without stubs at $|t| > 0.2$ GeV^2. There are 63 events without stubs and 7 events with stubs at $|t| < 0.1$ GeV^2. After normalization by a factor of 1.56 ± 0.26, the number of background events is estimated to be 10.9 ± 5.1. Thus the coherent signal at $|t| < 0.1$ GeV^2 is found to be 52.1 ± 9.4 events, where the error is purely statistical.

The signal was extracted for $|t| < 0.1$ GeV^2 and $|t| < 0.2$ GeV^2, as well as for a series of cuts on the stub momentum or stub multiplicity (Table 5.1). By comparing

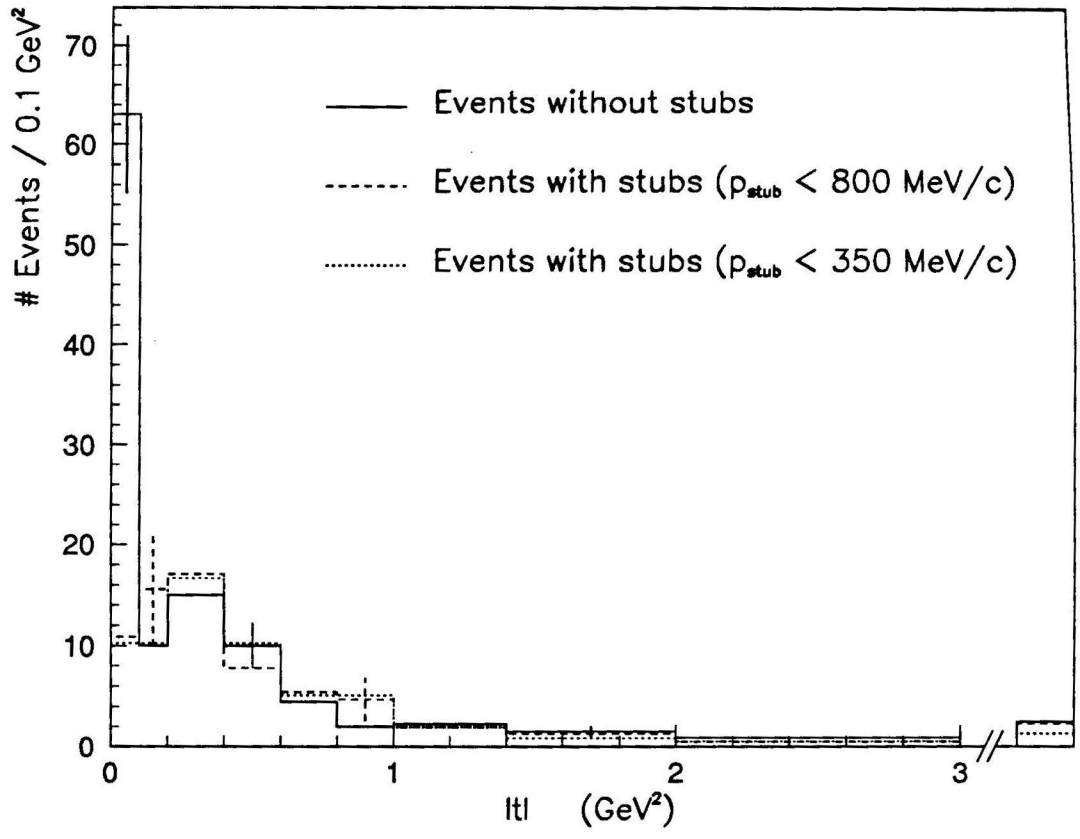

Figure 5.2: $|t|$-distributions for $\mu^{\pm}\pi^{\mp}$ events, normalized at $|t| > 0.2$ GeV^2.

those results we conclude that the signal is fairly insensitive to the particular choice of cut on $|t|$ or to the choice of background sample. Therefore, we will use the sample providing the largest background statistics, i.e. the one obtained with a cut on the stub momentum of 800 MeV/c. Note that the signal extracted using events with at least two stubs as background (last line in Table 5.1) gives large errors because the background sample contains only 13 events.

Table 5.1: Uncorrected signal for $\mu^{\pm}\pi^{\mp}$ events and various choices of the incoherent background sample, normalized at $|t| > 0.2$ GeV^2. The errors are purely statistical.

	$\|t\| < 0.1$ GeV^2	$\|t\| < 0.2$ GeV^2
$p_{stub} < 350$ MeV/c	52.7 ± 10.4	52.5 ± 12.3
$p_{stub} < 500$ MeV/c	48.9 ± 10.3	42.7 ± 12.8
$p_{stub} < 800$ MeV/c	52.1 ± 9.4	46.5 ± 11.5
$p_{stub} < 800$ MeV/c (# stubs = 1)	50.6 ± 10.2	54.4 ± 11.2
$p_{stub} < 800$ MeV/c (# stubs > 1)	52.4 ± 17.7	30.8 ± 31.4

5.2 Corrections to the Coherent Signal

5.2.1 Scanning Efficiency

The scanning efficiency is computed by comparing the number of $\mu\pi$ events found in two independent scans. Specifically, the combined and single scan efficiencies are given by the following expressions

$$\begin{aligned} \epsilon_1 &= \frac{N_{12}}{N_{12} + N_2^0} \\ \epsilon_2 &= \frac{N_{12}}{N_{12} + N_1^0} \\ \epsilon_{1+2} &= 1 - (1 - \epsilon_1)(1 - \epsilon_2) \end{aligned}$$

where N_{12} represents the number of events found in both scans and N_1^0 (N_2^0) represents the number of events found in scan 1 (2) only; ϵ_1 and ϵ_2 are the efficiencies of the first and second scans, whereas ϵ_{1+2} corresponds to the combined scanning efficiency. It should be noted that the above formulae only apply to the case where the scanning losses are purely random and do not apply if there is a systematic loss of events.

The quantities N_{12}, N_1^0 and N_2^0 were extracted for the $\mu\pi$ events satisfying all selection criteria. As discussed in Sec. 3.2, the quality of the bubble chamber

exposure varied during the data taking. Part of the film taken during the 1985 run was affected by timing problems which resulted in tracks that were faint, whereas part of the film taken during the 1987-88 run was affected by ice deposited onto the bubble chamber walls, thereby reducing the track visibility. Those sections of film are referred to as "faint/snowy" while the remainder of the film, unaffected by these problems, is referred to as "good". In the faint/snowy film, the reduced track visibility in certain sections of the bubble chamber resulted in 2-prong event rates (per incident proton on target) $\sim$ 20 % lower than the corresponding rates in the good film. Therefore, the scanning efficiencies were computed separately for the good and faint/snowy film. The scanning efficiency in the good film was found to be, at most, a few percent higher than for the rest of the film. This indicates that the lower rates are due to systematic losses rather than random losses. As a consequence, the scanning efficiency was computed for the good film only, and the efficiency for the rest of the film was inferred by comparing the event rates.

The scanning efficiency in the good film was determined to be $(89.1 \pm 2.1)\%$. This value was obtained by combining the efficiency of the first scan with the efficiency for the first and second scans combined, taking into account the fact that only 56% of the good film was double scanned.

The "effective" scanning efficiency in the faint/snowy film was then simply determined by comparing the observed $\mu\pi$ event rate with the corrected rate obtained in the good film. This was done separately for the 1985 and 1987-88 data since the event rates were different due to the different target densities. As a result, the combined 1985 and 1987-88 data effective efficiency was found to be $(63.1 \pm 9.9)\%$.

Finally, the overall efficiency was evaluated by combining the efficiency in the good film with the effective efficiency in the rest of the film, taking the relative fluxes into account. This yielded $\epsilon = (72.9 \pm 6.5)\%$.

As an independent check of the scanning efficiency in the good film, a special EMI directed scan was performed (see Sec. 3.2) on 16000 frames, representing 4.5 %

of the good film. Two new $\mu\pi$ events were found in this special scan, to be compared with 16 events found in the conventional scan for the same portion of the film. Based on the scanning efficiency in the good film, one would expect the total number of $\mu\pi$ events to be $(16 \pm 4)/(0.891 \pm 0.021) = 18.0 \pm 4.5$. Given that the EMI directed scan has an efficiency between 65 and 85% (depending on the lab) and that only two additional events were found in the directed scan, we conclude that there is no large systematic loss of $\mu\pi$ events.

Including in our data sample the measurements performed in the faint/snowy film may lead to biases in the kinematical variables. However, it was checked that there were no significant differences between the kinematical characteristics of the $\mu^{\pm}\pi^{\mp}X^{0}$ events found in the faint/snowy film and the good film.

5.2.2 $\frac{\Delta p}{p}$ Cut

The cut on the relative momentum error of the charged tracks, $\frac{\Delta p}{p} < 60\%$, reduced the initial 2-prong data sample from 1032 events to 935 events, i.e. by a factor of 0.906 ± 0.009.

Since the $\frac{\Delta p}{p}$ cut may introduce a momentum-dependent bias, we attempted to reproduce the momentum dependence of $\frac{\Delta p}{p}$ by using the results of the Monte Carlo simulation described in Sec. 4.2. Specifically, the simulation provided the fractions of charged pion and muon tracks passing the $\frac{\Delta p}{p} < 60\%$ cut in different momentum ranges. These fractions were then translated into probabilities for a track of given momentum to pass the cut. Each track of the data sample (after the $\frac{\Delta p}{p}$ cut was imposed) was then applied a weight equal to the inverse of its probability to pass the cut and the average weight for the whole sample was computed. This method gave a result very similar (within 5%) to that obtained from the fraction of all 2-prong events passing the cut. This similarity is due to the fact that most events failing the $\frac{\Delta p}{p}$ cut fail because of large errors on the momentum of the charged hadron (rather than the muon), and these errors depend mostly on the track length and only weakly

on the momentum (see Fig.4.7). The correction factor is thus 1.104 ± 0.011.

5.2.3 p_μ Cut

The fraction of events passing the muon momentum cut $p_\mu > 10$ GeV/c was determined to be 98.9 % from the coherent pion production Monte Carlo simulation with the Rein-Sehgal parametrization (see Sec. 4.2.1). The systematic error due to the choice of a particular model is estimated to be 0.2% by comparing the above fraction with that obtained using the Belkov-Kopeliovich parametrization (see Sec. 4.2.1). It should be noted that the cut on p_μ implies a cut on the total energy of $E > 10$ GeV.

5.2.4 $|t|$ Cut

The effect of the $|t|$ cut, a reduction of the signal by a factor of 0.921, was also determined from the Monte Carlo simulation. This number corresponds to the fraction of Monte Carlo events with $|t| < 0.1$ GeV^2, after all cuts other than the $|t|$ cut have been applied. As in the case of the correction for the p_μ cut, the correction factor was obtained using the Rein-Sehgal parametrization. The systematic error due to that particular choice was estimated to be 0.030 by comparing the correction factor with that obtained using the Belkov-Kopeliovich parametrization.

Another source of systematic error comes from the uncertainty in the (anti)neutrino beam direction (see Sec. 4.1.3). This uncertainty tends to make the $|t|$ distribution broader and thus affects the fraction of coherent events observed below the $|t|$ cut. In the Monte Carlo simulation, the uncertainty in the beam direction was set to 0.5 mrad. However, to test the sensitivity of our results to the uncertainty in the beam direction, the fraction of events passing the $|t|$ cut was computed for a series of values of the uncertainty in the beam direction: 0, 0.5, 1 and 1.5 mrad. The systematic error on the fraction of events passing the cut was then taken to be the r.m.s. of the

Table 5.2: Correction factors for coherent single pion events.

	ν	$\overline{\nu}$	All
$\frac{\Delta p}{p}$ cut correction (c_1)	1.104 ± 0.011		
Scanning efficiency (c_2)	0.729 ± 0.065		
Fraction with $p_\mu > 10$ GeV/c (c_3)	0.990 ± 0.003	0.984 ± 0.002	0.989 ± 0.002
Fraction with $\|t\| < 0.1$ GeV^2 (c_4)	0.914 ± 0.063	0.939 ± 0.047	0.921 ± 0.059
Total correction factor $c_1/(c_2 \cdot c_3 \cdot c_4)$	1.674 ± 0.189	1.639 ± 0.168	1.663 ± 0.183

distribution of those fractions where the fractions obtained with uncertainties of 0.5 and 1 mrad were assigned a weight twice that for 0. and 1.5 mrad. The systematic error due to the determination of the beam direction uncertainty is then estimated to be 0.051.

As a result, the fraction of events passing the $|t| < 0.1$ GeV^2 cut was found to be 0.921 ± 0.059, where the error was computed by adding, in quadrature, the systematic errors due to both the choice of parametrization and the uncertainty in the beam direction.

5.2.5 Total Correction

The various correction factors are summarized in Table 5.2 for $\mu^- \pi^+$ and $\mu^+ \pi^-$ events as well as for both types combined. The overall correction factor for $\nu_\mu + \overline{\nu}_\mu$ interactions is 1.663 ± 0.183.

The systematic error induced by the choice of $|t|$ cut value can be evaluated by extracting the coherent signal for different values of the cut and by comparing the signal corrected for the effect of the $|t|$ cut. Table 5.3 shows the corrected signal for cuts at 0.05, 0.1, 0.15 and 0.2 GeV^2. All four values are compatible within errors with an r.m.s. of 4.3 events. This can thus be interpreted as a systematic uncertainty

Table 5.3: Single pion coherent signal for different cuts on $|t|$. The $|t|$ distributions for events without and with stubs have been normalized at $|t| > 0.2$ GeV^2.

$\|t\|$ cut	# Events below $\|t\|$ cut		Signal	Fraction MC	Signal
(GeV^2)	w/o stubs	with stubs	observed	passing cut	corrected
0.05	41	2	37.9 ± 6.8	0.796	47.6 ± 10.2
0.1	63	7	52.1 ± 9.4	0.921	56.7 ± 10.2
0.15	69	12	50.3 ± 10.4	0.953	52.8 ± 10.9
0.2	73	17	46.5 ± 11.5	0.967	48.1 ± 11.9

of 8 % in the corrected signal.

5.3 Inclusive Charged Current Event Sample

In order to compute the cross section for single pion coherent production, we first determine the rate of single pion coherent events with respect to the total number of charged current events. However, the inclusive charged current event sample measured in this experiment represents only a small fraction of the film used in the analysis of low multiplicity events. Therefore, the numbers of events have to be scaled by their corresponding flux of protons incident on target.

For the inclusive charged current event sample, the events found in the good film are required to be inside the fiducial volume, without being clearly associated with another event upstream in the bubble chamber, and should contain at least one muon with momentum greater than 10 GeV/c. Note that only the good film is used here to avoid scanning/measuring inefficiencies. This leads to a sample of 574 (1220) ν_μ and 83 (260) $\overline{\nu}_\mu$ charged current events for the 1985 (1987-88) data, corresponding to 12.37×10^{15} (35.03×10^{15}) protons on target.

As detailed below, several correction factors have to be applied to the number of observed events to take into account scanning and measuring inefficiencies, fraction

of events on hydrogen nuclei, and cut on the muon momentum. The EMI muon detection efficiency was found to affect both low multiplicity and inclusive event samples in similar ways, and therefore drops out of the ratio of the number of single pion coherent interactions and the number of charged current interactions.

5.3.1 Scanning Efficiency

The measurement of events of all multiplicities was carried out in film that was double scanned, for the most part, with a combined efficiency for the two scans of $(99.8 \pm 0.1)\%$. Taking into account the small fraction of film which was only single scanned leads to an overall scanning efficiency of $(99.3 \pm 0.2)\%$.

However, this applies only to events with two or more prongs because of the systematic loss of events with only one prong. This loss affects mostly $\overline{\nu}_\mu$ charged current interactions because charge conservation implies that ν_μ charged current interactions have at least two charged particles in the final state (1-prong ν_μ events require that either the final state hadrons be totally absorbed inside the neon nucleus or that the hadronic final state consists of a proton with a range too short to be detected).

To estimate the loss of 1-prong events (i.e. events with no charged hadrons), we have used the KNO scaling distributions measured in $\overline{\nu}_\mu$-deuterium interactions [57] (distributions of the probability to find an event with n charged hadrons as a function of the variable $n/ < n >$). These results imply that, given the average charged hadron multiplicity observed in this experiment ($< n > = 5.0 \pm 0.2$ for $\overline{\nu}_\mu$ charged current interactions with one or more charged hadrons), the probability to produce a 1-prong $\overline{\nu}_\mu$ charged current event is 0.030 ± 0.007. Assuming that all 1-prong events are lost and that nuclear reabsorption can be neglected as a first approximation, the correction factor for $\overline{\nu}_\mu$ charged current events is estimated to be 1.031 ± 0.007.

Thus, multiplying this factor with that corresponding to the (random) scanning

efficiency gives overall correction factors of 1.007 ± 0.002 for ν_μ charged current events and 1.038 ± 0.007 for $\overline{\nu}_\mu$ charged current events.

5.3.2 Unmeasured Events

A small fraction of charged current events were too complicated to be measured, even partially. This usually occurred in the case of high multiplicity events or events with very intense electromagnetic showers. This loss of events is found to be negligibly small for the 1987-88 film but amounts to $(3.4 \pm 0.5)\%$ for the 1985 film, corresponding to a correction factor of 1.035 ± 0.005.

5.3.3 Fraction of Interactions on Neon Nuclei

The fraction of interactions on hydrogen nuclei is given by

$$f = \frac{(2 \times F_{H_2})\,\sigma_p}{(2 \times F_{H_2} + 10 \times F_{Ne})\,\sigma_p + (10 \times F_{Ne})\,\sigma_n}$$

where σ_p and σ_n are the total cross sections on proton and neutron targets, while F_{Ne} and F_{H_2} are the neon and hydrogen molar fractions of the Ne-H_2 mix. Those fractions are $75\% - 25\%$ and $63\% - 37\%$ for the 1985 and 1987-88 runs respectively. Using the quark-parton model predictions $\sigma_n^\nu/\sigma_p^\nu = 2$ and $\sigma_n^{\overline{\nu}}/\sigma_p^{\overline{\nu}} = 0.5$ (see Refs. [44, 58] for experimental verification), the fraction of charged current interactions on neon nuclei $(1 - f)$ is found to be 97.8% (96.2%) for neutrino interactions and 95.7% (92.7%) for antineutrino interactions in the 1985 (1987-88) data.

5.3.4 p_μ Cut

The largest correction is introduced to account for the loss of events with muon momentum smaller than 10 GeV/c. To determine this loss, we use the calculated (anti)neutrino flux shapes [31] and a recent fit to the data on structure functions [59].

In the framework of the quark-parton model, the differential cross sections for (anti)neutrino-proton charged current interactions are given by

$$\frac{d^2\sigma^{\nu p}}{dx\,dy} = \frac{G_F^2\,M\,E}{\pi}\,2\,x\,\left[d(x)+s(x)+\overline{u}(x)\,(1-y)^2\right]$$
$$\frac{d^2\sigma^{\overline{\nu} p}}{dx\,dy} = \frac{G_F^2\,M\,E}{\pi}\,2\,x\,\left[u(x)\,(1-y)^2+\overline{d}(x)+\overline{s}(x)\right]$$

where x and y are the Bjorken scaling variables and $u(x)$, $d(x)$ and $s(x)$ are the quark density functions. The (anti)neutrino-neutron cross sections are obtained via the isospin transformation $u(x) \leftrightarrow d(x)$. Thus, $\nu\,q$ and $\overline{\nu}\,\overline{q}$ interactions are characterized by a flat y distribution whereas $\nu\,\overline{q}$ and $\overline{\nu}\,q$ interactions are characterized by a $(1-y)^2$ distribution. For those two types of y distributions, the fractions of events passing the p_μ cut can be determined using the calculated (anti)neutrino flux : it is greater than 99 % in the case of $(1-y)^2$ distributions and it is 89.0 % (86.6 %) for ν ($\overline{\nu}$) flat y distributions. Moreover, using the above cross sections and the structure function data, the fraction of neutrino (antineutrino) interactions characterized by $(1-y)^2$ is determined to be 0.043 ± 0.003 (0.65 ± 0.05). Finally, the fraction of neutrino (antineutrino) charged current events passing the $p_\mu > 10$ GeV/c cut is estimated to be 0.894 ± 0.004 (0.947 ± 0.066). These fractions are compatible with those obtained from the Berkeley/Hawaii TUBES Monte Carlo.

5.3.5 Total Correction

The number of charged current events is corrected using the various correction factors presented in Table 5.4. These numbers are then scaled to correspond to the number of protons on target for the 2-prong event sample, i.e. 226.3×10^{15} and 312.6×10^{15} protons on target for the 1985 and 1987-88 runs respectively. The resulting corrected number of charged current interactions on neon nuclei (with $E > 10$ GeV) is 23761 ± 612 for ν_μ interactions and 4002 ± 313 for $\overline{\nu}_\mu$ interactions (see Table 5.5).

Table 5.4: Correction factors for charged current events in the inclusive data sample.

	ν 85	$\overline{\nu}$ 85	ν 87	$\overline{\nu}$ 87
Scanning losses (c_1)	1.007 ± 0.002	1.038 ± 0.007	1.007 ± 0.002	1.038 ± 0.007
Unmeasured events (c_2)	1.035 ± 0.005		—	
Frac. events on neon (c_3)	0.978	0.957	0.962	0.927
Frac. $p_\mu > 10$ GeV/c (c_4)	0.894 ± 0.004	0.947 ± 0.066	0.894 ± 0.004	0.947 ± 0.066
Total correction factor $(c_1 \cdot c_2 \cdot c_3)/c_4$	1.140 ± 0.007	1.086 ± 0.076	1.084 ± 0.005	1.016 ± 0.071

Table 5.5: Number of charged current events ($E > 10$ GeV).

	ν 85	$\overline{\nu}$ 85	ν 87	$\overline{\nu}$ 87
(a) Inclusive data sample				
N_{CC} (observed)	574	83	1220	260
N_{CC} (corrected)	654 ± 28	90 ± 12	1322 ± 38	264 ± 25
Flux ($\times 10^{15}$ protons)	12.37		35.03	
(b) Coherent $\mu\pi$ data sample				
Flux ($\times 10^{15}$ protons)	226.3		312.6	
Calculated N_{CC}	11964 ± 512	1646 ± 220	11797 ± 339	2356 ± 223
Totals	N_{CC} (ν 85 + ν 87) = 23761 ± 612			
	N_{CC} ($\overline{\nu}$ 85 + $\overline{\nu}$ 87) = 4002 ± 313			

5.4 Background

5.4.1 Incoherent Background

The procedure used to extract the coherent signal assumes that the $|t|$ distribution for the events with stubs provides a good description of the background and that the number of background events can be obtained after normalization to the $|t|$ distribution for events without stubs at high enough values of $|t|$. As a check of this procedure, and to make sure that the known incoherent processes do not produce an unexpected source of background, we examine some of the specific sources of incoherent background :

1. quasi-elastic proton production,

2. Δ and nucleon resonance production, and

3. neutrino-nucleon diffractive pion production.

These processes give rise to events with topologies similar to those expected from the coherent production of single pions, i.e. the final state is of the type $\mu^{\pm} h^{\mp}$, where h is either a charged pion or a proton. In the case of resonance production, the final state may also contain an additional proton or neutron (if h is a pion), or a π^0, which may or may not be detected. We assume that the cross sections for the above processes are energy independent far enough above threshold.

(a) Quasi-elastic Proton Production

The quasi-elastic production of protons in ν_μ charged current interactions on neutrons

$$\nu_\mu + n \rightarrow \mu^- + p \,, \tag{5.2}$$

is a source of background if the proton is not identified as a stopping track (i.e. it either interacts or leaves the bubble chamber) in which case it is treated as if it

were a pion. The cross section for process (5.2) has been measured in a number of experiments at lower energies indicating a value which is independent of energy above $\sim$ 1 GeV. We use a result of Ref. [60], $\sigma(\nu_\mu + n \rightarrow \mu^- + p) \simeq 1.0 \times 10^{-38}$ cm^2, obtained for energies greater than 5 GeV, as applicable in the energy range of our experiment, $E > 10$ GeV.

Quasi-elastic events were generated using the Monte Carlo simulation described in Sec. 4.2 but with kinematical variables entirely determined by the Q^2 dependence of the nucleon form factor [61]. Moreover, the effect of Fermi motion was taken into account following the model proposed by Bodek and Ritchie [62]. After all selection criteria have been applied, 1.6 % of the number of events generated were found to simulate $\mu\pi$ events with $|t| < 0.1$ GeV^2. Taking the cross section into account implies that 2.2 events should be observed in our data sample after all selection criteria are applied and the various efficiencies are accounted for. It should be noted that, as for the other background sources evaluated in this section, the predicted number of events is an upper limit since it does not take into account the loss due to nuclear reinteractions.

(b) Δ and Nucleon Resonance Production

The production of resonances in the invariant mass region $1 \lesssim W < 2$ GeV leads to events with final states of the type $\mu + N + \pi$. Rein and Sehgal [63] have proposed a model to describe the production of all known Δ and nucleon resonances, including the contribution of non-resonant nucleon-pion systems. The predicted cross sections for $W < 2$ GeV are

$$\begin{aligned}
\sigma(\nu_\mu + n \rightarrow \mu^- + n + \pi^+) &= 0.38 \times 10^{-38} \text{ cm}^2 , \\
\sigma(\nu_\mu + p \rightarrow \mu^- + p + \pi^+) &= 0.64 \times 10^{-38} \text{ cm}^2 , \\
\sigma(\nu_\mu + n \rightarrow \mu^- + p + \pi^0) &= 0.31 \times 10^{-38} \text{ cm}^2 , \\
\sigma(\overline{\nu}_\mu + n \rightarrow \mu^+ + n + \pi^-) &= 0.62 \times 10^{-38} \text{ cm}^2 ,
\end{aligned}$$

$$\sigma(\overline{\nu}_\mu + p \rightarrow \mu^+ + p + \pi^-) \;=\; 0.38 \times 10^{-38}\ \mathrm{cm}^2\ .$$

Processes $\nu_\mu + p \rightarrow \mu^- + p + \pi^+$ and $\overline{\nu}_\mu + n \rightarrow \mu^+ + n + \pi^-$ are dominated by the production of $\Delta(1232)$ resonances whereas, in addition to the Δ resonances, the other processes also include nucleon resonance production (e.g. $N(1440)$, $N(1520)$ and $N(1535)$). Most of the above cross sections have been measured and agree with the predictions of the model (see Refs. [64, 65, 66]).

Events were generated using the Soudan 2 Collaboration generator [67] embedded inside the Monte Carlo simulation described in Sec. 4.2. As a result, the fraction of events passing all selection criteria is found to vary between 4.3% and 9.3% depending on the channel. The expected number of events is 2.7 $\mu^- n\pi^+ + 3.2\ \mu^+ n\pi^-$ $+ 0.1\ \mu^- p\pi^0$ events simulating $\mu^\pm \pi^\mp$ events without stubs; and 5.9 $\mu^- p\pi^+ + 0.9$ $\mu^+ p\pi^-$ events simulating $\mu^\pm \pi^\mp$ events with stubs ($p_{\mathrm{stub}} < 800$ MeV/c).

(c) Single Nucleon Diffractive Production

There is little data and no good model on the production of single pions in (anti)neutrino-nucleon diffractive interactions. The only experimental results come from an (anti)neutrino-hydrogen bubble chamber experiment [65] which studied single pion production for hadronic masses W below and above 2 GeV. From that experiment, the measured cross sections for $W > 2$ GeV and $E > 30$ GeV are (see Fig. 8 from Ref. [65])

$$\sigma(\nu_\mu + p \rightarrow \mu^- + p + \pi^+) \;=\; (0.13 \pm 0.04) \times 10^{-38}\ \mathrm{cm}^2\ , \qquad (5.3)$$

$$\sigma(\overline{\nu}_\mu + p \rightarrow \mu^+ + p + \pi^-) \;=\; (0.20 \pm 0.04) \times 10^{-38}\ \mathrm{cm}^2\ . \qquad (5.4)$$

In a separate analysis of the data, Rein [68] attempted to interpret those events as due to the diffractive production of pions off protons. However, the experimental $|t|$ distributions are considerably flatter than expected for pure diffractive production and indicate that a large fraction of the single pion events observed at $W > 2$ GeV is still due to the production of pion-nucleon resonances. Indeed, the slopes of the t

distributions are found to be $b \simeq 2.5$ GeV^{-2} for $2 < W < \sqrt{8}$ GeV and $b \simeq 4$ GeV^{-2} for $W \geq \sqrt{8}$, while a slope of ~ 7 GeV^{-2} is expected for diffractive production.

Since no good model exists, no simulation of the above processes was performed. Therefore, we have used the numbers published in Ref. [65] to estimate approximately the number of events that would be expected in our experiment. From the experimental $|t|$ distributions in Ref. [65], it is observed that ~ 20 % of the data lies at $|t| < 0.1$ GeV^2. Given the measured cross sections (5.3) and (5.4), this implies that 4.9 $\mu^- p\pi^+$ and 4.0 $\mu^+ p\pi^-$ events would be produced in the present experiment with $W > 2$ GeV and $|t| < 0.1$ GeV^2. Similar numbers would be expected for final states involving neutrons rather than protons. Accounting for the scanning and muon identification efficiencies as well as for the $\frac{\Delta p}{p}$ cut (see Table 5.2) yields 3.0 $\mu^- p\pi^+$ and 2.5 $\mu^+ p\pi^-$ events. These numbers are overestimates because no p_μ or p_{stub} cut is applied and the experimental smearing conditions specific to this experiment are not taken into account. Additional effects like Fermi motion and nuclear reinteractions would reduce those numbers even further.

(d) Total Incoherent Background

In summary, the above results indicate that the incoherent background at $|t| < 0.1$ GeV^2 is small. An upper limit on the number of incoherent $\mu\pi$ events without (with) stubs satisfying all selection criteria is determined to be 8.2 (6.8) in the case of quasi-elastic and resonance production with $W < 2$ GeV. In the case of resonance production at $W > 2$ GeV and diffractive production on single nucleons, only a crude upper limit of 5.5 events with stubs was obtained. Extending those results to the case where neutrons are produced in the final state gives 5.5 $\mu\pi$ events without stubs.

These numbers are to be compared with the background estimated from the number of events with stubs at $|t| < 0.1$ GeV^2, i.e. 7 $\mu\pi$ events. After normalization to the $|t|$ distribution for events without stubs, the background to the $\mu\pi$ events

without stubs was estimated to be 10.9 ± 5.1. Therefore, we conclude that the background estimate extracted from the experimental $|t|$ distributions is consistent with the upper limits derived in this section.

5.4.2 Coherent Background

Coherent production of ρ and a_1 mesons can be a source of background to the single π coherent production channel. In the case of ρ production, the final state is $\mu^{\pm}\pi^{\mp}$ if the two photons coming from the $\rho^{\pm} \rightarrow \pi^{\pm}\pi^0$ and $\pi^0 \rightarrow \gamma\gamma$ decay chain are lost. Using the ρ production Monte Carlo, the γ detection efficiency (see Sec. 6.3.5) and the scanning efficiency, the uncorrected number of background events passing all selection criteria (including $|t| < 0.1$ GeV^2) is found to be 0.4 and 0.6 for the $R = 0$ and $R = 0.4\ Q^2/m_\rho^2$ parametrizations of the ratio between longitudinal and transverse ρ cross sections, respectively. This is to be compared with the observed signal of 52.1 ± 9.4 $\mu\pi$ events.

In the case of coherent a_1 production, a $\mu^{\pm}\pi^{\mp}$ final state may be obtained if the a_1 meson decays as $a_1^{\pm} \rightarrow \rho^{\pm}\pi^0$ (B.R. 50%) followed by the decay $\rho^{\pm} \rightarrow \pi^{\pm}\pi^0$ and if all four γ from the π^0 decays are lost. However, based on the estimated γ detection efficiency, the probability to lose all four γ is only 0.3%. Moreover, the cross section for coherent a_1 production [69] is not anticipated to be much larger than the cross section for coherent ρ production. Therefore, the background from coherent a_1 production is expected to be significantly smaller than that from coherent ρ production which is, as demonstrated above, negligible.

5.5 Cross Section Results

5.5.1 The Integrated Cross Section

As seen in Sec. 5.1, the observed signal at $|t| < 0.1$ GeV^2 is determined to be 52.1 ± 9.4 $\mu^{\pm}\pi^{\mp}$ events. After correcting for all identified losses (Sec. 5.2), the

Table 5.6: Single pion signal and cross section. The error on the corrected signal includes the systematic error introduced by the choice of $|t|$ cut.

	ν	$\overline{\nu}$	All
Events w/o stubs	134	34	168
Events with stubs	59	19	78
Events w/o stubs $\|t\| < 0.1$ GeV^2	46	17	63
Events with stubs $\|t\| < 0.1$ GeV^2	4	3	7
Signal $\|t\| < 0.1$ GeV^2 (observed)	39.4 ± 8.8	13.3 ± 5.4	52.1 ± 9.4
Signal (corrected)	66.0 ± 16.5	21.8 ± 9.1	86.6 ± 19.6
N_{CC}	23761 ± 612	4002 ± 313	27763 ± 689
N_{COH}/N_{CC} ($\times 10^{-2}$)	0.28 ± 0.07	0.54 ± 0.23	0.31 ± 0.07
σ_{COH} ($\times 10^{-40}$ cm^2)	337 ± 85	263 ± 112	313 ± 72

number of single pion coherent events is found to be 86.6 ± 19.6. Here, the error also includes the systematic error corresponding to the dependence on the particular choice of the $|t|$ cut. Table 5.6[1] summarizes our results for ν_μ and $\overline{\nu}_\mu$ interactions separately, as well as for $\nu_\mu + \overline{\nu}_\mu$ interactions combined.

The rate of coherent $\mu\pi$ interactions with respect to the total number of charged current events is determined to be $(0.28 \pm 0.07)\%$ for ν_μ interactions, $(0.54 \pm 0.23)\%$ for $\overline{\nu}_\mu$ interactions and $(0.31 \pm 0.07)\%$ for $\nu_\mu + \overline{\nu}_\mu$ interactions combined. A higher rate of coherent pion production in $\overline{\nu}_\mu$ interactions is expected because the total cross section for antineutrino charged current interactions is smaller ($\sim \frac{1}{2}$) than that for neutrino charged current interactions whereas the cross section for coherent processes is the same for neutrinos and antineutrinos.

The coherent single pion cross section per neon nucleus is then computed by

[1]Note that the signal for ν and $\overline{\nu}$ interactions has been extracted independently from the signal for the $\nu + \overline{\nu}$ interactions combined (column labelled "All") which explains why the sum of the ν and $\overline{\nu}$ signals is slightly different from the signal obtained by considering all charged current interactions.

using the above rates and the measured charged current cross sections

$$\sigma_{COH} = \frac{N_{COH}}{N_{CC}} 20\ \sigma_{CC} ,$$

where the total charged current cross sections per nucleon are given by [70]

$$\sigma^{\nu}_{CC} = < E_{\nu} > (0.666 \pm 0.020) \times 10^{-38}\text{cm}^2\ \text{GeV}^{-1} ,$$
$$\sigma^{\overline{\nu}}_{CC} = < E_{\overline{\nu}} > (0.324 \pm 0.014) \times 10^{-38}\text{cm}^2\ \text{GeV}^{-1} .$$

The average ν_μ and $\overline{\nu}_\mu$ beam energies determined from the calculated fluxes [31] are $< E_\nu > = 91.1$ GeV and $< E_{\overline{\nu}} > = 74.5$ GeV. The combined $\nu_\mu + \overline{\nu}_\mu$ cross section is obtained by taking the relative fluxes into account which gives an overall average beam energy of 86.3 GeV. Finally, the single pion cross sections for reactions (5.1) are found to be

$$\sigma_{COH}(\nu_\mu + Ne \rightarrow \mu^- + \pi^+ + Ne)$$
$$= (337 \pm 85) \times 10^{-40}\ \text{cm}^2/\ \text{neon nucleus}, \quad (5.5)$$
$$\sigma_{COH}(\overline{\nu}_\mu + Ne \rightarrow \mu^+ + \pi^- + Ne)$$
$$= (263 \pm 112) \times 10^{-40}\ \text{cm}^2/\ \text{neon nucleus}, \quad (5.6)$$

$$\sigma_{COH}(\nu_\mu(\overline{\nu}_\mu) + Ne \rightarrow \mu^-(\mu^+) + \pi^+(\pi^-) + Ne)$$
$$= (313 \pm 72) \times 10^{-40}\ \text{cm}^2/\ \text{neon nucleus}. \quad (5.7)$$

As expected, the neutrino and antineutrino cross sections are similar, with the antineutrino cross section being slightly smaller due to the lower average $\overline{\nu}_\mu$ beam energy.

Table 5.7 summarizes the experimental situation concerning the coherent production of single pions in (anti)neutrino charged current and neutral current interactions. Our new result, Eq. (5.7), is consistent with our previously published value of $(315 \pm 120) \times 10^{-40}$ cm^2 / neon nucleus obtained with a smaller sample including only data from the 1985 run and for energies greater than 40 GeV [71]. Our cross

section is higher than that obtained in other heavy liquid bubble chamber experiments, an increase which is consistent with the expected increase in the cross section at higher energy (see Sec. 5.5.2). All previous experiments were performed at lower energies, with average (anti)neutrino beam energies of $\sim$ 30 GeV for WA59 [72, 73] and E180 [74], and $\sim$ 7 GeV for SKAT [75].

Table 5.7 also presents the results on single π^0 coherent production in neutral current interactions which have been published by two counter experiments, Aachen-Padova [5] and CHARM [77], and two bubble chamber experiments, one using Gargamelle [76] and the other using the 15-foot Bubble Chamber [78].

5.5.2 The Energy Dependence

Our sample size allows us to divide the data into only two energy intervals : $10 < E < 80$ GeV and $E \geq 80$ GeV. Furthermore, only the energy dependence of the combined $\nu_\mu + \overline{\nu}_\mu$ sample is studied. The uncorrected number of coherent $\mu^\pm \pi^\mp$ events is 24.2 ± 7.8 for $10 < E < 80$ GeV and 27.9 ± 6.3 for $E \geq 80$ GeV. Following the same procedure as used to obtain the integrated result, the corrected number of single pion coherent interactions was found to be 38.7 ± 15.2 for $10 < E < 80$ GeV and 48.9 ± 15.2 for $E \geq 80$ GeV, whereas the rates with respect to the number of charged current interactions are $(0.38 \pm 0.15)\%$ and $(0.27 \pm 0.09)\%$ respectively. As anticipated, the rate for $E \geq 80$ GeV is smaller because $\sigma_{COH} \propto lnE$ at high energies [10]. The resulting cross sections are estimated to be $(211 \pm 84) \times 10^{-40}$ cm^2 / neon nucleus for $10 < E < 80$ GeV and $(467 \pm 147) \times 10^{-40}$ cm^2 / neon nucleus for $E \geq 80$ GeV.

The cross section as a function of energy is presented in Fig. 5.3 along with the predictions based on the Rein-Sehgal (R-S) and Belkov-Kopeliovich (B-K) models (see Secs. 2.4.2, 2.4.4 and 4.2.1). Several parametrizations of the pion-nucleus cross section are tested : the pole nucleon form factor with axial masses $m_a = m_{a_1} = 1.260$ GeV and $m_a = 1.050$ GeV, and the $\rho\pi$ cut form. The cross sections obtained for

Table 5.7 : Summary of experimental results on single pion coherent cross sections in (anti)neutrino charged and neutral current interactions.

Experiment	Reaction	$< E_\nu >$ (GeV)	A	Signal observed	Cross section (10^{-40} cm$^2/\mathcal{N}$)	N_{COH}/N_{CC}
This exp.	$\nu_\mu(\overline{\nu}_\mu)\, Ne \rightarrow \mu^-(\mu^+)\,\pi^+(\pi^-)\, Ne$	86	20	52 ± 9	313 ± 72	$(0.31 \pm 0.07)\%$
This exp. '85 [71]	$\nu_\mu(\overline{\nu}_\mu)\, Ne \rightarrow \mu^-(\mu^+)\,\pi^+(\pi^-)\, Ne$	95	20	20 ± 6	315 ± 120	$(0.26 \pm 0.10)\%$
WA59 [72]	$\overline{\nu}_\mu\ Ne \rightarrow \mu^+\,\pi^-\, Ne$	27	20	155 ± 20	175 ± 25	$(0.9 \pm 0.1)\%$
WA59 [73]	$\nu_\mu\ Ne \rightarrow \mu^-\,\pi^+\, Ne$	32	20	41 ± 8	250 ± 49	
E180 [74]	$\overline{\nu}_\mu\ Ne \rightarrow \mu^+\,\pi^-\, Ne$	30	20	61 ± 12		$(0.76 \pm 0.15)\%$
SKAT [75]	$\nu_\mu\ CF_3Br \rightarrow \mu^-\,\pi^+\, CF_3Br$	7	30	59 ± 8	106 ± 16	$(0.69 \pm 0.09)\%$
	$\overline{\nu}_\mu\ CF_3Br \rightarrow \mu^+\,\pi^-\, CF_3Br$	7	30	12 ± 4	113 ± 35	$(1.8 \pm 0.5)\%$
Aachen–	$\nu_\mu\ Al \rightarrow \nu_\mu\,\pi^0\, Al$	2	27	287 ± 100	29 ± 10	
Padova [5]	$\overline{\nu}_\mu\ Al \rightarrow \overline{\nu}_\mu\,\pi^0\, Al$	2	27	73 ± 20	25 ± 7	
Gargamelle [76]	$\nu_\mu\ CF_3Br \rightarrow \nu_\mu\,\pi^0\, CF_3Br$	2	30	39 ± 25	31 ± 20	
	$\overline{\nu}_\mu\ CF_3Br \rightarrow \overline{\nu}_\mu\,\pi^0\, CF_3Br$	2	30	62 ± 33	45 ± 22	
CHARM [77]	$\nu_\mu\ CaCO_3 \rightarrow \nu_\mu\,\pi^0\, CaCO_3$	31	20	$233 \pm 53 \pm 72$	96 ± 42	
	$\overline{\nu}_\mu\ CaCO_3 \rightarrow \overline{\nu}_\mu\,\pi^0\, CaCO_3$	24	20	$482 \pm 83 \pm 99$	79 ± 26	
15-foot [78]	$\nu_\mu\ Ne \rightarrow \nu_\mu\,\pi^0\, Ne$	20	20	32 ± 7		$(0.020 \pm 0.004)\%$

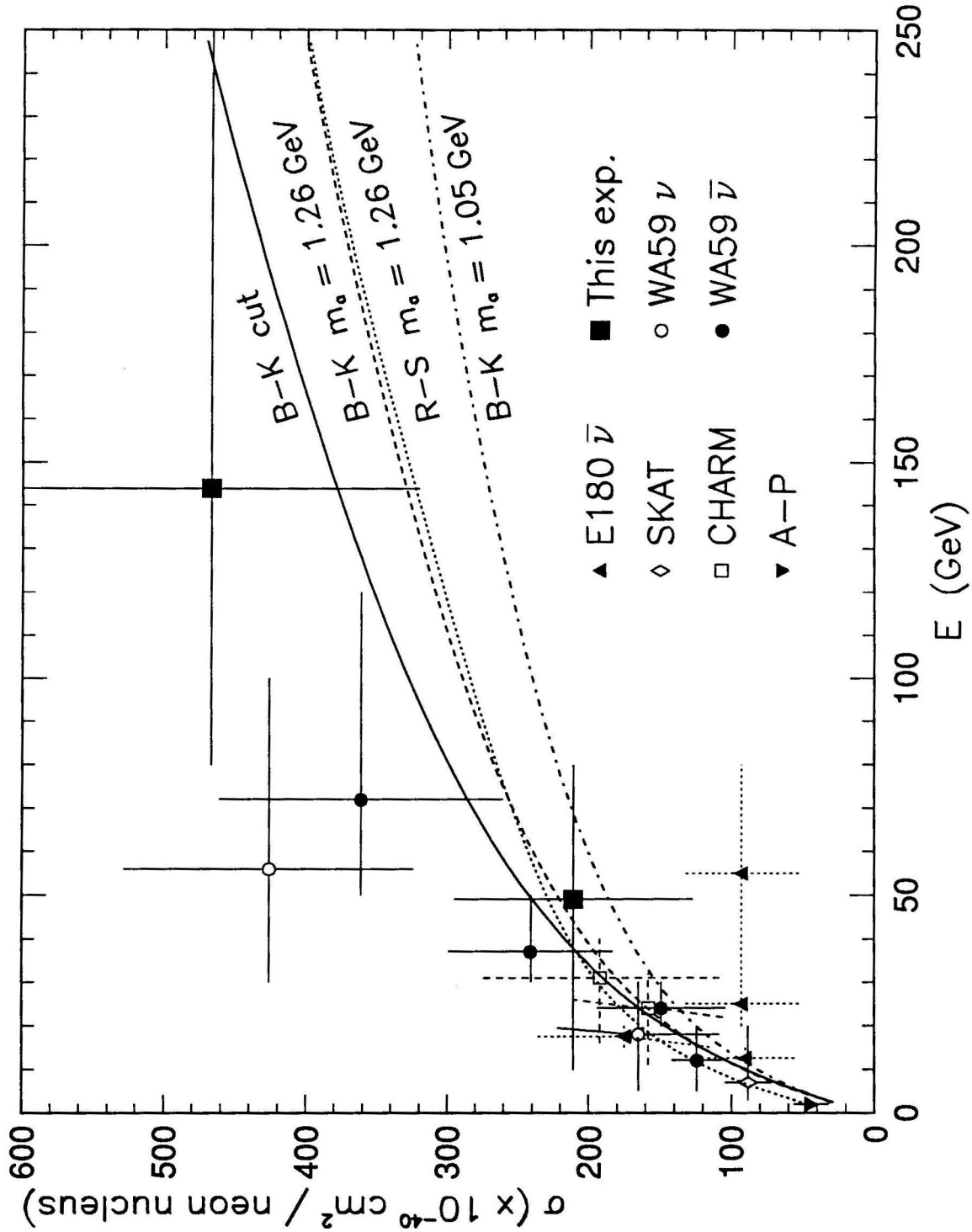

Figure 5.3: Single pion coherent cross section as a function of energy. The curves represent the predictions of the Rein-Sehgal and Belkov-Kopeliovich models (Sec. 4.2.1). The results from other experiments have been scaled to correspond to charged current interactions on neon nuclei, where necessary. Note that the horizontal error bar represents the range of energy used, except for the CHARM data where it represents the range of energy containing 68% of the events.

targets with atomic mass number A different from that of neon ($A = 20$) and/or for neutral current interactions have been scaled to correspond to charged current interactions on neon nuclei. This assumed that the charged pion coherent cross section is twice that for neutral pion production as predicted by the electroweak theory. Except for the E180 data, the agreement between the data and the various predictions is good at energies below 50 GeV. All the theoretical curves are below the data points at higher energies but our measured cross section at $E \geq 80$ GeV is not inconsistent with the predictions. The curve corresponding to an axial mass $m_a = 1.050$ GeV appears to be the least favored prediction. (This value of m_a is suggested by measurements of the nucleon form factor in (anti)neutrino quasielastic interactions.)

The uncertainty in the predicted cross sections is estimated to be $\sim 10 - 15$ %. This estimate includes the uncertainty in the total pion-nucleon cross section and, in the case of the R-S model, the uncertainty in the absorption factor F_{abs} and the slope parameter b, while in the case of the B-K model, it also includes the uncertainty in the slope parameter B_T and the total pion-nucleus cross section due to the effect of inelastic screening.

It should be pointed out that there is an inconsistency in the predicted cross section published by Belkov and Kopeliovich [10] : the cross section in Fig. 3 of their paper is about a factor of two lower than that given in their Fig. 4. Moreover, our computation of the cross section agrees with Fig. 4 of their paper. This point is important because the wrong cross section prediction was used in the E180 analysis [74].

5.6 Kinematical Characteristics

In this section, the distributions of the kinematical variables are compared with the predictions of the Rein-Sehgal and Belkov-Kopeliovich models. The events with

stubs have been subtracted from the distributions by assigning them a negative weight equal to the normalization factor between the $|t|$ distributions for events with and without stubs. Figs. 5.4–5.12 show the distributions of the total energy E, the energy transfer ν, the square of the W boson four-momentum Q^2, the invariant mass of the hadronic system W, the Bjorken x and y variables, the square of the momentum transfer to the nucleus $|t|$, the minimum value of $|t|$ needed to produce the final state pion t_{min} and the variable t'. See Appendix C for definitions of all the variables. Also shown in the figures are the Monte Carlo predictions of the Rein-Sehgal model with $m_a = 1.260$ GeV and the Belkov-Kopeliovich model with the $\rho\pi$ cut nucleon form factor. The model predictions have been normalized to 52.1 $\mu\pi$ events since we are mostly interested in the shape rather than the overall normalization of those distributions. The predictions of the B-K model with $m_a = 1.260$ GeV are not shown since they are not strikingly different from those obtained using the $\rho\pi$ cut form factor.

The overall agreement between the data and the models is good. As expected on the basis of the hadron dominance model, the data are concentrated at small values of Q^2 and x, although the models predict a significantly larger contribution at $Q^2 < 0.1$ GeV^2 than observed in the data (see Fig. 5.6). Both models seem to reproduce the E, ν, x and y distributions reasonably well. In the W distribution (Fig. 5.7), it is observed that most of the background events are in the interval $1 < W < 2$ GeV, where resonance production is important. The Rein-Sehgal prediction is large in that same interval because the total pion-nucleon cross section is larger while the absorption factor was chosen to be constant. The corresponding B-K prediction reproduces the W dependence well.

The $|t|$ distribution (Fig. 5.10) is somewhat flatter than predicted. Also, the predicted t' distribution (Fig. 5.12) appears to be steeper than the data. The slope s of the t' distribution was computed using the maximum likelihood method in the

t' interval of 0 to $t'_{max} = 0.1$ GeV$^2 - t_{min}$. The slope was determined to be

$$s = 32 \pm 6 \text{ GeV}^{-2} , \tag{5.8}$$

which is consistent with the interpretation of our $\mu\pi$ sample at $|t| < 0.1$ GeV^2 as due to the coherent production of pions off neon nuclei. A slope of ~ 7 GeV^{-2} would be expected if those events were due to diffractive pion production on single nucleons. The slope (5.8) is lower than the theoretical value of ~ 80 GeV^{-2} due to the experimental smearing of the coherent peak.

Table 5.8 presents the average values of the kinematical variables extracted from the data sample and compares them with the predictions of the various models. The average values of ν, Q^2, W, x and y appear to be higher than predicted but tend to be consistent with the Belkov-Kopeliovich model with a $\rho\pi$ cut form factor.

Kinematical characteristics have been studied in detail by the WA59 Collaboration [72, 73]. In these studies of coherent pion production in ν_μ and $\overline{\nu}_\mu$ charged current interactions, the predictions of the Rein-Sehgal model were found to be in excellent agreement with the data. Our data extend the range of energies over which the predictions based on the PCAC hypothesis and the hadron dominance model are successfully tested.

Table 5.8 : Average values of kinematical variables for single pion coherent events at $|t| < 0.1$ GeV^2. The predictions of the Monte Carlo simulation are given for the Rein – Sehgal (R – S) and Belkov – Kopeliovich (B – K) models (Sec. 4.2.1) with different parametrizations of the pion – nucleus differential cross section.

	Data	R-S pole $m_a = 1.26$ GeV	B-K pole $m_a = 1.26$ GeV	B-K pole $m_a = 1.05$ GeV	B-K cut
$< E >$ (GeV)	92.8 ± 7.7	88.4	91.5	91.3	93.4
$< p_\mu >$ (GeV/c)	77.6 ± 6.9	77.5	78.3	79.3	78.6
$< \nu >$ (GeV)	15.3 ± 2.2	10.8	13.1	12.0	14.6
$< Q^2 >$ (GeV^2)	1.15 ± 0.20	0.60	0.70	0.58	0.90
$< W >$ (GeV)	4.57 ± 0.38	3.74	4.21	4.01	4.44
$< x >$	0.070 ± 0.016	0.056	0.050	0.048	0.051
$< y >$	0.175 ± 0.021	0.131	0.155	0.142	0.168
$< \|t\| >$ (GeV^2)	0.037 ± 0.004	0.026	0.025	0.025	0.026
$< t_{min} >$ (GeV^2)	0.011 ± 0.004	0.007	0.005	0.005	0.005
$< t' >$ (GeV^2)	0.026 ± 0.004	0.020	0.020	0.020	0.021
t' slope (GeV^{-2})	32 ± 6	42	44	44	43

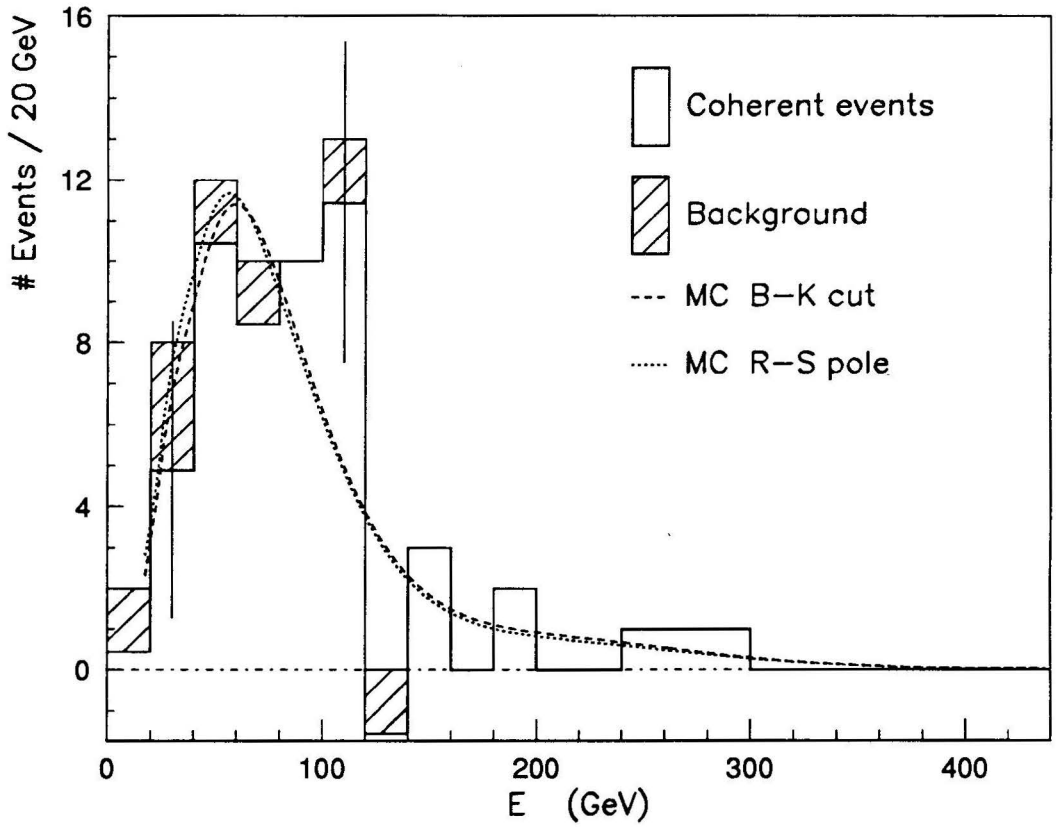

Figure 5.4: Distribution of the total $\mu^{\pm}\pi^{\mp}$ event energy E for $|t| < 0.1$ GeV^2. The distribution corresponds to that for events without stubs from which the normalized distribution for events with stubs (shown cross-hatched) is subtracted. The curves represent the Monte Carlo simulation, normalized to the signal, for the Belkov-Kopeliovich model with a $\rho\pi$ cut and for the Rein-Sehgal model with an a_1 pole (see Sec. 4.2.1).

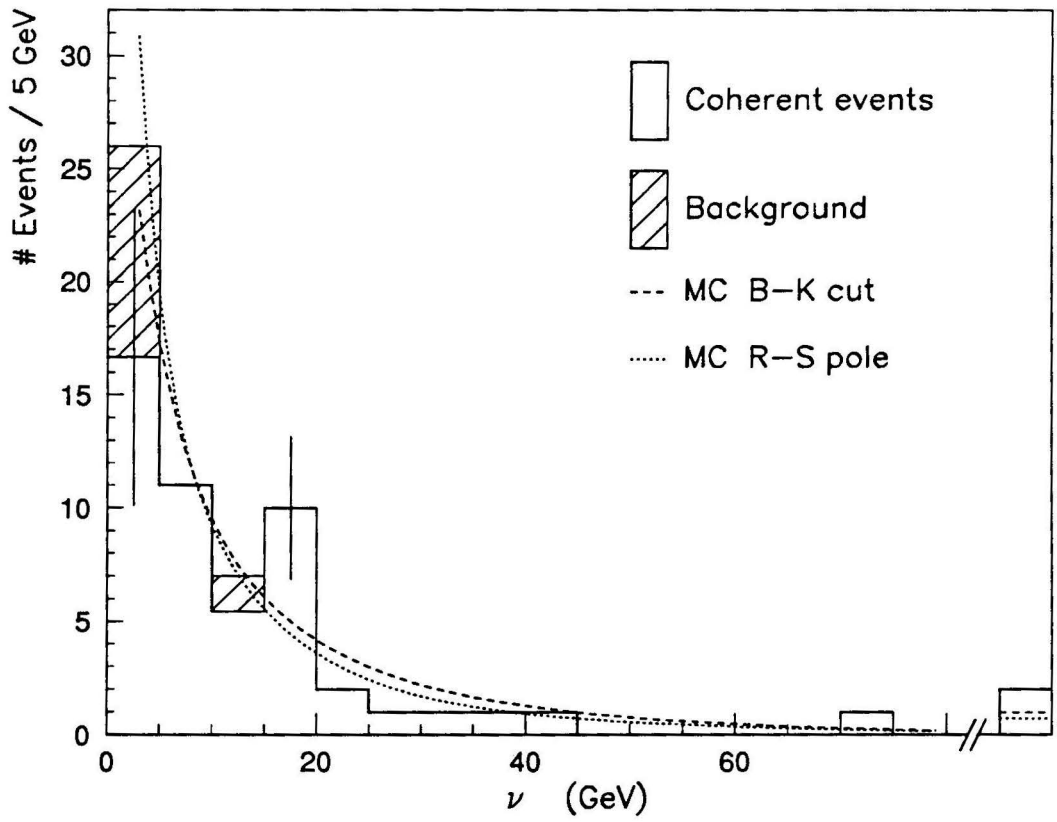

Figure 5.5: Distribution of the energy transfer ν for $|t| < 0.1$ GeV^2 (the curves are as in Fig. 5.4; overflow for $\nu > 80$ GeV is indicated).

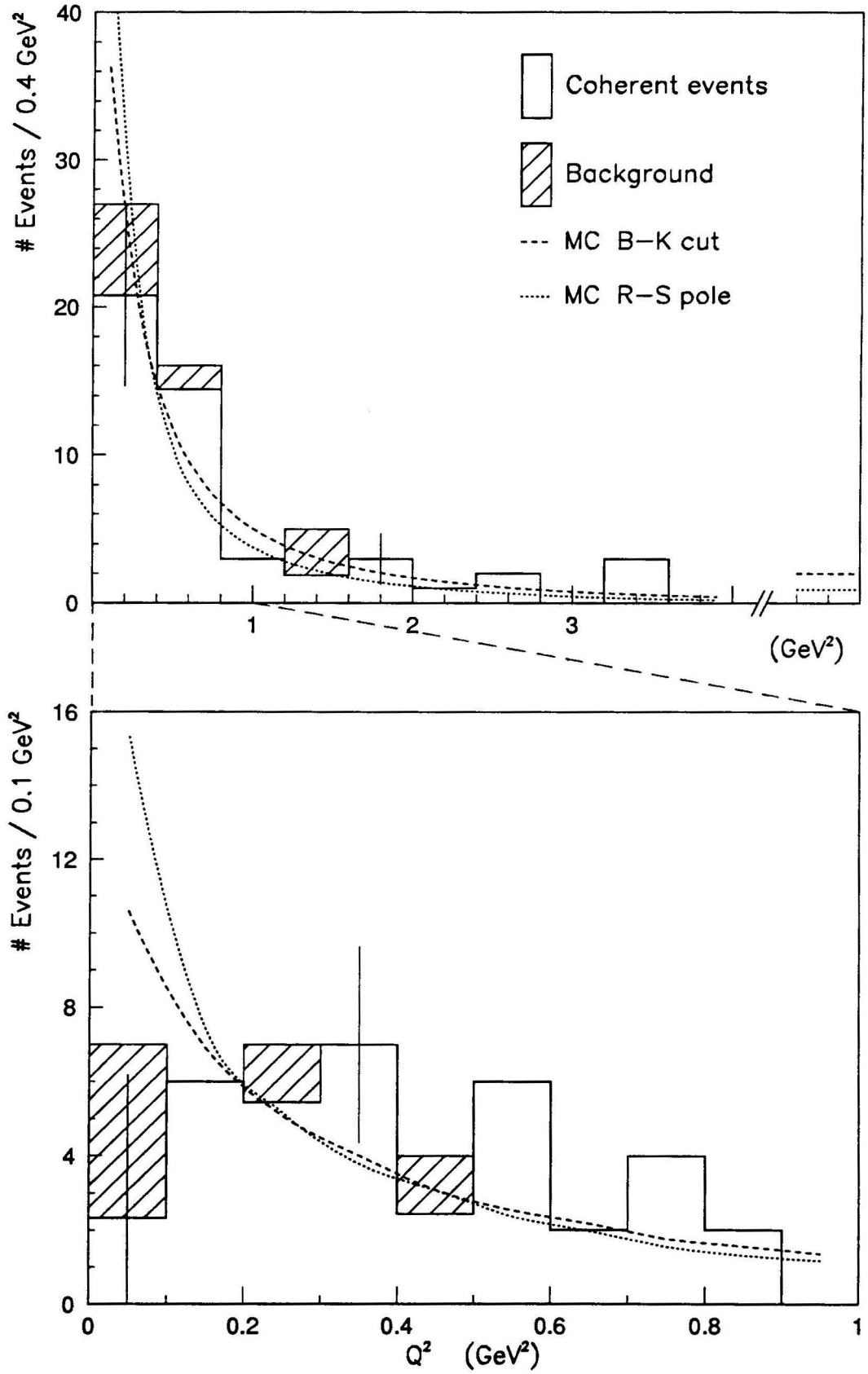

Figure 5.6: Distribution of the four-momentum transfer squared Q^2 for $|t| < 0.1$ GeV^2 (as in Fig. 5.4; overflow for $Q^2 > 4$ GeV^2 is indicated).

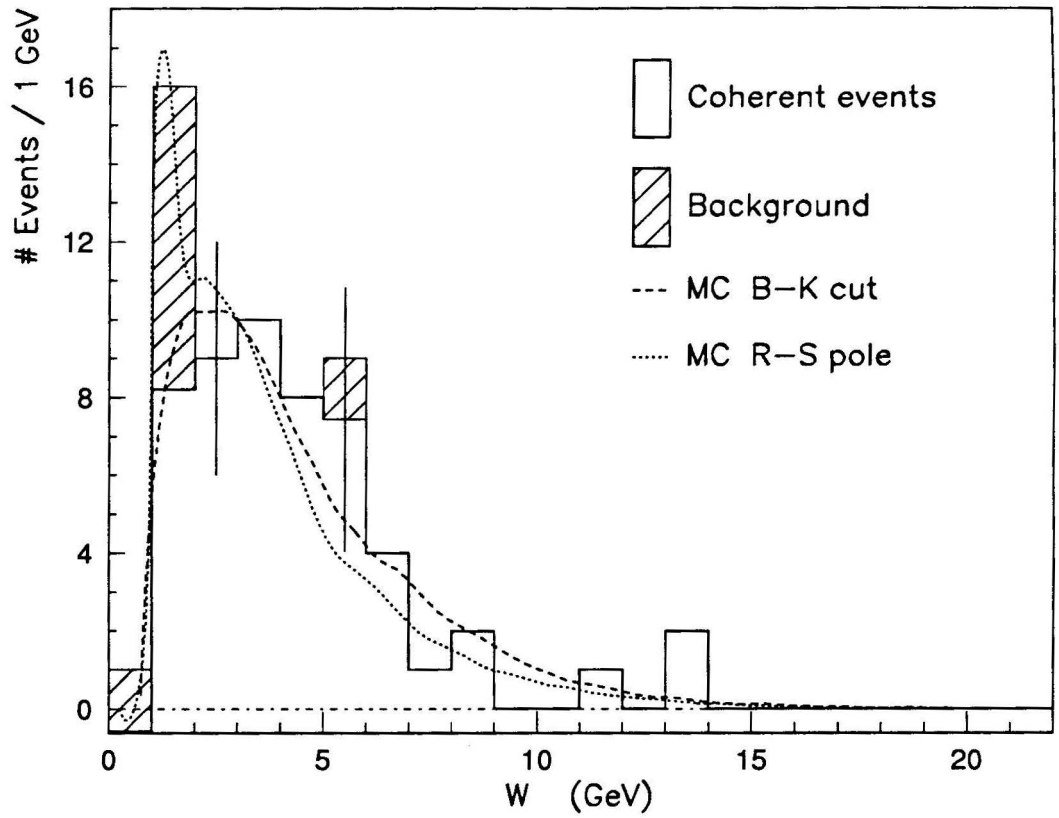

Figure 5.7: Distribution of the hadronic mass W for $|t| < 0.1$ GeV^2 (as in Fig. 5.4).

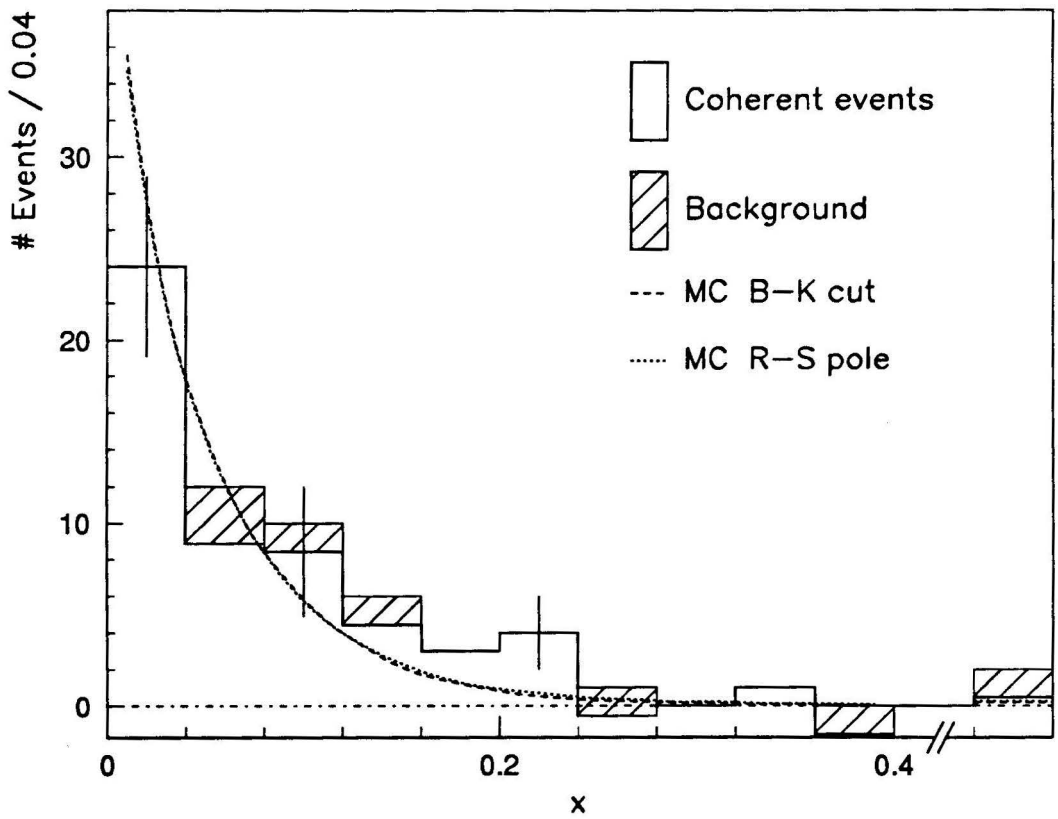

Figure 5.8: Distribution of the Bjorken x variable for $|t| < 0.1$ GeV^2 (as in Fig. 5.4; overflow for $x > 0.4$ is indicated).

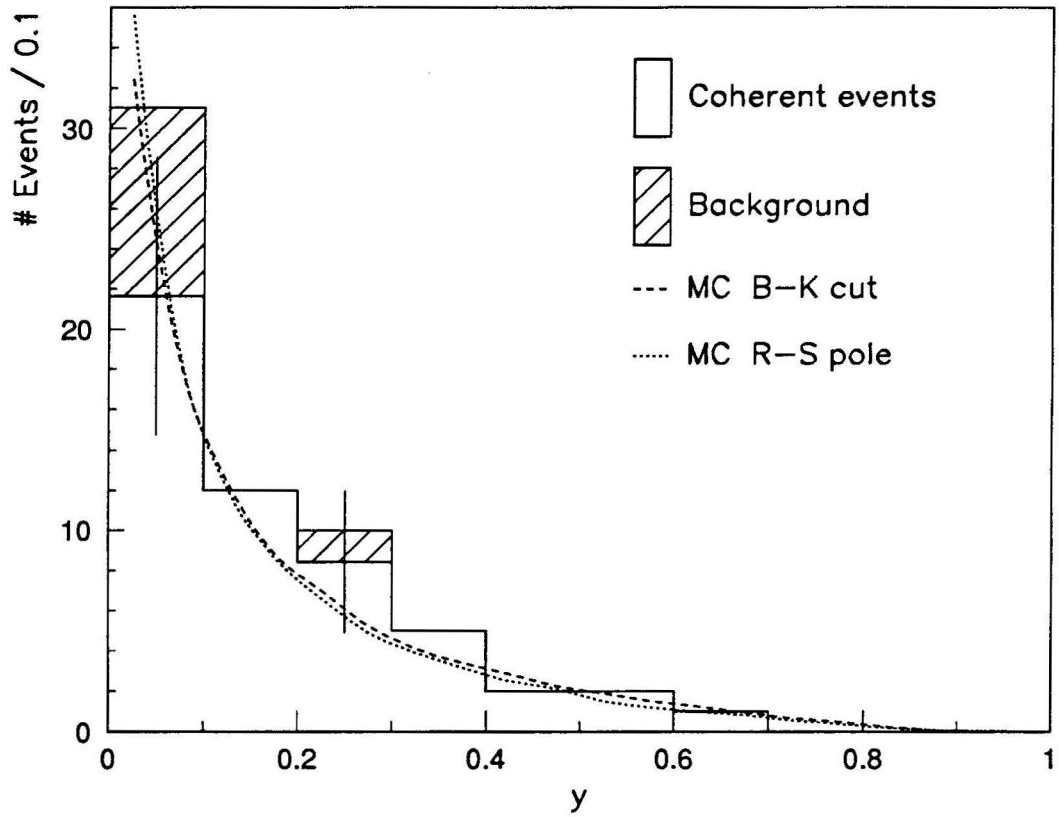

Figure 5.9: Distribution of the Bjorken y variable for $|t| < 0.1$ GeV^2 (as in Fig. 5.4).

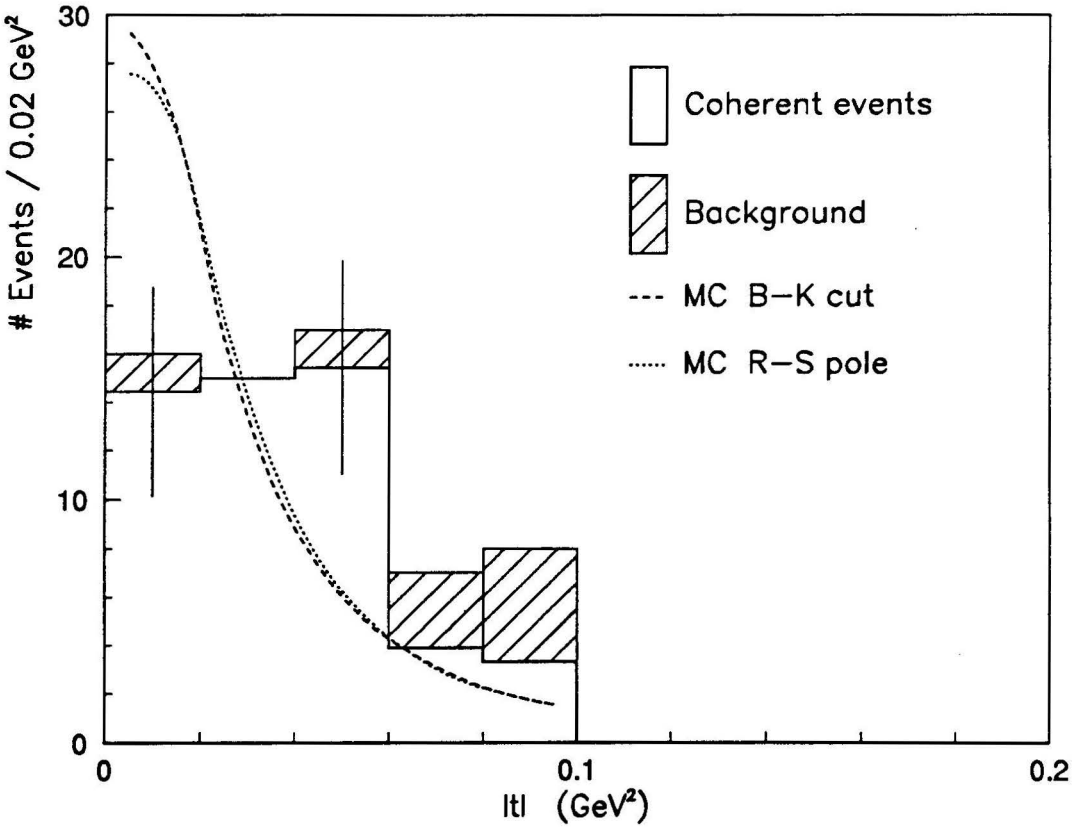

Figure 5.10: Distribution of the square of the momentum transfer to the nucleus $|t|$ for $|t| < 0.1$ GeV^2 (as in Fig. 5.4).

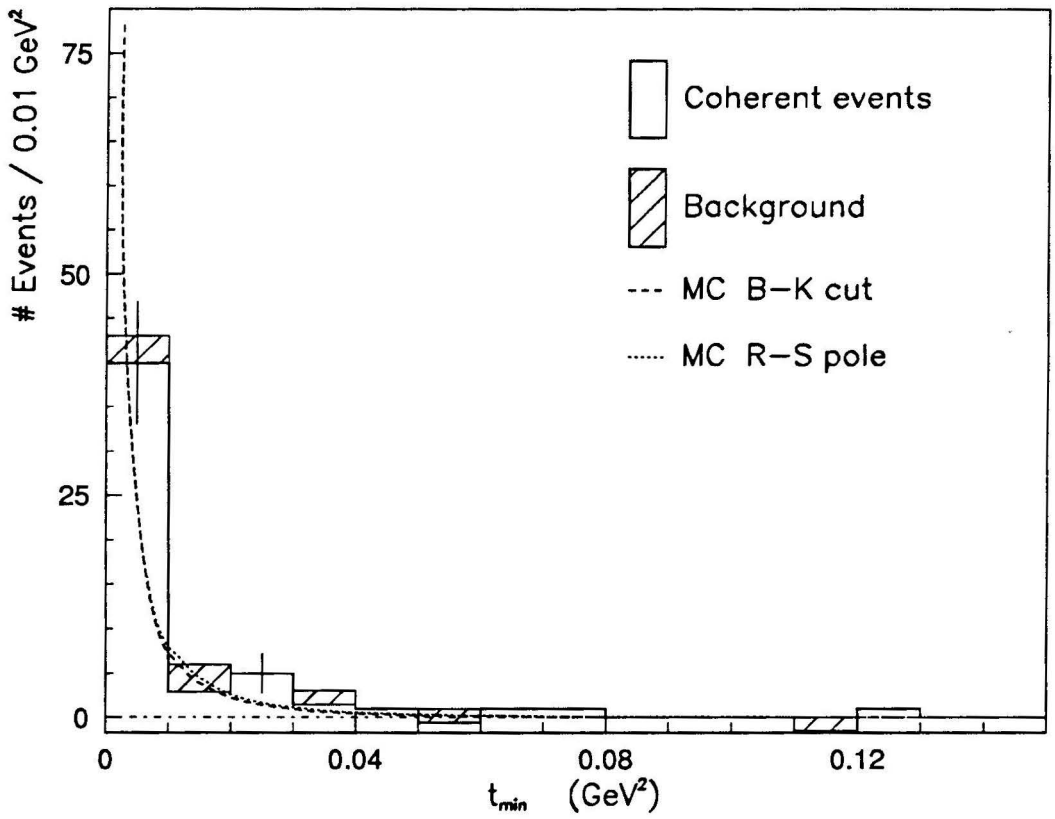

Figure 5.11: Distribution of the minimum momentum transfer t_{min} for $|t| < 0.1$ GeV² (as in Fig. 5.4).

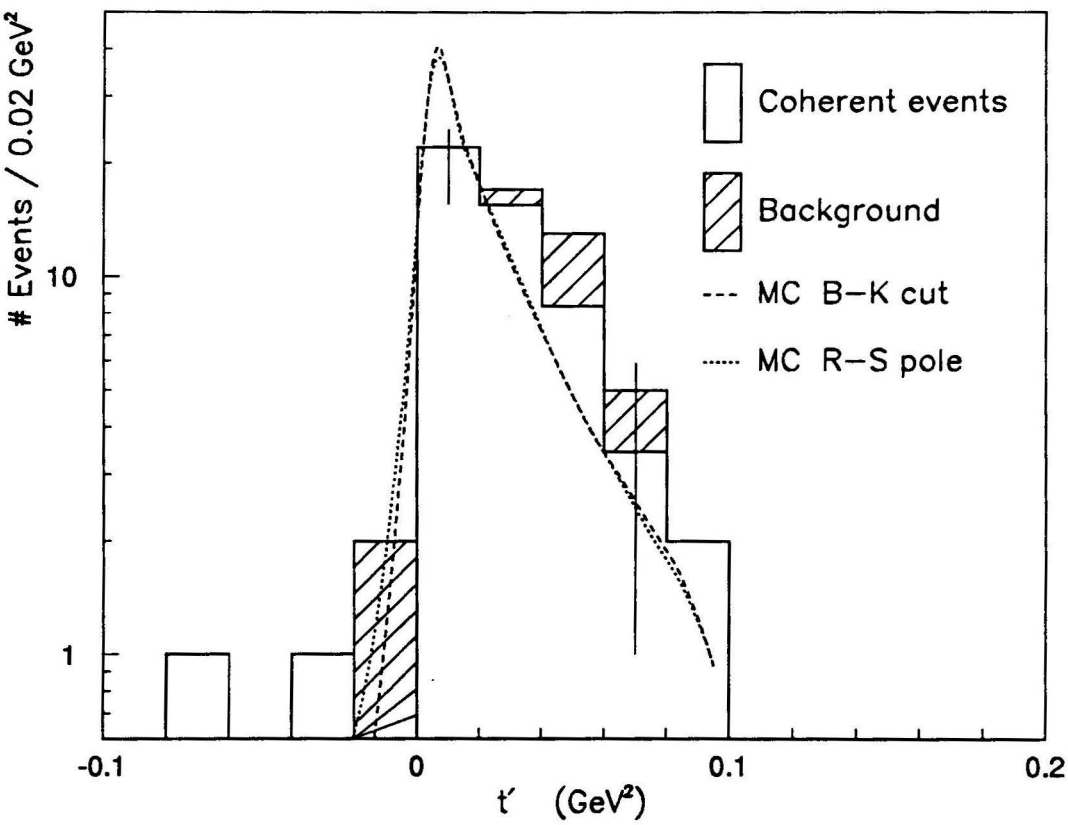

Figure 5.12: Distribution of the momentum transfer t' for $|t| < 0.1$ GeV² (as in Fig. 5.4).

Chapter 6

Single ρ Coherent Production

In Chapter 5, we studied the coherent production of single pions which constitutes the main contribution to the semi-inclusive 2-prong coherent signal extracted in Sec. 4.1.2. As will be shown in this chapter, another significant contribution to the semi-inclusive signal comes from the coherent production of single ρ mesons. Since the ρ mesons produced in charged current interactions decay into $\pi^{\pm}\pi^{0}$ pairs and the π^{0} subsequently decay into pairs of photons, we examine the problem of the evaluation of the γ detection efficiency in some detail. Other losses are taken into account in a manner similar to that described in Chapter 5.

In Section 6.1, the sample of coherent ρ event candidates is selected and the π^{0} reconstruction method is presented. In Section 6.2, the coherent signal is extracted from the $|t|$ distributions for events without and with stubs. In Section 6.3, we describe the correction factors introduced to account for the various losses, with an emphasis on the determination of the γ detection efficiency. In Section 6.4, the cross section results are presented and compared with previously published measurements. The energy dependence of the available results is then compared with the predictions of the hadron dominance model, using two different parametrizations of the ρ-nucleus cross section (Rein-Sehgal and Belkov-Kopeliovich) and two parametrizations of the ratio of longitudinal to transverse ρ production. Finally, we discuss the kinematical characteristics of the coherent ρ signal extracted at $|t| < 0.1$ GeV^2 in Section 6.5. These characteristics are also compared with the predictions of the model.

6.1 Selection of the Sample and π^0 Reconstruction

The focus of this chapter is the coherent production of single ρ mesons in charged current interactions of neutrinos and antineutrinos on neon nuclei (Fig. 6.1) :

$$\begin{aligned} \nu_\mu + Ne &\rightarrow \mu^- + \rho^+ + Ne\,, \\ \overline{\nu}_\mu + Ne &\rightarrow \mu^+ + \rho^- + Ne\,. \end{aligned} \tag{6.1}$$

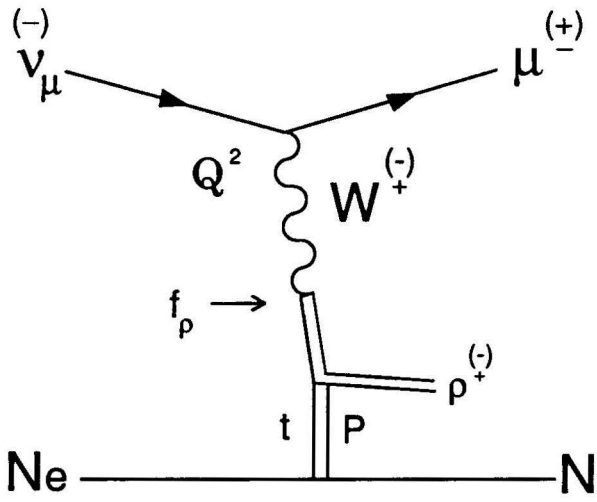

Figure 6.1: Diagram for the coherent production of single ρ mesons.

The ρ mesons are detected via their decay into a charged pion and a pair of photons:

$$\rho^\pm \rightarrow \pi^\pm \pi^0 \qquad \text{(B.R. } \sim 100\%)\,, \tag{6.2}$$

$$\pi^0 \rightarrow \gamma\gamma \qquad \text{(B.R. 98.8\%)}\,. \tag{6.3}$$

Thus, we select 2-prong events with total charge $Q_{ch} = 0$, with no associated V^0 fits and with 2 γ fits to the primary vertex. This leads to a sample of 177 $\mu^\pm \pi^\mp \gamma\gamma$ events. Events of the type $\mu^\pm \pi^\mp e^+ e^-$ or $\mu^\pm \pi^\mp e^+ e^- \gamma$ are not included in the sample. In order to reconstruct the π^0 meson, the $\gamma\gamma$ pair is constrained to fit the decay (6.3) by using a least squares method [79]. There is only one constraint in

the fit since the direction of the π^0 and the magnitude of its momentum before the decay are not measured (the one constraint is provided by fixing the π^0 mass).

The χ^2 function to be minimized is

$$\chi^2 = \frac{1}{2} \sum_{i=1}^{6} \sum_{j=1}^{6} (m_i - m_i^\circ)\, G_{ij}\, (m_j - m_j^\circ)$$

where m_i° and m_i are the measured and fitted quantities and G_{ij}^{-1} is the error matrix on the measured quantities. Moreover, there are a series of constraints on the measured and fitted quantities which are provided by the equations of four-momentum conservation,

$$\begin{aligned} E_{\pi^0} - E_{\gamma_1} - E_{\gamma_2} &= 0\,, \\ \vec{p}_{\pi^0} - \vec{p}_{\gamma_1} - \vec{p}_{\gamma_2} &= 0\,, \end{aligned} \tag{6.4}$$

where the four-momentum of both photons is measured directly and the three-momentum $\vec{p}_{\pi^0}$ is to be fitted. There are only three unknown quantities since $E_{\pi^0} = \sqrt{|\vec{p}_{\pi^0}|^2 + m_{\pi^0}^2}$.

The minimization process attempts to find the unknown quantities $\vec{p}_{\pi^0}$ by adjusting the measured momenta $\vec{p}_\gamma$ such as to minimize the χ^2 and satisfy the constraints, i.e. the following function is minimized

$$F = \chi^2 + \sum_{k=1}^{4} \alpha_k\, f_k(\vec{p}_{\pi^0}, \vec{p}_{\gamma_1}, \vec{p}_{\gamma_2})\,,$$

where the parameters α_k are the Lagrange parameters to be determined and the functions $f_k(\vec{p}_{\pi^0}, \vec{p}_{\gamma_1}, \vec{p}_{\gamma_2})$ are the four equations of constraint given by Eqs. (6.4).

The $\gamma\gamma$ invariant mass distribution for the 177 $\mu^\pm \pi^\mp \gamma\gamma$ events is shown in Fig. 6.2. A peak at the π^0 mass ($m_{\pi^0} = 0.135$ GeV) is observed. The background under the π^0 peak is small. It will be shown in Sec. 6.3.5 that the probability for an event with 2 π^0 to yield 2 observed γ compatible with coming from the same π^0 is only $(6.6 \pm 0.9)\%$, and the probability for an event with 3 π^0 to give 2 observed γ compatible with coming from the same π^0 is only $(0.6 \pm 0.1)\%$. The experimental resolution in the mass interval 0.08 to 0.19 GeV is determined to be ~ 0.026 GeV.

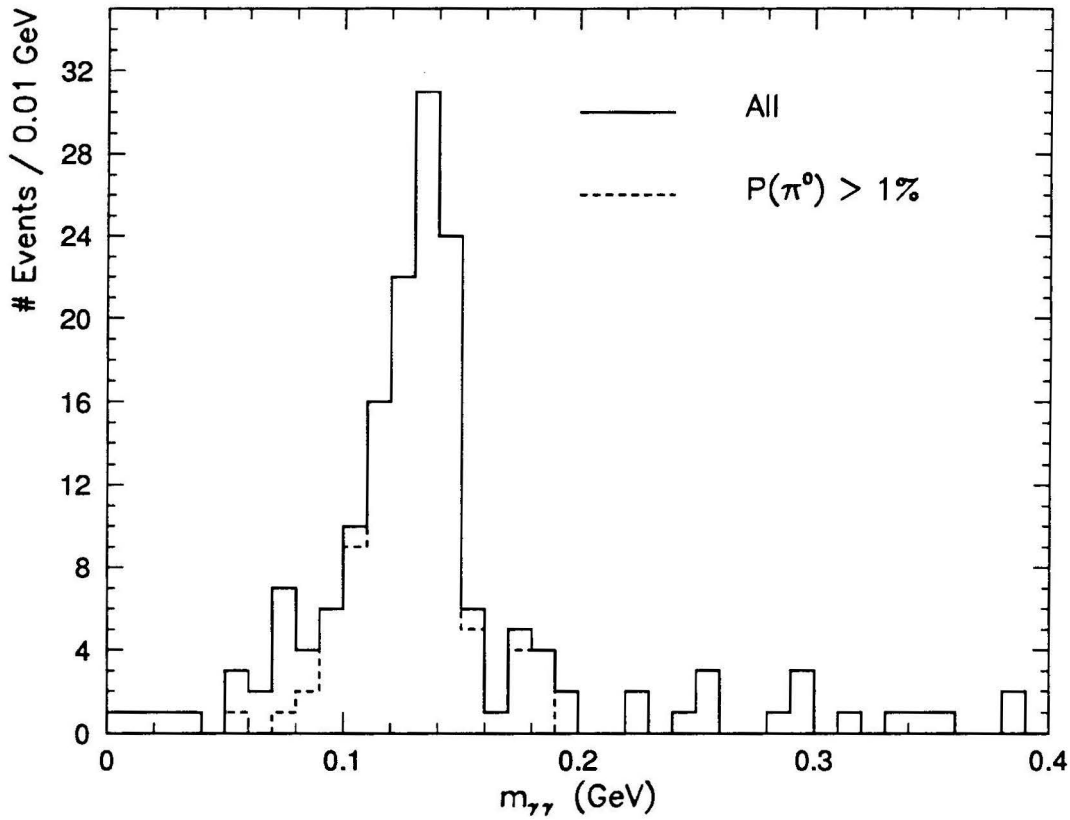

Figure 6.2: Invariant $\gamma\gamma$ mass distribution for all $\mu^{\pm}\pi^{\mp}\gamma\gamma$ events (14 events have $m_{\gamma\gamma} > 0.4$ GeV) and for events with π^0 fit probability greater than 1 %.

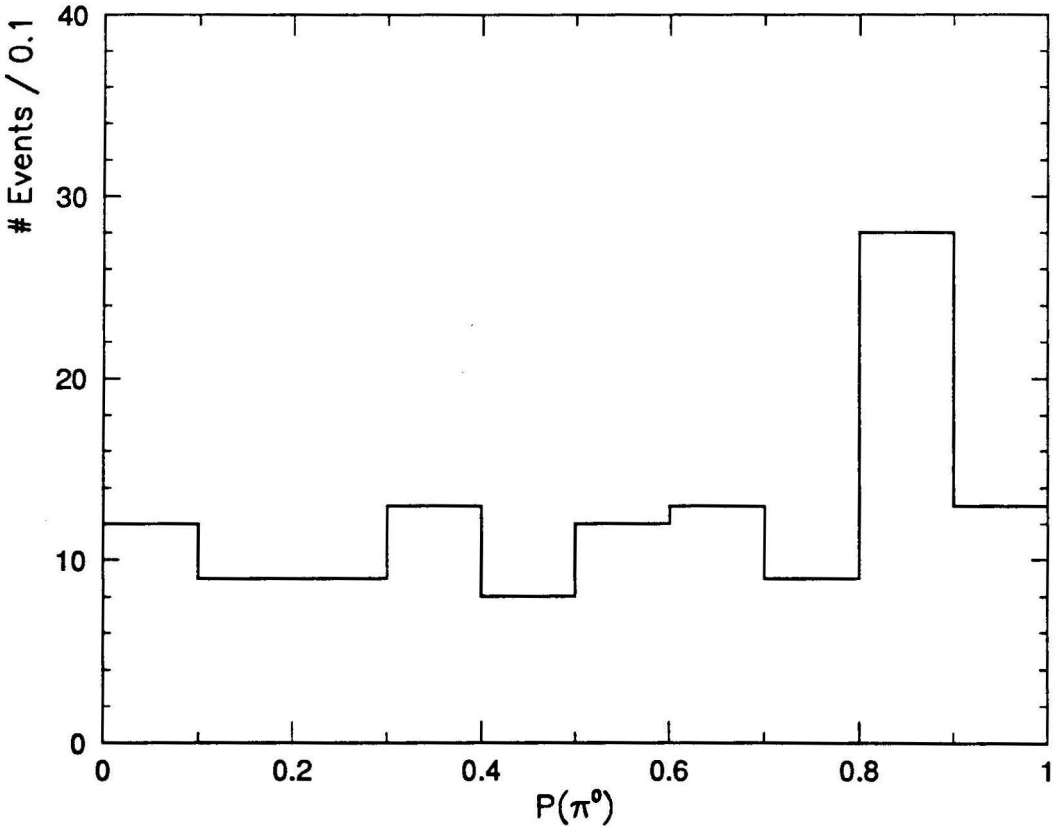

Figure 6.3: π^0 fit probability distribution for $\gamma\gamma$ pairs with $P(\pi^0) > 1\%$.

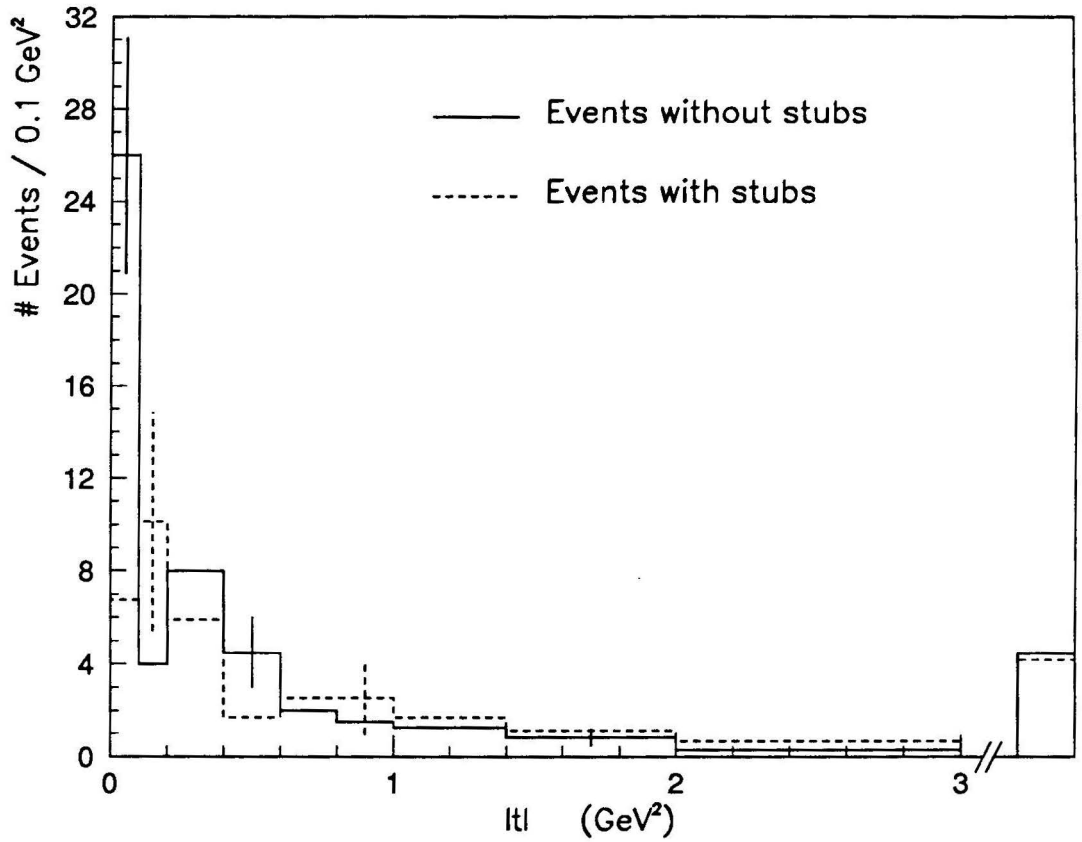

Figure 6.4: $|t|$-distributions for $\mu^{\pm}\,\pi^{\mp}\,\pi^{0}$ events, normalized at $|t| > 0.2$ GeV^2.

The dashed histogram in Fig. 6.2 is the $\gamma\,\gamma$ invariant mass distribution for $\gamma\,\gamma$ pairs with π^0 fit probability $P(\pi^0)$ greater than 1%. Requiring $P(\pi^0) > 1\%$ leads to a sample of 126 $\mu^{\pm}\,\pi^{\mp}\,\pi^{0}$ events. In the subsequent analysis of these events, the fitted π^0 three-momentum is used instead of the measured three-momentum of the $\gamma\,\gamma$ pair.

The fit probability distribution shown in Fig. 6.3 is reasonably uniform. This indicates that there is no under- or overestimate of the measurement errors for the γ conversions.

6.2 Extraction of the Signal

The $|t|$ distributions for the 126 $\mu^{\pm}\,\pi^{\mp}\,\pi^{0}$ events are shown in Fig. 6.4. There are 84 events without stubs and 42 events with stubs ($p_{\mathrm{stub}} < 800$ MeV/c). The distribution for the events with stubs is normalized to that for events without stubs

at $|t| > 0.2$ GeV^2 and the normalization factor is found to be 1.69 ± 0.38. As in the case of single pion production, there is a peak at $|t| < 0.1$ GeV^2 in the distribution for events without stubs. Specifically, the number of events without stubs is 26 whereas the number of events with stubs is 4. After normalization, the background is estimated to be 6.8 ± 4.5 events and the signal is estimated to be 19.2 ± 6.8 events, where the errors are purely statistical. The 26 events without stubs at $|t| < 0.1$ GeV^2 consist of 22 $\mu^- \pi^+ \pi^0$ events and 4 $\mu^+ \pi^- \pi^0$ events, whereas the 4 events with stubs consist of 3 $\mu^- \pi^+ \pi^0$ events and 1 $\mu^+ \pi^- \pi^0$ event. The number of $\mu^+ \pi^- \pi^0$ events is somewhat lower than expected in comparison with the number of $\mu^- \pi^+ \pi^0$ events. However, the statistics are small and the coherent ρ cross section is expected to be smaller in the case of $\overline{\nu}_\mu$ charged current interactions than that in the case of ν_μ charged current interactions because of the lower average $\overline{\nu}_\mu$ beam energy.

6.3 Corrections to the Coherent Signal

To compute the cross section, the coherent signal has to be corrected for the losses. Except for the gamma detection efficiency, the determination of the correction factors follows the same steps as in the case of the single pion production (see Sec. 5.2). Therefore, these corrections are described only briefly.

6.3.1 Scanning Efficiency

The scanning efficiency for $\mu^\pm \pi^\mp \pi^0$ events found in the "good" film is estimated to be $(95.9 \pm 2.0)\%$, whereas the effective scanning efficiency in the "faint/snowy" film is estimated to be $(73.5 \pm 15.6)\%$. The scanning efficiency for the faint/snowy film is evaluated separately for the 1985 and 1987-88 data since the event rates are expected to be different due to the differences in liquid densities. The efficiencies for the 1985 and 1987-88 data are then combined to give the above value for the effective efficiency in the faint/snowy film.

The overall scanning efficiency is then obtained by combining the efficiencies for the good and faint/snowy film, and is determined to be $\epsilon = (82.5 \pm 11.2)\%$. This efficiency is higher than that obtained for the $\mu\pi$ events : $\epsilon_{\mu\pi} = (72.9 \pm 6.5)\%$. A higher efficiency is expected because 2-prong events with additional neutral particles are easier to find in the bubble chamber film.

6.3.2 $\frac{\Delta p}{p}$ Cut

The effect of the cut on the relative error on the momentum of the charged tracks, $\frac{\Delta p}{p} < 60\%$, was estimated from the fraction of all 2-prong events passing the cut. This fraction was found to be $935/1032 = 0.906 \pm 0.009$ and the correction factor is thus 1.104 ± 0.011.

6.3.3 p_μ Cut

The fraction of events passing the muon momentum cut $p_\mu > 10$ GeV/c was determined to be 92.4 % from the coherent ρ production Monte Carlo simulation with the Rein-Sehgal parametrization of the ρ-nucleus differential cross section for $R = 0$ (see Sec. 4.2.2). The systematic error due to this choice of parametrization was estimated to be 1.6 % by comparing the above fraction with that obtained using the Belkov-Kopeliovich parametrization for $R = 0.4$ $Q^2/m_\rho^2 \leq 1$ (see Sec. 4.2.2).

6.3.4 $|t|$ Cut

The $|t|$ cut results in a reduction of the signal by a factor of 0.765 which was determined from the Monte Carlo simulation with the Rein-Sehgal parametrization of the ρ-nucleus differential cross section for $R = 0$. This fraction was obtained using an uncertainty in the beam direction of 0.5 mrad. The systematic error due to this choice of parametrization was estimated to be 0.007 by comparing the above factor with that obtained using the Belkov-Kopeliovich parametrization of the ρ-nucleus

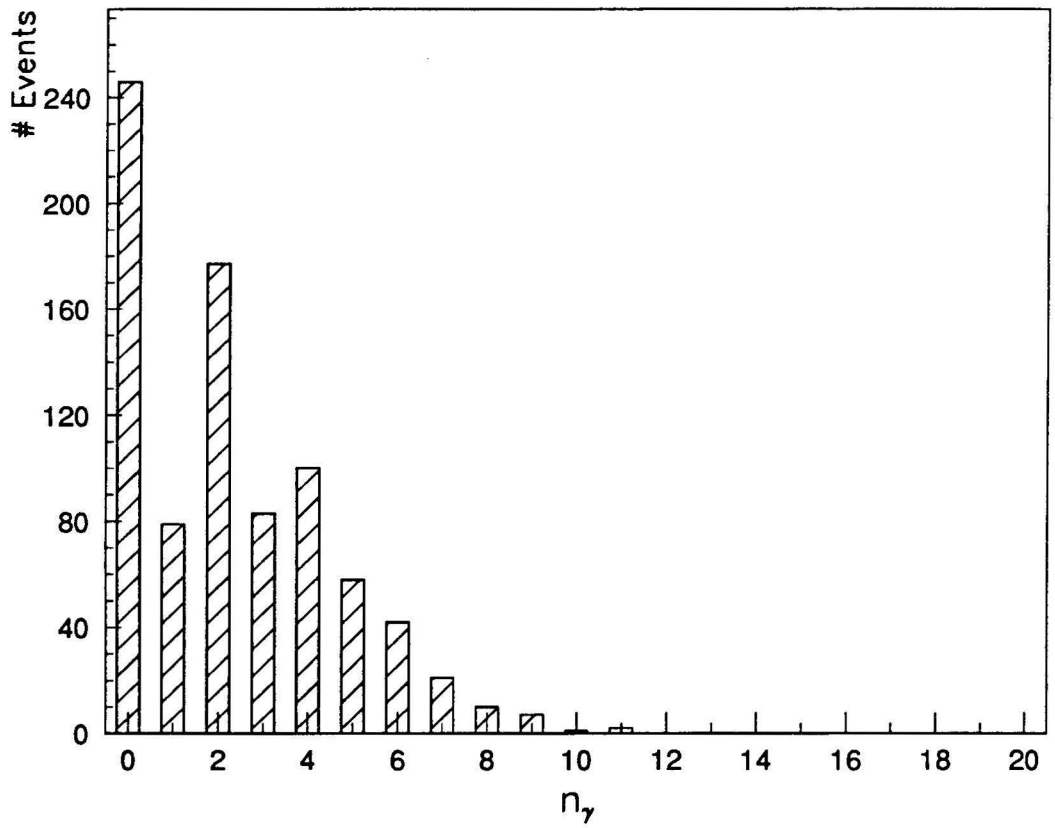

Figure 6.5: Gamma multiplicity distribution for $\mu^{\pm}\,\pi^{\mp}\,(n_\gamma\,\gamma)$ events.

differential cross section for $R = 0.4\ Q^2/m_\rho^2 \leq\ 1$.

To estimate a systematic error associated with the choice of beam direction uncertainty, we follow the same procedure as that followed in the case of the single pion channel (Sec. 5.2.4). The systematic error was estimated to be 0.036.

As a result, the fraction of events passing the $|t| < 0.1$ GeV^2 cut was determined to be 0.765 ± 0.037. The systematic errors due to both the choice of ρ-nucleus cross section parametrization and the uncertainty in the beam direction have been added in quadrature.

6.3.5 Gamma Detection Efficiency

The γ detection efficiency is determined using the γ multiplicity distribution for $\mu^{\pm}\,\pi^{\mp}\,(n_\gamma\,\gamma)$ events, where n_γ, the number of γ, is any integer ≥ 0. As seen in Fig. 6.5, the distribution shows peaks at $n_\gamma = 0, 2$ and, to a smaller extent, 4. Assuming

that only events with 1 π^0 produced contribute to the number of events with 1 or 2 γ, the following system of equations[1] is obtained

$$\begin{aligned} N_{1\gamma} &= 2\,\epsilon_\gamma\,(1-\epsilon_\gamma)\,N_{1\pi^0}\ , \\ N_{2\gamma\to\pi^0} &= \epsilon_\gamma^2\,N_{1\pi^0}\ , \end{aligned} \tag{6.5}$$

where $N_{1\gamma}$ is the number of events with one and only one associated γ, $N_{2\gamma\to\pi^0}$ is the number of events in the subsample of 2-γ events for which $P(\pi^0) > 1\%$ (i.e. we do require that the two γ are consistent with being daughters of the same π^0), $N_{1\pi^0}$ is the number of events with 1 π^0 produced in the final state and ϵ_γ is the γ detection efficiency. The system (6.5) allows the unknown $N_{1\pi^0}$ to be expressed in terms of ϵ_γ and thus the detection efficiency can be expressed as a function of the measured quantities $N_{1\gamma}$ and $N_{2\gamma\to\pi^0}$

$$\epsilon_\gamma = \frac{2\,N_{2\gamma\to\pi^0}}{N_{1\gamma}+2\,N_{2\gamma\to\pi^0}}\ . \tag{6.6}$$

In the sample of 826 $\mu^\pm\,\pi^\mp\,(n_\gamma\,\gamma)$ events, the number of events is $N_{1\gamma} = 79$ and $N_{2\gamma\to\pi^0} = 126$ leading to a detection efficiency $\epsilon_\gamma = (76.1 \pm 2.6)\%$.

Moreover, it is shown below that assuming that only the 1 π^0 events contribute to the number of events with 1 γ and 2 $\gamma \to \pi^0$, does not lead to a significant bias. This is due to the fact that events with 2 or more π^0 contribute to $N_{1\gamma}$ and $N_{2\gamma\to\pi^0}$ in a similar way. Using the efficiency calculated from (6.6), $\epsilon_\gamma = (76.1 \pm 2.6)\%$, we can determine the probability for an event with 2 π^0 to produce an event with only one detected γ : $P_1 = 4\,\epsilon_\gamma\,(1-\epsilon_\gamma)^3 = (4.2 \pm 1.1)\%$. On the other hand, the probability for a 2-π^0 event to produce an event with 2 $\gamma \to \pi^0$ is $P_2 = 2\,\epsilon_\gamma\,(1-\epsilon_\gamma)^2 = (6.6 \pm 0.9)\%$. Assuming that the number of events with 1 and 2 π^0 are the same, a modified γ detection efficiency may be written as

$$\begin{aligned} \epsilon'_\gamma &= \frac{2\,N_{2\gamma\to\pi^0}\,(1-P_2)}{N_{1\gamma}\,(1-P_1)+2\,N_{2\gamma\to\pi^0}\,(1-P_2)} \\ &= 0.757 \pm 0.063\ . \end{aligned}$$

[1]Throughout this chapter, we assume that all γ come from π^0 decays.

Furthermore, the events with 3 or more π^0 have very small probabilities to produce events with 1 γ or 2 $\gamma \rightarrow \pi^0$. As a consequence, we conclude that using Eq. (6.6) does not lead to biases in the determination of the γ detection efficiency.

It is also possible to write down the complete set of equations between the number of events with 1, 2, ..., 9 γ observed and the number of events with 1, 2, ..., 5 π^0 produced :

$$
\begin{aligned}
N_{1\gamma} &= 2\,\epsilon_\gamma\,(1-\epsilon_\gamma)\,N_{1\pi^0} + 4\,\epsilon_\gamma\,(1-\epsilon_\gamma)^3\,N_{2\pi^0} + 6\,\epsilon_\gamma\,(1-\epsilon_\gamma)^5\,N_{3\pi^0} \\
&\quad +8\,\epsilon_\gamma\,(1-\epsilon_\gamma)^7\,N_{4\pi^0} + 10\,\epsilon_\gamma\,(1-\epsilon_\gamma)^9\,N_{5\pi^0}\ , \\
N_{2\gamma} &= \epsilon_\gamma^2\,N_{1\pi^0} + 6\,\epsilon_\gamma^2\,(1-\epsilon_\gamma)^2\,N_{2\pi^0} + 15\,\epsilon_\gamma^2\,(1-\epsilon_\gamma)^4\,N_{3\pi^0} \\
&\quad +28\,\epsilon_\gamma^2\,(1-\epsilon_\gamma)^6\,N_{4\pi^0} + 45\,\epsilon_\gamma^2\,(1-\epsilon_\gamma)^8\,N_{5\pi^0}\ , \\
N_{3\gamma} &= 4\,\epsilon_\gamma^3\,(1-\epsilon_\gamma)\,N_{2\pi^0} + 20\,\epsilon_\gamma^3\,(1-\epsilon_\gamma)^3\,N_{3\pi^0} + 56\,\epsilon_\gamma^3\,(1-\epsilon_\gamma)^5\,N_{4\pi^0} \\
&\quad +120\,\epsilon_\gamma^3\,(1-\epsilon_\gamma)^7\,N_{5\pi^0}\ , \\
N_{4\gamma} &= \epsilon_\gamma^4\,N_{2\pi^0} + 15\,\epsilon_\gamma^4\,(1-\epsilon_\gamma)^2\,N_{3\pi^0} + 70\,\epsilon_\gamma^4\,(1-\epsilon_\gamma)^4\,N_{4\pi^0} \\
&\quad +210\,\epsilon_\gamma^4\,(1-\epsilon_\gamma)^6\,N_{5\pi^0}\ , \\
N_{5\gamma} &= 6\,\epsilon_\gamma^5\,(1-\epsilon_\gamma)\,N_{3\pi^0} + 56\,\epsilon_\gamma^5\,(1-\epsilon_\gamma)^3\,N_{4\pi^0} + 252\,\epsilon_\gamma^5\,(1-\epsilon_\gamma)^5\,N_{5\pi^0}\ , \\
N_{6\gamma} &= \epsilon_\gamma^6\,N_{3\pi^0} + 28\,\epsilon_\gamma^6\,(1-\epsilon_\gamma)^2\,N_{4\pi^0} + 210\,\epsilon_\gamma^6\,(1-\epsilon_\gamma)^4\,N_{5\pi^0}\ , \\
N_{7\gamma} &= 8\,\epsilon_\gamma^7\,(1-\epsilon_\gamma)\,N_{4\pi^0} + 120\,\epsilon_\gamma^7\,(1-\epsilon_\gamma)^3\,N_{5\pi^0}\ , \\
N_{8\gamma} &= \epsilon_\gamma^8\,N_{4\pi^0} + 45\,\epsilon_\gamma^8\,(1-\epsilon_\gamma)^2\,N_{5\pi^0}\ , \\
N_{9\gamma} &= 10\,\epsilon_\gamma^9\,(1-\epsilon_\gamma)\,N_{5\pi^0}\ .
\end{aligned}
$$

This system of nine equations with six unknowns ($N_{1\pi^0}$, $N_{2\pi^0}$, $N_{3\pi^0}$, $N_{4\pi^0}$, $N_{5\pi^0}$ and ϵ_γ) is then processed using MINUIT, a least squares minimization program [80]. Using the numbers from Fig. 6.5, the fit gives $N_{1\pi^0} = 229 \pm 18$, $N_{2\pi^0} = 170 \pm 18$, $N_{3\pi^0} = 126 \pm 19$, $N_{4\pi^0} = 40 \pm 15$, $N_{5\pi^0} = 22 \pm 10$ and $\epsilon_\gamma = (78.8 \pm 2.1)\%$ with a χ^2 per degree of freedom of $1.97/3 = 0.66$. Based on these numbers, we would expect to observe 756 ± 76 π^0 in the sample whereas 726 ± 38 are found. These 726 π^0 were not obtained by full reconstruction of the π^0 as described in Sec. 6.1, but were simply obtained by finding, for each event, the maximum number of $\gamma\gamma$ pairs with a mass within $3\,\sigma$ of the π^0 mass.

Thus, the fitted detection efficiency is close to that found using (6.6). However, we will use the results of (6.6) because several labs recorded only the first five upstream γ in events with 5 γ or more.

The determination of the γ detection efficiency, following Eq. (6.6), has the advantage that all sources of inefficiency are taken into account via their effect on the γ multiplicity distribution. For example, losses of genuine primary γ may arise in the process of removing bremsstrahlung γ from the sample, which would be translated into an increase in the number of 1 γ events. Such an increase would then be reflected by a decrease in the detection efficiency computed from (6.6).

In the remainder of this section we investigate some of specific sources of γ detection inefficiency : conversions outside the bubble chamber volume and scanning/measuring loss of conversions at large distances from the primary vertex.

The conversion probability is expressed as

$$\begin{aligned} P_{\rm conv} &= 1 - e^{-L_{pot}/C_0} \,, \qquad (6.7) \\ \text{with} \quad C_0 &= \frac{9}{7}\frac{X_0}{(1-\xi)} \,, \end{aligned}$$

where C_0 is the conversion length and L_{pot} is the potential length (i.e. the distance between the primary vertex and the nearest bubble chamber wall along the flight direction of the photon). The conversion length is given in terms of the radiation length X_0 and a function ξ which depends on the momentum ($\xi \to 0$ as $p \to \infty$). For neon, $\xi = 0.073$ at $p = 1$ GeV/c and $\xi = 0.012$ at $p = 10$ GeV/c [81]. The conversion length increases with decreasing momentum due to a corresponding decrease in the γ conversion cross section. In our sample of $\mu^{\pm}\pi^{\mp}(n_\gamma\,\gamma)$ events, the average potential length is ~ 210 cm and the momentum-dependent conversion length is shown in Fig. 6.6a. Two peaks are observed because the density of the bubble chamber liquid was different for the two data taking periods. The conversion probability computed as in Eq. (6.7) is shown in Fig. 6.6b. The average conversion probability is found to be $(92.0 \pm 0.2)\%$.

In addition to the probability to convert outside the bubble chamber, there is a scanning/measuring loss of γ conversions inside the bubble chamber but at large distances from the primary vertex. To investigate this, the distance distribution is mapped into a probability distribution in terms of the variable Q_d [82] :

$$Q_d = \frac{1 - e^{-d/C_0}}{1 - e^{-L_{pot}/C_0}} ,$$

where d is the distance between the conversion point and the primary vertex, and it is assumed that there is no loss at short distances. This assumption is reasonable because we are dealing with event topologies (events with only 2 prongs) for which the visibility near the interaction vertex is very good. This probability is expected to be distributed uniformly between 0 and 1. Fig. 6.6c compares the distribution obtained using the $\mu^{\pm}\,\pi^{\mp}\,(n_\gamma\,\gamma)$ sample with that obtained from our pseudo π^0 Monte Carlo simulation (Sec. 4.2). As expected, the distribution for the simulated π^0 decays is uniform. However, there is an indication of a loss of γ at $Q_d > 0.7$ which corresponds to a loss of γ conversions at large distances. Assuming a flat distribution and using the data at $Q_d < 0.7$ to find the total expected number of γ, the efficiency to detect conversions inside the bubble chamber is estimated to be $(92.6 \pm 3.0)\%$.

Combining this efficiency with the average conversion probability yields an upper limit on the overall efficiency of $(85.2 \pm 2.8)\%$. This value is expected to be higher than the value extracted from the γ multiplicity distribution, $\epsilon_\gamma = (76.1 \pm 2.6)\%$, since it does not include the random losses in the scanning/measuring process or possible losses in the removal of bremsstrahlung photons. Nevertheless, it indicates that ϵ_γ is a reasonable estimate of the overall γ detection efficiency.

6.3.6 Total Correction

The various correction factors are summarized in Table 6.1 for all $\mu^{\pm}\,\pi^{\mp}\,\pi^0$ events and the overall correction factor is determined to be 3.27 ± 0.50.

The signal was extracted for a series of different cuts on $|t|$ in order to determine

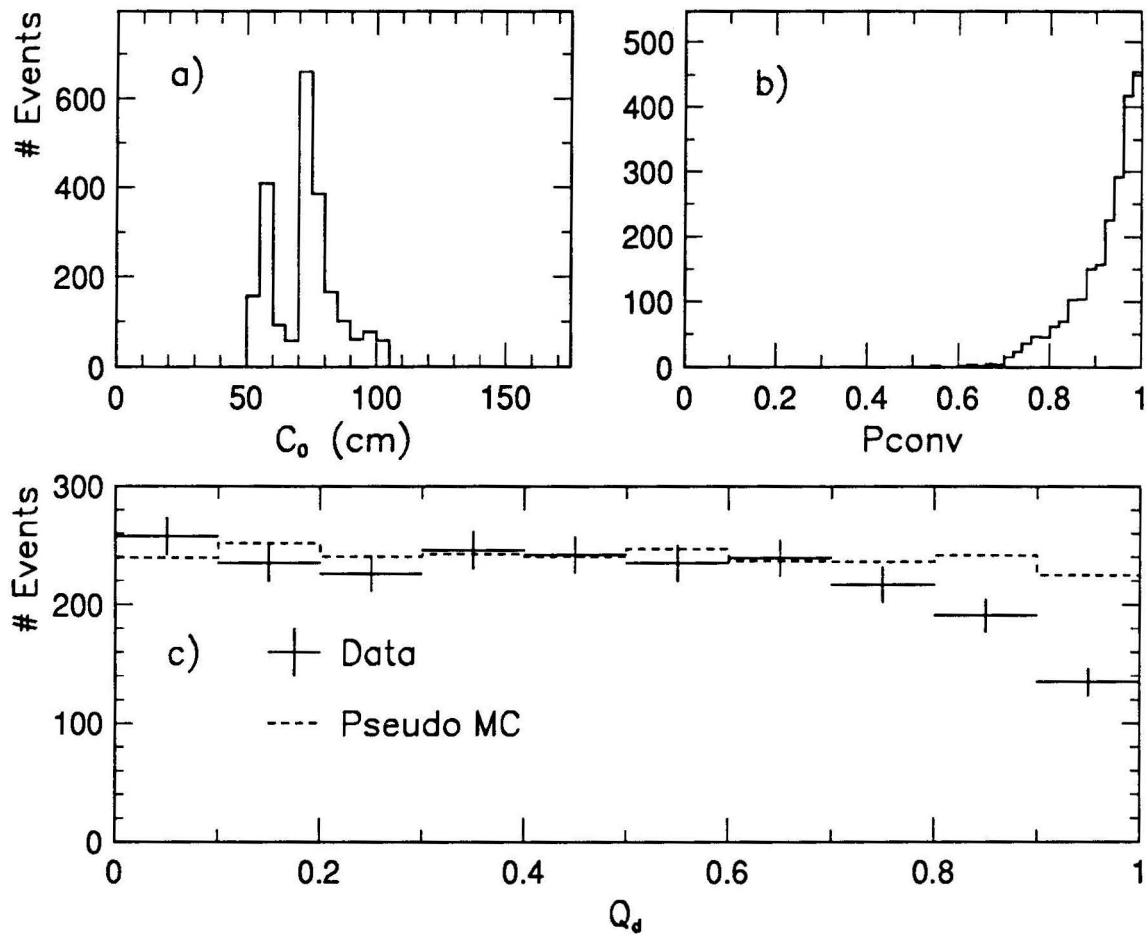

Figure 6.6: γ conversions in $\mu^{\pm}\,\pi^{\mp}\,(n_{\gamma}\,\gamma)$ events: a) conversion length distribution; b) conversion probability distribution; c) Q_d distribution, the crosses represent the data and the dashed histogram represents the π^0 pseudo Monte Carlo results normalized to the data at $Q_d < 0.7$.

the systematic error due to the particular choice of $|t|$ cut. Table 6.2 presents the corrected signal for the following values of the cut : 0.05, 0.1, 0.15 and 0.2 GeV^2. The corrected signals obtained for the first three cuts are consistent with one another whereas the signal obtained for $|t| < 0.2$ GeV^2 is lower. This last value is not inconsistent with the others but tends to increase the r.m.s. Note that a lower value of the signal at $|t| < 0.2$ GeV^2 was also obtained in the case of the $|t|$ distributions for $\mu^{\pm}\,\pi^{\mp}\,X^0$ events (Sec. 4.1.2). The r.m.s. for the four values of the corrected signal is 4.7 events based on which the systematic error due to our particular choice of $|t|$ cut is estimated to be 19 %.

Table 6.1: Correction factors for coherent single ρ events.

	$\nu + \overline{\nu}$
$\frac{\Delta p}{p}$ cut correction (c_1)	1.104 ± 0.011
Scanning efficiency (c_2)	0.825 ± 0.112
Fraction with $p_\mu > 10$ GeV/c (c_3)	0.924 ± 0.016
Fraction with $\|t\| < 0.1$ GeV^2 (c_4)	0.765 ± 0.037
Gamma detection efficiency (c_5)	0.761 ± 0.026
Total correction factor $c_1/(c_2 \cdot c_3 \cdot c_4 \cdot c_5^2)$	3.27 ± 0.50

Table 6.2: Single ρ coherent signal for different cuts on $|t|$. The $|t|$ distributions for events without and with stubs have been normalized at $|t| > 0.2$ GeV^2.

$\|t\|$ cut (GeV^2)	# Events below $\|t\|$ cut w/o stubs	with stubs	Signal observed	Fraction MC passing cut	Signal corrected
0.05	16	2	12.6 ± 5.2	0.585	21.5 ± 8.9
0.1	26	4	19.2 ± 6.8	0.765	25.1 ± 8.9
0.15	29	5	20.6 ± 7.3	0.839	24.6 ± 8.7
0.2	30	10	13.1 ± 8.5	0.878	14.9 ± 9.7

Table 6.3: Single ρ signal and cross section. The error on the corrected signal includes the systematic error introduced by the choice in $|t|$ cut.

	$\nu + \overline{\nu}$
Events w/o stubs	84
Events with stubs	42
Events w/o stubs $\|t\| < 0.1$ GeV^2	26
Events with stubs $\|t\| < 0.1$ GeV^2	4
Signal $\|t\| < 0.1$ GeV^2 (observed)	19.2 ± 6.8
Signal (corrected)	62.8 ± 27.0
N_{CC}	27763 ± 689
N_{COH}/N_{CC} ($\times 10^{-2}$)	0.23 ± 0.10
σ_{COH} ($\times 10^{-40}$ cm^2)	227 ± 98

6.4 ρ Production Results

6.4.1 The Integrated Cross Section

After correction for all identified losses, the number of single ρ coherent events is determined to be 62.8 ± 27.0, where the error includes the systematic error corresponding to the dependence on the particular choice of the $|t|$ cut.

The number of charged current events corresponding to the corrected signal is 27763 ± 689 (see Sec. 5.3). The resulting rate of ρ coherent production with respect to the total number of charged current interactions is thus $(0.23 \pm 0.10)\%$. The cross section is then computed using the measured total charged current cross section [70] and is found to be

$$\sigma_{COH}(\nu_\mu(\overline{\nu}_\mu) + Ne \rightarrow \mu^-(\mu^+) + \rho^+(\rho^-) + Ne) = (227 \pm 98) \times 10^{-40} \text{ cm}^2/\text{ neon nucleus} \quad (6.8)$$

for an average beam energy of 86 GeV. These results are summarized in Table 6.3.

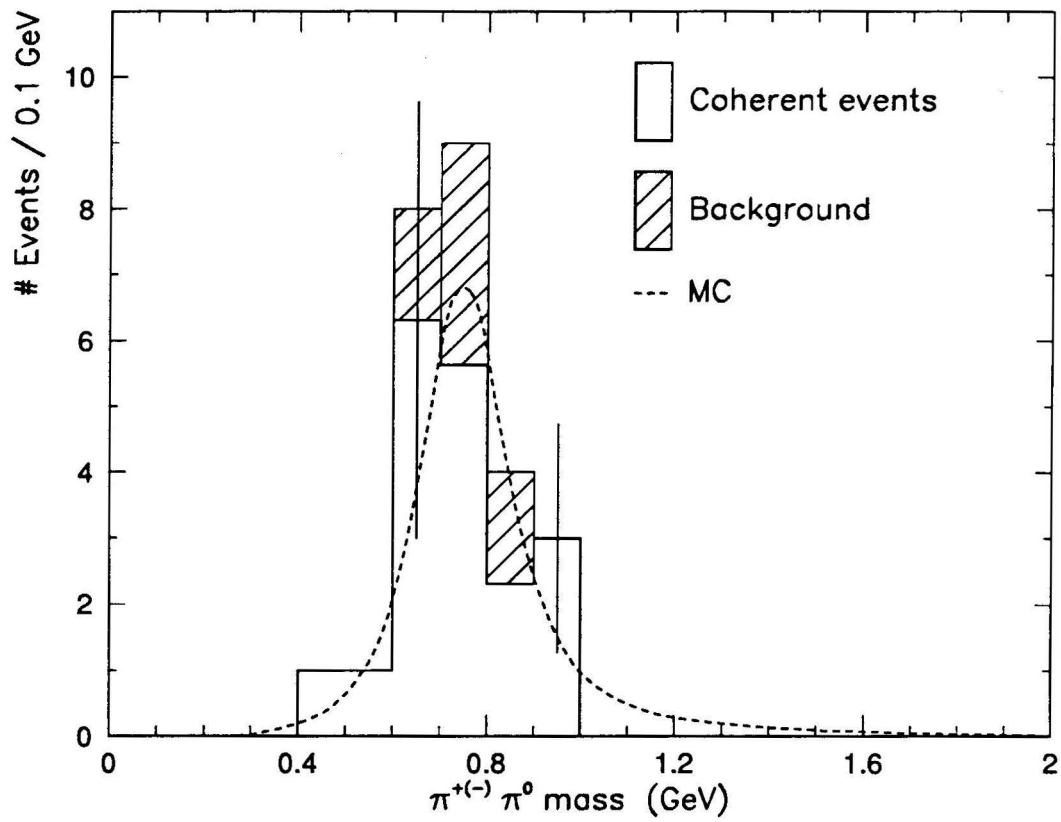

Figure 6.7: $\pi^{\pm}\,\pi^0$ invariant mass for $\mu^{\pm}\,\pi^{\mp}\,\pi^0$ events at $|t| < 0.1$ GeV^2. The events with stubs (shown cross-hatched) have been properly normalized and subtracted from the distribution for events without stubs. The dashed curve represent the simulated ρ line shape normalized to the observed coherent signal.

Fig. 6.7 shows the $\pi^{\pm}\,\pi^0$ invariant mass distribution for the $\mu^{\pm}\,\pi^{\mp}\,\pi^0$ events at $|t| < 0.1$ GeV^2. The simulated shape of the ρ resonance is superimposed for comparison and shows that most of the signal at $|t| < 0.1$ GeV^2 is indeed compatible with the decay $\rho^{\pm} \rightarrow \pi^{\pm}\,\pi^0$.

Contrary to the case of single pion coherent production, there is little experimental data on single ρ coherent production (see Table 6.4). Only two previous bubble chamber experiments have measured such cross section:

- Using the Fermilab 15-foot Bubble Chamber exposed to a ν_μ beam, the E546 collaboration reported a value of $\sigma = (190 \pm 60) \times 10^{-40}$ cm^2 per neon nucleus with an average neutrino beam energy of 51 GeV [83, 84].

- Using BEBC exposed to a $\overline{\nu}_\mu$ beam, the WA59 collaboration reported a value

Table 6.4 : Summary of experimental results on single ρ coherent cross sections in (anti)neutrino charged current interactions.

Experiment	Reaction	$< E_\nu >$ (GeV)	A	Signal observed	Cross section (10^{-40} cm$^2/\mathcal{N}$)	N_{COH}/N_{CC}
This exp.	$\nu_\mu(\overline{\nu}_\mu)\, Ne \rightarrow \mu^-(\mu^+)\, \rho^+(\rho^-)\, Ne$	86	20	19.2 ± 6.8	227 ± 98	$(0.23 \pm 0.10)\%$
E546 [83]	$\nu_\mu\ Ne \rightarrow \mu^-\, \rho^+\, Ne$	51	20	9.5 ± 3.5	190 ± 60 [84]	$(0.28 \pm 0.10)\%$
WA59 [85]	$\overline{\nu}_\mu\ Ne \rightarrow \mu^+\, \rho^-\, Ne$	27	20	33 ± 7	95 ± 25	$(0.52 \pm 0.10)\%$

of $\sigma = (95 \pm 25) \times 10^{-40}$ cm^2 per neon nucleus with an average antineutrino beam energy of 27 GeV [85].

6.4.2 $\mu\,\pi\,\gamma$ Events

As a check of the coherent signal and of the estimated γ detection efficiency, the signal for $\mu^{\pm}\,\pi^{\mp}\,\gamma$ events was also extracted. A signal of 10.0 ± 6.3 events is found at $|t| < 0.1$ GeV^2. This is to be compared with the signal expected on the basis of the observation of 19.2 ± 6.8 $\mu^{\pm}\,\pi^{\mp}\,\pi^0$ events at $|t| < 0.1$ GeV^2 :

$$N_{\mu\pi\gamma} = F_\gamma \, \frac{2\,\epsilon_\gamma\,(1-\epsilon_\gamma)}{\epsilon_\gamma^2} \, (19.2 \pm 6.8) \, ,$$

where F_γ is the fraction of $\mu^{\pm}\,\pi^{\mp}\,\pi^0$ events at $|t| < 0.1$ GeV^2 for which the value of $|t|$ remains below 0.1 GeV^2 if one γ is removed. Simulation of coherent ρ production predicts this fraction to be ~ 0.60. This value is consistent with the value extracted from our $\mu^{\pm}\,\pi^{\mp}\,\pi^0$ data at $|t| < 0.1$ GeV^2 : $F_\gamma = 35/60 = 0.58$ obtained by removing one of the two γ in each of the 30 events at $|t| < 0.1$ GeV^2. Thus, the number of $\mu^{\pm}\,\pi^{\mp}\,\gamma$ events at $|t| < 0.1$ GeV^2 is expected to be 7.2 ± 2.6, which is compatible with the observed signal of 10.0 ± 6.3 events.

6.4.3 The Energy Dependence

The coherent ρ production cross section as a function of energy is shown in Fig. 6.8 along with the predictions based on the Rein-Sehgal (R-S) and Belkov-Kopeliovich (B-K) parametrizations of the ρ-nucleus differential cross section (see Sec. 4.2.2). Two parametrizations of R, the ratio of longitudinal and transverse ρ production cross sections, were used : $R = 0$ and $R = 0.4\ Q^2/m_\rho^2$ ($R \leq 1$). The predicted cross section is significantly higher for the second parametrization but the existing data do not allow one to decide which one is the best representation. The uncertainty in the predicted cross sections is estimated to be $\sim 15 - 20$ %. This estimate includes the uncertainty in the total pion-nucleon cross section and the

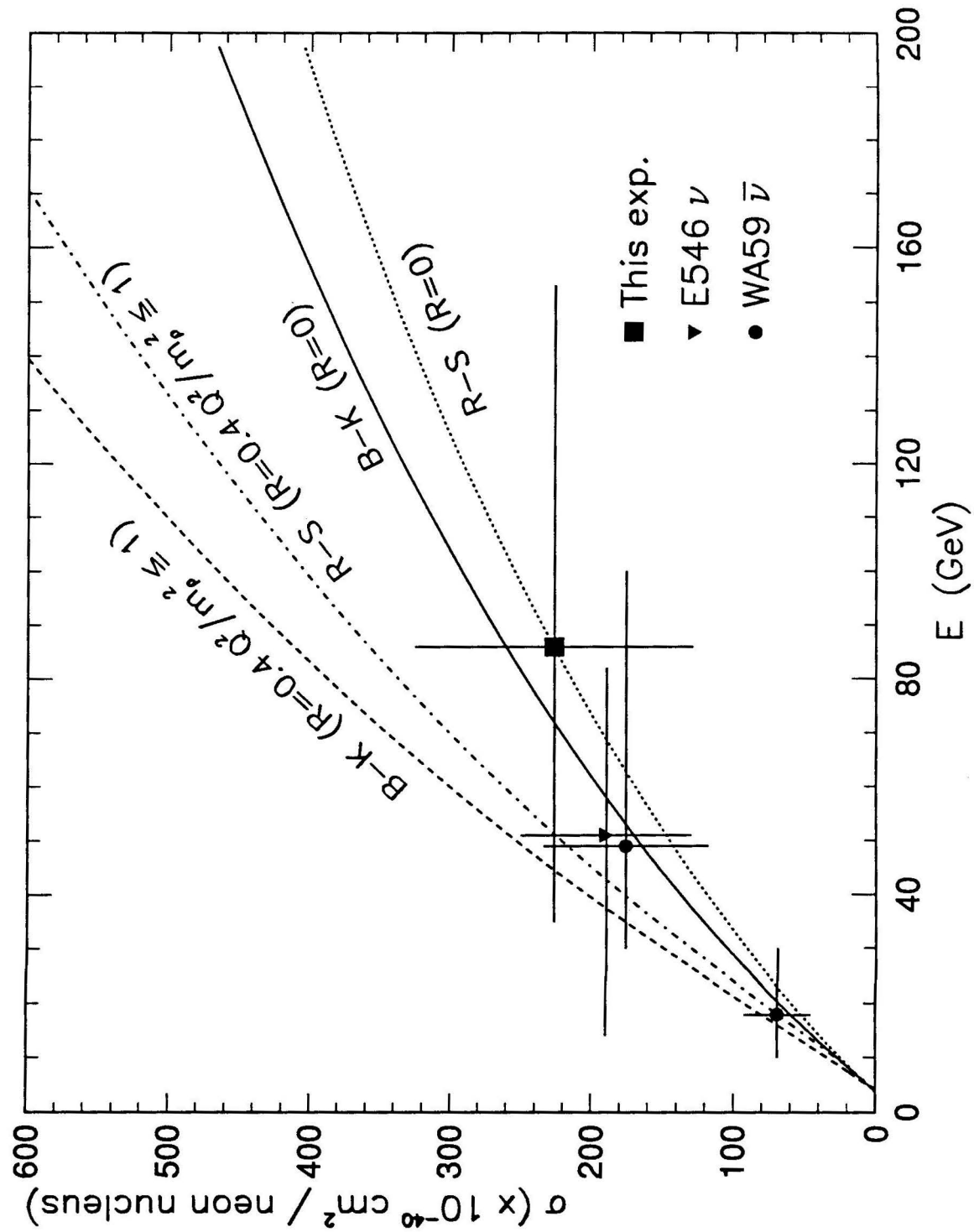

Figure 6.8: Single ρ coherent production cross section as a function of energy. The curves represent the predictions of the Rein-Sehgal and Belkov-Kopeliovich models (Sec. 4.2.2). Note that, for the WA59 data, the horizontal error bar represents the range of energy covered, whereas for the data from this experiment and from E546 it represents the energy range containing 68% of the (anti)neutrino flux.

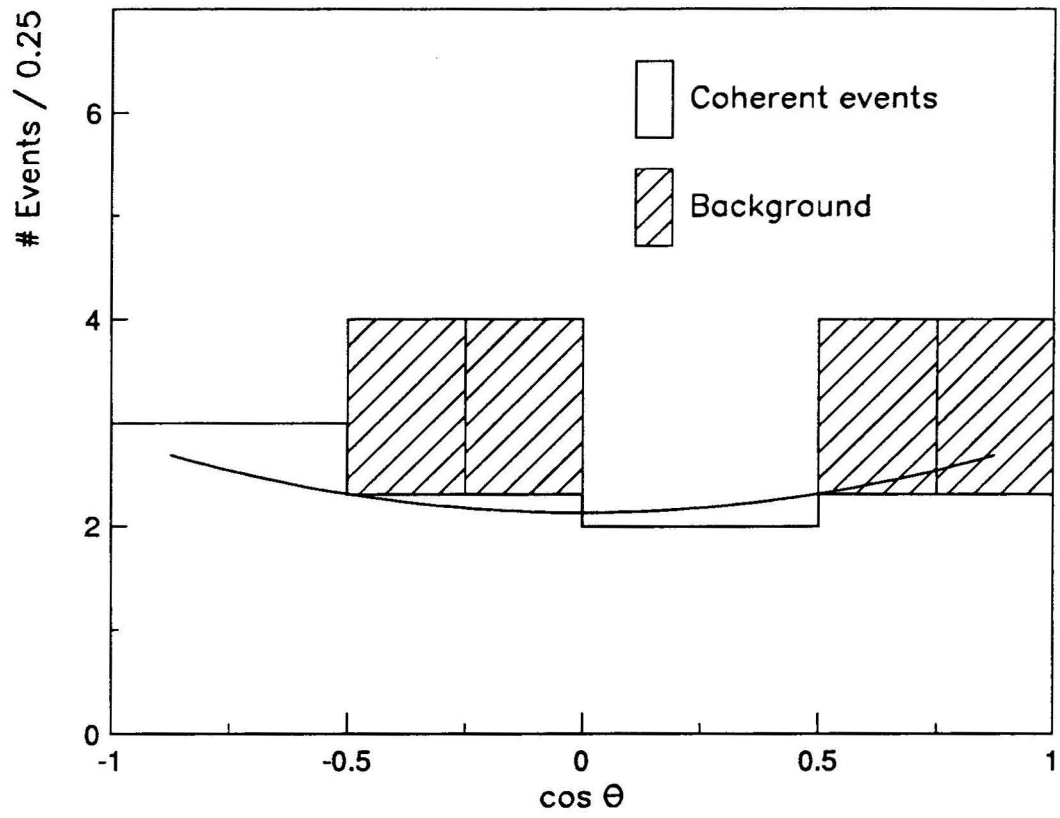

Figure 6.9: Distribution of the cosine of the angle between the daughter charged pion and the parent ρ flight direction in the ρ center of mass. The curve represents the fit described in the text.

coupling constant $f_{\rho^{\pm}}$. In addition, it also includes the uncertainty in the absorption factor F_{abs} and the slope parameter b in the case of the R-S model, whereas in the case of the B-K model, it includes the uncertainty in the slope parameter B_T and the total pion-nucleus cross section due to the effect of inelastic screening.

6.4.4 Longitudinal ρ Production

The angular characteristics of the events at $|t| < 0.1$ GeV^2 allow the fraction of longitudinally produced ρ mesons to be determined. The cosine of the angle between the daughter charged pion and the flight direction of the parent ρ meson in the ρ center of mass is shown in Fig. 6.9. The data were fitted to the ρ decay angular

distribution [3] :

$$W(cos\theta) \;=\; \frac{3}{4}\left[1 - r_{00}^{04} + (3r_{00}^{04} - 1)\, cos^2\theta\right] \;,$$

where r_{00}^{04} is one of the $\rho^{\pm}$ density matrix elements which represents the probability to produce a longitudinally polarized ρ meson. As a result of the fit, the ma element is determined to be $r_{00}^{04} = 0.40 \pm 0.18$. Furthermore, the value of the fraction between longitudinal and transverse production of ρ mesons is related to r_{00}^{04} via the expression [3]

$$R = \frac{\sigma_L}{\sigma_T} = \frac{1}{\epsilon}\frac{r_{00}^{04}}{1 - r_{00}^{04}} \;,$$

which implies that for the fitted value of r_{00}^{04} we find $R = 0.7 \pm 0.4$, i.e. there is a significant production of longitudinally polarized ρ mesons.

It is interesting to compare this result with that obtained in $\overline{\nu}_\mu$ charged current interactions by the WA59 Collaboration [85], $r_{00}^{04} = 0.41 \pm 0.19$ which implies a value $R = 0.8 \pm 0.4$. In the case of ν_μ interactions, E546 finds $R \simeq 0.2$ [83]. A large fraction of longitudinally polarized ρ^0 mesons was also observed in several electro- and muo-production experiments [86, 87, 88, 41] with beam energies ranging from $\sim$ 10 to 300 GeV. However, one muoproduction experiment [89] with beam energies of 100 and 150 GeV finds values of R at the 10% level.

6.5 Kinematical Characteristics

In this section, the distributions of a number of kinematical variables are compared with theoretical predictions. Figs. 6.10–6.18 show the distributions of the total energy E, the energy transfer ν, the square of the W boson four-momentum Q^2, the invariant mass of the hadronic system W, the Bjorken x and y variables, the square of the momentum transfer to the nucleus $|t|$, the minimum value of $|t|$ needed to produce the final state ρ meson t_{min} and the variable t'. See Appendix C for definitions of all the variables. The distributions correspond to the distributions

for events without stubs at $|t| < 0.1$ GeV^2 from which the normalized distributions for events with stubs at $|t| < 0.1$ GeV^2 (shown cross-hatched) are subtracted. Also shown in the figures are the results of the Monte Carlo simulation using the Belkov-Kopeliovich parametrization and two different parametrizations of R (see Sec. 4.2.2). Predictions based on the Rein-Sehgal parametrization (see Sec. 4.2.2) are not shown in those figures for which very little difference is found between the B-K and R-S curves. The model predictions have been normalized to the number of events observed (19.2 $\mu\pi$ events) rather than to the predicted number of events since we are mostly interested in the shape of the distributions.

Good agreement between the predicted curves and the data is observed in the E, Q^2 and x distributions, but the simulation predicts values of ν, W and y which seem to be somewhat higher than indicated by the data. In particular, the ν distribution (Fig. 6.11) shows a lack of events at high values of the energy transfer. There is no data at $\nu > 40$ GeV whereas the simulation predicts that ~ 25 % of the coherent signal should have $\nu > 40$ GeV. It is conceivable that this is partly due to a loss of high momentum π^0. However, the average π^0 and $\pi^{\mp}$ momenta, 9.1 ± 1.4 GeV/c and 9.2 ± 1.5 GeV/c respectively, do not indicate the existence of such a loss. A slight deficit of events at high ν was already observed by WA59, and was even more striking in the data reported by E546. For the latter, the average value of ν was found to be 20 ± 5 GeV with a predicted value of 36 GeV. Moreover, the E546 collaboration reported a large discrepancy between the expected and observed number of events at high energy: only one event was observed at $E > 80$ GeV where ~ 6 were expected. No such discrepancy is observed in our data sample (see Fig. 6.10).

Except for the Q^2 distribution, there is very little difference between the shapes of the predicted distributions obtained using $R = 0$ or $R = 0.4\ Q^2/m_\rho^2 \leq 1$. The predicted Q^2 distribution (Fig. 6.12) shows a decrease at very small values. This agrees with the data and the expectation according to which the cross section $\sigma \rightarrow 0$ as $Q^2 \rightarrow 0$ by virtue of the CVC hypothesis.

The distributions of the momentum transfer variables $|t|$ (Fig. 6.16) and t' (Fig. 6.18) appear flatter than expected. Here, we have shown the predicted distributions for both the R-S and B-K parametrizations; the distributions for $R = 0$ and $R = 0.4$ $Q^2/m_\rho^2 \leq 1$ are not shown but they are also nearly identical in shape. The slope s of the t' distribution was computed using the maximum likelihood method in the t' interval of 0 to $t'_{max} = 0.1$ GeV$^2 - t_{min}$. The slope was determined to be

$$s = 24 \pm 9 \text{ GeV}^{-2} , \tag{6.9}$$

which is consistent with the interpretation of our $\mu\pi\pi^0$ sample at $|t| < 0.1$ GeV^2 as due to the coherent production of ρ mesons off neon nuclei.

The average values of the kinematical variables are summarized in Table 6.5.

Table 6.5 : Average values of kinematical variables for single ρ coherent events at $|t| < 0.1$ GeV^2. The predictions of the Monte Carlo simulation are also given for the Belkov – Kopeliovich (B – K) and Rein – Sehgal (R – S) parametrizations of the ρ–nucleus cross section, as well as for two choices of R (see Sec. 4.2.2).

	Data	B-K $R = 0$	B-K $R = 0.4\ Q^2/m_\rho^2 \leq 1$	R-S $R = 0$	R-S $R = 0.4\ Q^2/m_\rho^2 \leq 1$
$< E >$ (GeV)	98.1 ± 11.6	104.2	106.4	101.8	103.5
$< p_\mu >$ (GeV/c)	79.9 ± 11.5	72.8	74.8	71.2	72.7
$< \nu >$ (GeV)	18.2 ± 2.0	30.8	31.0	29.9	30.1
$< Q^2 >$ (GeV^2)	2.03 ± 0.52	2.20	2.36	2.12	2.28
$< W >$ (GeV)	5.63 ± 0.33	6.90	6.94	6.79	6.83
$< x >$	0.055 ± 0.011	0.045	0.049	0.045	0.048
$< y >$	0.249 ± 0.032	0.327	0.324	0.323	0.321
$< \|t\| >$ (GeV^2)	0.037 ± 0.005	0.032	0.033	0.033	0.033
$< t_{min} >$ (GeV^2)	0.006 ± 0.002	0.006	0.007	0.006	0.006
$< t' >$ (GeV^2)	0.031 ± 0.005	0.026	0.026	0.026	0.027
t' slope (GeV^{-2})	24 ± 9	33	32	31	30
$< \epsilon >$	0.938 ± 0.015	0.869	0.875	0.871	0.876

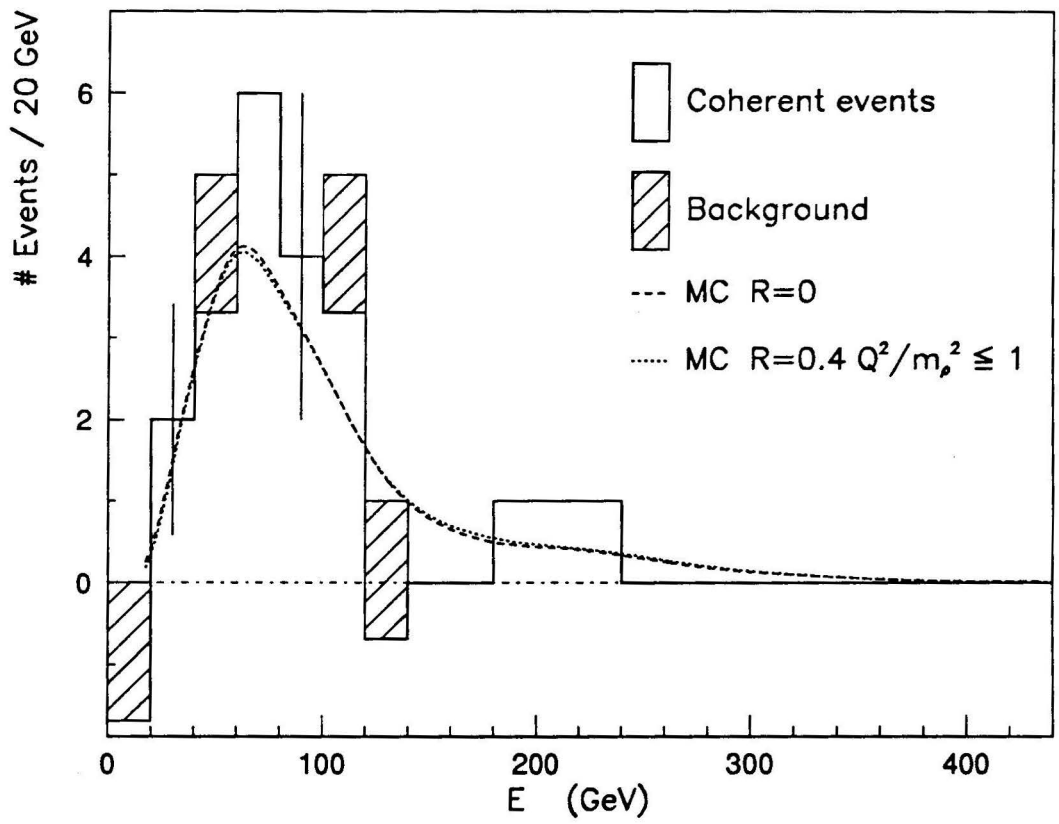

Figure 6.10: Distribution of the total $\mu^{\pm}\pi^{\mp}\pi^{0}$ event energy E for $|t| < 0.1$ GeV^2. The distribution corresponds to that for events without stubs from which the normalized distribution for events with stubs (shown cross-hatched) is subtracted. The curves represent the Monte Carlo simulation, normalized to the signal, using the Belkov-Kopeliovich parametrization of the ρ-nucleus differential cross section (Sec. 4.2.2).

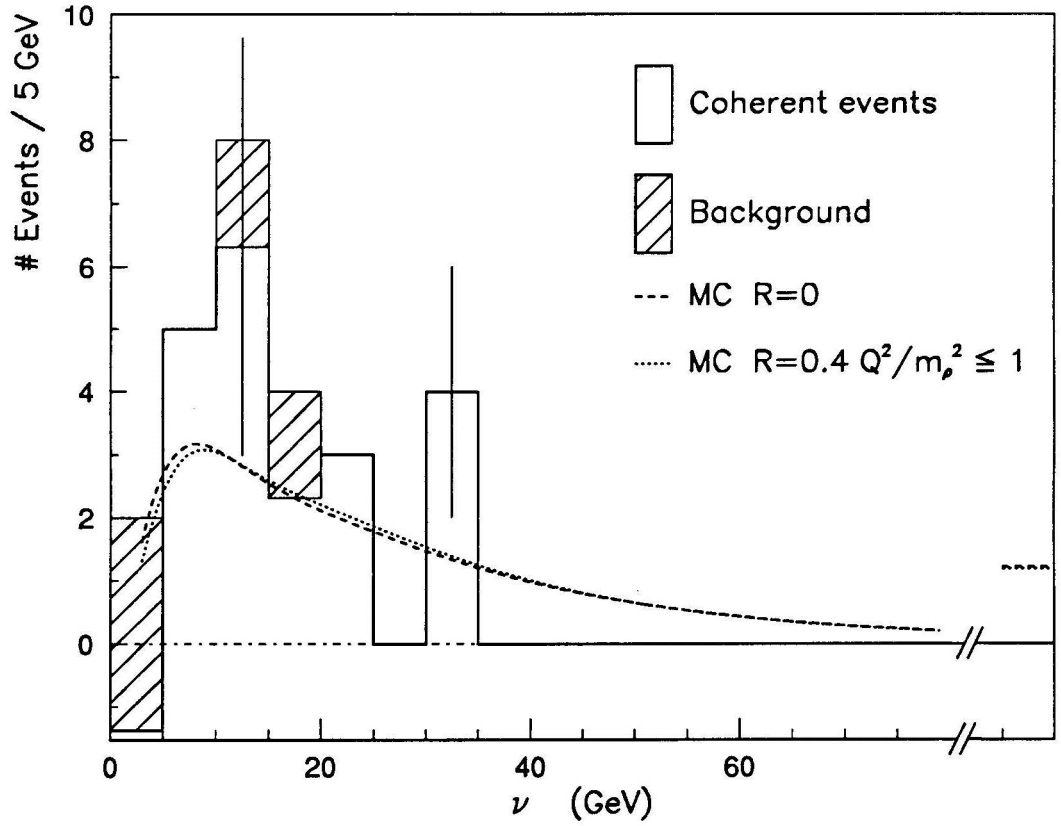

Figure 6.11: Distribution of the energy transfer ν for $|t| < 0.1$ GeV^2 (the curves are as in Fig. 6.10; overflow for $\nu > 80$ GeV is indicated).

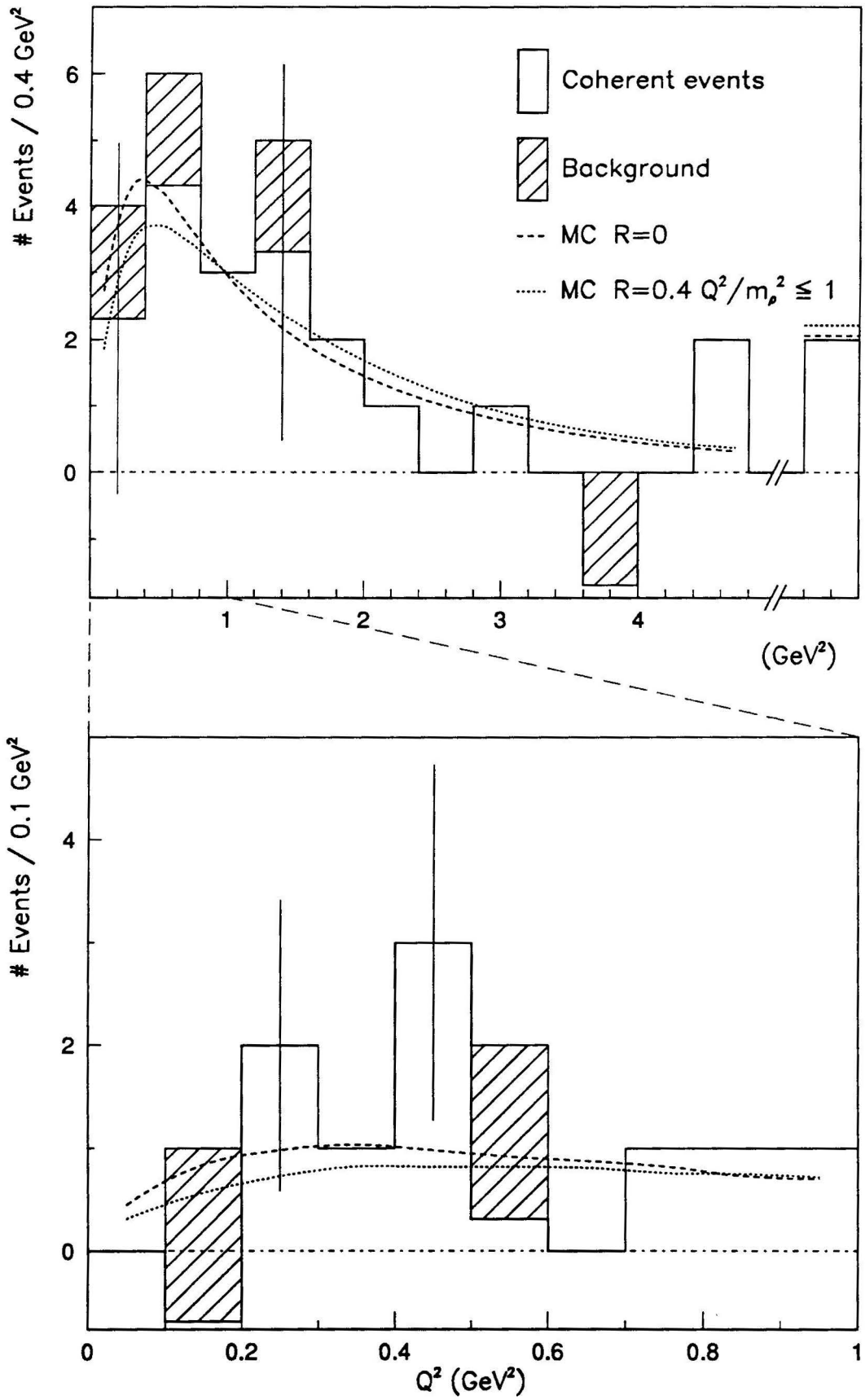

Figure 6.12: Distribution of the four-momentum transfer squared Q^2 for $|t| < 0.1$ GeV^2 (as in Fig. 6.10; overflow for $Q^2 > 4.8$ GeV^2 is indicated).

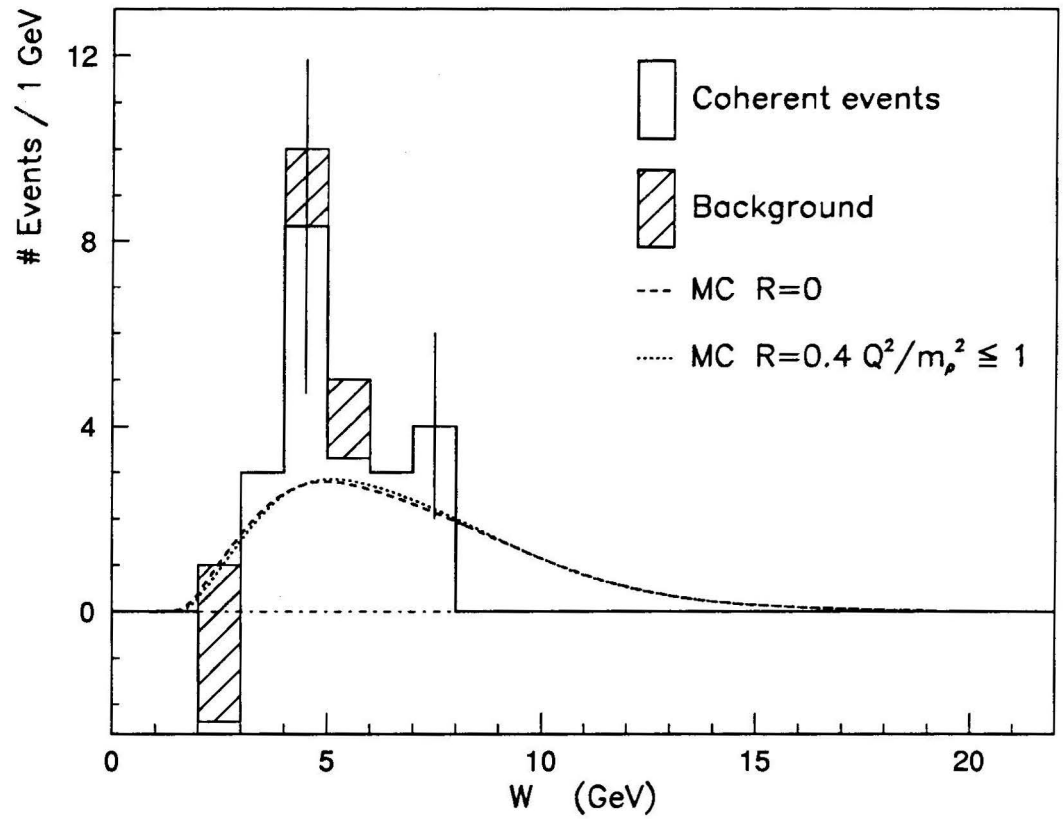

Figure 6.13: Distribution of the hadronic mass W for $|t| < 0.1$ GeV^2 (as in Fig. 6.10).

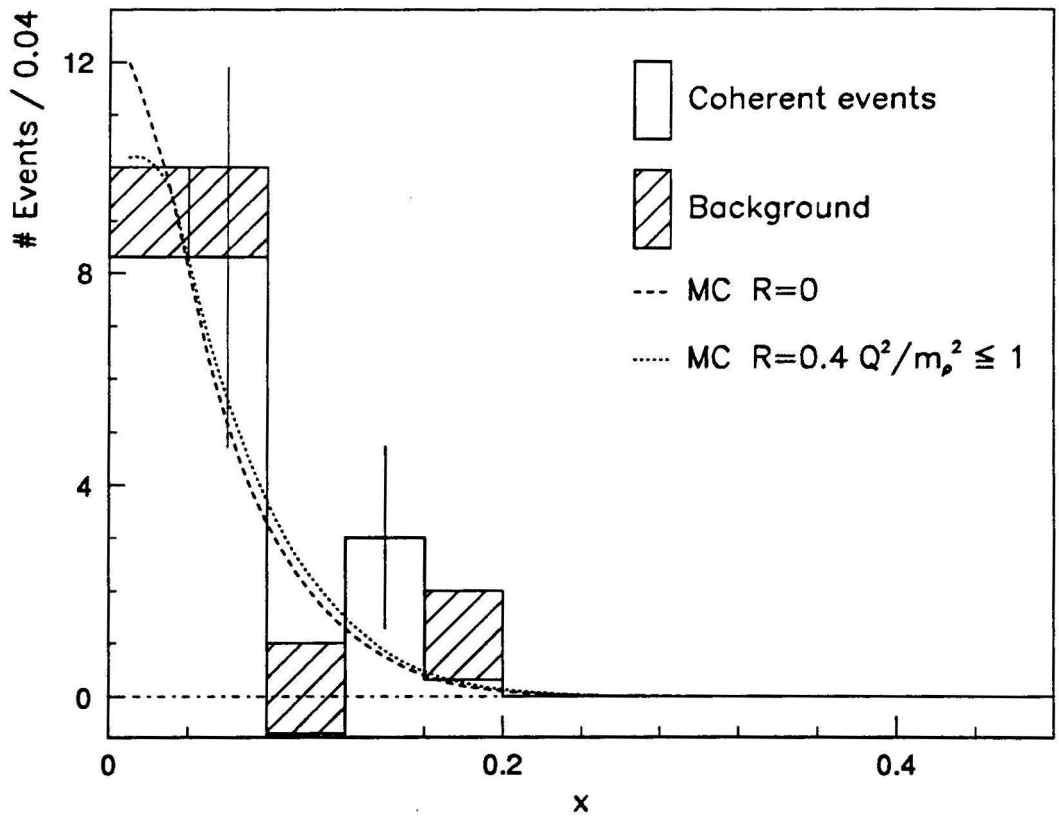

Figure 6.14: Distribution of the Bjorken x variable for $|t| < 0.1$ GeV^2 (as in Fig. 6.10).

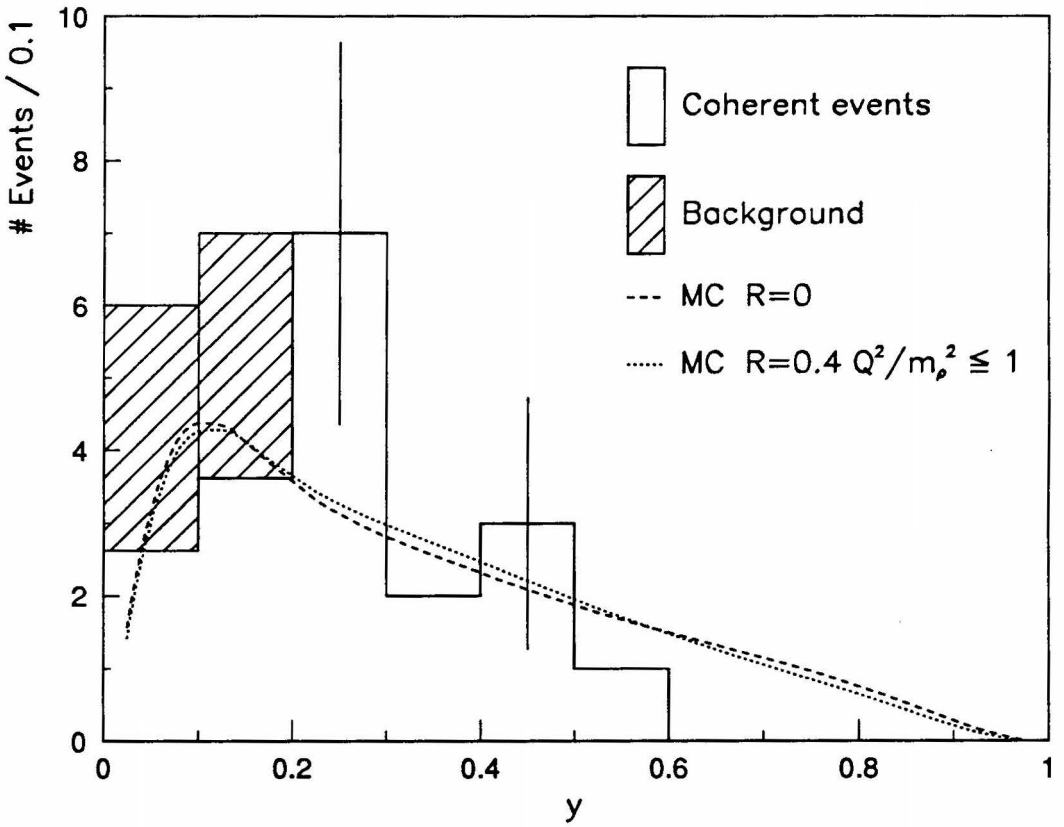

Figure 6.15: Distribution of the Bjorken y variable for $|t| < 0.1$ GeV^2 (as in Fig. 6.10).

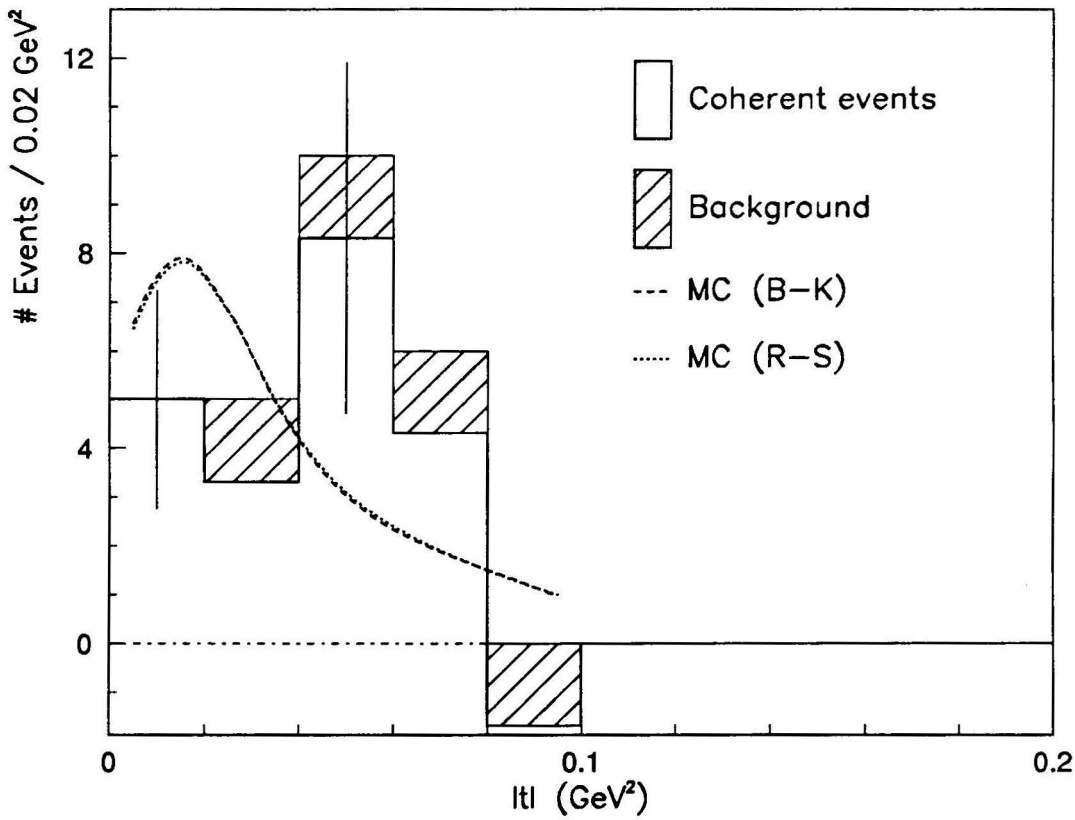

Figure 6.16: Distribution of the square of the momentum transfer to the nucleus $|t|$ for $|t| < 0.1$ GeV^2. The curves represent the Monte Carlo simulation using the Belkov-Kopeliovich and Rein-Sehgal parametrizations of the ρ-nucleus differential cross section (Sec. 4.2.2).

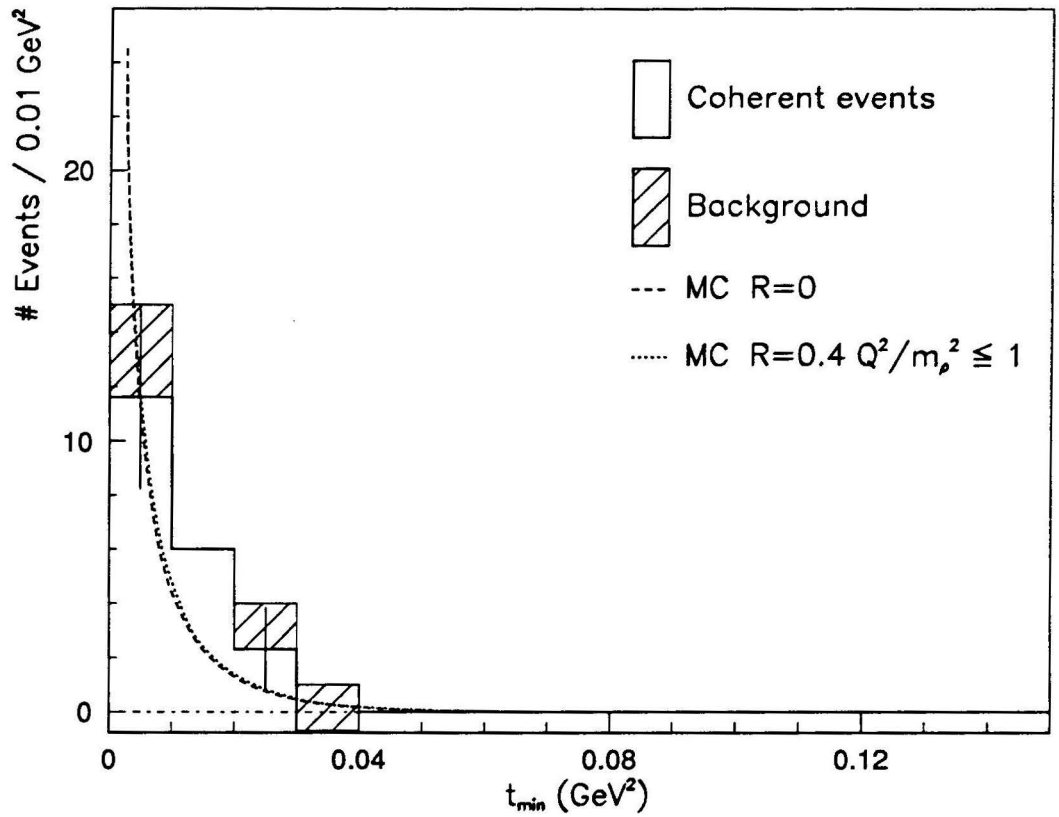

Figure 6.17: Distribution of the minimum momentum transfer t_{min} for $|t| < 0.1$ GeV^2 (as in Fig. 6.10).

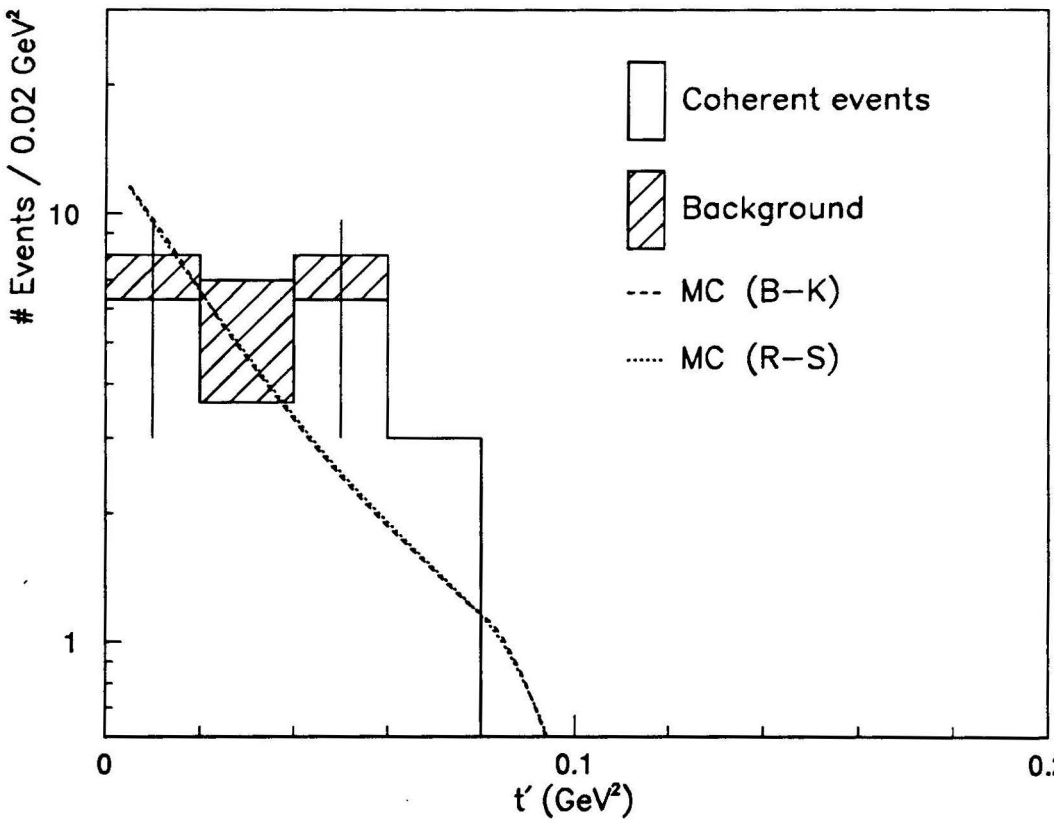

Figure 6.18: Distribution of the momentum transfer t' for $|t| < 0.1$ GeV^2 (as in Fig. 6.16).

Chapter 7
Summary of Results

Using the Fermilab 15-foot Bubble Chamber, we have studied the coherent production of pions and ρ mesons in (anti)neutrino charged current interactions on neon nuclei. The bubble chamber, filled with a heavy Ne–H_2 liquid, was exposed to the Fermilab Quadrupole Triplet beam produced by 800 GeV protons from the Tevatron. The muons were identified using the EMI and IPF arrays of proportional tubes.

The present work comes from the analysis of 330 000 frames, corresponding to 5.5×10^{17} protons on target. All neutral interactions with two prongs were measured in those frames, whereas 29% (78%) of the number of events with three (four) prongs were measured.

7.1 Coherent Production of Single Pions

For the study of the coherent production of single pions in ν_μ and $\overline{\nu}_\mu$ charged current interactions, we selected a sample of 246 $\mu^\pm \pi^\mp$ events, 168 without stubs and 78 with stubs. Using the $|t|$ distributions for events without and with stubs, a coherent signal of 52.1 ± 9.4 events is extracted for $|t| < 0.1$ GeV^2. In that range of $|t|$ values, there are 63 $\mu^\pm \pi^\mp$ events without stubs and 7 $\mu^\pm \pi^\mp$ events with stubs. Several tests were carried out to ensure that the signal is fairly insensitive to the choice of background sample. The losses have been evaluated and the overall correction factor is estimated to be 1.663 ± 0.183, leading to a corrected coherent signal of 86.6 ± 19.6 events.

The number of inclusive ν_μ and $\overline{\nu}_\mu$ charged current interactions on neon nuclei corresponding to the sample of 2-prong interactions used in this work, has been estimated to be 27763 ± 689 after correction for the losses. The rate for single pion coherent production with respect to the total number of charged current interactions is thus found to be $(0.31 \pm 0.07)\%$ for ν_μ and $\overline{\nu}_\mu$ interactions combined. It is $(0.28 \pm 0.07)\%$ for ν_μ interactions and $(0.54 \pm 0.23)\%$ for $\overline{\nu}_\mu$ interactions. Using the measured inclusive charged current interaction cross sections and the calculated average beam energies, the coherent cross sections are determined to be $\sigma_{COH}(\nu_\mu Ne \rightarrow \mu^- \pi^+ Ne) = (337 \pm 85) \times 10^{-40}$ cm^2 / neon nucleus for an average ν_μ beam energy of 91.1 GeV, $\sigma_{COH}(\overline{\nu}_\mu Ne \rightarrow \mu^+ \pi^- Ne) = (263 \pm 112) \times 10^{-40}$ cm^2 / neon nucleus for an average $\overline{\nu}_\mu$ beam energy of 74.5 GeV and $\sigma_{COH}(\nu_\mu(\overline{\nu}_\mu) Ne \rightarrow \mu^-(\mu^+)\pi^+(\pi^-) Ne) = (313 \pm 72) \times 10^{-40}$ cm^2 / neon nucleus for a combined $\nu_\mu + \overline{\nu}_\mu$ average beam energy of 86.3 GeV.

The cross section as a function of energy was compared with the predictions of two models based on the hadron dominance model and the PCAC hypothesis: the Rein-Sehgal model and the Belkov-Kopeliovich model. Good agreement with our data and previous experimental data is observed at energies $\lesssim 50$ GeV but the predicted cross sections appear to be systematically below the data at high energy. Our measured cross section at energies greater than 80 GeV is higher than the predicted cross sections but consistent with them.

The kinematical characteristics of the coherent interactions at $|t| < 0.1$ GeV^2 have been compared with the predictions of the above models. Good overall agreement is obtained. The comparison of average values of kinematical variables seem to favor the results of the Belkov-Kopeliovich model with a $\rho\pi$ cut nucleon form factor. Finally, the slope of the t' distribution was found to be 32 ± 6 GeV^{-2} which agrees with the expected slope for coherent interactions on neon nuclei.

Our results thus corroborate the findings of previous experiments at lower energy and provide a successful test of PCAC at higher energies.

7.2 Coherent Production of Single Rho Mesons

We have also studied the coherent production of single ρ mesons in ν_μ and $\overline{\nu}_\mu$ charged current interactions. Here, the data sample consists of 126 $\mu^\pm \pi^\mp \pi^0$ events, 84 without stubs and 42 with stubs. Using the $|t|$ distributions for events without and with stubs, a coherent signal of 19.2 ± 6.8 events is extracted for $|t| < 0.1$ GeV^2. In that range of $|t|$ values, there are 26 $\mu^\pm \pi^\mp \pi^0$ events without stubs and 4 $\mu^\pm \pi^\mp \pi^0$ events with stubs.

Losses have been taken into account and the overall correction factor was estimated to be 3.27 ± 0.50 leading to a corrected number of $\mu^\pm \pi^\mp \pi^0$ events of 62.8 ± 27.0. Thus, the production rate with respect to the total number of charged current events is found to be $(0.23 \pm 0.10)\%$. Using this rate, the measured total charged current cross sections and the average $\nu_\mu + \overline{\nu}_\mu$ beam energy of 86.3 GeV, the cross section for $\rho^\pm$ coherent production is measured to be $\sigma_{COH}(\nu_\mu(\overline{\nu}_\mu)\, Ne \rightarrow \mu^-(\mu^+)\, \rho^+(\rho^-)\, Ne) = (227 \pm 98) \times 10^{-40}$ cm^2 / neon nucleus.

The cross section was compared with the predictions based on the hadron dominance model using the Rein-Sehgal and the Belkov-Kopeliovich parametrizations of the ρ-nucleus differential cross section, as well as two forms of R, the ratio of longitudinal and transverse ρ production : $R = 0$ and $R = 0.4\ Q^2/m_\rho^2 \leq 1$. The angular characteristics of the ρ decay indicate that a large fraction of the ρ mesons are produced with a longitudinal polarization.

The kinematical characteristics of the $\mu^\pm \pi^\mp \pi^0$ events at $|t| < 0.1$ GeV^2 were compared with the predictions of the model. Good agreement was observed for the E, Q^2 and x distributions but a significant deficit of events was observed in the ν distribution at high values of ν. The slope of the t' distribution was found to be 24 ± 9 GeV^{-2}, in agreement with the value expected for coherent scattering off neon nuclei.

Appendix A
E632 Collaboration

H. C. Ballagh, H. H. Bingham, W. B. Fretter, J. Lys, G. P. Yost

University of California, Berkeley, USA.

P. J. W. Faulkner, G. T. Jones, R. W. L. Jones, R. J. Krawiec, K. E. Varvell

University of Birmingham, UK.

M. Barth, E. De Wolf, P. Marage, J. Moreels, J. Sacton, L. Verluyten

Inter-University Institute for High Energies (ULB-VUB), Brussels, Belgium.

G. Harigel, D. R. O. Morrison, P. Schmid, H. Wachsmuth

CERN, Switzerland.

M. M. Aggarwal, T. K. Chatterjee, M. Kaur, J. M. Kohli, I. S. Mittra, J. B. Singh, P. M. Sood

Panjab University, India.

J. Hanlon, W. Smart, L. Voyvodic

Fermilab, USA.

R. J. Cence, F. A. Harris, V. Jain, M. D. Jones, M. W. Peters, V. Z. Peterson

University of Hawaii, USA.

R. C. Campbell, E. F. Clayton, D. B. Miller, M. M. Mobayyen, P. Nailor, S. Wainstein

Imperial College of Science, Technology and Medicine, UK.

R. A. Burnstein, P. Kasper, R. Naon, H. A. Rubin

Illinois Institute of Technology, USA.

P. V. K. S. Baba, S. K. Badyal, Devanand, V. K. Gupta, G. L. Kaul, N. K. Rao

University of Jammu, India.

M. Aderholz, N. Schmitz, W. Wittek

Max-Planck-Institut für Physik und Astrophysik, Munich, Germany.

P. P. Allport, G. Corrigan, G. Myatt

Department of Nuclear Physics, Oxford, UK.

D. DeProspo, P. Jacques, M. Kalelkar, M. Lauko, R. Plano, P. Stamer

Rutgers University, USA.

J. Guy, R. Sekulin, S. Sewell, W. Venus

Rutherford Appleton Laboratory, UK.

J. P. Baton, C. Coutures, M. A. Jabiol, P. Kasper, M. Neveu

DPhPE, Centre d'Etudes Nucléaires, Saclay, France.

E. B. Brucker, E. L. Koller

Stevens Institute of Technology, USA.

H. Akbari, T. Kafka, W. A. Mann, R. H. Milburn, A. Napier, D. Passmore,

B. Saitta, J. Schneps, S. Willocq

Tufts University, USA.

Appendix B

Derivation of the formula for $|t|$

Let us consider the case of an interaction with a target nucleus initially at rest and with no stubs in the final state. Given the four-momentum vectors for the target nucleus in the initial and final state,

$$\begin{aligned} \mathcal{N}_i &= (M_{\mathcal{N}}, 0) \,, \\ \mathcal{N}_f &= (E_{\mathcal{N}}, \vec{p}_{\mathcal{N}}) \,, \end{aligned}$$

the square of the four-momentum transfer to the nucleus becomes

$$\begin{aligned} |t| \equiv -t &= -(\mathcal{N}_f - \mathcal{N}_i)^2 \\ &= -(E_{\mathcal{N}} - M_{\mathcal{N}})^2 + |\vec{p}_{\mathcal{N}}|^2 \\ &= |\vec{p}_{\mathcal{N}}|^2 - K_{\mathcal{N}}^2 \,, \end{aligned} \tag{B.1}$$

since $E_{\mathcal{N}} = M_{\mathcal{N}} + K_{\mathcal{N}}$, with $K_{\mathcal{N}}$ the kinetic energy of the nucleus in the final state. Momentum conservation implies

$$\vec{p}_{\mathcal{N}} = \vec{p}_\nu - \sum_i \vec{p}_i \,,$$

where the sum is over all the particles observed in the final state. Moreover,

$$\vec{p}_\nu = E_\nu \, \hat{x} = \Big[\sum_i E_i + K_{\mathcal{N}}\Big] \, \hat{x} \,,$$

with $\hat{x} = \vec{p}_\nu / |\vec{p}_\nu|$ a unit vector along the neutrino beam direction. The nucleus momentum can then be expressed as

$$\begin{aligned} \vec{p}_{\mathcal{N}} &= \Big[\sum_i E_i + K_{\mathcal{N}}\Big] \, \hat{x} - \sum_i \vec{p}_i \\ &= \Big[\sum_i (E_i - p_{iL}) + K_{\mathcal{N}}\Big] \, \hat{x} - \sum_i \vec{p}_{iT} \,, \end{aligned}$$

where the final state three-momenta have been separated into longitudinal and transverse components with respect to the neutrino direction. Consequently, the square of the four-momentum transfer becomes

$$\begin{aligned} |t| &= \left[\sum_i (E_i - p_{iL}) + K_{\mathcal{N}}\right]^2 + \left[\sum_i \vec{p}_{iT}\right]^2 - K_{\mathcal{N}}^2 \\ &= \left[\sum_i (E_i - p_{iL})\right]^2 + \left[\sum_i \vec{p}_{iT}\right]^2 + 2\sum_i (E_i - p_{iL})\, K_{\mathcal{N}} \qquad \text{(B.2)} \\ &\simeq \left[\sum_i (E_i - p_{iL})\right]^2 + \left[\sum_i \vec{p}_{iT}\right]^2 . \end{aligned}$$

Neglecting the last term in (B.2) leads to an error of

$$\begin{aligned} \frac{\Delta|t|}{|t|} &= \frac{2\sum (E_i - p_{iL})\, K_{\mathcal{N}}}{|t|} \\ &\leq \frac{2\sqrt{|t|}\, K_{\mathcal{N}}}{|t|} = \frac{2\sqrt{|t|}}{|t|}\, \frac{|\vec{p}_{\mathcal{N}}|^2}{2M_{\mathcal{N}}} . \end{aligned}$$

From (B.1), $|\vec{p}_{\mathcal{N}}|^2 \simeq |t|$ because $K_{\mathcal{N}}^2 < 10^{-5}$ GeV^2 for $|t| < 0.1$ GeV^2. Thus,

$$\frac{\Delta|t|}{|t|} \lesssim \frac{\sqrt{|t|}}{M_{\mathcal{N}}}$$

which is $\lesssim 1.2\%$ for $|t| = 0.05$ GeV^2 and $\lesssim 1.7\%$ for $|t| = 0.1$ GeV^2, with the mass of the neon nucleus $M_{\mathcal{N}} = 18.9$ GeV.

Appendix C

Definition of the Kinematical Variables

The kinematical variables used to describe the scattering of leptons off nucleon or nuclear targets are the following (see Fig. C.1):

$q = k - k'$ the four − momentum transfer,

$\nu = \frac{q \cdot p}{M}$

$= E - E'$ (LAB) the energy transfer in the lab frame,

$Q^2 = -q^2$ the square of the four − momentum transfer,

$\simeq 4\,E\,E' \sin^2\frac{\theta}{2}$ where θ is the scattering angle in the lab frame and the lepton masses have been neglected,

$x = \frac{Q^2}{2\,M\,\nu}$ the Bjorken x variable, which in the quark−parton model corresponds to the fraction of momentum carried by the struck quark,

$y = \frac{q \cdot p}{k \cdot p}$ the Bjorken y variable, which represents the

$= \frac{\nu}{E}$ (LAB) fractional energy transfer in the lab frame,

$W^2 = (p+q)^2$ the square of the invariant mass of the

$= M^2 + 2\,M\,\nu - Q^2$ hadronic system,

$= M^2 + Q^2\left(\frac{1}{x} - 1\right)$

The initial and final lepton four-momenta are represented by k and k' whereas the target initial four-momentum is represented by p and M is the mass of the target.

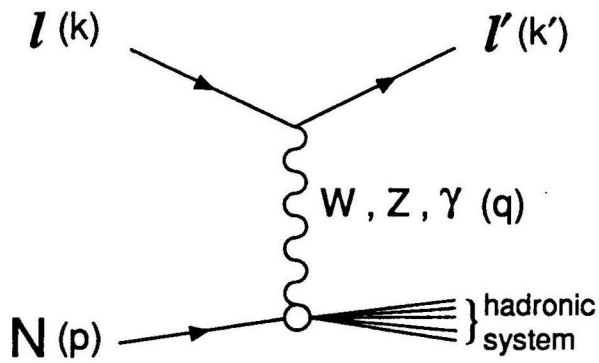

Figure C.1: Feynman diagram for the scattering of leptons off nucleon or nuclear targets.

To describe the diffractive scattering of hadrons off nucleon or nuclear targets, the following momentum transfer variables are also introduced:

- t, which is the square of the momentum transfer to the target,
- t_{min}, which is the minimum value of the momentum transfer $|t|$ necessary to produce a final state hadron V of mass m_V. t_{min} is usually approximated by

$$t_{min} \simeq \left(\frac{Q^2 + m_V^2}{2\nu}\right)^2 ,$$

but the exact expression for t_{min} is given by [90]

$$\begin{aligned} t_{min} &= \frac{A_2 - \sqrt{A_2^2 - A_1 A_3}}{A_1} , \\ \text{with} \quad A_1 &= 1 + \frac{2\nu}{M} - \frac{Q^2}{M^2} , \\ A_2 &= 2(Q^2 + \nu^2) - \left(1 + \frac{\nu}{M}\right)(Q^2 + m_V^2) , \\ A_3 &= (Q^2 + m_V^2)^2 , \end{aligned}$$

- t', which is the difference between the square of the momentum transfer to the target and its minimum value

$$t' \equiv |t| - t_{min} .$$

References

[1] F. Reines, in *International Colloquium on the History of Particle Physics, Paris, 1982*, Journal de Physique **43**, C8-237 (1982).

[2] B. Z. Kopeliovich, P. Marage, submitted to Int. J. Mod. Phys. A.
See also P. Marage, Thèse d'agrégation, Université Libre de Bruxelles, 1991 (unpublished).

[3] T. H. Bauer, R. D. Spital, D. R. Yennie, F. M. Pipkin, Rev. Mod. Phys. **50**, 261 (1978).

[4] C. A. Piketty, L. Stodolsky, Nucl. Phys. **B15**, 571 (1970).

[5] H. Faissner et al., Aachen-Padova Collaboration, Phys. Lett. **125B**, 230 (1983).

[6] P. P. Allport et al., WA59 Collaboration, Phys. Lett. **B232**, 417 (1989).

[7] G. T. Jones et al., WA21 Collaboration, Z. Phys. C **37**, 25 (1987).

[8] G. T. Jones et al., WA21 Collaboration, Z. Phys. C **43**, 527 (1989).

[9] D. Rein, L. M. Sehgal, Nucl. Phys. **B223**, 29 (1983).

[10] A. A. Belkov, B. Z. Kopeliovich, Sov. J. Nucl. Phys. **46**, 499 (1987).

[11] J. D. Bjorken and S. D. Drell, *Relativistic Quantum Mechanics*, McGraw-Hill, New York, 1964.

[12] M. Aguilar-Benitez et al. (Particle Data Group), Phys. Lett. **239B**, 1 (1990).

[13] R. P. Feynman, M. Gell-Mann, Phys. Rev. **109**, 193 (1958).
The possibility of vector current conservation was first pointed out in S. S. Gershtein, J. B. Zeldovich, Sov. Phys. JETP **2**, 576 (1957).

[14] M. Gell-Mann, M. Lévy, Nuovo Cimento **16**, 1729 (1960).

[15] G. Ebel et al., Springer Tracts Mod. Phys. **55**, 239 (1970).

[16] J. M. Gaillard, M. K. Gaillard, F. Vannucci, in *Weak Interactions*, eds. M. K. Gaillard and M. Nikolic, I N2 P3, Paris 1977, p. 61.

[17] For an introduction to gauge theories and to the concepts leading to the electroweak theory, see, for example, E. S. Abers, B. W. Lee, Phys. Rep. **C9**, 6 (1973).

[18] E. D. Commins, P. H. Bucksbaum, *Weak Interactions of Leptons and Quarks*, Cambridge University Press, Cambridge 1983.

[19] T. Cheng, L. Li, *Gauge Theory of Elementary Particle Physics*, Oxford University Press, Oxford 1984.

[20] S. L. Adler, Phys. Rev. **135**, B963 (1964).

[21] J. S. Bell, in *Hadronic Interactions of Electrons and Photons*, eds. J. Cumming and H. Osborn, Academic Press, London 1971, p. 369.

[22] D. W. G. S. Leith, in *Electromagnetic Interactions of Hadrons*, eds. A. Donnachie and G. Shaw, Plenum Press, New York 1978, Vol. I, p. 345.

[23] A. Donnachie, G. Shaw, in *Electromagnetic Interactions of Hadrons*, eds. A. Donnachie and G. Shaw, Plenum Press, New York 1978, Vol. II, p. 169.

[24] F. E. Close, *An Introduction to Quarks and Partons*, Academic Press, London 1979.

[25] L. Stodolsky, in *Methods in Subnuclear Physics, Proceedings of the International School of Elementary Particle Physics, Herceg-Novi, 1968*, ed. M. Nikolic, Gordon and Breach Science Publ. 1970, Vol. IV, p. 259.

[26] R. J. Glauber, in *Lectures in Theoretical Physics* Vol. I, eds. W. E. Brittin and L. G. Dunham, Interscience Publ., New York 1959.

[27] M. L. Goldberger, K. M. Watson, *Collision Theory*, John Wiley & Sons, New York 1964.

[28] G. Grammer, J. D. Sullivan, in *Electromagnetic Interactions of Hadrons* eds. A. Donnachie and G. Shaw, Plenum Press, New York 1978, Vol. II, p. 321.

[29] K. S. Lackner, Nucl. Phys. **B153**, 526 (1979).

[30] H. DeVries, C. W. DeJager, C. DeVries, At. Data and Nucl. Data Tables **36**, 495 (1987).

[31] L. Stutte (Fermilab), NUADA program run for E632, private communication, 1988.
For a description of the NUADA program, see D. C. Carey, June 1975 (unpublished).

[32] L. Stutte, Fermilab Technical Memo TM–1305, 1985.

[33] For a detailed description of the 15-ft Bubble Chamber Holographic System, see:
H. Akbari, Ph.D. Thesis, Tufts University, 1987 (unpublished);
L. Verluyten et al., Nucl. Instr. and Meth. **A292**, 313 (1990);
L. Verluyten et al., Nucl. Instr. and Meth. **A292**, 571 (1990);

H. Bingham et al., Nucl. Instr. and Meth. **A297**, 364 (1990);
L. Verluyten, Ph.D. Thesis, Universiteit Antwerpen, 1991 (unpublished).

[34] H. Foeth et al., Nucl. Instr. and Meth. **A253**, 245 (1987).

[35] M. Aderholz et al., E632 Collaboration, Phys. Rev. D. **45**, 2232 (1992).

[36] V. Jain, Ph.D. Thesis, University of Hawaii, 1988 (unpublished).

[37] V. Jain et al., E632 Collaboration, Phys. Rev. D **41**, 2057 (1990).

[38] D. DeProspo, Ph.D. Thesis, Rutgers University, 1991 (unpublished).

[39] P. Marage et al., WA59 Collaboration, Phys. Lett. **140B**, 137 (1984).

[40] J. H. Friedman and M.H. Wright, SLAC Computation Group Technical Memo CGTM No. 193, 1980. See also CERN Program Library write-up D151.

[41] J. J. Aubert et al., EMC Collaboration, Phys. Lett. **161B**, 208 (1985).

[42] K. J. Foley et al., Phys. Rev. **181**, 1775 (1969).

[43] V. Flaminio, W. G. Moorhead, D. R. O. Morrison, N. Rivoire, *Compilation of Cross Sections : π^+ and π^- induced reactions*, Report CERN-HERA 83-01, 1983. See also reference [44].

[44] A. Baldini, V. Flaminio, W. G. Moorhead, D. R. O. Morrison, *Total Cross Sections for Reactions of High Energy Particles*, Landolt-Börnstein Series, Group I Vol. 12a, ed. H. Schopper, Springer-Verlag, Berlin 1988.

[45] P. Murthy et al., Nucl. Phys. **B92**, 269 (1975).

[46] A. Gsponer et al., Phys. Rev. Lett. **42**, 9 (1979).

[47] J. G. Asbury et al., Phys. Rev. Lett. **19**, 865 (1967).

[48] H. Alvensleben et al., Nucl. Phys. **B18**, 333 (1970).

[49] G. McClellan et al., Phys. Rev. D **4**, 2683 (1971).

[50] See reference [22], Tables 11 and 12, p. 429. Note that the values found in those tables have to be multiplied by a factor of 4 because of a different definition of the coupling constant.

[51] P. Callahan et al., Preprint Fermilab-Pub-84/36-E, 1984.

[52] See reference [3], Table 33 p. 387 and Table 35 p. 393.

[53] J. D. Jackson, Nuovo Cimento **34**, 1644 (1964).

[54] R. G. Glasser, Naval Research Laboratory Report 6150, 1964.

[55] For a description of the Berkeley/Hawaii TUBES Monte Carlo and the implementation of Glasser's smearing formulae, see
M. D. Sokoloff, Ph.D. Thesis, University of California, Berkeley, 1983 (unpublished); and
T. J. Lawry, Ph.D. Thesis, University of California, Berkeley, 1985 (unpublished).

[56] H. G. Heilmann, Internal Note WA21-int-1, University of Bonn, 1978.

[57] S. Barlag et al., WA25 Collaboration, Z. Phys. C **11**, 283 (1982).

[58] N. Armenise et al., BEBC TST Collaboration, Phys. Lett. **102B**, 374 (1981).

[59] P. N. Harriman, A. D. Martin, W. J. Stirling, R. G. Roberts, Phys. Rev. D **42**, 798 (1990).

[60] T. Kitagaki et al., E545 Collaboration, Phys. Rev. D **28**, 436 (1983).

[61] W. A. Mann (Tufts University), private communication, 1991;
see also W. A. Mann, W. Leeson, Soudan 2 Internal Memo PDK-485, 1991.

[62] A. Bodek, J. L. Ritchie, Phys. Rev D **23**, 1070 (1981).

[63] D. Rein, L. M. Sehgal, Ann. Phys. **133**, 79 (1981);
D. Rein, Z. Phys. C **35**, 43 (1987).

[64] D. Allasia et al., WA25 Collaboration, Z. Phys. C **20**, 95 (1983).

[65] P. Allen et al., WA21 Collaboration, Nucl. Phys. **B264**, 221 (1986).

[66] H. J. Grabosch et al., SKAT Collaboration, Z. Phys. C **41**, 527 (1989).

[67] G. D. Barr, Ph.D. Thesis, Oxford University, 1987 (unpublished).

[68] D. Rein, Nucl. Phys. **B278**, 61 (1986).

[69] P. Marage et al., WA59 Collaboration, Z. Phys. C **49**, 385 (1991).

[70] P. S. Auchincloss et al., CCFR Collaboration, Z. Phys. C **48**, 411 (1990).

[71] M. Aderholz et al., E632 Collaboration, Phys. Rev. Lett. **63**, 2349 (1989).

[72] P. Marage et al., WA59 Collaboration, Z. Phys. C **31**, 191 (1986).

[73] P. Marage et al., WA59 Collaboration, Z. Phys. C **43**, 523 (1989).

[74] V. V. Ammosov et al., E180 Collaboration, Sov. J. Nucl. Phys. **45**, 1029 (1987).

[75] H. J. Grabosch et al., SKAT Collaboration, Z. Phys. C **31**, 203 (1986).

[76] E. Isiksal, D. Rein, J. G. Morfin, Phys. Rev. Lett. **52**, 1096 (1984).

[77] F. Bergsma et al., CHARM Collaboration, Phys. Lett. **157B**, 469 (1985).

[78] C. Baltay et al., E53 Collaboration, Phys. Rev. Lett. **57**, 2629 (1986).

[79] D. Bertrand, Subroutine FICOUR, Inter-University Institute for High Energies Note, Brussels, 1986.

[80] F. James, M. Roos, MINUIT version 2.0, CERN Program Library write-up D506.

[81] Y. S. Tsai, Rev. Mod. Phys. **46**, 815 (1974).

[82] J. R. Elliott et al., Phys. Rev. D **17**, 83 (1978).

[83] H. C. Ballagh et al., E546 Collaboration, Phys. Rev. D **37**, 1744 (1988).

[84] J. Lys (U. C. Berkeley), private communication, 1992.

[85] P. Marage et al., WA59 Collaboration, Z. Phys. C **35**, 275 (1987).

[86] C. del Papa et al., Phys. Rev. D **19**, 1303 (1979).

[87] D. G. Cassel et al., Phys. Rev. D **24**, 2787 (1981).

[88] I. Cohen et al., Phys. Rev. D **25**, 634 (1982).

[89] W. D. Shambroom et al., Phys. Rev. D **26**, 1 (1982).

[90] M. K. Gaillard, C. A. Piketty, Phys. Lett. **68B**, 267 (1977).